



Integration of a single photon source on a planar dielectric waveguide

Josslyn Beltran Madrigal

► To cite this version:

Josslyn Beltran Madrigal. Integration of a single photon source on a planar dielectric waveguide. Optics / Photonic. Université de Technologie de Troyes, 2017. English. NNT: 2017TROY0007 . tel-02418314

HAL Id: tel-02418314

<https://theses.hal.science/tel-02418314>

Submitted on 18 Dec 2019

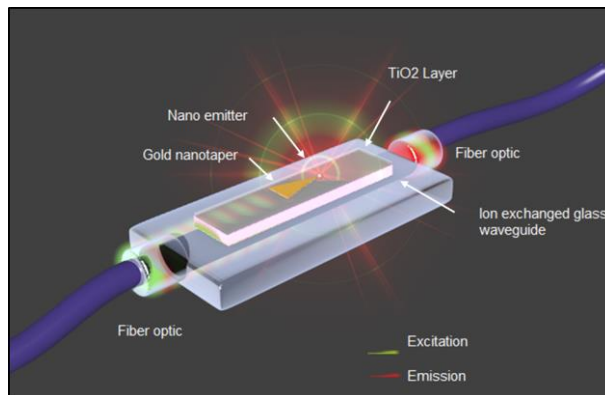
HAL is a multi-disciplinary open access archive for the deposit and dissemination of scientific research documents, whether they are published or not. The documents may come from teaching and research institutions in France or abroad, or from public or private research centers.

L'archive ouverte pluridisciplinaire **HAL**, est destinée au dépôt et à la diffusion de documents scientifiques de niveau recherche, publiés ou non, émanant des établissements d'enseignement et de recherche français ou étrangers, des laboratoires publics ou privés.

Thèse
de doctorat
de l'UTT

Josslyn BELTRAN MADRIGAL

Integration of a Single Photon Source on a Planar Dielectric Waveguide



Spécialité :
Matériaux, Mécanique, Optique et Nanotechnologie

2017TROY0007

Année 2017

THESE

pour l'obtention du grade de

DOCTEUR de l'UNIVERSITE DE TECHNOLOGIE DE TROYES

Spécialité : MATERIAUX, MECANIQUE, OPTIQUE ET NANOTECHNOLOGIE

présentée et soutenue par

Josslyn BELTRAN MADRIGAL

le 14 mars 2017
&

Integration of a Single Photon Source on a Planar Dielectric Waveguide

JURY

M. S. HUANT	DIRECTEUR DE RECHERCHE CNRS	Président
M. R. BACHELOT	PROFESSEUR DES UNIVERSITES	Examinateur
M. D. BARBIER	DOCTEUR	Examinateur
M. Y. DE WILDE	DIRECTEUR DE RECHERCHE CNRS	Rapporteur
M. J. A. SANCHEZ GIL	INVESTIGADOR CIENTIFICO	Rapporteur

Personnalités invitées

M. S. BLAIZE	MAITRE DE CONFERENCES	Directeur de thèse
M. R. SALAS-MONTIEL	INGENIEUR DE RECHERCHE UTT	Directeur de thèse

Dedication

*To my parents, my sister, my brother and the kids. I
hope you feel proud of me. As some famous man
once said...*

*"The Lord gave us the atoms, and it's up to us to make
them dance." -Homer Simpson*

Acknowledgements

Firstly, I would like to thank to the "Agence Regional de la Recherche" under the project SINPHONIE, by the support given for my PhD thesis. To the Institute Néel and the Teem photonic company for all their support in this project.

To Dr. Sylvain BLAIZE and Dr. Rafael SALAS MONTIEL for their guidance, support, advice and friendship during all this process. Thank you for giving the opportunity to work with you and for sharing your time and knowledge with me .

To the members of the jury, Dr. Serge Huant, Dr. Yannick De Wilde, Dr. José Sánchez Gil and Dr. Renaud Bachelot, for taking the time to read my manuscript and for their review. I would particularly like to thank Dr. Denis Barbier for give me the opportunity to make a stage at Teem Photonics. This experience helped me to reaffirm my vocation.

To Dr. Wei Geng, Dr. Nancy Rahbany and Martin Berthel for their help in the experiments presented in this thesis.

To the technical and the administrative staff of the University of Technology of Troyes (UTT). Thanks for your welcome and support during this time.

To my family for all your love and support. Thank you for your lessons and for believing in me. To my nieces and nephew for laughing and playing with me. To all my friends in Mexico who are always supportive of me. I love you guys !

To my best friend Mauricio for being there in all the important moments for the last ten years and for believing in me all this time.

To all the members of the Laboratoire de Nanotechnologie et d'Instrumentation Optique (LNIO) of the UTT to make me feel at home. Special thanks to the lunch team of the first floor.

To my special friends in the LNIO, Dr. Clothaire Chevalier Cesar, Dr. Hyun Jeong and the future doctors Avril Meza Olivo and Jean Philippe Girard. To Dr. Ricardo Tellez

Limón for being with me each day hearing and helping me. To my friends from others laboratories of UTT, as LOSI, LASMIS and Tech-cico. You know how much your friendship means for me.

To the babel association for give me the opportunity to share my language and my culture, for being my friends and for all the nights together. To all the Mexican community in Troyes. To my roommates and friends Marie Lacasse and Carol Auz Orbe for everything.

Last but not least, to my partner in this trip, thank you Dr. Malte Paskuda to show me what are the important things in this life. Also thank you to all the Paskuda family to your kindness and friendship.

As a big rock star once said... *"Not only would I have been nothing without you, if not for all of the people who were around me since the beginning; some who are still with me to this very day. Thank you very much! (Gracias totales!)"* Gustavo Cerati

General introduction

Devices miniaturization plays an important role in our lives. Electronic devices that once occupied large volumes now fit in a small integrated circuit that can be found in current devices as computers and smartphones. The current miniaturization technologies bring us closer to the manufacturing of atomic-scale devices with the promise to be the basis of next advances in information processing and a powerful tool in the detection of micro- and nano- organisms.

For devices at this scale, electron transport is replaced by the manipulation of individual particles, the photon being the most commonly used among them. In quantum information, the single photon as a quantum of energy (*qubits*) represents the analogous case of the classical *bit* of information [1]. Each *qubit* can be distinguished and classified according to the information of the superposition of its two eigenstates [2, 3]. Studies show that the use of *qubits* could improve some tasks as cryptography [4–6], data processing [7, 8], and quantum information.

In addition to applications in quantum information, the control of the emission from single photons has been studied in several research areas. Just to mention a few of them, single-photon sources have been used as biomarkers [9–11], biosensors [12–16] and localized sources [17, 18]. These new promising applications have made the integration of single-photon sources on-chips a recurrent subject of study in the last years. The propagation of photons through complex circuits along long distances with low losses remains a challenge that requires high-quality devices.

In this thesis we present a contribution on the design, fabrication, and characterization of photonic-plasmonic structures towards the integration of a single-photon source on optical chips across the visible spectrum. For the design, we explore the efficient excitation and collection of the emission of a nanoemitter with plasmonic and photonic modes on

a gold nanotaper and an integrated optics structure formed by a high-index waveguiding layer of titanium dioxide (TiO_2) and a low-index contrast ion exchanged waveguide on glass (IEW).

Following the reciprocity theorem of electromagnetism, we demonstrated the efficient excitation and collection of the spontaneous emission radiated by a nanoemitter with the use of waveguides modes on a dielectric photonic structure. Furthermore, we experimentally demonstrated an enhancement of the photoluminescence intensity and spontaneous emission rate of nanoemitters integrated on such structure compared to the free space elements.

For an hybrid photonic-plasmonic structure, we use the coupling between photonic and plasmonic modes, which allows an efficient transfer of the energy between a weakly confined mode in the IEW to a plasmonic mode confined in an effective volume of few cubic nanometers. This confined mode can interact with a nanosource and enhance its florescence emission through Purcell factor effect. This enhanced emission can be then efficiently coupled back into the IEW mode in a reciprocal scenario.

The materials used in the design of the structures were selected in order to obtain low-propagation losses and high enhancement of the fluorescence of the nanosource (NS). The IEWs on glass are singlemode waveguides with low propagation losses in the visible spectrum and present high compatibility with commercial optical fibers, which makes the design attractive for classical and quantum communications systems. The TiO_2 layer, placed on top of the IEW, works as a high index medium that confines the photonic mode and enhances the amplitude of the electric field over the surface of the hybrid structure. A gold nanotaper additionally placed on top of the TiO_2 layer, works as an adiabatic mode coupler to allow the slowly energy transfer from the photonic to the plasmonic modes. The tapered shape of the plasmonic structure provides a nanofocusing effect of light at its apex which has a diameter of 50 nm.

In this work, we also present an experimental part that include the fabrication of the hybrid structure and its optical characterization. Characterizations were performed in the far and in the near field with the use of the scanning near-field optical microscopy (SNOM) in perturbation and scattering modes. Moreover, we proposed a SNOM configuration that mimics the interaction of a NS and guided systems, mapping the local density

of guided modes (LDOM). With this configuration, an experimental verification of the reciprocity theorem of electromagnetism was done.

This thesis was made in collaboration with the Institute Néel and the Teem Photonics Company within the SINPHONIE project (SINgle PHOTon source iNtegrated on an hybrid Ion Exchange waveguide platform) funded by the French National Research Agency (ANR, l'Agence nationale de la recherche).

The manuscript of the thesis is structured as follows :

Chapter 1 : The first part of this chapter is dedicated to the description of the interaction between the single-photon source and its surrounding environment from the point of view of electrodynamics. In this part, we describe the concepts of spontaneous decay rate, lifetime, local density of states, and Purcell factor. In the second part, we briefly describe the types of single-photon sources commonly used and its integration into plasmonic structures.

Chapter 2 : In this chapter, we describe in detail the design of the photonic structures. We presented a theoretical study of the mode coupling. Using the reciprocity theorem of electromagnetism, we studied the interaction of a NS and a guided system. In this chapter is also presented the numerical simulations of the collection efficiency at the end of the IEW, Purcell factor, and fluorescence enhancement based on the finite-difference time-domain method.

Chapter 3 : This chapter is dedicated to the description of the methods used in the fabrication and the characterization of the hybrid integrated structures. We briefly describe the SNOM setups for the characterization of the sample. We present the description of the SNOM configuration that allows us to obtain a measure of the collected light at the end of the IEW, when it is excited by a dipole oscillating close to its surface. An experimental verification of the reciprocity theorem of the electromagnetism was done with the use of this SNOM configuration.

Finally, in this chapter, we present the measurements of the fluorescence signal and lifetime of nanocrystals placed on top of one of our designed structures presented in chapter 2.

Chapter 4 : This chapter is aim at the study of a prismatic gold nanotaper integrated on top of a guided photonic system. We discuss about the design of the plasmonic structure,

its use as enhancer of Purcell Factor, and how it is possible to excite this structure with IEW guided modes.

We present the modeling of the integration of a single photon source in this hybrid structure and its optimization. This structure is also presented as an integrated system able to efficiently excite and collect the emission from the nanosource.

In the experimental part of this chapter, we present the fabricated structures and photoluminescence intensity maps of the nanotaper.

At the end, a general conclusion and perspectives are given.

Contents

Acknowledgements	iii
General introduction	v
1 Basic concepts of nanosources integrated into optical devices	1
1.1 Ideal single photon sources	2
1.1.1 Local density of electromagnetic states	3
1.1.2 Fermi's golden rule	5
1.1.3 Spontaneous decay in terms of the partial local density of states .	7
1.1.4 Spontaneous decay rate by Green's function	9
1.1.5 Total LDOS	9
1.1.6 Purcell's Factor and quantum yield	10
1.2 Real nanosources	13
1.2.1 Deterministic sources	14
1.2.2 Probabilistic sources	16
1.3 Surface enhanced fluorescence by plasmonic fields	16
1.3.1 Surface plasmon polariton	17
1.3.2 Localized surface plasmons	20
1.4 Objective of the thesis	23
2 Integrated photonic structure on glass	25
2.1 Basic concepts of waveguides	26
2.1.1 Field distribution of modes	27
2.1.2 Two-mode coupling	28
2.1.3 Dispersion relation	30

2.1.4	Reciprocity theorem of electromagnetism	31
2.2	Hybrid photonic structure	33
2.2.1	Electric field enhancement at the surface	34
2.2.2	Two reciprocal scenarios	38
2.3	Tapered TiO ₂ ridges	41
2.4	Conclusion	42
3	Experimental validation of the integrated photonic structure	44
3.1	Ions exchanged waveguides on glass	44
3.1.1	TiO ₂ overlayer on IEWs	46
3.1.2	Fabricated samples	48
3.2	Optical near field characterization techniques for the integrated photonic structure	54
3.2.1	SNOM in perturbation mode	54
3.2.2	SNOM in scattering mode	57
3.3	Experimental results of SNOM	60
3.3.1	Results of the p-SNOM	60
3.3.2	Results of s-SNOM	64
3.4	SNOM in illumination mode : towards the measurement of the Local Density of Guided Modes (LDOM)	67
3.4.1	Results of i-SNOM	71
3.5	Enhancement of the photoluminescence of CdSe/CdS nanocrystals with the integrated photonic structure on IEW	74
3.5.1	Photoluminescence intensity measurements	76
3.5.2	Time-resolved photoluminescence and Purcell factor measurements	81
3.6	Conclusion	83
4	Integration of an adiabatic photonic-plasmonic mode coupler	85
4.1	Prismatic gold nanotaper as a enhancer of LDOS	85
4.1.1	Fluorescence mapping of the prismatic gold nanotaper on glass .	87
4.2	Integration of a prismatic gold nanotaper into the hybrid IEW platform .	89
4.2.1	Plasmonic-photonic mode coupling analysis	91

4.2.2	Analysis of the field propagation along the hybrid integrated plasmonic-photonic structure	93
4.2.3	Analysis of the field propagation along the hybrid integrated plasmonic-photonic structure : the reciprocal scenario	95
4.2.4	Optimal shape of the adiabatic photonic mode coupler	101
4.3	Fabrication of the plasmonic-photonic structure	104
4.4	Conclusion	106
5	General conclusion	108
6	Résumé en français	111
6.1	Concepts préliminaires	113
6.1.1	Une source de photons uniques idéale	113
6.1.2	Nano émetteurs	118
6.1.3	Exaltation de la fluorescence par des champs plasmoniques	119
6.1.4	Rappels d'optique guidée	121
6.2	Conception d'une structure hybride photonique-plasmonique : vers l'intégration de sources de photons uniques sur guide d'onde	123
6.2.1	Exaltation du champ sur la surface	124
6.2.2	Théorème de réciprocité de l'électromagnétisme	126
6.2.3	Coupleur adiabatique de modes plasmoniques (Nano-Taper)	127
6.2.4	Nano émetteur intégré sur une structure hybride plasmonique-photonique	130
6.3	Mesure de la LDOM	133
6.4	Guides hybrides en verre pour l'amélioration de la photoluminescence de nano-émetteurs dans du spectre visible	137
6.4.1	Mesure de photoluminescence	139
6.4.2	Mesure de la durée de vie et du facteur de Purcell	140
6.5	Conclusion générale	142
Appendix		145
A	Green's functions formalism : spontaneous decay in a two-levels atom	145

B K-vector for a surface plasmon polariton	147
B.1 Surface polariton plasmon	147
C Orthogonality property of modes	150
D Scanning near-field optical microscopy concepts	152

Chapter 1

Basic concepts of nanosources integrated into optical devices

The concept of photon as the elementary particle or quantum of the electromagnetic radiation was introduced by Planck in 1900 in order to explain the black-body radiation spectrum [19]. Nowadays, photons could be the master key to fabricate high performance devices at nanometric scale. The characteristics of a photon as its high speed transition and spin promise to improve some quantum information task. While its small size makes it a excellent tool to increase the storage information. The manipulation and propagation of single photons through complex circuit by long distances and low losses remains a challenge. In the last years there are several works that proposed new designs of optical systems in order to integrate single-photon sources on chip.

The present chapter is an introduction to the basic concepts that will help us to understand the interaction between light and the matter at the nanometer scale. Firstly, we give a description of the light-matter interaction making use of the electrodynamics, where we introduce the lifetime, the Purcell's factor, and the concept of local density of states. Then we briefly describe the single-photon sources that are commonly used and we show some recent works about the interaction between single-photon sources and surface plasmons in plasmonic structures.

1.1 Ideal single photon sources

In the ideal single-photon source, only one photon is released at regular interval times determinated by the user (Deterministic source) [20–22]. In this kind of sources the probability of emitting a single photon is 100% and the probability of multiple-photon emission is 0%. These sources can be seen as a two-level energy atoms, as it is shown in figure 1.1. In this figure, we represent the steps to get a photon emission in a two internal levels system. In the first state, one external photon is absorbed and $|e\rangle$ state is excited. Then, after a time delay τ the state decays to the ground state emitting a photon (fluorescence effect). This τ time is known as the fluorescence *lifetime*.

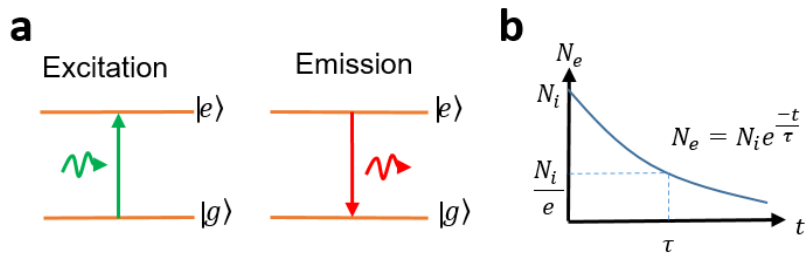


FIGURE 1.1 – Single photon sources. a) Excitation and emission of a ideal single photon source. b) Fluorescence decay with N_i the number of excited atoms at $t = 0$, τ the fluorescence lifetime.

In this system at time $t = 0$ after the excitation, the population N_e of excited atoms in the $|e\rangle$ state starts to decrease exponentially to the ground state $|g\rangle$. This exponential decay can be described as

$$N_e(t) = N_i e^{-t/\tau}, \quad (1.1.1)$$

where N_i is the initial population at $t = 0$. At the time $t = \tau$ the population N_e is equal to N_i/e (the population was reduced to 38% of the initial population). The lifetime is also defined in terms of the decay rate γ as

$$\tau = 1/\gamma. \quad (1.1.2)$$

1.1.1 Local density of electromagnetic states

We consider that the two-level system is in a volume $V \ll \lambda^3$, with λ the excitation wavelength (figure 1.2). The ground state $|g\rangle$ and the excited state $|e\rangle$ are separated by an energy gap $E = \hbar\omega_0$ ($\omega_0 = 2\pi c/\lambda$) .

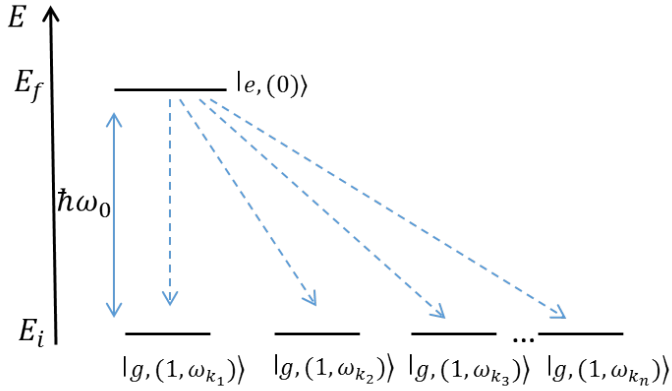


FIGURE 1.2 – Transition from an excited state e to a set of final states g with difference between initial and final energies is $(E_i - E_f) = \hbar\omega_0$ (image reproduced from [23]).

The system can be modeled by the Maxwell's equations for a homogeneous medium without external currents [23] :

$$\nabla \cdot \mathbf{E} = 0, \quad (1.1.3a)$$

$$\nabla \cdot \mathbf{H} = 0, \quad (1.1.3b)$$

$$\nabla \times \mathbf{E} = -\mu \frac{\partial \mathbf{H}}{\partial t} \quad (1.1.3c)$$

$$\nabla \times \mathbf{H} = \epsilon \frac{\partial \mathbf{E}}{\partial t}. \quad (1.1.3d)$$

From these equations it possible to show that

$$\nabla \times \nabla \times \mathbf{E} = -\mu \epsilon \frac{\partial^2 \mathbf{E}}{\partial t^2}. \quad (1.1.4)$$

Assuming that \mathbf{E} is a wave and $e_k = e_{k0}e^{i\omega t}$, then equation 1.1.4 becomes,

$$\nabla \times \nabla \times e_k(\mathbf{r}, \omega_k) - \frac{\omega_k^2}{c^2} e_k(\mathbf{r}, \omega_k) = 0, \quad (1.1.5)$$

where c is the speed of light in vacuum. This is better-known as the Lagrangian equation of the Helmholtz equation. Here, $e_n(\mathbf{r}, k)$ are the eigenvectors of the Helmholtz equation and the eigenmodes of the system and ω_k are the eigenfrequencies. These solutions correspond to the mode field profile of the photons.

These e_k eigenvectors are ortho-normal and therefore, they obey the orthogonality condition

$$\int_V e_k(\mathbf{r}, \omega_k) \cdot e_k'^*(\mathbf{r}, \omega_k) d^3r = \delta_{kk'}. \quad (1.1.6)$$

The density of eigenstates (DOS) describes the number of states per unit of energy per volume (or number of modes) per unit of frequency (energy) in a volume V, it can be written as [24] :

$$\rho(\omega) = \frac{1}{V} \sum_k \delta(\omega - \omega_k). \quad (1.1.7)$$

The local density of states (LDOS) $\rho_e(\mathbf{r}, \omega)$ is a summation over the full set of eigenmodes, each eigenmode being weighted by its normalized amplitude at a specific location \mathbf{r} into space. This reads as follows :

$$\rho_e(\mathbf{r}, \omega) = \sum_n |e_n(\mathbf{r})|^2 \delta(\omega - \omega_k). \quad (1.1.8)$$

Obviously, using the orthogonality condition 1.1.9 with $k' = k$, we find out that the LDOS is linked to the DOS by

$$\int_V \rho_e(\mathbf{r}, \omega) d^3r = \rho(\omega). \quad (1.1.9)$$

Variations of the system can cause changes in the LDOS. From equations 1.1.7 and 1.1.8, it is possible to observe its relation with the amplitude of the modes and the volume of the interaction, but these eigenmodes are also related with the decay rate of the photons, its lifetime, its polarization and the power of emitted light from the NS, only to mention a few. The understanding of these relationships is the base of our work, it aspect help us to better design structures able to increase the LDOS of the system and manipulate the emission of the NS. The objective of the next sections is show how these aspects can be related all together in terms of the enhancement of the LDOS.

1.1.2 Fermi's golden rule

Firstly, to describe the LDOS in terms of rate decay between the $|g\rangle$ state and the $|e\rangle$ we use the Fermi's golden rule [23, 25]. It is defined as the probability to decay per unit of time. The derivation of this law is commonly made by making use of the perturbation theory.

Here ; we define the Hamiltonian of the system from the figure 1.2 as

$$\hat{\mathbf{H}} = \hat{\mathbf{H}}_0 + \hat{\mathbf{H}}' \quad (1.1.10)$$

with $\hat{\mathbf{H}}_0$ an Hamiltonian operator of the Schrödinger equation and $\hat{\mathbf{H}}'$ an additional Hamiltonian operator that represent some extra potential due to applied electric fields (a perturbation of the system). According with the time-dependent Schrödinger equation

$$i\hbar \frac{\delta |\psi(t)\rangle}{\delta t} = (\hat{\mathbf{H}}_0 + \hat{\mathbf{H}}') |\psi(t)\rangle \quad (1.1.11)$$

with

$$|\psi(t)\rangle = \sum_e e^{-iE_e t/\hbar} a_e(t) |e\rangle \quad \text{and} \quad \hat{\mathbf{H}}_0 |e\rangle = E_e |e\rangle \quad (1.1.12)$$

Using equation 1.1.12 in equation 1.1.11, we can obtain

$$i\hbar \frac{\delta \sum_e e^{-iE_e t/\hbar} a_e(t) |e\rangle}{\delta t} = (\hat{\mathbf{H}}_0 + \hat{\mathbf{H}}') \sum_e e^{-iE_e t/\hbar} a_e(t) |e\rangle. \quad (1.1.13)$$

Multiplying equation 1.1.13 by eigenstate $\langle g|$, using $\langle g|e\rangle = \delta_{ge}$ and integrating from $t = 0$ to t ,

$$a_g(t) - a_g(0) = \frac{-i}{\hbar} \sum_e \int_0^t e^{iE_g t'/\hbar} \langle g| \hat{\mathbf{H}}'(t') |e\rangle e^{-iE_e t'/\hbar} a_e(t') dt'. \quad (1.1.14)$$

In the small perturbation regime $a_g(t) \approx a_g(0)$ [25]. For simplicity, we consider that the system is in the state $|g\rangle$ at $t = 0$, with $a_n(0) = 1$ and all other $a_n(t) = 0$. Then

equation 1.1.14 becomes

$$a_g(t) = \frac{-i}{\hbar} \hat{\mathbf{H}}'_{ge}(t) \int_0^t e^{-i(E_g - E_e)t/\hbar} dt' = \frac{-1}{\hbar} \hat{\mathbf{H}}'_{ge}(t) \frac{e^{-i(E_g - E_e)t/\hbar} - 1}{-i(E_g - E_e)t/\hbar}. \quad (1.1.15)$$

where $H'_{ge} = \langle g | H'(t') | e \rangle$. Therefore, we can rewrite equation 1.1.15 as

$$|a_g(t)|^2 = \frac{4}{(\hbar\omega_{ge})^2} |\hat{\mathbf{H}}'_{ge}(t)|^2 \sin^2 \frac{\omega_{ge}t}{2}, \quad (1.1.16)$$

with $\omega_{ge} = (E_g - E_e)/\hbar$.

The probability to found the system in the state g is give as

$$P(t) = \sum_g |a_g(t)|^2 = \frac{4}{(\hbar\omega_{ge})^2} |\hat{\mathbf{H}}'_{ge}(t)|^2 \sin^2 \frac{\omega_{ge}t}{2}. \quad (1.1.17)$$

For a continuum, the summation is replaced by an integral, so that

$$P(t) = \sum_g |a_g(t)|^2 = |\hat{\mathbf{H}}'_{ge}(t)|^2 \int_{\infty}^{\infty} \frac{4}{(\hbar\omega_{ge})^2} \sin^2 \frac{\omega_{ge}t}{2}. \quad (1.1.18)$$

Here we use two mathematical tricks [25] :

$$\delta(x) = \lim_{a \rightarrow \infty} \frac{\sin ax}{\pi x} \quad \text{and} \quad \int_{\infty}^{\infty} \frac{\sin^2 x}{x^2} = \pi \quad (1.1.19)$$

And we rewrite equation 1.1.18 as

$$P(t) = \frac{2\pi t}{\hbar} |\hat{\mathbf{H}}'_{ge}|^2 \delta(E_e - E_g). \quad (1.1.20)$$

The decay rate (Fermi's golden rule) is defined as the probability to decay by a time unit and it can be written as

$$\gamma = \frac{2\pi}{\hbar} |\hat{\mathbf{H}}'_{ge}|^2 \delta(E_e - E_g). \quad (1.1.21)$$

Fermi's golden in the bra-ket notation is

$$\gamma = \frac{2\pi}{\hbar} |\langle g | \hat{\mathbf{H}} | e \rangle|^2 \delta(E_e - E_g). \quad (1.1.22)$$

1.1.3 Spontaneous decay in terms of the partial local density of states

A single photon source can be represented by a dipole point with current \mathbf{j} and dipole moment \mathbf{p} . In this section we describe the spontaneous decay rate in terms of the dipole moment and a partial local density of states. The Hamiltonian $\hat{H} = -\hat{\mathbf{p}} \cdot \hat{\mathbf{E}}$ describe a dipole interaction [23]. Using 1.1.22,

$$|\langle g | \hat{\mathbf{H}} | e \rangle|^2 = \langle g | \hat{\mathbf{p}} \cdot \hat{\mathbf{E}} | e \rangle \langle g | \hat{\mathbf{p}} \cdot \hat{\mathbf{E}} | e \rangle , \quad (1.1.23)$$

where the $\hat{\mathbf{E}}$ operator is defined as

$$\hat{\mathbf{E}} = \sum_k [\mathbf{E}_k^+ \hat{\mathbf{a}}_k(t) + \mathbf{E}_k^- \hat{\mathbf{a}}_k^\dagger(t)] \quad (1.1.24)$$

with $E_k^+ = (E_k^-)^*$ and

$$\hat{\mathbf{a}}_k^\dagger(t) = \hat{\mathbf{a}}_k^\dagger(0) e^{i\omega_k t}, \quad \hat{\mathbf{a}}_k(t) = \hat{\mathbf{a}}_k(0) e^{-i\omega_k t} \quad (1.1.25)$$

the annihilation and creation operators, respectively. To describe the decay of the ground state g and the excitation of the state e , we represent $\hat{\mathbf{p}}$ as

$$\hat{\mathbf{p}} = \mathbf{p}[\hat{\mathbf{r}}^+ + \hat{\mathbf{r}}] \quad \text{with} \quad \hat{\mathbf{r}}^+ = |e\rangle\langle g| \quad \text{and} \quad \hat{\mathbf{r}} = |g\rangle\langle e|. \quad (1.1.26)$$

To describe the interaction of the states and the creation and annihilation operators we represent the zero-photon states as $|\{0\}\rangle$ and the one-photon state as $|\{1\omega_k\}\rangle$ with a k' mode and frequency $\omega_0 = (E_e - E_g)$ such that the $\langle i |$ and $\langle f |$ can be represented as

$$\langle e | = \langle e, \{0\} | = \langle e | \{0\} \rangle \quad \langle g | = \langle g, 1\omega'_k | = \langle g | 1\omega'_k \rangle , \quad (1.1.27)$$

when we use the $\hat{\mathbf{a}}_k^\dagger$ and $\hat{\mathbf{a}}_k$, we observe that

$$\hat{\mathbf{a}}_k^\dagger(0) |\{0\}\rangle = |\{1\omega_k\}\rangle \quad \hat{a}_k(0) |\{1\omega_k\}\rangle = \{0\}. \quad (1.1.28)$$

Once we know all of elements, we use equation 1.1.24 to obtain

$$-\hat{\mathbf{p}} \cdot \hat{\mathbf{E}} = -\sum_k p \cdot \left[\mathbf{E}_k^+ \hat{r}^+ \hat{\mathbf{a}}_k(t) + \mathbf{E}_k^- \hat{\mathbf{r}}^- \hat{\mathbf{a}}_k^\dagger(t) + \mathbf{E}_k^+ \hat{\mathbf{r}}^+ \hat{\mathbf{a}}_k(t) + \mathbf{E}_k^- \hat{\mathbf{r}}^- \hat{\mathbf{a}}_k^\dagger(t) \right]. \quad (1.1.29)$$

Using equations 2.1.15, 1.1.26, 1.1.28, 1.1.27 in eq. 1.1.29 and operating by $\langle g |$ and $|e\rangle$, it gives

$$\langle g | \hat{\mathbf{p}} \cdot \hat{\mathbf{E}} | e \rangle = p \cdot \sum_k \mathbf{E}_k^+ e^{-i\omega_k t} \langle g |, \{1\omega'_k\} | g \rangle, \{1\omega_k\} \quad (1.1.30)$$

while operating by $\langle e |$ and $|g\rangle$ gives

$$\langle e | \hat{\mathbf{g}} \cdot \hat{\mathbf{E}} | g \rangle = p \cdot \sum_k \mathbf{E}_k^- e^{i\omega_k t} \langle g |, \{1\omega_k\} | g \rangle, \{1\omega'_k\} \quad (1.1.31)$$

With this result we rewrite the rate decay described in equation 1.1.21 as

$$\begin{aligned} \gamma &= \frac{2\pi}{\hbar^2} \sum_k \sum_{k''} \left[\mathbf{p} \cdot \mathbf{E}_{k''}^+ \mathbf{E}_{k''}^- \cdot \mathbf{p} \right] e^{(\omega_k - \omega_{k''})t} \times \\ &\sum_{k'} \langle g, \{1\omega_{k''}\} | g, \{1\omega_{k'}\} \rangle \langle g, \{1\omega_{k'}\} | g, \{1\omega_k\} \rangle \delta(\omega_k - \omega_0). \end{aligned} \quad (1.1.32)$$

This equation is simplified with the use of the orthogonality of eigenmodes, where only interaction between the eigenmodes $k' = k'' = k$ is different to zero, thus

$$\gamma = \frac{2\pi}{\hbar^2} \sum_k \left[\mathbf{p} \cdot \mathbf{E}_k^+ \mathbf{E}_k^- \cdot \mathbf{p} \right] \delta(\omega_k - \omega_0). \quad (1.1.33)$$

Finally to rewrite γ in terms of ω and ε , we define

$$\mathbf{E}_k^+ = \sqrt[2]{\frac{\hbar\omega_k}{2\varepsilon_0}} e_k, \quad \mathbf{E}_k^- = \sqrt[2]{\frac{\hbar\omega_k^*}{2\varepsilon_0}} e_k. \quad (1.1.34)$$

and we obtain

$$\gamma = \frac{2\omega_0}{3\hbar\varepsilon_0} |\mathbf{p}|^2 \rho_p(\mathbf{r}_0, \omega_0), \quad \text{and} \quad \rho_p(\mathbf{r}_0, \omega_0) = 3 \sum_k [\mathbf{n}_p \cdot (\mathbf{e}_k \mathbf{e}_k) \cdot \mathbf{n}_p] \delta(\omega_k - \omega_0), \quad (1.1.35)$$

where ρ_p is the partial LDOS for a dipole oscillating in p direction and n_p is the unit vector along \mathbf{p} .

1.1.4 Spontaneous decay rate by Green's function

In this section we describe the equation 1.1.35 in terms of the Green's function of the system. The Green's function will allow to observe the system's response due to the presence of the source. We use the Lagrangian equation of the Helmholtz equation 1.1.5 in terms of its eigenvector e_k and eigenfrequencies ω_k .

The Green's function of the system have to satisfies equation 1.1.5, then

$$\nabla \times \nabla \times \mathbf{G}^E(\mathbf{r}, \mathbf{r}'; \omega) - \frac{\omega_n^2}{c^2} \mathbf{G}^E(\mathbf{r}, \mathbf{r}'; \omega) = \mathbf{I}\delta(\mathbf{r} - \mathbf{r}') \quad (1.1.36)$$

with \mathbf{I} a unit tensor.

Using an algebraic process described in Appendix A, the Green's function can be written as

$$\mathbf{G}^E(\mathbf{r}, \mathbf{r}'; \omega) = \sum_k \left(\frac{c^2 e_k'^*(\mathbf{r}', \omega) e_k(\mathbf{r}, \omega_k)}{\omega_k^2 - \omega^2} \right). \quad (1.1.37)$$

The description of the set equation 1.1.35 by the Green's function can be written as

$$\gamma = \frac{2\omega_0}{3\hbar\varepsilon_0} |\mathbf{p}|^2 \rho_u(\mathbf{r}_0, \omega_0) \quad \text{and} \quad \rho_p(\mathbf{r}_0, \omega_0) = \frac{6\omega_0}{\pi c^2} [\mathbf{n}_p \cdot \text{Im} \{ \mathbf{G}^E(\mathbf{r}, \mathbf{r}'; \omega) \} \cdot \mathbf{n}_p] \quad (1.1.38)$$

The detailed process to obtain the set of equations 1.1.38 can be also found in the Appendix B.

1.1.5 Total LDOS

The total local density of states is the summation and average of the partial LDOS over the various orientations of the dipole. This average can be described as :

$$\langle n_p \cdot \text{Im} \{ \mathbf{G}^E(\mathbf{r}, \mathbf{r}'; \omega) \} \cdot n_p \rangle = \frac{1}{3} \text{Im} \{ \text{Tr} [\mathbf{G}^E(\mathbf{r}, \mathbf{r}'; \omega)] \}. \quad (1.1.39)$$

The trace of the Green's function represents the weighted summation of the dipoles oriented in the directions of the three coordinates axis. From equation 1.1.38, we can defined the total local density of states as

$$\rho(\mathbf{r}_0, \omega_0) = \frac{2\omega_0}{\pi c^2} \text{Im} \left\{ \text{Tr} [\mathbf{G}^E(\mathbf{r}, \mathbf{r}'; \omega)] \right\} = \sum_k |e_k(\mathbf{r})|^2 \delta(\omega_k - \omega_0). \quad (1.1.40)$$

In free space the imaginary part of the trace of the Green's function is [23, 24]

$$\text{Im} \left\{ \text{Tr} [\mathbf{G}^E(\mathbf{r}, \mathbf{r}'; \omega)] \right\} = \frac{\omega_0}{6\pi c} \quad (1.1.41)$$

Then, using equation 1.1.35 the total density of states and the decay rate in vacuum are

$$\rho_0 = \frac{\omega_0^2}{3\pi^2 c^3} \quad \text{and} \quad \gamma_0 = \frac{\omega_0^3 |\mathbf{p}|^2}{3\hbar\varepsilon_0\pi c^3}. \quad (1.1.42)$$

1.1.6 Purcell's Factor and quantum yield

In 1965 Purcell [26] was the first to show that the atom decay rate could vary when subjected to a change of its surrounding local environment. The enhancement factor of the decay rate is known as the Purcell's factor (PF) and is defined as γ/γ_0 . In this section we continue to consider a dipole source with radiated power P . Using the results previously obtained, we show that PF can be related to the total LDOS of the system and the radiated power of the dipole.

We start using the set of equations 1.1.38 and 1.1.42 in order to obtain

$$\frac{\gamma}{\gamma_0} = \frac{6\pi c}{\omega_0} \text{Im}[\mathbf{n}_p \cdot \mathbf{G}^E(\mathbf{r}_s, \mathbf{r}_s, \omega) \cdot \mathbf{n}_p]. \quad (1.1.43)$$

Since the partial LDOS can be written in terms of the Green's function, the Purcell's factor (equation 1.1.43) can also be written as

$$\frac{\gamma}{\gamma_0} = \frac{\pi^3 c^3}{\omega_0^2} \rho_u(\mathbf{r}_0, \omega_0) = \frac{\rho(r, \omega_0)}{\rho_0(r, \omega_0)}. \quad (1.1.44)$$

In order to describe the total LDOS and the rate decay in terms of the power radiated by a dipole we take equation 1.1.37, which is a solution of the Helmholtz equation. We

write the radiated electric field of the dipole as [24]

$$\mathbf{E}(\mathbf{r}) = \mu_0 \omega_0^2 \mathbf{G}^E(\mathbf{r}, \mathbf{r}', \omega) \mathbf{p}, \quad (1.1.45)$$

with the dipolar moment \mathbf{p} at the \mathbf{r}' position of the dipole. Then, we work with the power radiated P by a point dipole source described in electrodynamics as [27]

$$P = -\frac{1}{2} Re \int \mathbf{j}^*(\mathbf{r}) \cdot \mathbf{E}(\mathbf{r}) d^3(\mathbf{r}), \quad (1.1.46)$$

where $\mathbf{j}(\mathbf{r})$ is the dipole current density.

Using \mathbf{j} in terms of the dipole moment $\mathbf{j}(\mathbf{r}) = i\omega \mathbf{p} \delta(\mathbf{r} - \mathbf{r}_s)$ and equation 1.1.45 in equation 1.1.46, we obtain

$$P = \frac{\mu_0 \omega_0^3}{2} |\mathbf{p}|^2 [\mathbf{n}_p \cdot Im \{ \mathbf{G}^E(\mathbf{r}, \mathbf{r}'; \omega) \} \cdot \mathbf{n}_p]. \quad (1.1.47)$$

Due to the relation between the Green's function and the LDOS, we can use equations 1.1.38 and 1.1.47 to describe P as :

$$P = \frac{\pi \omega_0^2}{4\epsilon_0} |\mathbf{p}|^2 \rho_u(\mathbf{r}, \omega) \quad (1.1.48)$$

We use equation 1.1.42 in equation 1.1.48 and we obtain the power of the dipole, when it is placed in vacuum

$$P_0 = \frac{\omega_0^4}{12\pi\epsilon_0 c^3} |\mathbf{p}|^2. \quad (1.1.49)$$

This result shows that we recover the well known expression for the power radiated by a dipole in free space P_0 described by the classic electrodynamics [27]. The ratio between the P and P_0 (equations 1.1.48 1.1.49) is

$$\frac{P}{P_0} = \frac{\pi^3 c^3}{\omega_0^2} \rho_u(\mathbf{r}_0, \omega_0). \quad (1.1.50)$$

This ratio is equal to the ratio of the decay rates (equation 1.1.44). Furthermore, the ratio in equation 1.1.50 can also be written in terms of the partial LDOS (equation 1.1.38) as

$$\frac{P}{P_0} = \frac{\rho(r, \omega_0)}{\rho_0(r, \omega_0)}. \quad (1.1.51)$$

Using equations 1.1.44 and 1.1.51 we observe that

$$\frac{\gamma}{\gamma_0} = \frac{P}{P_0} = \frac{\rho(\mathbf{r}, \omega_0)}{\rho_0(\mathbf{r}, \omega_0)} = \frac{\tau_o}{\tau}. \quad (1.1.52)$$

where τ the lifetime of the system.

The equation 1.1.52 shows that rate decay of the system can be enhanced changing the properties of the system. However, we have to consider that the total γ takes into account all permitted decay channels. The radiative channels represent photons radiating to the far-field, i.e. far away from the emitter, while the non-radiative channels correspond to direct non-radiative energy transfer between the emitter and the materials in its environment.

In order to know the photon emission efficiency, we define the quantum yield as :

$$\eta = \frac{\gamma_{rad}}{\gamma_{rad} + \gamma_{abs}}. \quad (1.1.53)$$

This quantity takes into account the states that decay by non radiative processes (γ_{abs}) and those who decay by radiative process (γ_{rad}). It is important to notice that the absorption term here includes all non radiative decay channels and is not limited to absorptive electromagnetic modes. This analysis can be extrapolated to the LDOS concept such as the total LDOS can be write as

$$\rho(r, \omega_0) = \rho_{abs}(\mathbf{r}, \omega_0) + \rho_{rad}(\mathbf{r}, \omega_0), \quad (1.1.54)$$

with $\rho_{rad}(\mathbf{r}, \omega_0)$ the part of total LDOS that describe the states that radiate in far-field and $\rho_{abs}(\mathbf{r}, \omega_0)$ the absorption in the materials of the environment.

1.2 Real nanosources

The NS or nanoemitters (NE) are nanostructured materials able to emit photons after some external excitation (fluorescence materials). In contrast to “an ideal single photon source”, a common fluorescent material has several excited states (figure 1.3).

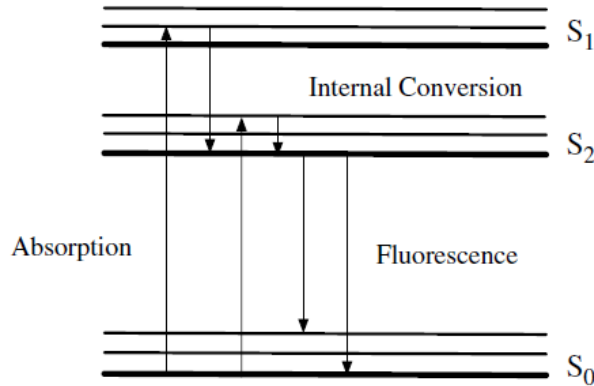


FIGURE 1.3 – Diagram of photoluminescence process where we illustrate the internal decay of states and the fluorescence process (Image taken from reference [28])

When the light is absorbed by the material, the high energy states (S_1 and S_2 in figure 1.3) can be excited. The process of decaying to lower energy states different from the S_0 state is called *internal conversion* whereas the decay of excited states to the ground state S_0 is defined as *fluorescence process* [28]. The average decay time is the lifetime τ defined in the previous sections.

Nowadays, the NS most commonly used are the deterministic and no-deterministic sources. The deterministic sources have a high probability to emit only one photon at interval time τ , whereas the no-deterministic sources generate photon pairs by spontaneous process.

The deterministic sources are demanded in specific research areas such as quantum cryptography, data processing, and bio-sensing. The processing with single photons allows the propagation of individual energy quanta useful to study the interaction between light and matter at nano scale. Furthermore, the single photon detection promises to improve the parallel data processing and the data encryption. While the probabilistic sources are used in specific quantum information tasks as the quantum simulation and quantum processing .

1.2.1 Deterministic sources

The deterministic or "on-demand" sources deliver only one photon at a interval time determined by the user. One good approximation to the single photon emission are the sources with a single emitter. Some examples of these are semiconductor quantum dots [29, 30], single molecules [31, 32], single atoms [33, 34], single ions [35, 36], and color centers [37, 38]. But in this work we will be focused mainly on semiconductor quantum dots and color centers.

Quantum dots

The semiconductor quantum dot (QD) consists in a smaller-band-gap semiconductor (the core) embedded in a larger-band-gap semiconductor (the shell) (figure 1.4a). Due to its small size quantum dots have a discrete energy structure of electrons and holes. In the weak-excitation regime, a single electron-hole pair can be produced by an external excitation. Then, through an electron-hole recombination, the excited electron may relax non-radiatively into the conduction band or recombine radiatively to the valance band by emitting a photon (Fig 1.4 a). The frequency of the emitted photon depends on the bandgap, the gap energy states between the valance and conduction bands, and the size of the quantum dot (fig 1.4 b and c).

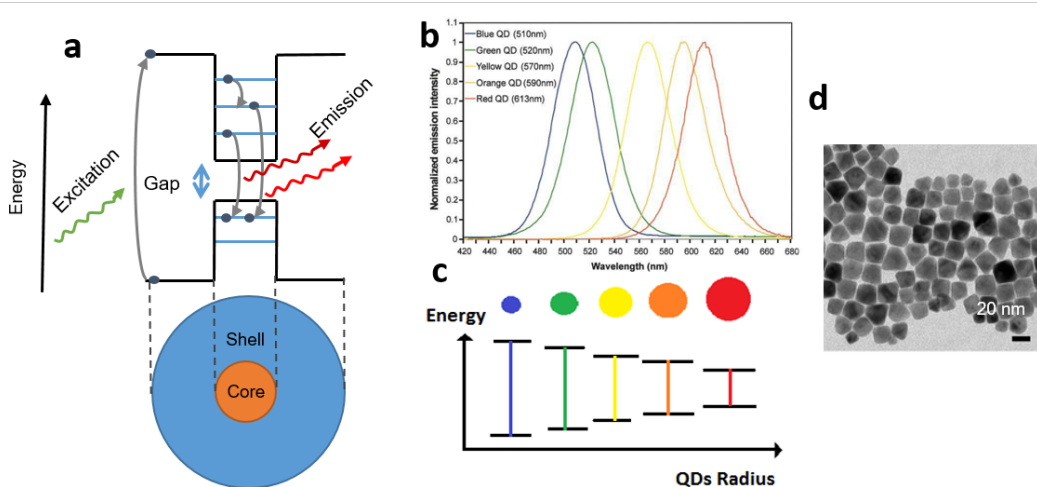


FIGURE 1.4 – Quantum dots. a) Schematic diagram of photoluminescence in a quantum dots. b) Emission spectra of CdSe/ZnS QDs (water-soluble QDs excited at 350 nm), illustration of size-tunable QDs and its bandgap size (Images taken from reference [39]). c) Transmission electron microscopy image of the 5.5 nm CdSe seed (Image taken from reference [28])

Examples of optically active quantum dots include CdSe (figure 1.4d) in ZnS, InP in GaInP, and InAs in GaAs, while an example of an electrically driven quantum dot is InAs.

Color centers

Color centers as a nitrogen-vacancy (NV) are point defects in a diamond. These defects are substitutional nitrogen atoms at some points in the lattice of the diamond. The NV centers are modeled by a three-level energy system (figure 1.5a). In this system we consider two states $|g\rangle$ and $|e\rangle$ (as in the previous case) and a metastable state $|s\rangle$.

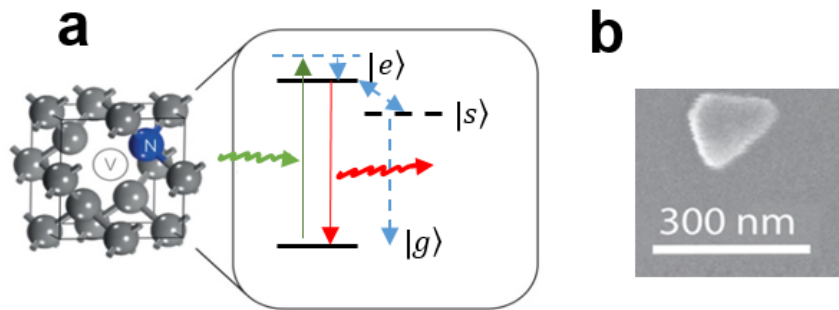


FIGURE 1.5 – Nitrogen-vacancy diamond source. a) Schematic diagram of photoluminescence in NV diamond, b) scanning electron microscopy image of a nanodiamond (Image taken from <https://engineering.psu.edu/shalaev/projects.php>).

After an external excitation, the system decays to the ground state $|g\rangle$ and emits a single photon. Other possibility is that the system decays to intermediate state $|s\rangle$ before the decay to $|g\rangle$. A long lifetime of this intermediate state decreases the single photon emission rate and this could be a disadvantage in areas such as fast information and quantum processing. Some advantage of using NV centers are their stability, their high quantum efficiency at room temperature and their strong electron-photon interaction and a broad spectrum ranging from 600 nm to 850 nm.

NV color centers in diamond can be fabricated by chemical vapor deposition growth [40], or by the generation of a Silicon-vacancy (SiV) [41] and nickel-nitrogen defects (NE8) [42]. However the reproducibility of the fabrication of diamond nanocrystals containing single optical centers is low [43–45].

1.2.2 Probabilistic sources

This kind of sources generate correlated pairs of photons by the excitation of a nonlinear optical material [46]. These sources are not studied in the thesis but we show some examples in order to illustrate its differences with the deterministic sources.

Parametric downconversion

In the spontaneous parametric downconversion (SPDC), a pump laser with frequency ω_p illuminates a nonlinear $\chi^{(2)}$ material creating two photons due to momentum and energy conservation [47]. Because of momentum conservation constraints, these sources are highly directional but the phase matching condition is generally difficult to obtain.

The problem can be resolved by using techniques whereby the effective index of the material can be controlled. Some materials commonly used are crystals as KDP (potassium dideuterium phosphate, KD_2PO_4), BBO (beta barium borate, BaB_2O_4), $LiNbO_3$ (lithium niobate), and $LiIO_3$ (lithium iodate).

Four-wave mixing

Spontaneous four-wave mixing (SFWM) is a $\chi^{(3)}$ nonlinear process in which two pump photons are absorbed by an atom and this emits two correlated photons. Single-photon emission by SFWM can be generated in photonic crystal fibers (PCF) [48], birefringent single-mode fibers (BSMF) [49] or in silicon-on-insulator waveguides [50].

1.3 Surface enhanced fluorescence by plasmonic fields

The surface enhanced fluorescence (SEF) is a technique based on the design of micro- or nano-structured surfaces in the vicinity of the emitter [28]. Some examples are the design of nano cavities [51, 52], nanoantennas [53], metal waveguides [54–56], photonic crystals [57, 58] and SNOM probes [59, 60]. In recent years plasmonics is considered as one of the most promising research fields for SEF because it allows ultra high electrical field confinement at sub-wavelength scales.

1.3.1 Surface plasmon polariton

A surface plasmon polariton (SPP) is a collective oscillation of free electrons in metals that propagates as a surface wave along the interface between a metal and a dielectric material. When light propagates through the interface, this oscillation of charges generates an evanescent electromagnetic field whose amplitude decreases exponentially away from the interface (Figure 1.6). The decay length of the field in the dielectric medium (δ_d) is in the range of half the wavelength of the incident light, whereas in the metallic material it is (δ_m) a couple or tens of nanometers.

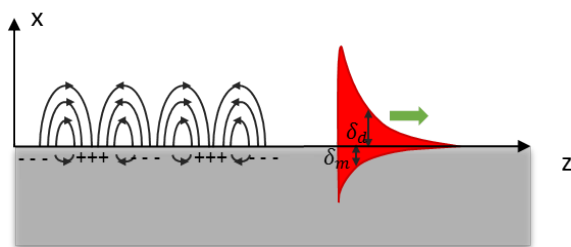


FIGURE 1.6 – Schematic representation of a surface plasmon polariton with the distribution of charges on the surface and the electric field profile in red.

By solving the Maxwell's equations, it is possible to demonstrate that a SPP wave can be found under appropriate boundary conditions (appendix B). The bounded SPP is characterized by wavevector k_{SPP} parallel to the interface given by :

$$k_{SPP} = \frac{\omega}{c} \sqrt{\frac{\varepsilon_d \varepsilon_m}{\varepsilon_d + \varepsilon_m}}, \quad (1.3.55)$$

where ε_d and ε_m are the dielectric constants of the dielectric and the metal, respectively. Figure 1.7 shows the dispersion relation of a SPP in comparison with the light line $\omega = ck/\sqrt{\varepsilon_d}$. The mismatch between the SPP and the light line shows that SPP can not be excited with plane waves propagating in free space.

In figure 1.8 we observe the classic configurations for the excitation of SPPs. The most common configurations to excite SPP are based on the photon and SPP wavevector matching by using photon tunneling in the total internal reflection geometry (Krestschmann and Otto configurations). In the Krestschmann configuration (Fig 1.8a), the metal film is illuminated through a dielectric prism at an angle θ_{sp} in total internal reflection. The angle θ_{sp} coincides with the SPP wavevector direction at the air-metal interface. On the other

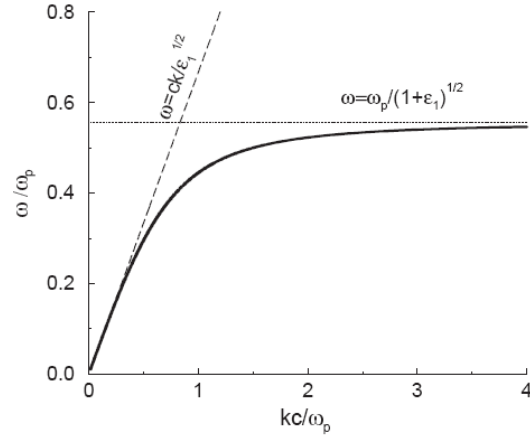


FIGURE 1.7 – Dispersion of SPP at a dielectric-metal interface. Also plotted is the dispersion of light in the dielectric medium, and the corresponding surface plasmon frequency. The assumed parameters are $\omega_p = 11.9989 \times 10^{15}$ rad/s (silver) and $\varepsilon_d = \varepsilon_1 = 2.25$ (image taken from [61]).

hand in the Otto configuration (Figure 1.8b) the prism is placed close to the metal surface with a air gap between them. Here, the total internal reflection is also implemented, the photon tunneling through the air gap is coupled to the SPP.

SPP can be also excited using diffraction effects. In these techniques it is expected that the components of the scattered light have a wavevector that coincides with the SPP wavevector. In figure 1.8 c, we can see how a metal film can be illuminated by a scanning near-field microscopy tip. Here, evanescent components of the coupling of diffracted light and SPP is made in the near-field. Diffraction effects can be also reproduced by diffraction grids (Figure 1.8 d) and surface features (figure 1.8e).

Coupling between SPPs and nanoemitters

The interaction between a nanoemitter and a SPP in a thin metal film depends on the distance of the emitter to the surface. A metal film acts as a mirror that reflects the radiated light of the dipole generating interference effects. Constructive interference can increase the nanoemitter fluorescence. At small nanoemitter-metal distances, a quenching fluorescence effect can be observed due to the energy transfer into the metal. This phenomenon can be understood by the study of the interaction between a dipole and a mirror [62].

In figure 1.9 we show the results obtained by Barnes *et al.* [63] for the coupling between a dipole and SPPs. The plots show the fraction of power dissipated into different

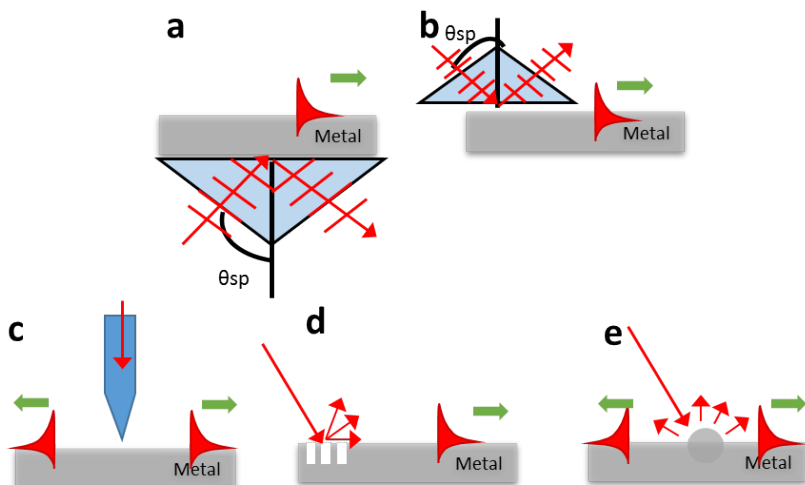


FIGURE 1.8 – SPP excitation configurations : a) Kretschmann geometry, b) Otto geometry, c) excitation with a SNOM probe, d) diffraction on a grating, and e) diffraction on surface features (image reproduced from [61]).

decay channels relative to the orientation of a dipole and the dipole-metal distance. For small distances (shorter than 20 nm), we observe that the dipole is mainly coupled to lossy waves. At this scale, the transfer of energy from the dipole to the metal can generate an electron-hole pair and this energy can be dissipated by the metal. On the other hand, the system can also decay in so-called non-radiative SPP modes. If the system decays in radiative channels the energy is transferred to radiative modes. These results show that up to 93% of the light can be coupled to the SPP using a dipole oscillating along a perpendicular direction to the metal surface.

The strong coupling between SPPs and nanoemitters changes the decay rate. It has been shown that for small distances the quantum yield increases and the lifetime tends towards zero. This kind of results allows the study of ultrafast processes. The nanoemitters can be also used as local probes of evanescent waves of SPPs through the imaging of fluorescence of molecular films close to SPPs [64].

Current works show new designs of integrated systems for the excitation of nanoemitters by SPPs and viceversa. For example, to excite quantum dots and NV centers, we can find works where the authors use the diffraction gratings [65–67], corrugated surfaces [68,69], plasmonic gaps [70], nanowire [71], spiral plasmonic cavities [72], to name a few.

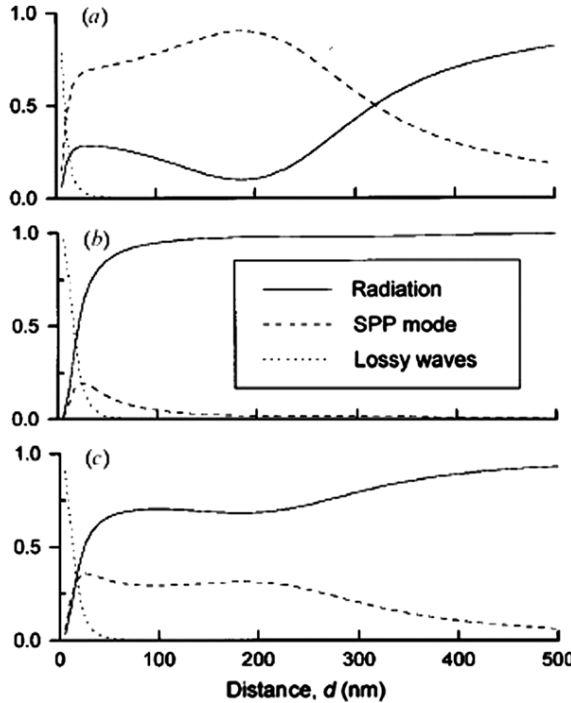


FIGURE 1.9 – Normalized fraction of power dissipated in each relaxation channel, i.e. radiation, SPP mode, and lossy waves, for various dipole-metal distances a) for a dipole oriented perpendicular to the surface, b) parallel to the surface and c) for an isotropic distribution (image taken from [28]).

1.3.2 Localized surface plasmons

Localized surface plasmons or LSP are non-propagating excitations of the conduction electrons of metallic nanostructures coupled to the electromagnetic field [73]. For a metal nanostructure shorter than the wavelength of the incident light, the phase of the oscillating electromagnetic field is almost constant over the particle volume, so the calculation of the electric field distribution can be obtained by assuming the simplified problem of a particle in an electrostatic field (figure 1.10). In contrast to SPP, the LSP can be excited by direct light illumination.

The resonance frequency of a LSP has a high sensitivity to the nanoparticle geometry. This effect can be observed in figure 1.11 where we show the results obtained by Chen *et al.* about the simulation of the absorption spectra of gold nanorods with different sizes and surrounding materials.

The distribution of confined electric field generated by a LSP is also related to the geometry of the particle and the polarization of the incident light. The abrupt change of radius of curvature in the surface of the metal generates strong hot spots where a high

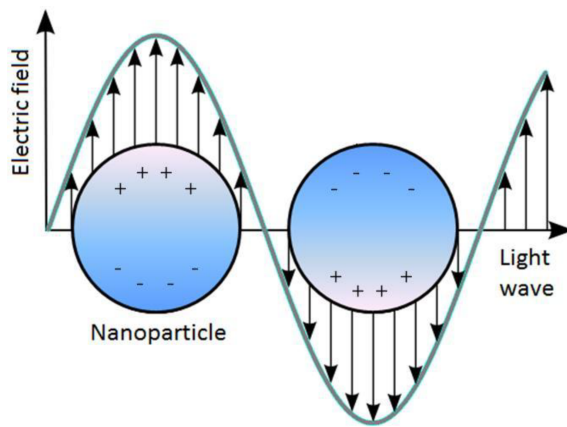


FIGURE 1.10 – Schematic of localized surface plasmon resonance where the free conduction electrons in the metal nanoparticle are driven into oscillation due to strong coupling with incident light. (Image taken from [74]).

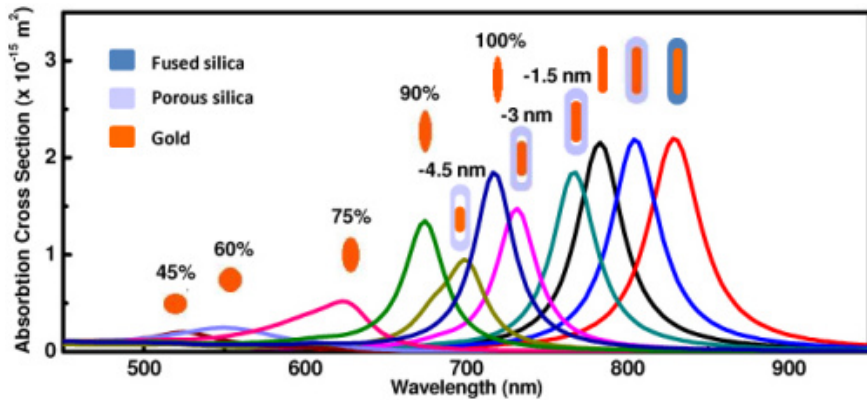


FIGURE 1.11 – FDTD simulated absorption cross section spectra for unpolarized light for various gold nanoparticles. Ellipsoids have the same volume as the original nanorod and are labeled as the fraction of the long axis relative to the original nanorod length. Shortened silica-coated nanorods are labeled for their reduction at each end. For details see the text (image taken from [75]).

density of the electromagnetic field is concentrated.

Coupling between LSP and nanoemitters

The strong confinement of the electromagnetic field generated by a LSP can be used for fluorescence enhancement. Figure 6.7 shows the results obtained by Krachmalnicoff *et al.* about the study of the fluorescence intensity in the near-field of a gold nanoantenna. The antenna is formed by three gold nanodisks separated by 50 nm on a glass substrate, the intensity fluorescence and topography maps are acquired with a aperture scanning near-field optical microscope (SNOM) with QDots emitters grafted at its apex. Due to the presence of gold, the fluorescence intensity of the QDots is minimum when the tip is on

the nanodisks. In the other hand, the decay rate is enhanced in the gap regions due to the strong enhancement of the LSP field.

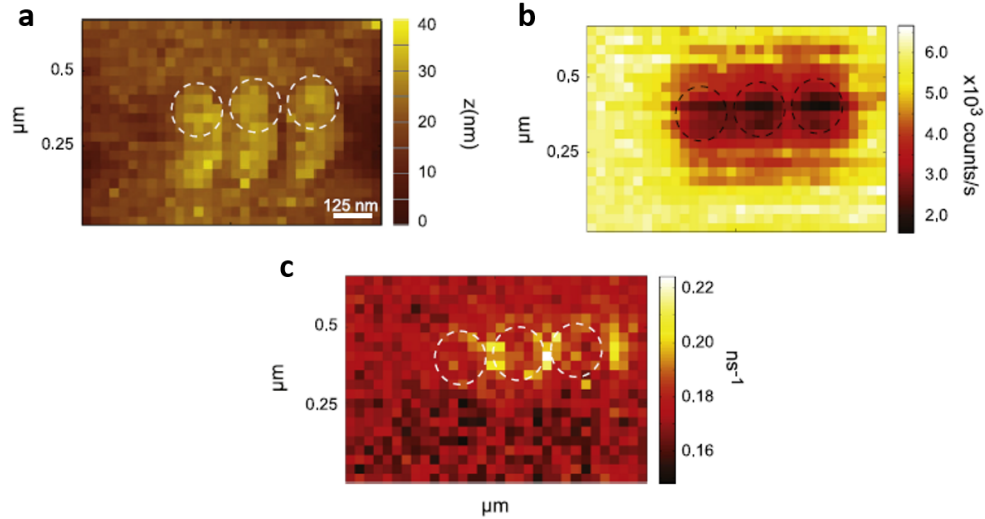


FIGURE 1.12 – Fluorescence and decay rate for a gold nanoantenna. a) Topography of the sample. b) Fluorescence intensity map. c) Decay rate map. The contour of the gold nanodisks is represented with a white dashed line. (Image taken from [76]).

Another interesting example is the work by Aremesh *et al.*. It is shown a parametric study of the maximum transmitted power through an aluminum rod excited with light from a NV color center. Figure 1.13 shows the electric field distribution of the LSP excited by the NV placed close to the interface of the aluminum. The numerical simulations show the influence of the NV orientation on the LSP and the emission power from the bottom and top extremities of the nanowire.

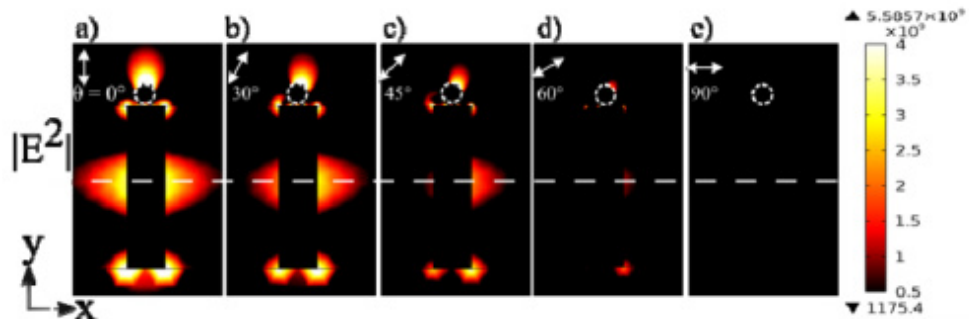


FIGURE 1.13 – Numerical simulation of the interaction between a LSP in an aluminum nanorod and a NV single-photon source. Electric field along a silver nanowire near a NV color center with different orientations : a) 0, b) 30, c) 45, d) 60, and e) 90 (with nanorod diameter D = 70 nm and length L = 240 nm). (Image taken from [77]).

The development of fabrication tools at the nanoscale has allowed the emergence of new designs of plasmonic systems able to control the excitation and the emission of single-photon sources. More examples of SEF using LSP are the use of metal nanostructures [78, 79], nanocrystals [80, 81], nanoneedles [82], and metal nanoparticles [83, 84]. However, challenges remain to design and to fabricate quantum optical circuits able to propagate single photons through long distances with low propagation losses. The quantum circuit could be the key for the understanding of the atomic world and a new tool for the future development of data storage and processing technologies.

1.4 Objective of the thesis

The objective of this thesis is the development of a chip able to integrate a single-photon source with minimal photon losses across the visible spectrum. We require a integrated structure capable to provide high Purcell factor and collection efficiencies. To meet this objective, we propose the design of an integrated optical device based on the coupling between nanoemitters and plasmonic modes on an integrated photonic overlaid structure on glass waveguides.

The proposed structure consists of an ion exchange glass waveguide (IEW) connected to commercial optical fibers, an titanium oxide (TiO_2) overlayer, a gold nanotaper, and a single-photon source placed in the vicinity of the nanotaper apex (Figure 1.14).

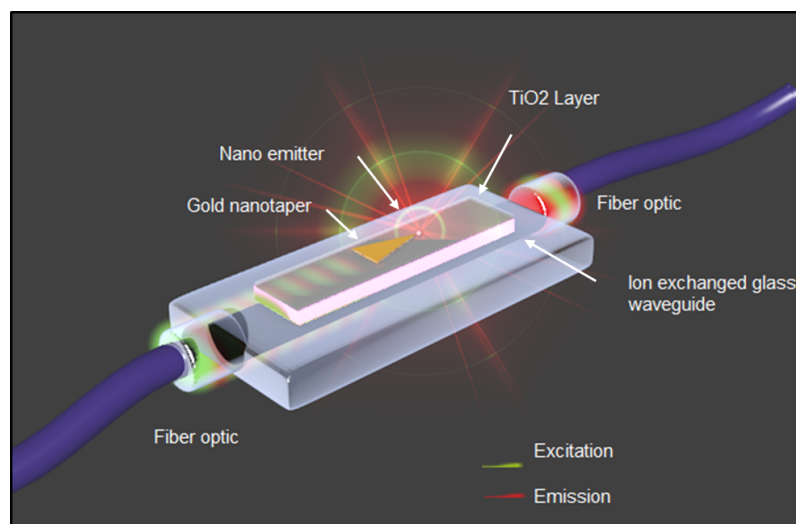


FIGURE 1.14 – Schematic representation of the proposed structure for the integration of nanoemitters on chip.

A brief working principle of the structure is this : light at the excitation wavelength of the nanoemitter is sent through the left optical fiber (green light) and is coupled into the modes supported by the hybrid photonic structure formed by an IEW and a TiO₂ overlayer. These photonic modes are slowly transformed into plasmonic modes due to its interaction with a gold nanotaper placed on top of the TiO₂ layer. The adiabatic mode transformation generates a strongly confined mode at the apex of the gold nanotaper. This electromagnetic field excites the spontaneous emission of the nanoemitter placed in the vicinity of the apex and consequently the excited states decay in radiative channels, generating photon emission. The radiated light from the nanoemitter (red light) can be propagated in the reciprocal path of the excitation, that is, the emitted photons couple to the plasmonic modes of the gold nanotaper and these can be slowly transformed into photonic backward modes of the IEW, which can be detected at the end of the left optical fiber. During this process, part of the emitted photons also excite photonic forward modes as well as radiate modes.

The strong confined field interacting with the nanoemitter generates enhancement in the emission rate and consequently enhancements in the Purcell Factor and LDOS can be found. A high percentage of emitted photons can be collected through the optical fiber for structures with an efficient photonic-plasmonic mode coupling. The main challenge is to create a design with high performance at both excitation and emission wavelengths.

In next sections we discuss the fundamental physical principles for the design of the structure. For the analysis, we divided the structure into two stages. The first is a photonic stage formed by the interaction between the IEW and the TiO₂ overlay and the second is a plasmonic stage formed for an adiabatic photonic-plasmonic mode coupler (the gold nanotaper). The chapter 2 and 3 are dedicated to the photonic stage, where we present the design and the characterization of the integrated photonic structure. The chapter 4 is dedicated to the design and experimental results of the plasmonic stage.

Chapter 2

Integrated photonic structure on glass

This chapter is dedicated to the design of the integrated photonic structures on glass used for the excitation and collection of the photons emitted by a NS integrated on top of these structures. These structures are made of ion exchange waveguides on glass (IEW). We use these structures as the photonic stage of the structure described in the last part of chapter two (figure 1.14). We expect an enhancement of the radiation emitted by a NS placed on top of the structure due to Purcell factor effects. Additionally, we investigated the coupling of this radiation into the guided modes of the IEW, and subsequently, collected at its ends with optical fibers.

In order to describe the physical process involved in the design of the integrated photonic structures, we start with the basic concepts of mode coupling in dielectric waveguides, then we present a parametric study of the geometry of the structure, and finally we interpret numerical simulation results of the light propagation through the structure. The coupling of the photon emitted by the NS and the guided modes of the IEW is described with the use of the reciprocity theorem of the electromagnetism.

According to the design presented in figure 1.14, this photonic structure is also able to excite the plasmonic modes of a gold nanotaper placed through a efficiently photonic-plasmonic mode coupling, however this aspect will be discussed in chapter 4.

2.1 Basic concepts of waveguides

A planar waveguide can be represented by a system of three materials with refractive index n_1 , n_2 , and n_3 , with $n_2 > n_1, n_3$ (figure 2.1). For a plane wave with wavelength λ and wavevector \mathbf{k} traveling at an angle θ in the material 2, for $n = n_1 = n_3$ and θ an angle lower than the total internal reflection angle of surrounded material, internal reflections are generated and this allows light to propagate along material with n_2 .

For each reflection, the wave has a π rad phase shift but its amplitude and its polarization are constant. When the wave reflects twice, the total phase shift is equal to 2π rad and the wave reproduces itself. The fields with these properties are called *modes of the waveguide*.

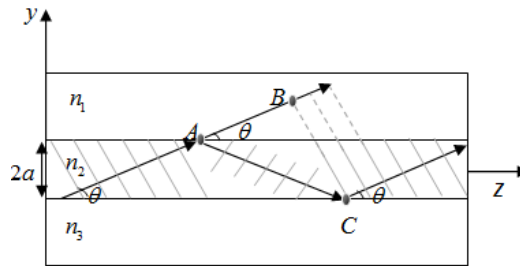


FIGURE 2.1 – Beam propagation of a plane wave incident at a θ angle in a waveguide. (Image reproduced from [85])

In figure 2.1, we observe that the 2π rad phase shift is obtained when light travels from point A to point C and therefore, the relation between the k vector and the distances \bar{AC} and \bar{BC} can be written as

$$\mathbf{k}\bar{AC} - \mathbf{k}\bar{BC} - 2\pi = 2\pi p, \quad p = 1, 2, \dots \quad (2.1.1)$$

Using trigonometric functions and writing $k = 2\pi/\lambda$, we obtain

$$\sin \theta_m = \frac{\lambda m}{4a}, \quad m = p + 1 = 1, 2, \dots \quad (2.1.2)$$

Considering the components of k as $(0, k_y, k_z)$ with $k_y = k \sin \theta_m$ and $k_z = \beta = k \cos \theta_m$, and inserting them into equation 2.1.2, we obtain

$$k_{ym} = m\pi/2a, \quad (2.1.3a)$$

$$\beta_m^2 = k^2 - \frac{m^2\pi^2}{4a^2}. \quad (2.1.3b)$$

The set of equations 2.1.3 shows that the solution space of \mathbf{k} is discretized. This means the number of possible values of \mathbf{k} is determined by the number of finite solutions of the system (the modes). Because $\sin \theta_m < 1$, the maximum value of m in equation 2.1.2 is

$$M = \frac{4a}{\lambda} \quad (2.1.4)$$

and therefore, M is the maximum number of modes of the system.

For incident light at angle θ greater than the total reflection angle, we have to consider the transmitted light into the materials 1 and 3. This information can be obtained resolving the Helmholtz equation with boundary conditions at the interface of the materials.

2.1.1 Field distribution of modes

We consider a plan wave interacting with the system shown in figure 1.14 and we solve the Helmholtz equation of the system. Following the process described in appendix B (B.1.5 and B.1.6 equations) and considering the boundary conditions in $x = a$ and $x = -a$, we obtain the distribution for the TE modes as $E_x(x, z) = A_m U_m(x) e^{-i\beta_m z}$ and for the TM modes as $H_y = B_m U_m(x) e^{-i\beta_m z}$ with A_m and B_m scalar amplitudes and

$$U_m = \begin{cases} \cos(\alpha_{2m}a) e^{-\alpha_{1m}(x-a)}, & x > a \\ \cos(\alpha_{2m}x), & -a \leq x \leq a \\ \cos(\alpha_{2m}a) e^{\alpha_{3m}(x+a)}, & x < -a \end{cases} \quad (2.1.5)$$

with

$$\alpha_{2m} = \sqrt{k^2 n^2 - \beta_m^2}, \quad (2.1.6a)$$

$$\alpha_{1m} = \sqrt{\beta_m^2 - k^2 n_1^2}, \quad (2.1.6b)$$

$$\alpha_{3m} = \sqrt{\beta_m^2 - k^2 n_3^2} \quad (2.1.6c)$$

where $m = 0, 1, 2, 3, \dots$, the mode order.

Figure 2.2 shows the field distributions of different mode orders with $m=1,2,3$ and 8, and α_{im} being real values ($\alpha_{im} \in \mathbb{R}$). From equation 2.1.5 and figure 2.3 we observe that for real values of α_{im} the modes are preferentially confined in the medium 2 and they decrease exponentially in the surrounding media. This kind of modes are propagated through the material with n_2 or core of the waveguide, with low losses (*guided modes*). On the other hand, for imaginary values of α_{im} the mode is radiated into the surrounding media (*radiation modes*).

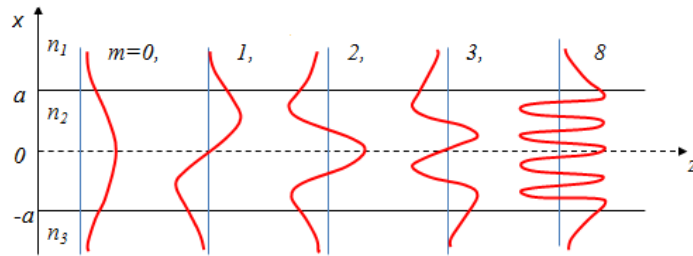


FIGURE 2.2 – Guided modes of a waveguide for the orders 0, 1, 2, 3, and 8. According to equation 2.1.5
(Image reproduced from [85])

From equation 2.1.6 we observe that for real values of α_{im}

$$n_3 < \frac{\beta}{k_0} < n_2. \quad (2.1.7)$$

Here we introduce the definition of effective index (n_{eff}) as the relation between the β and k_0 vectors :

$$n_{eff} = \frac{\beta}{k_0}. \quad (2.1.8)$$

From this, we obtain the restriction for the n_{eff} values for guided modes as

$$n_3 < n_{eff} < n_2. \quad (2.1.9)$$

2.1.2 Two-mode coupling

In a system formed by two parallel waveguides placed in close proximity to each other, it is possible to observe a mode coupling between its fundamental modes due the interaction of its evanescent waves as it is shown in figure 2.3. The evanescent wave of the mode in waveguide 1 can excite the modes of the waveguide 2. Since the solutions

of the system allow the propagation of the wave through both waveguides, the energy of a mode propagating through the waveguide 1 can be transferred to the waveguide 2 and vice versa. The highest transfer of energy is done after a propagation distance L_C , which is known as *coupling length*.

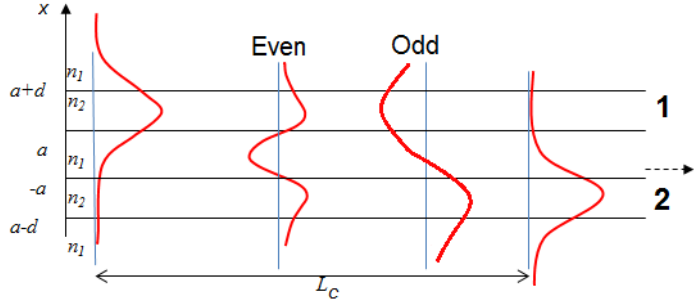


FIGURE 2.3 – Coupling mode and energy transfer between the modes of two waveguides placed in close proximity to each other. Image reproduced from [85]

For waveguides very close to each other ($a \rightarrow 0$), the evanescent waves of the modes are strongly transformed and it is necessary to recalculate the modes of the new *hybrid structure*. The new modes or *hybrid modes* are strongly related with the phase matching of the original modes. The modes with a symmetric phase matching are called *even modes*, while the modes with asymmetric phase matching are called *odd modes*. As in the previous case, the fundamental modes of the structure generate an energy transfer between both waveguides. Considering the field distribution of a hybrid mode as

$$E(x, z) = E_e(x)e^{-i\beta_e z} + E_o(x)e^{-i\beta_o z}, \quad (2.1.10)$$

with e the even modes and o the odd modes [86] and that the field E has the following properties :

$$|E(x, 0)| = E_1, \quad (2.1.11a)$$

$$|E(x, L_c)| = E_2, \quad (2.1.11b)$$

$$|E(x, z)| = |E_e(x) + E_o(x)e^{i(\beta_e - \beta_o)z}| \quad (2.1.11c)$$

From this, we can write the coupling length as :

$$L_c = \frac{\pi}{\beta_e - \beta_o}. \quad (2.1.12)$$

2.1.3 Dispersion relation

The dispersion relation shows the dependence of the effective index of modes in relation with the wavelength of light. In a hybrid system, this relation helps us to understand how the hybrid modes look in comparison to the modes of each individual waveguide.

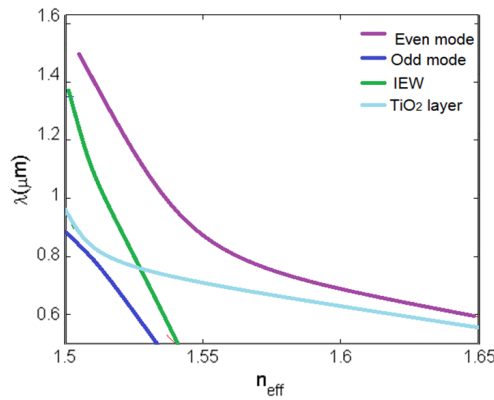


FIGURE 2.4 – Dispersion relation of a hybrid structure formed by a 160-nm-thick TiO₂ overlayer on top of an IEW.

Figure 2.4 shows the dispersion relation for a hybrid structure formed by a TiO₂ layer placed on top of a IEW (structure of interest in this thesis and studied in next sections). These dispersion relations were calculated with a mode solver based on the finite element method (FEMSim by Rsoft [87]). The cyan line represents the dispersion relation of the an isolated TiO₂ layer with thickness t=120 nm, the green line is for the isolated IEW and violet and blue lines represent the even and odd hybrid modes of the hybrid structure. Here, we observe that the curves corresponding to the hybrid modes look like a hyperbolic function that asymptotically is approaching to the curves that correspond to the dispersion relation of the IEW and of the TiO₂ layer. It shows that the modes of the hybrid structure preserve some information of the original mode of the waveguides. In this figure, we also observe that the center of the hyperbola corresponds to a working point where the IEW and TiO₂ layer lines cross. At this point the transfer of energy is maximum between the

two parallel waveguides.

2.1.4 Reciprocity theorem of electromagnetism

The next step is to understand how the NS interacts with this kind of guided structures. To model the coupling of the radiated light from a NS into the guided modes of our integrated photonic structure, we used the reciprocity theorem of electromagnetism [88]. The NS is modeled as a point dipole placed at position r_0 close to the surface of a waveguide as is shown in figure 2.5. The light that excites the guided modes of the system can

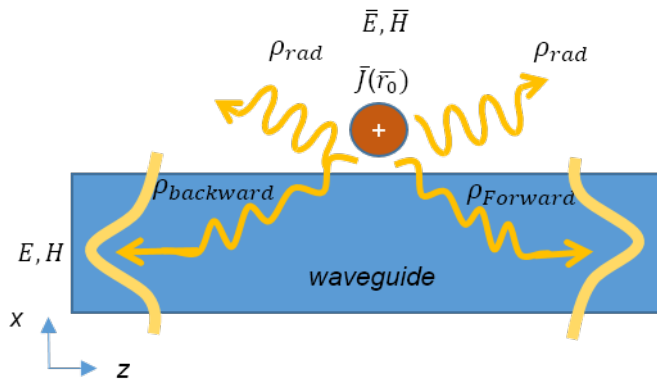


FIGURE 2.5 – Sketch of the coupling of light radiation from a dipole into a waveguide

be collected at the end of the waveguide and the light that excites the radiation modes is propagated into the free space. According with equation 1.1.52, the collected power can be associated with a collected LDOS (ρ_c) and this can be represented as a sum of the collected power due to the excitation of the forward guided modes ($\rho_{backward}$ and $\rho_{forward}$, respectively) . In the same way, the radiated light is associated with a radiated LDOS (ρ_{rad})

The electromagnetic fields created by the dipole (\bar{E} and \bar{H}) and the electromagnetic field of the modes (E and H) can be described using the reciprocity theorem of electromagnetism.

According to this theorem, fields \bar{E} , \bar{H} and E , H generated by the current densities J and \bar{J} , separated by a medium in a volume V are related by the following equation :

$$\frac{\partial}{\partial z} \int_{A_\infty} (E \times \bar{H}^* + \bar{E}^* \times H) \cdot \hat{z} dA = \int_{A_\infty} \nabla \cdot (E \times \bar{H}^* + \bar{E}^* \times H) dA, \quad (2.1.13)$$

where A is a cross section.

We write \bar{E} as a sum of all the modes of the waveguide (the guided and the radiation modes), such as

$$\bar{E} = \sum_k a_k E_k(\omega_0, r) + E_{rad}(\omega_0, r), \quad \bar{H} = \sum_k a_k H_k(\omega_0, r) + H_{rad}(\omega_0, r), \quad (2.1.14)$$

where k represents the k_{tm} guided mode of the system and a_k its amplitude. While rad represents the sum of all the radiation modes.

While E and H unbarred correspond to a superposition of guided modes of the system that could arrive at the end of the IEW. In order to simplify the problem, we reduce E and H as the electromagnetic field of a k_{tm} guided mode with $E = e_j e^{i\beta_j z}$ and $H = h_j e^{i\beta_j z}$.

Following the process described in appendix C, we can introduce \bar{E} and E in equation 2.1.13 and obtain that

$$a_k = -\frac{1}{4N_k} \int \int_{A_\infty} e_k(\omega_0) \cdot \bar{J}(\omega_0) dAdz, \quad (2.1.15)$$

where $N_k = \frac{1}{2} \int e_k \times h_l dA$ is the normalization factor associated to the orthogonality property of the guided modes (appendix C).

Here we use the dipole current $\bar{J} = j\delta(r - r_o)$ and its dipolar moment $p(r_0, \omega_0) = \int j\delta(r - r_0, \omega_0) dV$ in (2.1.15) for obtaining

$$a_k = \frac{p \cdot e_k(r_0, \omega_0)}{4N_i}. \quad (2.1.16)$$

Since a_k is the amplitude of the k_{tm} guided mode, it is defined as the coupling efficiency of the dipole into the k_{tm} guided mode of the system.

In order to know the fraction of dipole power into the j_{tm} mode (the collected power efficiency), we use the equation (2.1.14), the orthogonality property of modes and definition of the Poynting vector [89] to obtain that

$$\frac{P_k}{P_0} = \frac{1}{P_0} (a_k^2 N_k^2), \quad (2.1.17)$$

where P_0 is the power radiated by the dipole in vacuum.

As we mentioned before, the total normalized power at the end of IEW is the sum of the contribution of each guided mode. This collected power efficiency can be described as :

$$\frac{P_c}{P_0} = \sum_k \frac{|p \cdot E_k(r_0, \omega_0)|^2}{16P_0}, \quad (2.1.18)$$

where P_c is the total power coupled to the guided modes of the waveguide.

As we can notice equation (2.1.18) is related to the position of the dipole, for this reason the coupling efficiency can be seen as a local density of guided modes (LDOM) excited by the dipole. The LDOM can be seen as an enhancement of the collected LDOS (ρ_c/ρ_0) and according with the process previously described in section 1.1.6, the LDOM is also related to the Purcell factor and the life time (equation 1.1.52).

2.2 Hybrid photonic structure

In this thesis we work with a hybrid structure formed by an ion exchanged glass waveguide and a high-index layer of TiO_2 , as it is shown in figure 2.6a. The IEW has a gradient distribution of refractive index due to the thermal diffusion of silver ions into the glass substrate (figure 2.6b). The highest refractive index of the IEW is around 1.57 and the refractive index of glass is considered as 1.5, obtaining a index difference of $\Delta n = 0.07$. The TiO_2 layer used has a refractive index close to 2 for wavelengths between 550 nm and 700 nm (figure 2.6c), which was obtained by ellipsometry [90]. The waveguide is singlemode in the wavelength range from 400 nm to 800 nm.

We are interested in working at two wavelengths :

The first one, $\lambda=542$ nm as excitation wavelength of the NS and the second one, $\lambda=640$ nm as the emission wavelength the NS that we want to integrate into our structure. These wavelengths were selected according to available sources at the LNIO/UTT and the

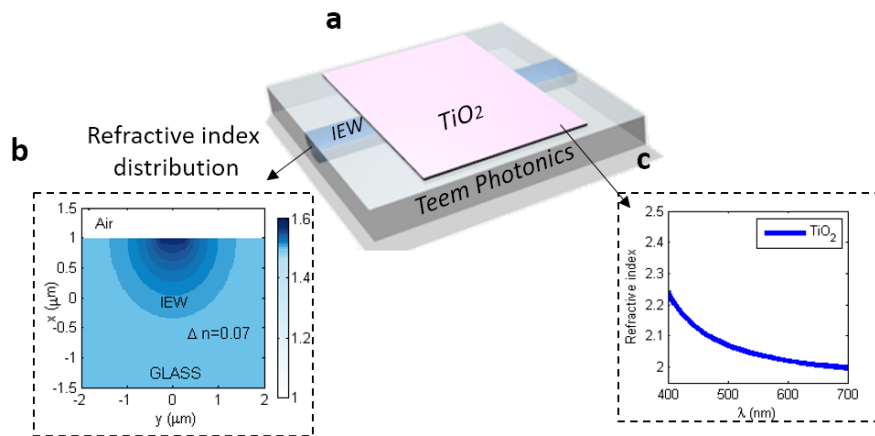


FIGURE 2.6 – Photonic hybrid structure. a) Structure formed by an IEW and a TiO₂ layer on top, b) the refractive index distribution of the IEW and c) the refractive index of the TiO₂ layer as a function of the wavelength.

properties of NV centers in diamond [91] and nanocrystals [92] used in the SINPHONIE project. These NS absorb green light (530 nm to 560 nm) and emit light between 580 nm and 800 nm.

2.2.1 Electric field enhancement at the surface

Due to the low difference between the refractive index of the glass and the core of the IEW (figure 2.6b), the modes of the IEW are weakly confined and the electric field on the surface has a low amplitude. As a result, a NS placed on top of a IEW will be weakly excited. In order to increase the electric field confinement to the surface, we place a thin layer of TiO₂ above the IEW to form a hybrid structure. When the guided mode propagates through structure, the hybrid modes with higher effective indices are created. Due to the proximity of both structures, the evanescent wave of the guided mode of the IEW, is able to excite the modes of the TiO₂ slab, resulting in a two waveguides coupled system. As we discussed in the last sections, this interaction gives rise to hybrid modes that allow periodic energy transfer between both waveguides [93, 94](figure 2.7a).

The electric field distribution resulting from the interference between hybrid modes is changing as it propagates through the hybrid structure. In our case, the fundamental mode of the IEW (figure 2.7b) is transformed into a hybrid mode confined mainly to the TiO₂ layer when the mode is approaching to the even mode distribution (figure 2.6c) and

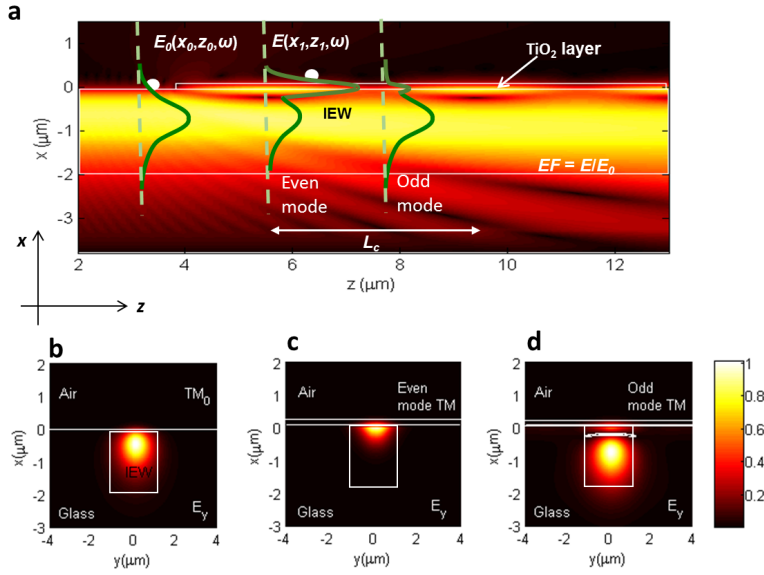


FIGURE 2.7 – Propagation of the guided modes through the photonic structure. a) Modeling of the electric field distribution through the photonic structure, where is shown the interference between hybrid modes that produces energy exchange between both waveguides. b) FDTD calculation of the mode profile (distribution of the electric field intensity of the fundamental TM mode into the IEW. c) and d) show the intensity distribution of the even and odd modes into the hybrid structure, respectively.

mainly confined in the IEW when the mode is approaching to the odd mode (figure 2.6d). As it is seen in this figure, the even mode is strongly confined and thus, the field on the surface of the TiO_2 layer is enhanced relatively to the field on top of the IEW. In order to quantify this enhancement, we define the enhancement factor as $EF = |E_0| / |E|$, where E_0 is the electromagnetic field measured on the surface of the IEW and E the electromagnetic field measured in the point of maximal intensity on the top surface of the TiO_2 layer.

The figures 2.8a and b show the EF values as a function of the thickness of the TiO_2 layer and the wavelength, for the TE and TM modes. These simulations were done with the finite-difference time-domain method (FDTD) [95] implemented in Fullwave by Rsoft [96]. For all simulations we use perfectly matched layer as boundaries. We observe that for a 50-nm-thick layer we obtain a maximal $EF=3.9$ for the TE mode at 542 nm, while the maximum value of $EF = 3.96$ at 640 nm is found for a thickness of 65 nm for the TE polarization. For a TM mode the peaks of EF are 11 and 8.3, they are found for a thickness of 90 nm and 115 nm at wavelengths of 542 nm and 640 nm, respectively. In the

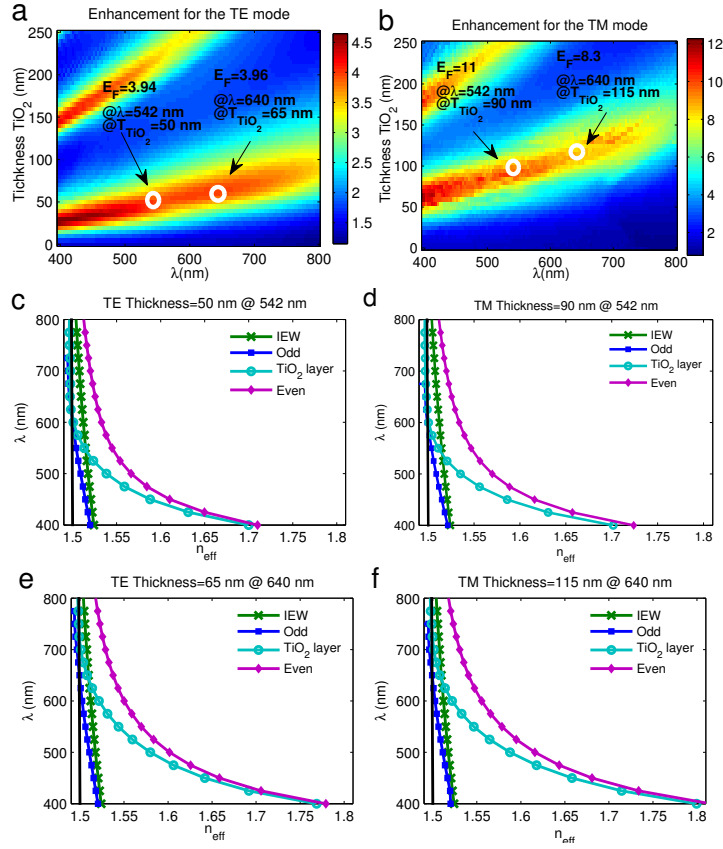


FIGURE 2.8 – Enhancement factor of electric field (EF) and dispersion relation. Calculated EF as a function of the wavelength (λ) and thickness of the TiO_2 layer for the a) TE and b) TM incident IEW modes. The white circles correspond to the highest EF factor at $\lambda = 542 \text{ nm}$ and $\lambda = 640 \text{ nm}$. Dispersion relations of the an isolated ion-exchanged waveguide on glass (green x), of an isolated TiO_2 layer on glass (cyan circles), the coupled hybrid structure (violet diamonds and blue squares) and the black line the refractive index of glass (1.5) for the TE and TM modes. c), d), e) and f) the dispersion of the hybrid structure presents an anti-crossing point at the four points in a) and b).

range of 400 nm to 700 nm we can observe that when the thickness increases, a second EF peak appears, that means that the structure involves the propagation of higher order modes for thicknesses greater than 150 nm. The amplitude of the second EF peak is lower because the field is weaker confined for higher order modes. For our purpose, it is then necessary to deal with TiO_2 thicknesses lower than 150 nm to ensure a maximum EF.

In the figures 2.8c-f we show the dispersion relations $n_{\text{eff}}(\lambda)$ of the different modes marked in figure 2.8a and b (white circles). Herein, the fundamental mode of the IEW is plotted with green x, and the mode supported by the TiO_2 layer on top of a glass substrate (without the presence of the IEW) with cyan circles. The violet diamonds and blue squares correspond to the even and odd branches of the hybrid mode, respectively. These curves

confirm that the enhancement factor EF is maximum when the phase mismatch between the two even and odd hybrid modes is minimized, i.e. when the dispersion curves of both isolated structures (IEW and TiO_2 waveguides) are crossing. This anticrossing minimizes the difference $\beta_e - \beta_0 \rightarrow 0$ (equation 2.1.12), allowing a maximum energy transfer in a minimum coupling length L_c between the two waveguides (where EF reached its maximum value). The black line represents the refractive index of glass equal to 1.5 in order to show the limit between radiation and guided modes (equation 2.1.9).

The other parameter that influences the EF is the width W of the TiO_2 layer. In the figure 2.9 we see that for an incident mode launched into the IEW at $\lambda=542$ nm, we observe that for the TE and TM modes (figures a and b) the EF increases as W decreases. This behavior is the same for an incident wavelength at $\lambda = 640$ nm (figures c and d). This enhancement can be simply explained by the increase of the lateral confinement of the guided mode into the TiO_2 ridge. The mode volume is reduced by the lateral confinement, resulting in an increase of the electric field amplitude at the surface.

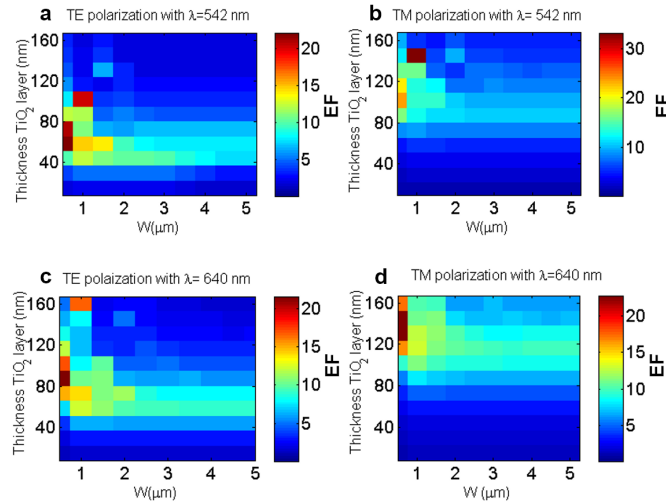


FIGURE 2.9 – Enhancement of electric field. Calculated EF as a function of the wavelength and width (W) of the TiO_2 layer for the a) TE and b) TM incident IEW modes with $\lambda = 542$ nm and d) TE and d) TM with $\lambda = 640\text{nm}$.

From this figure we found that the maximum EF at $\lambda= 542$ nm are close to 20 for the TE mode and close to 30 for the TM mode. Both maxima of the EF are found for a $W= 500$ nm, while the thickness of the TiO_2 ridge is found to be 70 nm and 170 nm for TE and TM modes, respectively. In the case of $\lambda= 640$ nm, we found EF values close to 20

for both modes, $W=500$ nm, and a ridge thickness of 90 nm and 150 nm for TE and TM modes, respectively.

2.2.2 Two reciprocal scenarios

We used the FDTD method to model the interaction between a dipole localized at 25 nm above the surface of a TiO_2 layer with a thickness of 83 nm and $W \Rightarrow \infty$ over the IEW (figure 2.10)a. The TiO_2 layer thickness was selected in order to compare some experimental results that will be presented in the next chapter. The NS is modeled as an electric dipole oscillating in a constant direction at $\lambda = 640$ nm.

The dipole is scanned across the yz -plane at a constant height of $x_0=25$ nm from the surface of the TiO_2 layer. The same simulation is performed for a dipole in interaction with a bare IEW (without TiO_2) as it is shown in figure 2.10a.

The output power at the left end of the IEW was calculated for each position of the dipole.

Figures 2.10b and c show the fraction of collected power for each position of the dipole in the scanning plane. The white dashed line represents the IEW edges and the white solid line shows the discontinuity between the hybrid structure and the input IEW. The simulations are performed for two orientations of the dipole : TE is a dipole oscillating in the y direction, while TM is a dipole oscillation in the x direction. The results depicted in figure 2.10 demonstrate that the collected power depends strongly on the position of the dipole and on its orientation. Additionally, we observe that the TiO_2 layer increases the coupling strength of the NS into the guided modes of the IEW.

In a second step, we simulated the propagation of a fundamental mode of the IEW at 640 nm. The mode propagates from left to right through the photonic structure. We calculate the electric field distribution in an observation plane located at a constant height of 25 nm above the surface of the structure as it is show in figure 2.10b (the same scanning plane as in the previous case).

The field intensity profile in the observation plane for the fundamental TE and TM modes are shown in figure 2.10e and f respectively. The electric field is normalized to the field measured on top of the bare IEW. Here we observe a similar intensity distribution

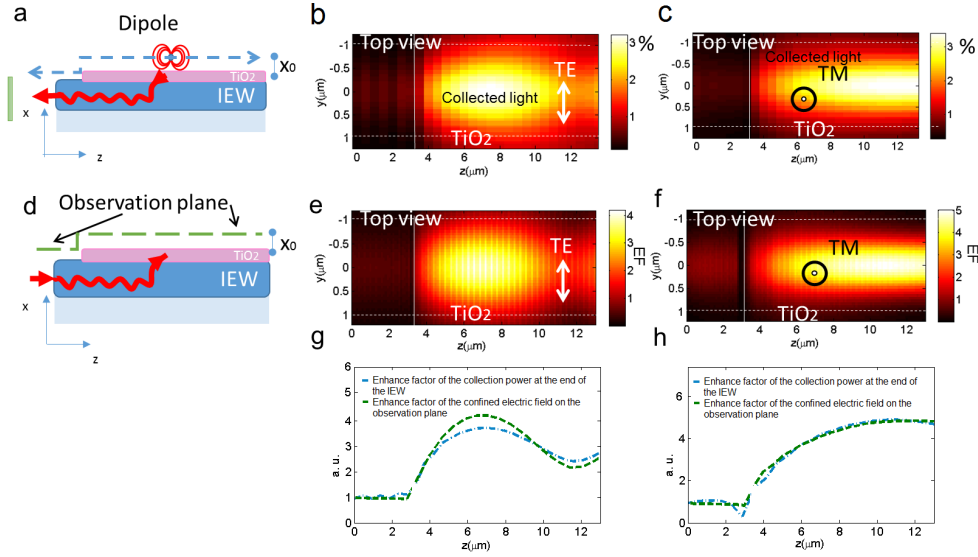


FIGURE 2.10 – Reciprocity of the interaction between a NS and guided modes of the photonic structure. a) Dipole position relative to the structure. b) and c) FDTD simulations of the field intensity radiated by a dipole and collected into the IEW as a function of the dipole position and orientation in respectively x and y directions. d) Excitation by the fundamental mode into the IEW and position of the observation plane. e) and f) FDTD simulations of the electrical field intensity in the observation plane for respectively TM and TE polarization. g) and h) the blue dashed line is the percent of the collected power at the left end of the IEW normalized by the collected power when the dipole is on top of the IEW (taken from images a and b), the green dashed line is the power in the observation plane which is normalized by the power calculated at x_0 from the top of the IEW (taken from image e and f).

than that of figures b and c. It is because the two cases are reciprocal. The dipole position that produces the maximum power coupled into the IEW coincides with the position of the intensity maximum in the reciprocal case (guided mode source). Figures 2.10g and h show horizontal profiles taken at the center of figures b, e and c, f in order to emphasize the reciprocal behavior.

In this simulation, we also measured the propagation losses due to the transformation of the IEW mode into the hybrid modes. The losses of TE and TM modes are 17% and 20%, respectively. These similar values obtained from the simulation are attributed to the transformation of hybrid modes into IEW modes.

Another interesting information for our study is the achievable Purcell factor. It will help us to quantify the physical interaction between the NS and the photonic structure, and more precisely its dynamics through the relaxation rate. In order to calculate this factor, we repeat again the simulation done by FDTD of scanning the dipole over the sample

(figure 2.10a). But we add numerical power monitors all around the photonic structure as its shown in figure 2.11 and two extra power monitors at the ends of the IEW. These two last allows calculating the total coupled light into the IEW (equation 2.1.18).

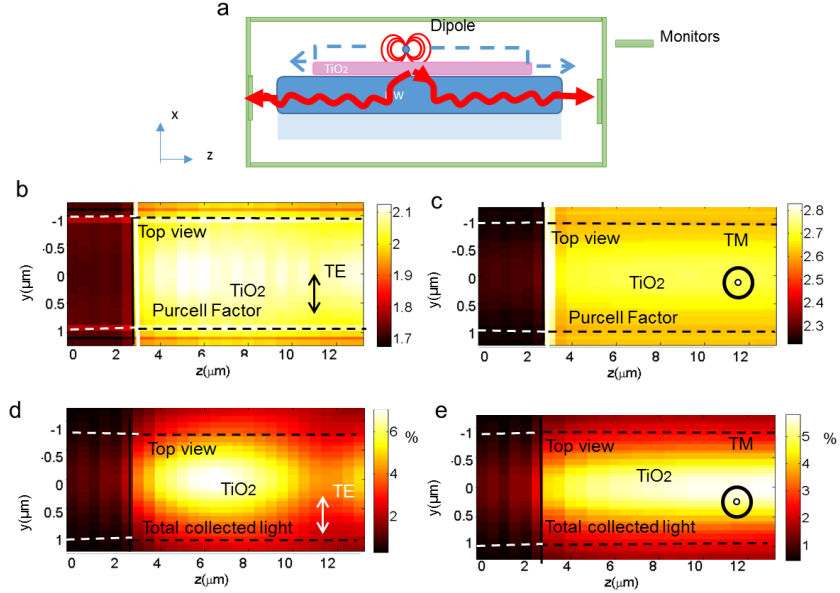


FIGURE 2.11 – Local density of states and coupling efficiency. Scheme of the position of the dipole on the photonic structure showing the calculations planes in the simulation. b) and c) Purcell factor for each position of the dipole due to the scanning of the surface. d) and e) the total coupling power at both ends of the IEW normalized by the total power of the dipole.

The monitors take the information of the radiated light to the free space (the total power P). Similar simulations were made for the dipole in the air in order to obtain P_0 . The Purcell factor is calculated as the ratio between P and P_0 . In figures 2.11b and c, we see the Purcell factor for each position of the dipole in the observation plane for TE and TM orientations. As in the previous figure, the dashed lines show the limit of the IEW and the solid line the interface between the TiO_2 layer and the glass. From these images we can notice that the Purcell factor is higher when the dipole is on top of the TiO_2 layer than when it is on top of the glass due to the higher index of the TiO_2 . We also observe that the Purcell factor in the zone of the IEW is higher than the Purcell factor in glass, this behavior is because of the increase of effective refractive index generated by the index distribution of the IEW (figure 2.6b). From these figures we notice that the highest Purcell factor corresponds to a dipole with TM orientation.

Finally in this section, we present the simulation for the total collected efficiency of the dipole as the sum of the power at both ends of the IEW normalized to the power of the dipole (the sum of the radiated power from the monitors). We observe in figure 2.11d and e, as in the previous examples, that the collected efficiency is higher for the dipole above the TiO₂ layer. The highest value of the coupling efficiency is 6% for the TM polarization and 5% for the TE.

2.3 Tapered TiO₂ ridges

Tapered TiO₂ ridges can be used to favor the selective excitation of the even hybrid mode. Compared to the directional coupling mechanism, the tapered shape transforms adiabatically the fundamental mode of the IEW into the even hybrid mode of the hybrid structure allowing strong confinement of the field into the TiO₂ layer while minimizing the interference contrast between the odd and even modes. This can be useful to get homogeneous distribution of the energy along the TiO₂ ridge waveguide and consequently facilitate the integration of a NS on top of the structure.

By using the beam propagation method (BPM) implemented in Beamprop software by Rsoft [96], we simulated a TiO₂ waveguide ridge with a width $W = 4 \mu m$, thickness 120 nm, and length L_{Taper} placed on top of an IEW(figure 2.12a). For a TM mode, we observe the energy transfer from a lateral view for three lengths of the taper : 5 μm , 270 μm , and 400 μm (figures b,c, and d).

In figures 2.12 b, c, and d we observe that for a short taper (figure a) the spatial beating of the hybrid mode leads to periodic energy transfer between the TiO₂ and the IEW. This is exactly how directional coupling is working (see previous section about coupled mode theory). Along the propagation, an important portion of the light is confined to the IEW. However, when the length of the taper is increased (figure b and c), the amplitude of the oscillations due to the energy transfer decreases and the energy remains mainly confined in the TiO₂ ridge waveguide. This tapered ridge can be used as an adiabatic mode coupler that smoothly transforms the IEW modes into the even mode of the hybrid structure, filtering out the odd hybrid mode.

Figure 2.12 e and f, show the power ratio of the incident light that is confined to

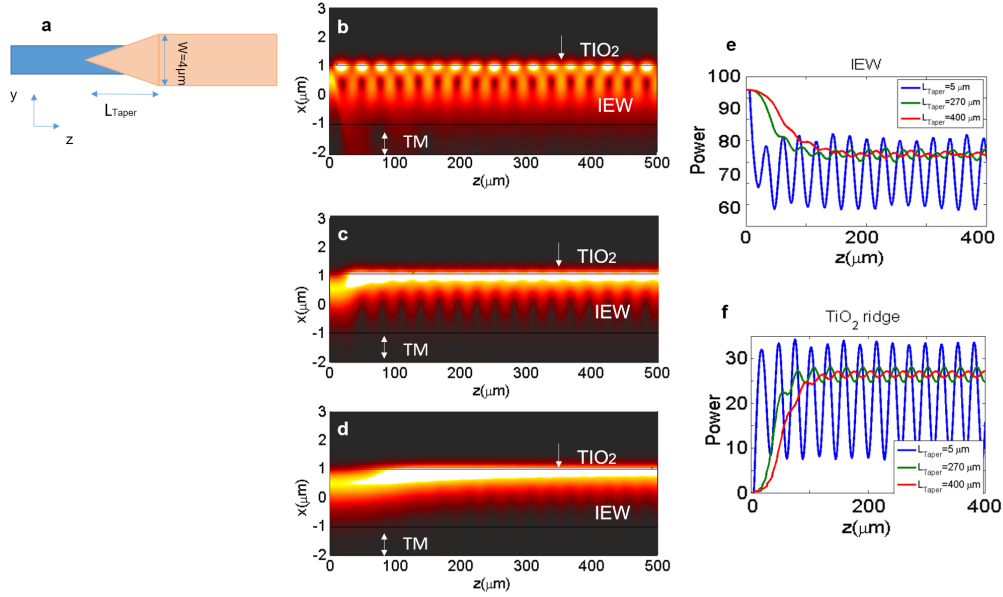


FIGURE 2.12 – a) Tapered ridge of TiO_2 with width $W = 4\mu\text{m}$, thickness 120 nm, and length L_{Taper} . Lateral view of the electric field distribution in the structure for the propagation of a TM mode of the IEW for L_{Taper} of b) 5 μm , c) 270 μm and d 400 μm . Percent of confined power in the e) IEW and f) in the TiO_2 ridge for these threes lengths of taper.

the IEW and the TiO_2 waveguide ridge, respectively. In these figures, we see that the amplitude of energy transferred between them decreases as the taper length increases (as we discussed before). This kind of tapered structure can be used to facilitate the collection of an emitter radiation. However the long length of the taper makes the FDTD simulation time very long and it was not possible to reproduce all the results by using these tapered structures in the framework of this project. As the case of the no-structured layer of TiO_2 (section 2.2.2), we calculated the propagation losses due to the transformation from the IEW to the hybrid modes of the tapered ridge of TiO_2 . We obtained losses of 8%, 4% and 2% for tapers with lengths of 5 μm , 270 μm and 400 μm , respectively.

2.4 Conclusion

We presented the design of a photonic hybrid waveguide system as a potential device to integrate a single-photon source on chip. The structure formed by an IEW and a TiO_2 layer was designed based on the mode coupling theory and the reciprocity theorem of electromagnetism.

We showed that this hybrid structure allows to transform a weakly confined mode of the IEW into a hybrid mode strongly confined to the surface of the structure. This transformation had as a consequence an enhancement of the confined field on top of the hybrid structure in comparison with the confined field on the IEW surface. We presented a parametric study of the influence of the parameters of TiO_2 layer in this enhancement. In a first study we found that for a simple TiO_2 it is possible to obtain a EF up to 11. The second study showed that for structured layer a EF up to 30 was found. From these results, we conclude that structured TiO_2 layers allow to enhance the confined field due to the reduction of the concentration area of the hybrid mode. The study of the collection efficiency of a dipole radiation on top of the photonic structure, showed that it possible to collect close to the 6 % of the light at the ends of the IEW, when the dipole is oscillating in x direction.

We presented a study of the reciprocity behavior of the excitation of the hybrid modes, when they are excited for guided modes or for a dipole placed on its surface. We observed that for a point over the structure, the collection efficiency is proportional to the EF.

Despite the photonic structure allowed us to enhance the LDOS of the system and collect the radiated light of a NS, the enhancement factor and the collection efficiency is still low. To improve the performance of this system, we have to consider the design of structures that supports strongly confined modes.

Chapter 3

Experimental validation of the integrated photonic structure

This chapter presents the experimental work done in the framework of this thesis project including the fabrication and the characterization of the hybrid IEW structures designed for the integration of a single-photon source.

We describe the scanning near-field optical microscopy (SNOM) configurations that were useful for the characterization of our guided device. More precisely, we introduce an experimental method to measure the local density of guided modes (LDOM). This experimental approach mimics the coupling of a dipole radiation into the waveguiding structures considered in this work.

Finally, we present preliminary experimental results obtained with the hybrid IEW platform using semiconductor quantum dots as nanoemitters in the visible spectrum.

3.1 Ions exchanged waveguides on glass

The IEW were fabricated by Teem Photonics company. The fabrication process relies on a local exchange between sodium ions and silver ions into a glass substrate. In this process, a matrix of SiO_2 glass with alkaline ions weakly bonded is put in contact with a molten salt bath with silver ions (Ag^+), some ions from the bath can penetrate into the glass silica matrix due to the thermal diffusion and electrical conduction processes (figure 3.1a). At the same time, some sodium ions (Na^+) diffuse from the glass to the bath. This

ions exchange process between Na^+ and Ag^+ ions locally change the refractive index of the glass close to its surface. Because the polarizability of Ag^+ is higher than the polarizability of Na^+ , the process generates a local increase of the glass refractive index. The diffusion process obeys to the well known Fick's diffusion law and gives rise to a gradient profile of the refractive index in the glass substrate (figure 2.6a).

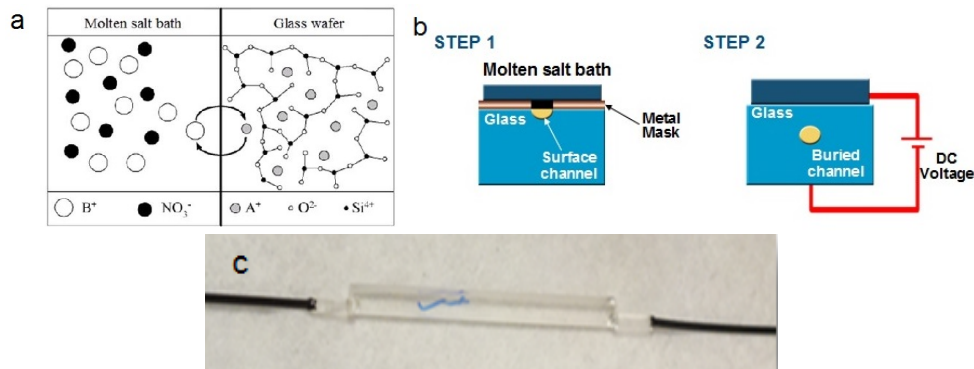


FIGURE 3.1 – Fabrication process of ion exchange waveguides on glass. a) Ions exchange process between a molten salt bath and a glass wafer. The process is divided into two-steps. The step one consists in diffusing at high temperature silver ions into the glass wafer through a metal mask and the second step moves the waveguide deeper into the glass through the action of an external electric field. c) IEW platform connected to commercial optical fibers.

The fabrication process made by the company consists of two steps. In the first, a glass substrate is covered with a metallic mask and a molten salt bath. The mask consists on diffusion windows of about $1\ \mu m$ wide that defines the future waveguides (figure 3.1b). Then a diffusion at high temperature of silver ions into the glass occurs, the refractive index is altered and the waveguide is created. The second step moves the waveguide deeper into the glass substrate by the application of an external electric field.

The parameters (duration and temperature of the diffusion process) of the ion exchange can be selected in order to control the core size of the waveguide and its polarization properties. Other advantage is its high compatibility with commercial optical fibers, which allow the manufacturing of samples connected to optical fibers as it is shown in figure 3.1c. In some experiments of this thesis the IEW were connected to polarization maintain fibers (PMF), but this aspect is clarified in the next sections. All the information about the technology and products developed by Teem Photonics can be found on its website [97].

The platform has a square shape of 1 mm by 1 mm area and it contains up to 200

waveguides separated by $51 \mu m$ (figure 3.2a). The width of the surface waveguides is approximately $2 \mu m$ and they are designed to support a singlemode across a spectral range ranging from 400 nm to 830 nm (figure 3.2b). The spectrum of the IEW shows two main peaks, these corresponding to the TE and the TM mode. The cut-off wavelength for the TM mode is 750 nm and 830 nm for the TE mode. The transparency of the glass regenerates low propagation losses.

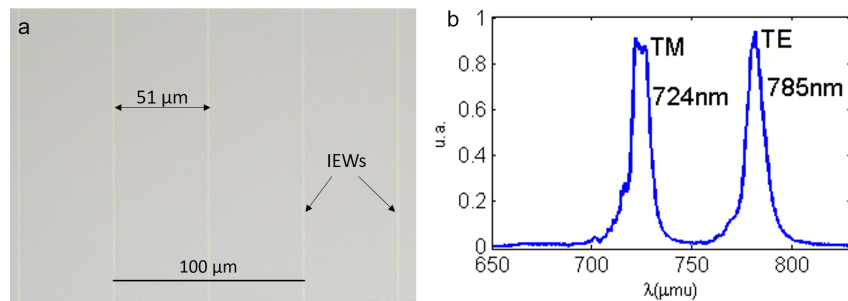


FIGURE 3.2 – Ion exchange waveguide on glass. a) Optical microscopy image of the platform of ion exchanged glass waveguides used in this thesis. We observe 5 IEW separated by a distance of $50 \mu m$. b) Normalized spectrum of the IEW.

3.1.1 TiO_2 overlayer on IEWs

Figure 3.3 shows the fabrication process of the hybrid structures showed in chapter 2. This process was divided into 7 steps :

1. **Sample cleaning.** The wafer containing the IEW is cleaned with a ultrasonic bath of acetone for 1 min. After that, the sample is immersed in a ethanol and isopropanol bath. Finally the sample is dried with compressed air.
2. **PMMA deposition.** The Poly(methyl methacrylate) or PMMA is an electron sensitive resist commonly used in electron beam lithography process. The PMMA with concentration of 30 g/L is deposited on top of the IEW platform by spin coating. The spin coating have a duration of 30 s with a speed of 4000 rpm. The deposited PMMA layer has a thickness around 160 nm. After the deposition, the samples were heated during 3 hours at 170°C in an oven.
3. **ESPACER deposition.** The ESPACER is a resist used to avoid the diffusion of charges on the surface of the PMMA and to obtain a better penetration of electrons

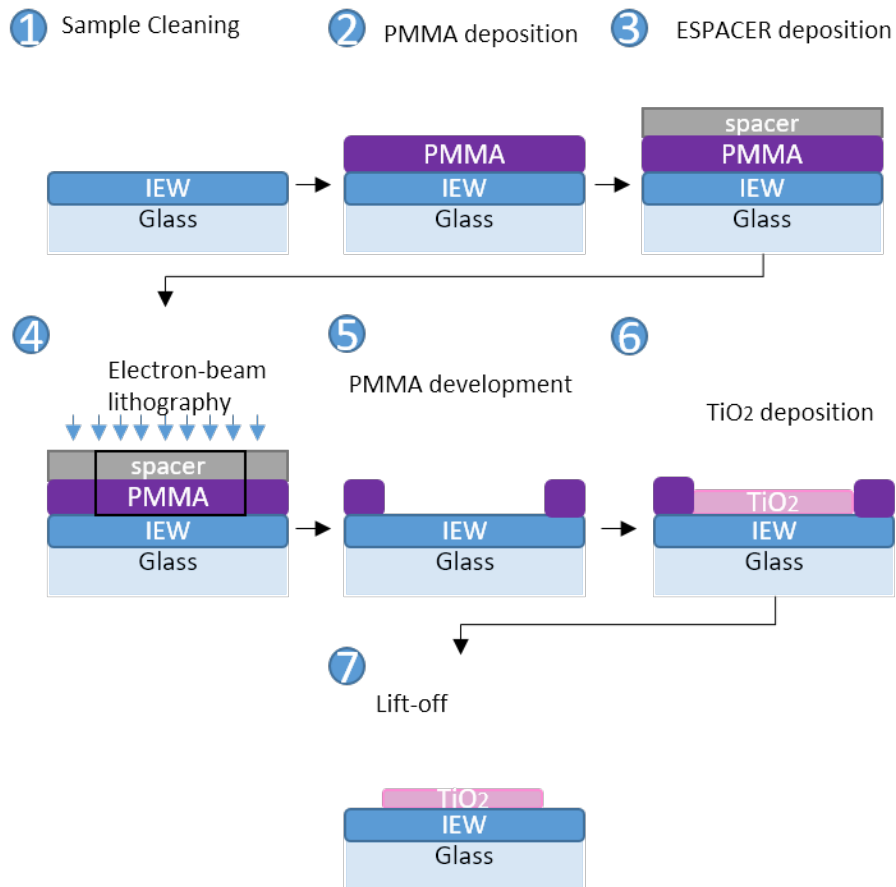


FIGURE 3.3 – Fabrication of TiO_2 overlay on ion-exchanged waveguide on glass. 1 sample cleaning, 2 PMMA deposition on the IEW platform, 3 ESPACER deposition on top of the PMMA layer, 4 electron-beam lithography, 5 PMMA development, 6 TiO_2 deposition and 7 the lift-off process.

into PMMA. The ESPACER was deposited by spin coating for 30 s with a speed of 3000 rpm.

4. Electron-beam lithography. We use a electron beam microscope Raith eLiNE for the lithography. The electron beam spot on the surface of the PMMA has a diameter of 20 nm. A mask is designed in order to excite only a desired zone where the TiO_2 will be deposited. After electron beam exposure, the PMMA acts as a positive resist, the large molecules of PMMA are broken down to small molecules, which are more soluble than large molecules, so it is easier to wash away by a development process.

5. PMMA development. We immersed the sample in a water bath for to 2 min in order to removed the ESPACER. Then, we put the sample in a MIBK :IPA bath

for 1 min to remove the exposed PMMA. After that, we use isopropanol to clean residues of exposed PMMA in the sample. The result is a hole localized in the exposed zone by the electron beam.

6. **TiO₂ deposition.** The TiO₂ was deposited by thermal deposition.
7. **Lift-off.** The last part of the fabrication process is to immerse the sample in an acetone bath for 2 days. The acetone removes the remain of PMMA.

Table 3.1 shows the selection of lithographic parameters for the electron-beam lithography and the material parameters in the electron-beam evaporator.

TABLE 3.1 – Parameters of electron beam lithography for the fabrication of TiO₂ layer and Au nano-structure.

Parameter	Value
EHT (Extra High Tension)	10 kV
Working distance	5.6 mm
Aperture	30 μ m
Dose area	140 pC/cm ²
Dose line	-
Step size (area)	0.0048 μ m
Step size (line)	-
Beam current	164 pA

3.1.2 Fabricated samples

We fabricated two kinds of samples. The first one, a TiO₂ layer evaporated on top of the IEW platform in order to observe the electric field enhancement and the coupling mode described in the chapter 2. The second sample is a rectangular TiO₂ ridge placed on top of the IEW in order to increase the electric field enhancement and bring us closer to the fabrication of the sample described at the end of chapter 1. Both samples were fabricated according to the process shown in figure 3.3.

Figure 3.4a shows the scheme of the first sample, where we observe a TiO₂ slab with a width of 1500 μ m width, a thickness of 90 nm and a variable length between 30 to 130 μ m. We designed this TiO₂ slab in order to observe the electric field confined over the IEW with and without the TiO₂ layer. The thickness was selected to promote a high EF for the TM mode propagation at 542 nm, according with figure 2.8. While the variable

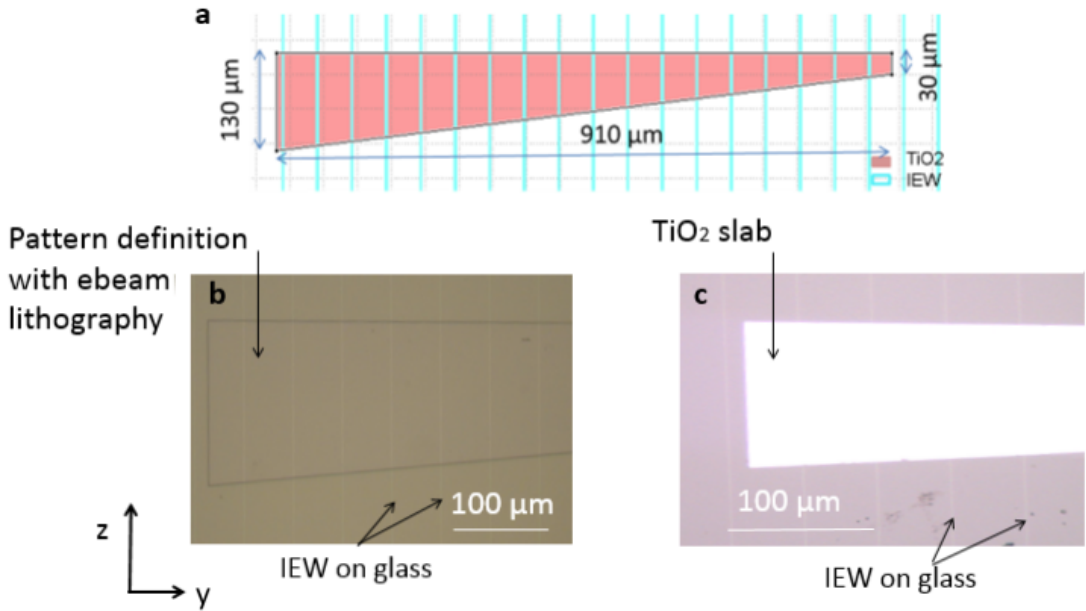


FIGURE 3.4 – Sample 1. a) Scheme of the designed shape of sample 1, b) optical microscopy image of the ion exchanged glass waveguides after the electron beam lithography and c) optical microscopy images of the sample after the TiO_2 deposition and lift-off.

length of the TiO_2 was designed to observe the absorption losses. Figure 3.4b and c show optical microscope images of the sample after the electron beam lithography and after the TiO_2 deposition and lift-off, respectively.

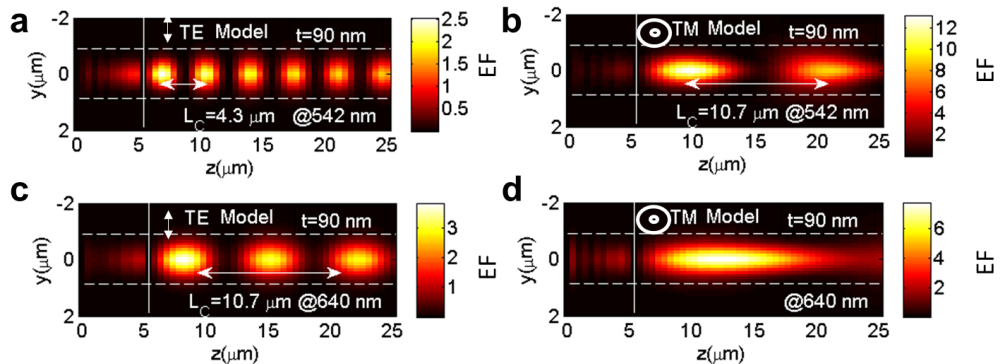


FIGURE 3.5 – Numerical FDTD simulation of the propagation of a guided mode through the photonic structure with a TiO_2 slab thickness of $t = 90 \text{ nm}$ at $\lambda = 542 \text{ nm}$ for a) TE and b) TM modes and for b) TE and d) TM modes at $\lambda = 640 \text{ nm}$.

We perform numerical simulations with the FDTD method in order to observe the expected behavior of the sample 1. Figure 3.5 shows the results for a TiO_2 slab with thickness $t=90 \text{ nm}$ placed on top of a IEW where the IEW mode is injected from left

side. These simulations were done for TE and TM modes at $\lambda=542$ nm (figures a and b, respectively) and $\lambda=640$ nm (figure c and d, respectively). From these results we expect an $EF = 2.3$ and $L_C=4.3 \mu m$ as the period of the spatial beating of hybrid modes for the TE mode at $\lambda=542$ nm. For a TM mode, $EF=7.7$ and $L_C=10.7 \mu m$ are expected. For $\lambda=640$ nm we expect an $EF=2.3$ and $L_C=10.7 \mu m$ for TE mode and, $EF=9.8$ and $L_C=31 \mu m$ for the propagation of a TM mode. Table 3.2 shows the calculate effective indices for the hybrid modes for the four cases presented in figure 3.5.

TABLE 3.2 – Calculated effective indices for sample 1.

Wavelength	Mode	n_{eff} (even mode)	n_{eff} (odd mode)
542 nm	TE	1.58	1.503
	TM	1.52	1.49
640 nm	TE	1.64	1.509
	TM	1.54	1.502

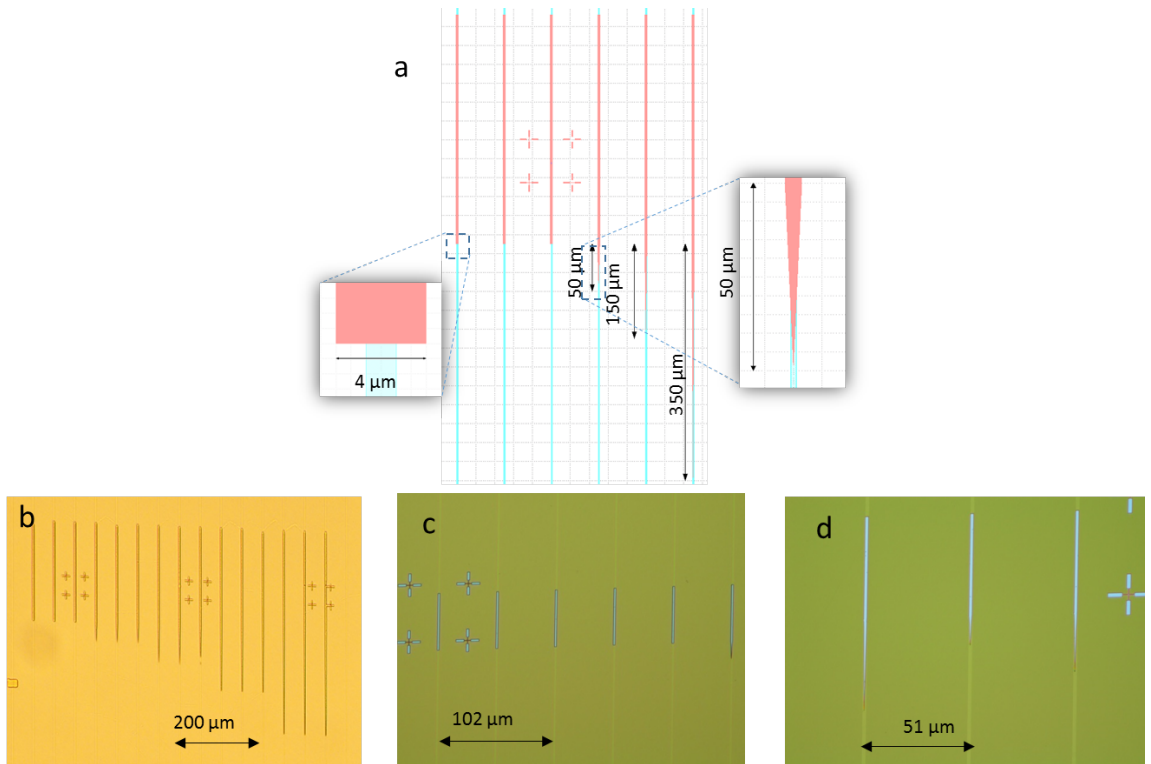


FIGURE 3.6 – Sample 2. a) Scheme of the designed shape of sample 2, where the details show the TiO_2 ridges with and without tapered end. b) Optical microscopy image of the platform of ion exchanged glass waveguides after the electron beam lithography. c) The sample 2 after the TiO_2 deposition where we observe the ridge without and d) with tapered ends.

In figure 3.6 we show the scheme of the second kind of sample that we fabricated

(sample 2). This sample contains structured TiO_2 ridges placed over each IEW. In the detail of figure 3.6a we observe a rectangular ridge with a width of $4 \mu\text{m}$ and length of $250 \mu\text{m}$. For this sample the desired thickness is 120 nm in order to have the highest EF for a the propagation of a TM mode at $\lambda=640$ nm as was shown in chapter 2. In this sample, we also designed ridges with a tapered end, the taper has a triangular shape with lengths of 50, 150, 200, and $350 \mu\text{m}$. These tapers were fabricated in order to reproduce the results showed in chapter 2. Figure 3.6b shows the optical microscope image of the sample after the electron beam lithography and figures c and b the images of the sample after the TiO_2 deposition.

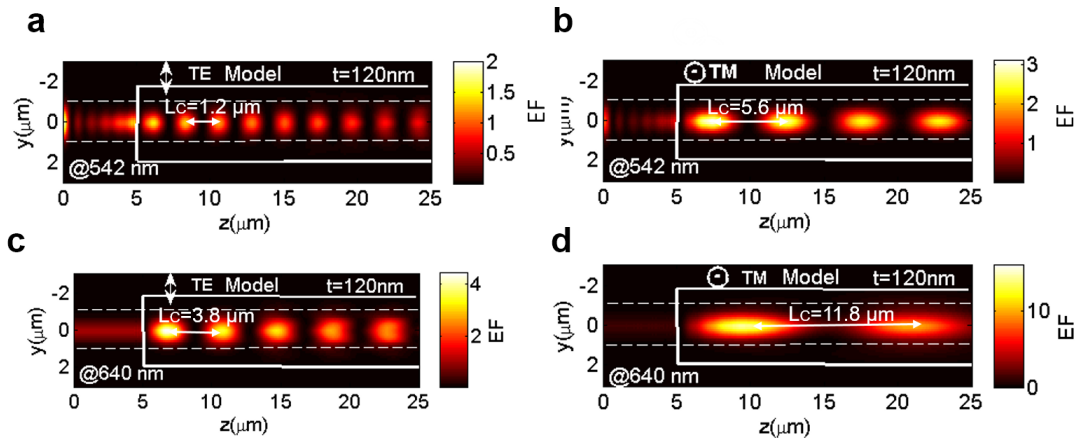


FIGURE 3.7 – Numerical simulation for the propagation of a guided mode at $\lambda=542$ nm, which is propagating through the sample 2 with a TiO_2 ridge of thickness $t= 120$ nm. a) Results for a TE mode and b) TM mode and for c) TE and d) TM modes at $\lambda=640$ nm.

As we made for sample 1, we simulated the propagation of TE and TM modes through the sample 2. Figure 3.7 shows the numerical results for this propagation at $\lambda=542$ nm (figures a and b) for $\lambda=640$ nm (figures c and d). For the TE mode at $\lambda=542$ nm we calculated an $\text{EF}= 1.5$ and $L_C=1.2 \mu\text{m}$, $\text{EF}=3$ and $L_C=5.6 \mu\text{m}$ are calculated for the TM mode. For $\lambda=640$ nm we obtained an $\text{EF}=4.0$ with $L_C=3.8 \mu\text{m}$ for the propagation of the TE mode. While for a TM mode, we calculated an $\text{EF}=15.6$ with $L_C= 11.8 \mu\text{m}$. Table 3.3 shows the effective indices calculated for the hybrid modes for the four cases presented in figure 3.5.

TABLE 3.3 – Calculated effective indices for sample 2.

Wavelength	Mode	n_{eff} (even mode)	n_{eff} (odd mode)
542 nm	TE	1.72	1.51
	TM	1.58	1.507
640 nm	TE	1.65	1.504
	TM	1.54	1.50

Fabrication issues

During the fabrication process previously shown in figure 3.3 we found critical steps that caused some problems.

In the electron beam lithography process we observe two main problems, the RAM memory saturation of electronic microscope and the alignment of the designed mask relative to the IEW (figure 3.8). The electron beam microscope makes the excitation of the sample on exposition areas of $100 \times 100 \mu m$ and the spot diameter of the electron beam is close to 20 nm. Because of this reason, the fabrication of the TiO_2 slab (3.4a) was defined in several exposition areas each one with a high number of exposure points. The high number of process in the computer that controls the electron beam microscope generated a physical memory RAM saturation and as consequence some process were stopped before its end. The process could be re started at the stop points but generated some misalignment problems as is shown in figure 3.8a. Other problem with the electron beam lithography process was the poor visibility of the IEW in the scanning electron microscope (SEM) images (figure 3.8b). It is due to the low contrast index between the IEWs and the glass making difficult the alignment with the center of the IEW. At the beginning we considered that the IEWs were separated for a distance of $50 \mu m$ according to measures taken from the optical microscope image but the resolution was not enough to adequately measure this correct distance of $51 \mu m$. This alignment of the mask generates some issues as it is shown in figure 3.8c, where it is possible to observe a shift between the desired patterns and the fabricated patterns.

We fabricated thicker TiO_2 layers in order to promote the propagation of TM modes at 640 nm. For a TiO_2 slab with thickness of 120 nm we observe problems in the process of TiO_2 deposition. This thickness is almost the same as the PMMA layer (figure 3.3, process 2 and 3), therefore the TiO_2 exceeds the PMMA and we observe a low quality in

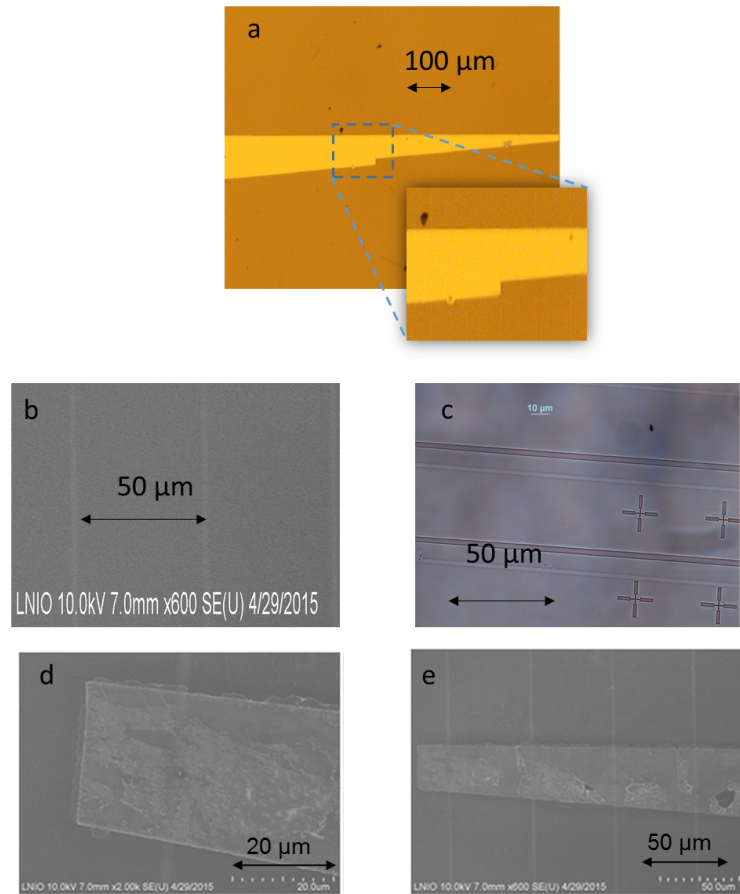


FIGURE 3.8 – Fabrication issues. a) Alignment issue due to the high density of exposed points. b) SEM image with poor definition of the edges of the IEW and c) Optical microscopy image of a sample out of the IEW due to alignment issues. d) and e) fabrication imperfections, where TiO_2 exceeds the designed pattern, generating undefined edges of the TiO_2 slab.

the precision of the edges of the electron beam pattern (figure 3.8d and e).

In the fabrication process of TiO_2 ridges with a thickness of 120 nm, we observe problems after the lift-off process (figure 3.3 process 7). As the previous fabrication issue, the thickness of the TiO_2 is almost the thickness of the PMMA. After the lift-off we observe remnants of TiO_2 over the whole surface of the sample (figure 3.9a). These remnants can be found as united ridges, defects and deformations (figure 3.9b and c). These remnants were cleaned using a ultrasonic Decon-90 bath for 5 min followed by a rinse of ion water, a acetone bath and a drying process with compressed air. Figure 3.9d and e show the optical microscope image of the sample after cleaning, here we observe some little remnants of TiO_2 and some damage of the structure.

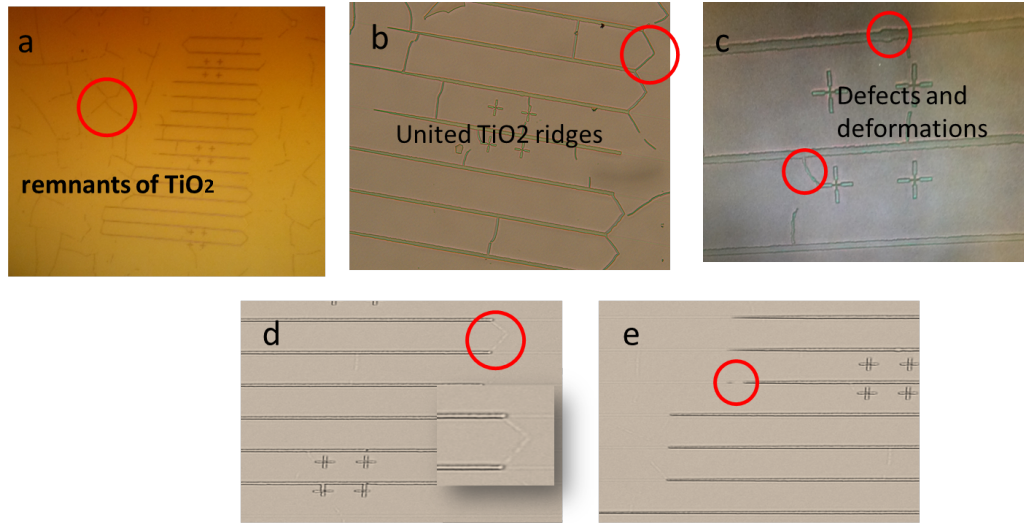


FIGURE 3.9 – Optical microscopy images for the fabrication of sample 2 which have fabrication imperfections. a) remnants of TiO₂ over the whole sample, b) United TiO₂ ridges due to the remnants of TiO₂, c) defects and deformations of the edges of the designed structure, d) sample after cleaning process where the remnants of TiO₂ was almost removed and e) sample after cleaning where it is observed the damage of the tapered ridges.

3.2 Optical near field characterization techniques for the integrated photonic structure

In order to characterize the distribution of the electric field over the structure when light is sent through the IEW, we use a the scanning near-field optical microscopy (SNOM) in apertureless mode, which is adapted from an atomic force microscopy (AFM). The physical principles of the SNOM and AFM are briefly shown in appendix D.

We used a AFM M5 Park Scientific Instrument system with conical silicon tip Bruker. We adapted the system to excite the sample with light at 640 nm propagating through the IEW. The AFM tip oscillates at a frequency ω_0 and intermittently touches the sample (tapping mode, see appendix D), perturbing the near field confined on the surface of the sample and generating scattering light. In the next sections we present three configurations of SNOM used to measured the light propagation in our device.

3.2.1 SNOM in perturbation mode

Figure 3.10 shows the scheme of the SNOM in perturbation mode or *p-SNOM*. Here the sample is excited by light sent through an optical fiber placed at the input of the IEW.

The fiber is a polarization maintaining optical fiber (PMF) at 680 nm connected to a polarization controller and a laser source at 640 nm (simulations presented in chapter 2). We consider that the power at the input is P_i . The transmission power P_f is collected by a PMF optical fiber placed at the output of the IEW. This fiber is also connected to a polarization control and a detector CD12703-01 of Hamamatsu photonics. The confined field in the surface of the sample is perturbed by the AFM tip that is in contact with the surface of the sample in a tapping mode with a osculation frequency of ω_0 . As a consequence of this perturbation, scattering light P_s is generated, changing the transmission power P_f .

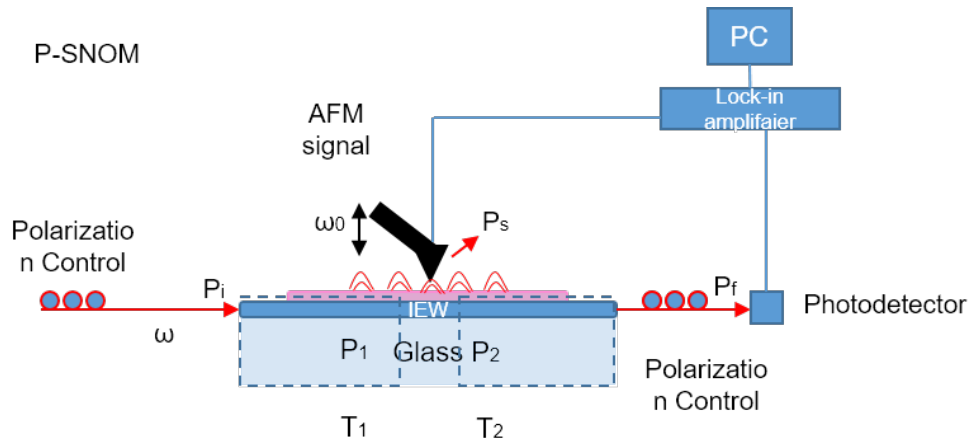


FIGURE 3.10 – Scheme of the perturbation SNOM configuration.

We consider two important zones : the zone 1 as the region before the perturbation point by the tip and the zone 2 as the region after the perturbation. The zone 1 has a transmitted power P_1 due to a transmittance T_1 and similarly zone 2 has a $P_2 = P_f$ due to a T_2 . In the absence of the tip, the transmitted power can be written as :

$$P_{f0} = T_2 P_1 = T_2 T_1 P_i, \quad (3.2.1)$$

where P_{f0} represent the initial case in absence of the AFM tip. When the AFM interacts with the evanescent electric field at the surface, the transmitted power is affected as

$$P_f = T_2(T_1 P_1 - P_s). \quad (3.2.2)$$

The transmission difference can be calculated taking the equations (3.2.1) and (3.2.2) :

$$\Delta T = \frac{P_s}{P_i T_1}. \quad (3.2.3)$$

The P_f is measured by a photodetector and the information is sent to a lock-in amplifier that also receives the information of the oscillation frequency of the AFM tip and the height value measured by the AFM head (figure 3.10).

In order to understand the information processing by the lock-in amplifier (LIA), we can consider that P_i is due to a electric field E_i with oscillation frequency ω whereas P_f is affected by the oscillation frequency of the AFM tip.

The oscillation frequency of E_i is the range of THz and it can not be detected by the photodetector. Therefore, the electric field detected by the lock-in amplifier has a oscillation frequency of ω_0 (the oscillation frequency of the tip). This generates a voltage signal as

$$V_d = V_f \sin(\omega_0 t + \theta_0), \quad \text{with} \quad V_f \propto |E_f^2| \quad (3.2.4)$$

This signal is mixed with the reference signal of the LIA. In this case the reference signal corresponds to the signal of the oscillation AFM tip $V_r = V_{ref} \sin(\omega_0 t + \theta_{ref})$. The combination of both signals can be written as

$$V_f \sin(\omega_0 t + \theta_0) V_{ref} \sin(\omega_0 t + \theta_{ref}) = \frac{1}{2} V_f V_{ref} (\cos(\theta_0 - \theta_{ref}) - \cos(2\omega_0 t + \theta_t + \theta_{ref})). \quad (3.2.5)$$

Then the LIA filters the frequency ω_0 , the equation 3.2.5 can be rewritten as $X = V_f V_{ref} \cos(\theta)$ with $\theta = \theta_f - \theta_{ref}$. This process is repeated with $\theta_{ref} + 90^\circ$, and we obtain $Y = V_f V_{ref} \sin \theta$. These signals are measured in the output of the LIA as :

$$R = \frac{1}{2} V_f V_{ref} = \sqrt{X^2 + Y^2}, \quad (3.2.6a)$$

$$\theta = \tan^{-1}(Y/X) = \theta_0 - \theta_{ref}. \quad (3.2.6b)$$

Here R is a voltage proportional to P_f , while the phase θ represent a mechanical phase of the system. The output signal of the LIA is sent to a computer, which also receives the information about the topography of the sample from the AFM. It should be mentioned

that P_f is only a value proportional to the P_s but it is not the real value of the confined field on the surface.

3.2.2 SNOM in scattering mode

In this section, we present the scattering SNOM or s-SNOM configuration (Figure 3.11) that we used to directly measure the scattered light P_s and obtain information about the effective indices of the modes in the structure. Here light at 640 nm (frequency ω) and incident power P_i , is sent through the IEW by using a PMF fiber connected to a polarization control. As for p-SNOM, the AFM tip oscillates in tapping mode with frequency ω_0 generating a scattering light due to the perturbation of the near-field confined to the surface. In the s-SNOM configuration, the scattered light is collected by a external optical system.

The scattered light is collected by a microscope objective and the light propagates through a beam splitter 50/50. Here, one part of the light is focused on a CCD camera and the other is sent to a second microscope objective focused on the input of a PMF optical fiber connected to a photodetector. The signal of the photodetector is sent to the LIA that also receive the information of the oscillation frequency of the AFM tip. The signal from the LIA is finally sent to the PC computer where we can obtain the topography images of the sample and the mapping of the P_s over the structure.

One interesting feature about the s-SNOM is the analysis of the collected light for the optical system. Due to the numerical aperture of the microscope objective, the optical system will collect the scattered light from the surface in an area of some μm^2 . Since, the radius of the AFM tip used was about 20 nm, the optical system is able to collect the scattering light from sources in the vicinity of the tip. These sources can be small defects at the surface.

In order to understand the image formation process, in figure 3.11 b we represent the optical path through the optical system. This scheme has a coordinate system with origin at the position 0 of the tip. Here, the guided mode is represented as a k-vector that is propagating in the \vec{k}_i direction. The scattering light generated by the tip and collected by the optical system, is represented by the k-vector \vec{k}_{da} . The signal collected by the optical system can be described as

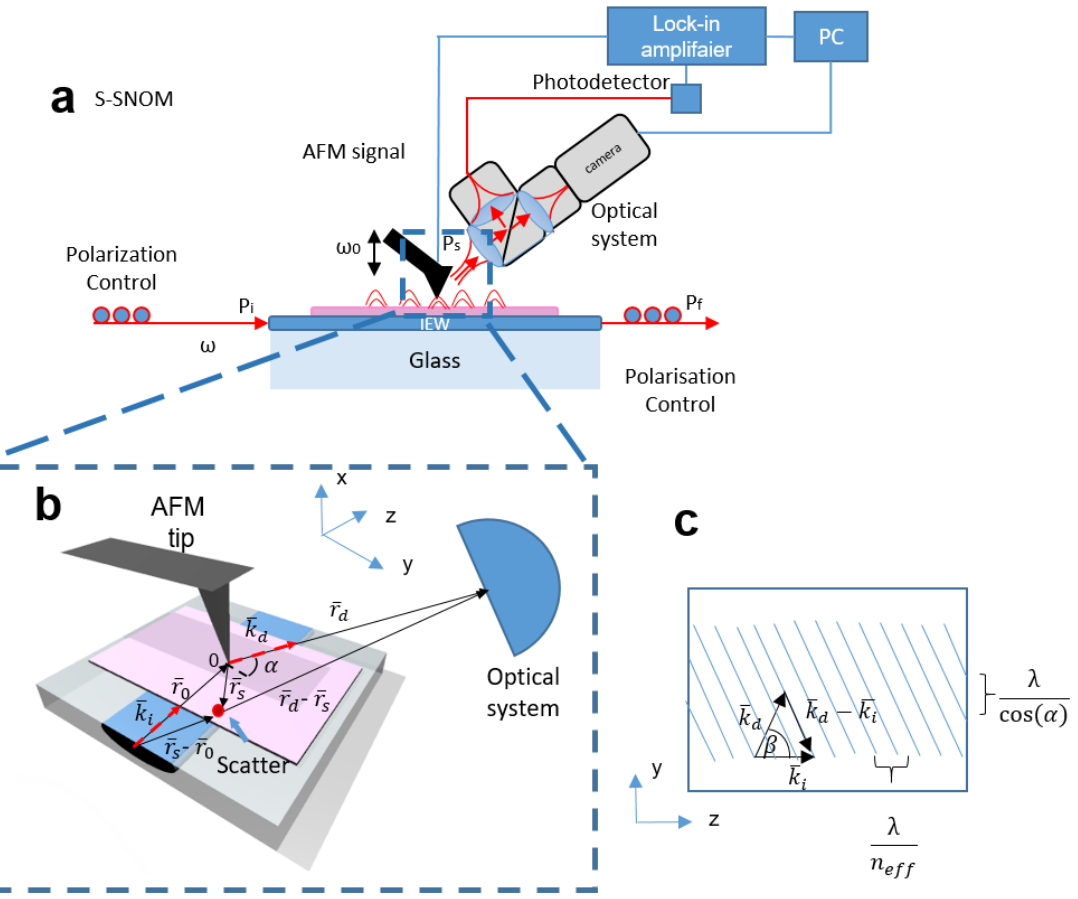


FIGURE 3.11 – a) Scheme of the scattering SNOM configuration. b) Optical paths involved in the image formation process and c) interference pattern expected in the detected signal measured by the photodetector during the scanning of tip.

$$A e^{-i \vec{k}_i \cdot \vec{r}_0} e^{i \vec{k}_d \cdot \vec{r}_d}. \quad (3.2.7)$$

On the other hand, the scattered light from the tip is propagating in the direction of \vec{k}_s and it arrives to some scatter on the surface. Then, light from the scatter is propagating in the direction of $\vec{r}_d - \vec{r}_s$ and finally it arrives to the optical system. In this case, this signal can be written as

$$B e^{i \vec{k}_i \cdot (\vec{r}_s - \vec{r}_0)} e^{i \vec{k}_d \cdot (\vec{r}_d - \vec{r}_s)}. \quad (3.2.8)$$

The total signal collected by the optical system is a superposition of both signals,

therefore the total signal on the optical system is

$$| Ae^{-i\vec{k}_i \cdot \vec{r}_0} e^{i\vec{k}_d \cdot \vec{r}_d} + Be^{i\vec{k}_i \cdot (\vec{r}_s - \vec{r}_0)} e^{i\vec{k}_d \cdot (\vec{r}_d - \vec{r}_s)} |^2. \quad (3.2.9)$$

Working with equation 3.2.9, we obtained

$$A^2 + B^2 + AB[e^{i(\vec{k}_i - \vec{k}_d) \cdot \vec{r}_s} + e^{-i(\vec{k}_i - \vec{k}_d) \cdot \vec{r}_s}]. \quad (3.2.10)$$

This equation can be written in terms of the trigonometric functions as

$$A^2 + B^2 + 2AB\cos(\Delta\phi), \quad (3.2.11)$$

where $\Delta\phi = (\vec{k}_i - \vec{k}_d) \cdot \vec{r}_s$. From equation 3.2.11, we deduce that the signal collected for the optical system has a periodic distribution (an interference pattern).

According to figure 3.11b the vectors \vec{k}_i , \vec{K}_d and \vec{r}_s can be written as

$$\vec{k}_i = (0, 0, k_0 n_{eff}), \quad (3.2.12a)$$

$$\vec{k}_d = (k_0 \sin(\alpha), k_0 \cos(\alpha), 0), \quad (3.2.12b)$$

$$\vec{r}_s = (0, y, z), \quad (3.2.12c)$$

With α the angle of inclination of the detector (optical system) in relation with the yz plane. From these equations, we deduce that the $\Delta\phi$ period can be described as

$$\Delta\phi = k_0 [n_{eff}z - \cos(\alpha y)]. \quad (3.2.13)$$

From equation 3.2.13 and using $k_0 = 2\pi/\lambda$ we can predict an interference pattern with period λn_{eff} in the z direction and $\lambda \cos \alpha$ in the y direction. As it is shown in figure 3.11c, where the lines have a inclination angle β which corresponds to the angle of the $\vec{k}_i - \vec{k}_d$ vector.

3.3 Experimental results of SNOM

In these sections we present the experimental results obtained from the optical near field measurement of the photonic structure. The sections are divided according to the configuration used in each experiment.

3.3.1 Results of the p-SNOM

Figure 3.12 shows the p-SNOM results for a hybrid structure formed by one IEW and a TiO_2 slab (sample 1). In figure 3.12a we can observe the topography of the sample from a top view. According with the AFM measurements, the thickness of the fabricated sample is 83 nm and not 90 nm as it was expected. In these figures, the yellow part corresponds to the TiO_2 slab and the darker part corresponds to the glass surface without TiO_2 . The white lines show the IEW edges and the interface between the TiO_2 and the glass. Figure 3.12b and 3.12c show the optical signal detected using p-SNOM for TE and TM polarization of the incident light respectively. Figures 3.12d and 3.12e show, the FDTD numerical simulations for the propagation of the fundamental modes for respectively TE and TM polarization of the IEW at 640 nm and $t = 83$ nm, where the mode is propagating from left to right. From figure 2.8a and b, we observe that for a thickness of 83 nm, the calculated EF is EF=3.2 for TE mode and EF=5.8 for TM mode. We found from the experimental results 3.12b and c similar values of the enhancement factor (EF=3.5 and 5.5 for the TE and TM modes, respectively) and similar field distributions as in figures 3.12d and e. Figure 3.12f and g show a profile taken from center of the images 3.12b, c, d and f in order to compare the EF obtained with numerical calculations and the experimental results. The solid dark line and dashed green line represent the modeling for a TiO_2 thickness of $t=83$ nm and 90 nm, respectively. The solid blue line correspond to the experimental results (figure b and c). Here we observe that the simulations results agree very well with the experimental results and that the 7 nm error in the TiO_2 deposition affects the expected values of EF.

Figure 3.13 shows the results for the sample with TiO_2 waveguide ridges that was described in chapter 2 and the first part of this chapter (figure 3.6). We notice in figure 3.13a and 3.13b the fabrication imperfections during the TiO_2 deposition. The details in

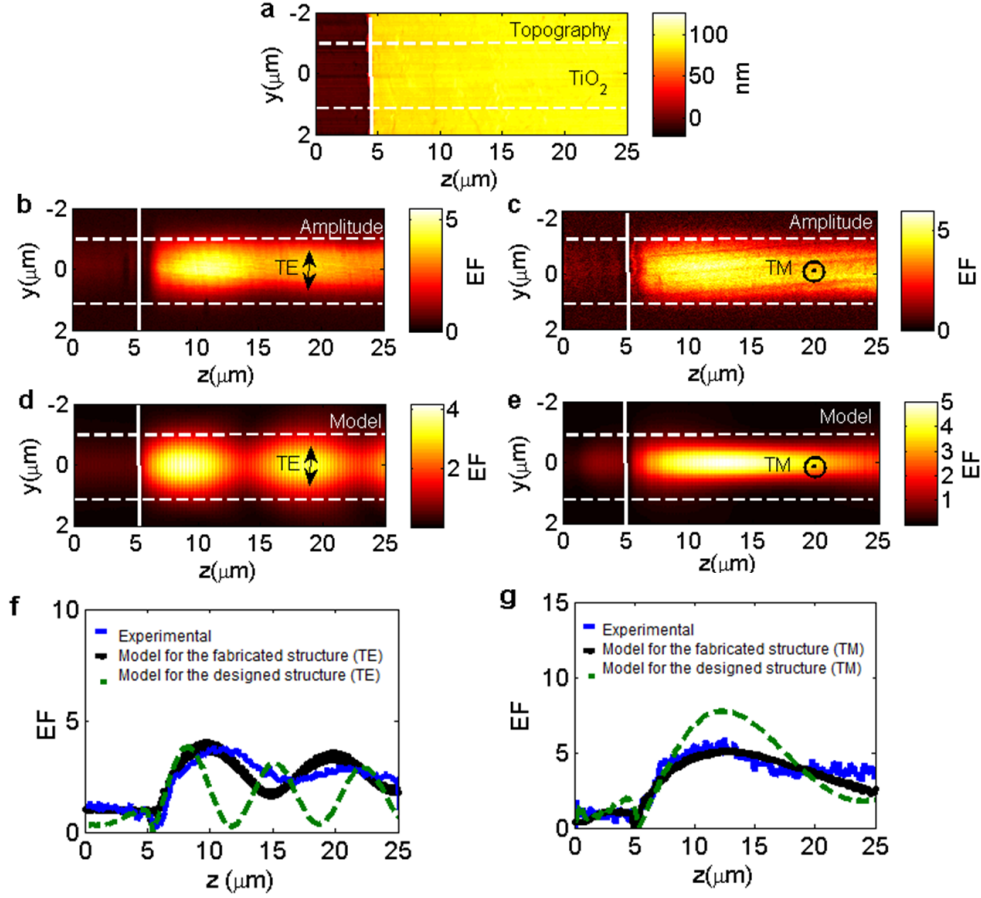


FIGURE 3.12 – p-SNOM images for the TiO_2 slab. a) Topography images from the AFM. b) and c) Experimental enhancement factor deduced from the p-SNOM optical signal (light is propagating from left to right) for TE and TM polarizations respectively. d) and e) FDTD numerical simulations of the enhancement factor for respectively TE and TM polarization. The solid white line represents the edge of the TiO_2 slab and the dashed white line represents the edge of the IEW. f) and g) Comparison of the longitudinal centered profiles taken from images b)-e) with the theoretical EF profile from the designed sample of figure 3.5.

figure 3.13a and b show the profile of the topography taken at the position of the dashed green line. Here we observe that the average thickness of the TiO_2 is 160 nm and not 120 nm as expected. Other fabrication issues can be observed with the AFM measurements. In the detail of figure 3.13b, a profile taken in the y direction (dashed green line in figure b) we find that surface defects generate height variations of more than 100 nm, at the edge of the structure.

In figure 3.13c and d, are shown the experimental enhancement factors deduced from the optical signal recorded with the p-SNOM, for an excitation from left to right with the TE and TM modes respectively. The solid white line represents the edges of the ridges and the dashed white line the edge of the IEW. For TE mode a noisy signal with low

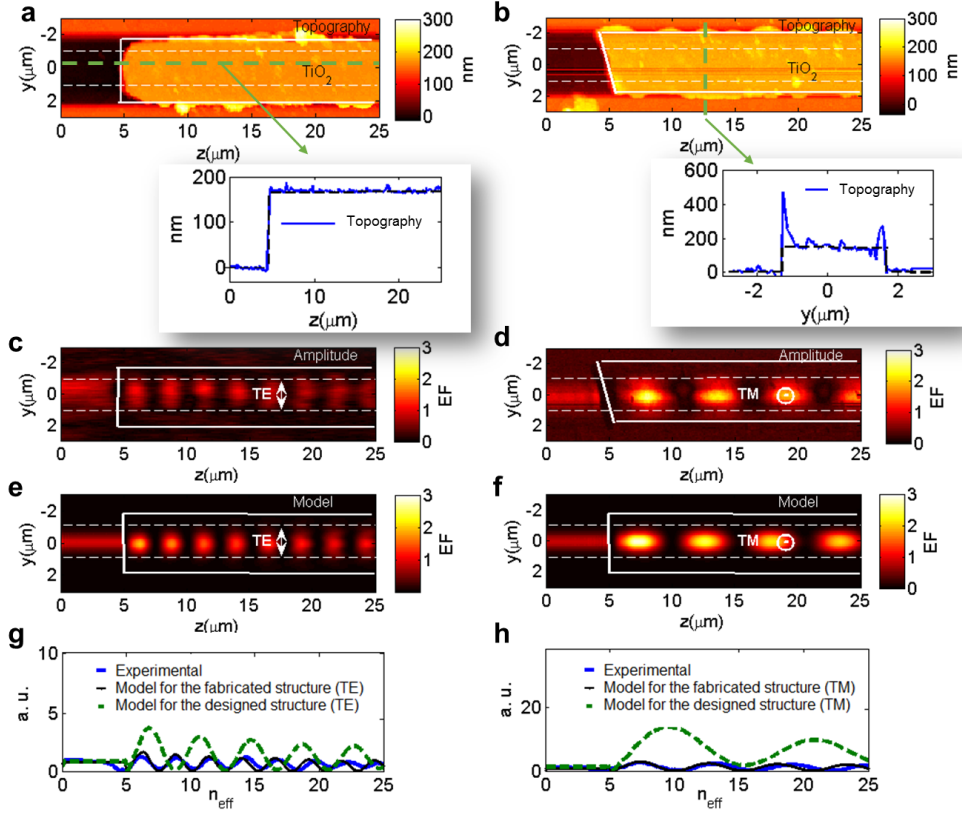


FIGURE 3.13 – p-SNOM images for the TiO_2 ridge. a) and b) AFM topography images. In the detail we observe the plot of the center profile (green line in figure a) and b)). c) and d) Experimental enhancement factor deduced from the P-SNOM optical signal for TE and TM polarization respectively . e) and f) Numerical simulations made with FDTD of the enhancement factor for respectively TE and TM modes and $t=160$ nm. The solid white line represents the edge of the TiO_2 ridge and the dashed white line represents the edge of the IEW. g) and h) Comparison of the longitudinal centered profiles taken from images b-e) with the theoretical EF profile from the designed sample of 3.7.

EF of 1.4 is obtained, while the EF for the TM mode is 2.6. These results are far from the expected theoretical predictions of $\text{EF} = 4$ for TE and $\text{EF} = 15.6$ for TM polarization (section 3.2.1). This mismatch can be linked to the fabrication imperfections during the TiO_2 deposition (3.13 a and b) This can be verified in figure 3.13e and 3.13f where we simulated the propagation of a TE and TM mode respectively for the structure designed in section 3.2.1 but with a different thickness of $t=160$ nm. For that modified height, we reproduce the pattern observed in the experimental results and we obtained an $\text{EF}=1.9$ for TE and $\text{EF}=2.8$ for the TM mode, in agreement with the experimental results. As in figure 3.6, figures 3.13g and 3.13h show the EF profile (solid blue and black lines) taken along an horizontal line in the middle of the structure. We also add the theoretical EF profile (dashed green line) of designed (see figure 3.7). From these results we can

conclude that good agreement between the experimental results (images b and c) and the numerical model (figure d and e) is obtained; validating both methods. However, these results also show that it is important to have a precise control of the process of the TiO_2 layer deposition.

The TiO_2 tapered ridges were also studied with the p-SNOM, however we found two main problems in the characterization process :

- The limited scanning area of the AFM which is close to $70 \times 70 \mu\text{m}$. This makes difficult the scan of tapers with lengths longer than $50 \mu\text{m}$.
- The damage on the sample and the broken tapers after the cleaning process described in section 3.2.2.

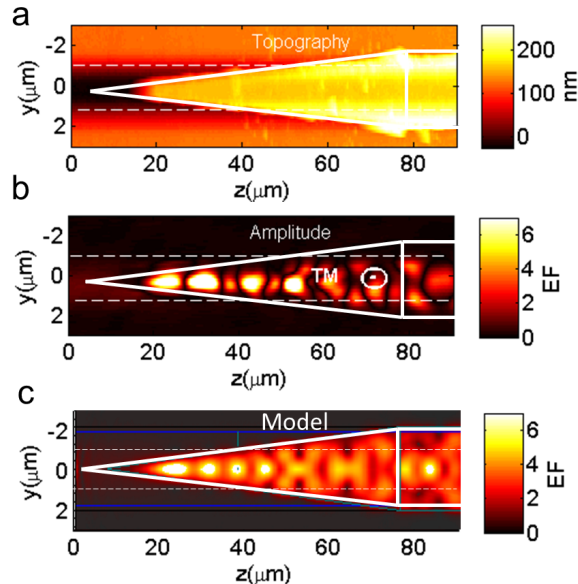


FIGURE 3.14 – p-SNOM images for a TiO_2 tapered ridge . a) Topography images from the AFM. b) Experimental enhancement factor deduced from the p-SNOM optical signal for a TM incident mode. The solid white line represents the edge of the TiO_2 taper and the dashed white line represents the edge of the IEW. c) FDTD simulations of the enhancement factor for a TiO_2 layer thickness of $t=160 \text{ nm}$.

In figure 3.14, we show the results for a taper with $50 \mu\text{m}$ length excited by a TM mode propagating from left to right. In these images the solid white line represents the designed tapered shape and the white dashed lines the IEW edges. In figure 3.14a, we observe some fabrication issues in the taper tip. Here the taper apex has a curvature radius of $1 \mu\text{m}$, it is due to the imperfections of the TiO_2 deposition. Some TiO_2 remains can be observed at the base of the taper (close to $z=60 \mu\text{m}$ in figure a). Since the tapers are part

of the structures in the sample 2, its thickness is 160 nm. The optical signal presented in figure 3.14b shows an interference pattern due to the spatial beating of several modes. We simulated the propagation of a TM mode from left to right in the designed structure in chapter 2 but with thickness $t=160$ nm. In this numerical model (figure c), we also observe an interference pattern but with some differences in the distribution. The differences are significant when the taper width increases. It is due to the extra reflections at the rough surface. Because of these important differences between the designed and the fabricated structures, we decided to consider only the characterization of the sample 1.

3.3.2 Results of s-SNOM

Figure 3.15 shows s-SNOM characterization results obtained for a bare IEW (without TiO_2 layer). The topography of the sample is depicted in figure 3.15a where the dashed white lines represents the IEW edges. Figures 3.15b and c are the s-SNOM signals for respectively TE and a TM mode excitation. Light is propagating from right to left (the propagation direction is indicated by a white arrow (\vec{k}_i)). Figures 3.15d and e are the Fourier transforms of signals 3.15 b and c multiplied by $\lambda=640$ nm in order to obtain the information of n_{eff} and the angle α (equation 3.2.13). For the TE mode in figure d, we observe a principal harmonic and its negative counterpart due to the symmetric properties of the Fourier transform. The corresponding period is found in a oblique line due to the inclination of the interference pattern of figure 3.15b (black lines). The measured refractive index is $n_{eff}=1.508$, while the angle $\alpha=25.17^\circ$. The associated error of n_{eff} is 0.02, due to the size of the images. In the case of the TM polarization, we found different periods. One of them localized in $n_{eff}=1.51$ and $\alpha=25.17^\circ$. Others periods are found for $n_{eff} < 1.5$, they correspond to radiation modes produced by scattering defects visible in the topography (white square in figure 3.15a and c). These radiation modes generate contrasted fringes more as it is shown in figure 3.15c. The comparison between the refractive index obtained with the s-SNOM and the refractive index calculated by the numerical simulations (1.51 for TE and 1.508 for TM) agreed with an error of less than 5%.

For the hybrid structure of the sample 1, we performed a s-SNOM scanning in a zone of overlap between the TiO_2 slab and the IEW. Figure 3.16a shows the topography of the sample obtained by the AFM. The solid and dashed white lines are used as in the previous

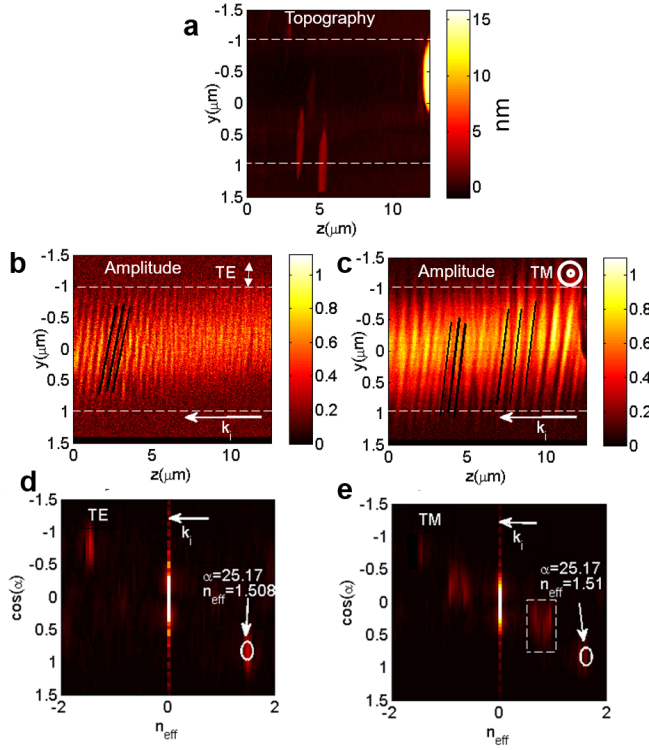


FIGURE 3.15 – S-SNOM characterization of a bare IEW. a) Topography images from the AFM. b) and c) s-SNOM optical signal for respectively TE and TM polarization. Light is traveling from right to left inside the waveguide. d and e) Fourier transform maps of images b) and d). The dashed white lines represent the IEW edges.

examples in figures 3.12 and 3.13.

Figures 3.16b and 3.16c show the results obtained with the s-SNOM when a TE mode is traveling into the waveguide respectively from left to right and from right to left. As expected, we see that the inclination of the fringes pattern is inverted when the direction of propagation \vec{k}_i is changed. The Fourier maps depicted in figure 3.16d and e are useful to identify the optical modes that are involved. In figure 3.16d, two main harmonics close to $n_{eff}=1.5$ (white circles) are visible. They correspond to the odd and even hybrid modes with respective measured effective indexes of $n_{eff,o} = 1.48$ and $n_{eff,e} = 1.56$. According to numerical simulations ,the effective indexes were expected to be $n_{eff,o} = 1.503$ and $n_{eff,e} = 1.58$. These oblique patterns that generate these harmonics are found with an angle $\alpha=29.5^\circ$.

Another group of harmonics is located close to $\alpha=0^\circ$ and corresponds to a vertical fringes patterns with larger periods. These features correspond to the excitation of leaky modes (resonance of radiation modes) with $n_{eff} < 1.5$ that are excited at the edge of

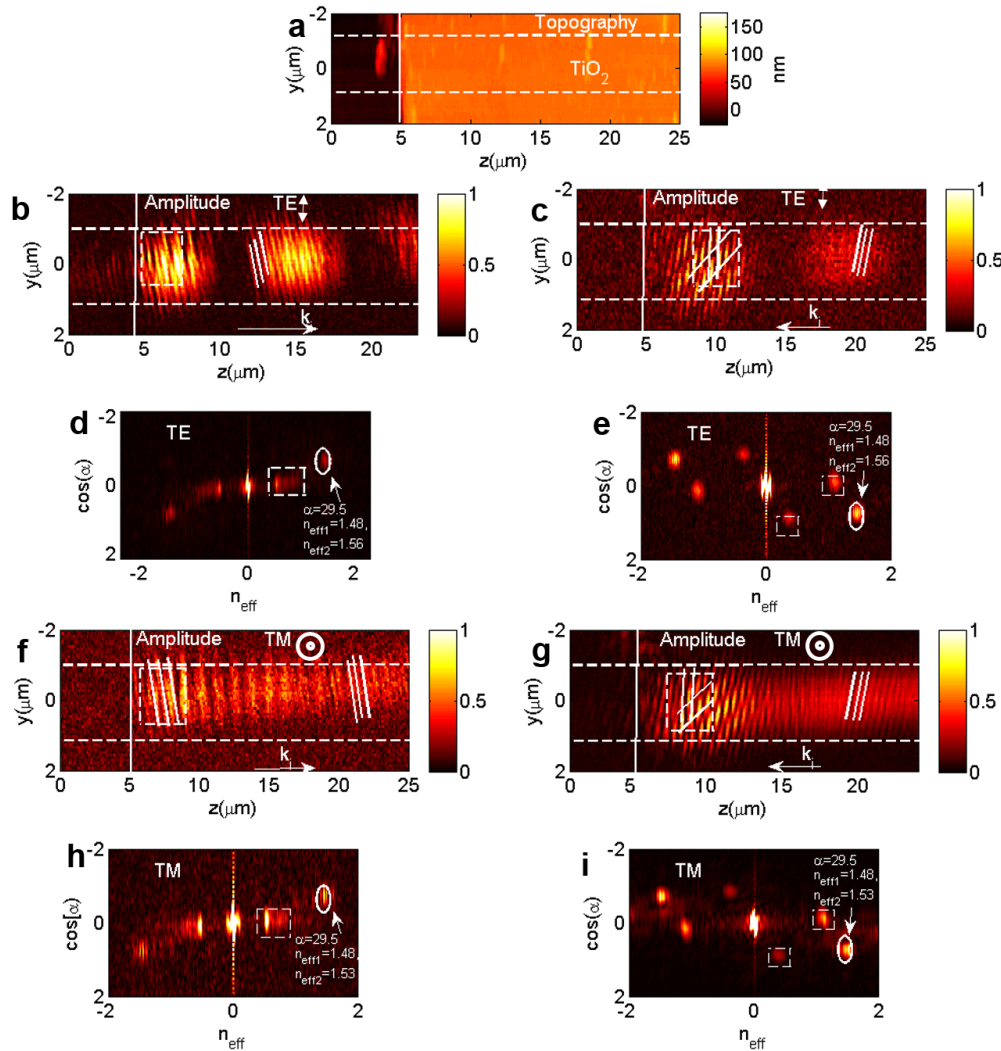


FIGURE 3.16 – S-SNOM images of the hybrid structure including the TiO_2 layer. a) AFM topography. b) and c) s-SNOM optical signal for TE polarization. Light is traveling from left to right in b) and from right to left in c). d) and e) Fourier transforms of images b) and c). f) and g) s-SNOM optical signal for TM polarization. Light is traveling from left to right in f) and from right to left in g). h) and i) Fourier transforms of images f) and g). Here solid white lines represent the edge of the TiO_2 slab and the dashed white lines represent the edge of the IEW. White oblique lines represent the interference pattern inclinations. White circles show the harmonic in the Fourier maps corresponding to the hybrid modes and white squares show localized sources of radiation modes.

the TiO_2 layer. They are visible into the optical signal image inside the white squares of figure 3.16b and c. From figure 3.16e, we observe the effective index of the hybrid modes as $n_{eff,o} = 1.48$ for the odd mode and $n_{eff,e} = 1.56$ for the even mode. The interference patterns close to the edge of the TiO_2 have two periods. The first at $\alpha=0^\circ$ correspond to the radiation modes reflected from the edge (as in figure d) and the second at $\alpha=29.5^\circ$ correspond to radiated light from the sample with the same direction of \vec{k}_d .

Figures 3.16 f and g show s-SNOM images for the propagation of a TM mode from left to right and from right to left, respectively. In these images we observe a similar behavior than figures b and c : The inclination of the lines change in relation with the direction of \vec{k}_i , the distribution of the electric field distribution changes according to propagation direction of the mode, more extra interference patterns are localized close to the edge of the TiO_2 layer, which correspond to the radiation modes excited for the reflections from the edge (white square in figure 3.16f and g). This interference effect is clearly evident for the propagation from right to left due to the fact that the edge is a obstacle for the propagation of the mode, generating scattering light which better excites the radiation modes. Figures 3.16 h and i are the Fourier transforms of figures f and g, respectively. As mentioned in the previous example for the TE polarization, the effective index in the white circle correspond to the hybrid modes with $n_{eff,o} = 1.48$ for the odd mode and $n_{eff,e} = 1.53$ for the even mode with $\alpha = 29.5^\circ$ for the figures h and i. The effective index $n_{eff} < 1.5$ correspond to radiation modes.

Compared to p-SNOM, s-SNOM allows measuring the effective index of radiation and guided modes. However, the process of acquiring s-SNOM images is more laborious than that for the p-SNOM due to the difficulties of the alignment of the system and the low signal from the scattering light produced by the tip.

3.4 SNOM in illumination mode : towards the measurement of the Local Density of Guided Modes (LDOM)

Inspired by the high performance of the s-SNOM, in this section we present a new configuration of SNOM that allows us to obtain images of the collected light from the IEW when the structure is excited by a point source placed in close proximity of the sample surface. As we presented in chapter 2, the coupling between a NS and a guided system can be represented as the interaction of a dipole oscillating close to the sample surface. When the radiated light from the dipole is coupled into the guided modes of the IEW, they are able to be detected at the end of the waveguide. Also as we mentioned in chapter 2, this collected power can be related to the LDOM of the system according to the equation (2.1.18)

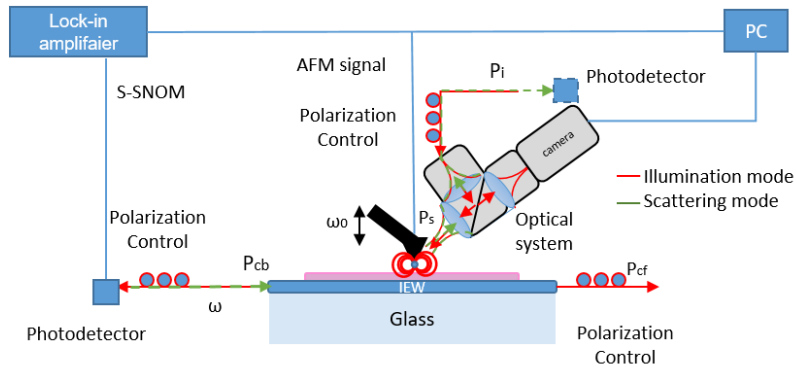


FIGURE 3.17 – Scheme of the illumination SNOM mode (red path of light) in comparison with the scattering mode (green path of the light).

In order to mimic a point source scanning the sample's surface, we used a configuration of SNOM that we call illumination mode or i-SNOM. Figure 3.17 shows the scheme of this configuration (green path), where we couple light from a PMF optical fiber connected to the optical system. One part of the light arrives to the camera and another part illuminates the apex of the AFM tip. Since the diameter of the apex is smaller than $\lambda = 640$ nm and also smaller than the illumination spot area, the apex tips acts as a punctual scatter surrounded by a electric field \vec{E} . In this situation the tip radiates light like a dipole oscillating in the same direction of the polarization of the incident light. When the tip is close to the surface, the radiated light from the tip apex excites the guided modes of the structure and these are propagated through the guided system. The power is collected by an optical fiber connected at one of the end of the IEW (as we shown in figure 3.1c). Finally the collected power is measured by a photodetector. The interesting point about this technique is that this excitation is the reciprocal case of the s-SNOM as we can observe in figure 3.17 for the red path, but we will come back to this point in the course of this section. In a first test, we use the illumination setup described in figure 3.17 and we change the polarization of the incident light that illuminates the apex of the AFM tip. For this propose, we represent the polarization direction as a variation of the angle Ω (figure 3.18a). Here, we considered that the angle α is small (figure 3.11) and the plane of the illumination is mainly placed over the xz plane. Figures 3.18b,c and d show the results of the LDOM or collected power by the optical fiber for $\Omega=0, 45$ and 90° , respectively. In these images, we observe the same interference patterns as in the s-SNOM configuration,

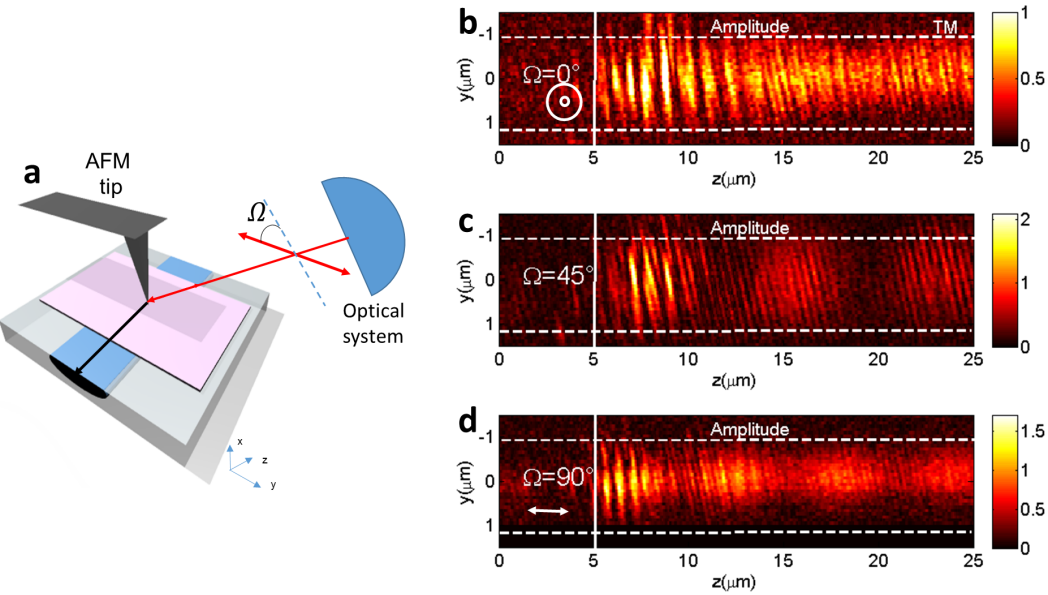


FIGURE 3.18 – Illumination mode and the angle Ω . a) Scheme of the angle Ω in comparison with the sample. I-SNOM images for b) $\Omega=0^\circ$, c) $\Omega=45^\circ$ and d) $\Omega=90^\circ$.

where we see oblique fringes and more interference patterns close to the edge of the TiO_2 layer. For $\Omega=0^\circ$ (figure b), we observe an electric field distribution similar to that obtained for the propagation of a TM mode. For $\Omega=45^\circ$ and 90° , we observe a change in the spatial distributions but the field distribution corresponding to the TE polarization is not well reproduced. To solve this problem, the dipole has to oscillate along the y direction.

For this reason, we decided to rotate the sample relatively to the optical system, as it is shown in figure 3.19.

Figures 3.19a and b show schematically the optical paths involved in the two reciprocal SNOM setups, i.e. i-SNOM and s-SNOM respectively. For scattering mode, light from the optical system is propagating in the \vec{r}_0 direction until the apex tip. Then, the radiated light from the apex tip is coupled into the guided modes and the signal detected with a k vector \vec{k}_d in the \vec{k}_i direction until the left end of the IEW. As the scattering mode, the signal at the end of the IEW can be written as :

$$A e^{-i \vec{k}_i \cdot \vec{r}_0} e^{i \vec{k}_d \cdot \vec{r}_d}. \quad (3.4.14)$$

On the other hand, the scattered light from the tip is propagating in the direction of \vec{k}_s and it arrives to the scatter. The light from the scatter can be also propagated in the

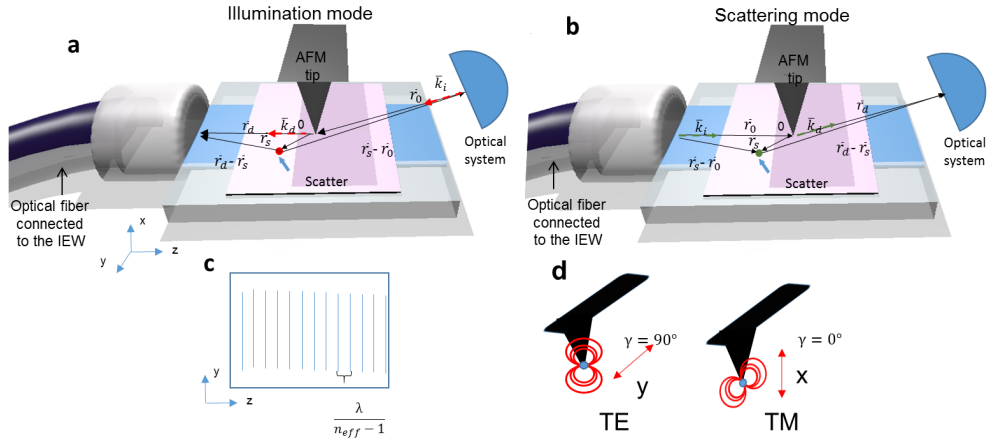


FIGURE 3.19 – The spacial distribution of vectors involved in the scattering light detection for the a) i-SNOM configuration and b) s-SNOM configuration. Where an optical fiber was connected at the left end of the IEW. c) interference pattern expected in the detected signal measured by the photodetector. b) The TE and TM dipoles reproduced by incident light with polarization at $\Omega = 90^\circ$ and $\Omega = 0^\circ$, respectively.

direction of $\vec{r}_d - \vec{r}_s$ and finally it arrives at the left end of the IEW. This last signal can be written as :

$$Be^{i\vec{k}_i \cdot (\vec{r}_s - \vec{r}_0)} e^{i\vec{k}_d \cdot (\vec{r}_d - \vec{r}_s)}. \quad (3.4.15)$$

As the scattering mode, the total signal collected by the PMF optical fiber is a superposition of both signals :

$$| Ae^{-i\vec{k}_i \cdot \vec{r}_0} e^{i\vec{k}_d \cdot \vec{r}_d} + Be^{i\vec{k}_i \cdot (\vec{r}_s - \vec{r}_0)} e^{i\vec{k}_d \cdot (\vec{r}_d - \vec{r}_s)} |^2. \quad (3.4.16)$$

Following the same process than section 3.3.2, we obtain

$$A^2 + B^2 + 2AB\cos(\Delta\phi), \quad (3.4.17)$$

where $\Delta\phi = (\vec{k}_i - \vec{k}_d) \cdot \vec{r}_s$. From equation 3.4.17, we observe that the signal collected for the optical fiber has also a periodic distribution.

According with the vectors shown in figure 3.19a :

$$\vec{k}_i = (k_0 n_{eff} \sin \alpha, 0, k_0 n_{eff} \cos \alpha) \quad (3.4.18a)$$

$$\vec{k}_d = (0, 0, k_0) \quad (3.4.18b)$$

$$\vec{r}_s = (0, y, z) \quad (3.4.18c)$$

From these vectors we can obtain the period of the interference pattern as

$$\Delta\phi = k_0(n_{eff} - \cos\alpha)z \quad (3.4.19)$$

Using $k_0 = 2\pi/\lambda$, we obtain a period of $\lambda/(n_{eff} - \cos\alpha)$ for the interference pattern in the z direction. For the scattering mode, we follow the same process and we obtained that

$$\vec{k}_i = (0, 0, k_0 n_{eff}) \quad (3.4.20a)$$

$$\vec{k}_d = (k_0 n_{eff} \sin\alpha, 0, k_0 \cos\alpha) \quad (3.4.20b)$$

$$\vec{r}_s = (0, y, z) \quad (3.4.20c)$$

Therefore

$$\Delta\phi = k_0(n_{eff} - \cos\alpha)z. \quad (3.4.21)$$

This result show that for this configuration we expect an interference pattern along on z axis with period equal to $k_0(n_{eff} - \cos\alpha)z$. These results show than the scattering mode and the illumination mode are reciprocal due to the reciprocity of the system, as the example in chapter 2 about the reciprocity theorem of electromagnetism.

3.4.1 Results of i-SNOM

From the results in figure 3.16 we will make the approximation that $\cos\alpha z$ is close to 1 (with α small). Then the interference pattern will have a period of $k_0(n_{eff} - 1)z$ (figure 3.19c). In this system, the TE polarization can be reproduced when we rotate the polarization to $\Omega=90^\circ$ and TM with $\Omega=0^\circ$ (figure d).

Figure 3.20 shows a comparison between the results obtained by i-SNOM and s-SNOM at the interface between the TiO₂ and the IEW. These images were obtained using the setup shown in figure 3.17 and the detector position as it is shown in figure 3.19b. As in the previous examples white solid lines represent the interface between the TiO₂ slab and the IEW without TiO₂ while the dashed lines show the edges of the IEW. In figure 3.20a, we observe the topography of the sample obtained from the AFM signal. Figures

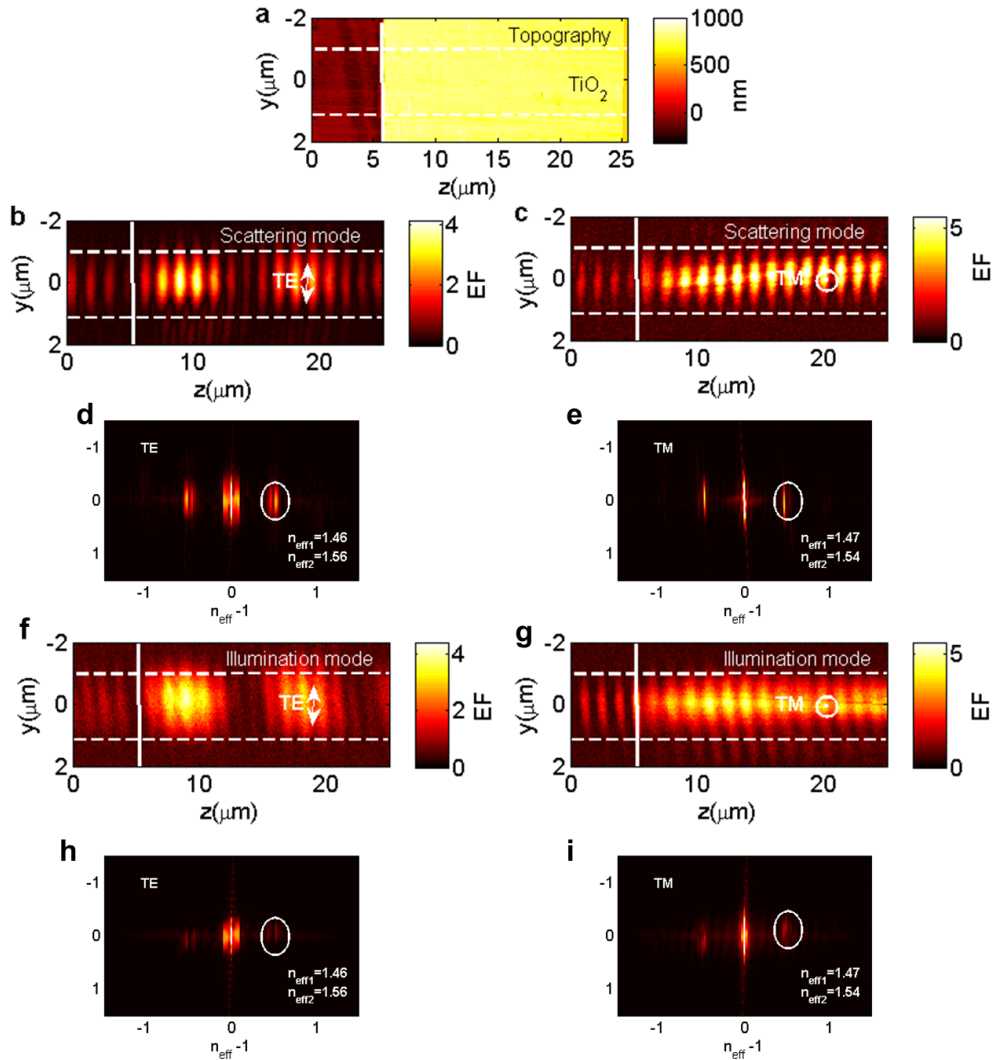


FIGURE 3.20 – Comparison between S-SNOM and i-SNOM results. a) AFM topography images. b) and c) Enhancement factor deduced from the optical signal in s-SNOM configuration TE and TM excitation respectively. Light is traveling from left to right. d) and e) Fourier transforms of b) and c) respectively. f) and g) Enhancement factor deduced from the optical signal in i-SNOM configuration for TE and TM polarization respectively. h) and i) Fourier transforms of f) and g). Here solid white lines represent the edge of the TiO_2 slab and the dashed white lines represent the edge of the IEW. White circles show the effective index corresponding to the effective index of the hybrid modes.

3.20b and c are the s-SNOM optical signal for respectively TE and TM modes excitation (light traveling from left to right). Here we observe a vertical fringes pattern generated by the interference between the scattered light from the scatters and guided modes of the IEW. It is worth to notice that the pattern is no more oblique since we rotate the sample. In these images, we also observe the characteristic spatial beating period corresponding to the TE and TM hybrid modes, as we have observed in the last sections. Figures 3.20d and e are the Fourier transform maps of images 3.20b and c. Here we observe that in

contrast with figure 3.16d, e, d and i, the main period is found in the horizontal axis. For TE polarization, we obtain $n_{eff,o}=1.48$ and $n_{eff,e}=1.56$ corresponding to the odd and even hybrid mode, respectively. While for the TM polarization these indexes are $n_{eff,o}=1.48$ and $n_{eff,e}=1.53$.

In the case of the i-SNOM, figures 3.20f and g show the results for the collected light for the optical fiber at the left end of the IEW. As it was mentioned in chapter 2, the maps shown in figure 3.20f and g represent the measure of LDOM excited by the AFM tip for each tip position over the sample. The optical signal distribution in s-SNOM (figures 3.20b and f), and in i-SNOM (3.20c and e) look very similar due to the reciprocity of the system that was also explained in chapter 2. From the Fourier transform maps of images 3.20f and g (figure 3.20 h and i, respectively), we obtain that for TE polarization $n_{eff,o}=1.46$ and $n_{eff,e}=1.56$ while for the TM polarization $n_{eff,o} = 1.47$ and $n_{eff,e}=1.54$.

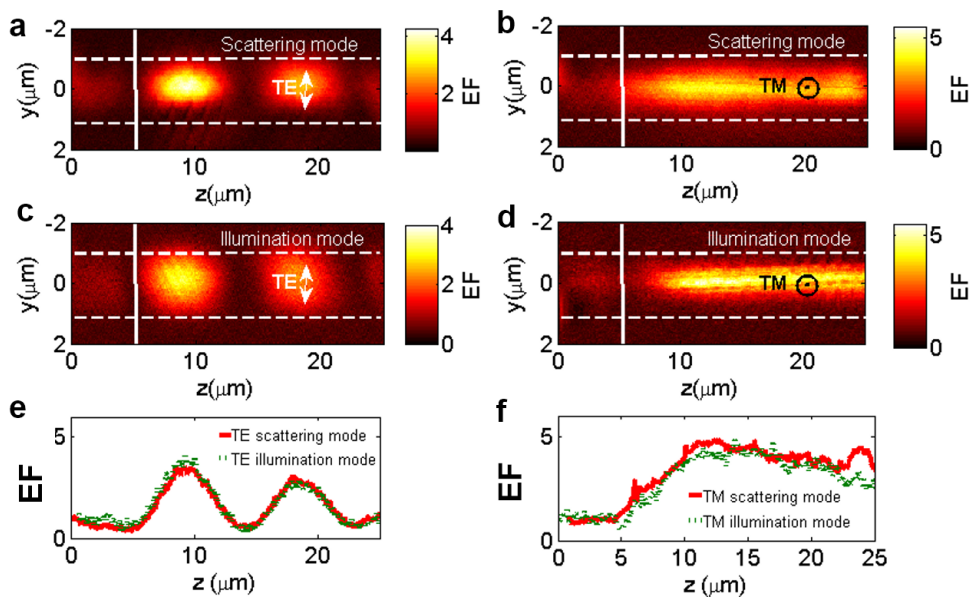


FIGURE 3.21 – I-SNOM results after using a spatial filter to remove the interference pattern shown in figure 3.26 for a) s-SNOM images in TE polarization and b) TM polarization. c) and d) I-SNOM images TE and TM polarization respectively. e) longitudinal profiles taken in the middle of images a) and c) . f) longitudinal profiles taken in the middle of images b) and d).

We use a mathematical process in Matlab over the figures 3.20 b, c, f and g, in order to filter out the high frequencies corresponding to the interference pattern between the background light scattered by surface defects and the light scattered by the SNOM tip. We obtain images 3.21 a, b, c and d, respectively. It is clear that with the s-SNOM and

i-SNOM configurations we can reconstruct the images obtained by the p-SNOM configuration. Figures 3.21e and f show the plot of longitudinal profiles taken at the middle of the images a, c and b, d, in order to emphasize this result.

This study confirms experimentally the reciprocity theorem of the electromagnetism.

Due to the agreement between the experimental and the theoretical results presented in these sections, we conclude that the characterization of the sample is complete in terms of enhancement of electric field on the surface of the TiO₂ layer and also in terms of the prediction of effective index.

In order to explore the potential use of this sample for the excitation of nanoemitters, we carry out some experiments with semiconductor quantum dots as nanoemitters, which we describe in the next section.

3.5 Enhancement of the photoluminescence of CdSe/CdS nanocrystals with the integrated photonic structure on IEW

In this experiment, we placed on the surface of the sample 1 a solution of Cadmium Selenide/Cadmium Sulfide (CdSe/CdS) nanocrystals and we measured the intensity of time-resolved photoluminescence (PL). The nanocrystals consist of a CdSe spherical core of 2.7 nm in diameter, surrounded by an elongated shell of CdS to form a rod shape with dimensions of 50 nm in length and 7 nm in diameter. A high concentration of NCs (10^{-6} mol/L) was mixed in a Poly(methyl methacrylate) (PMMA) solution and randomly distributed on top of the hybrid structure by spin coating process (figure 3.22a). In figure 3.22b we observe the images of these crystals over the surface of the sample from a top view taken with a CCD camera.

The nanocrystals placed on top of the integrated photonic structure were excited with a laser at a wavelength of 532 nm at the input of the IEW. We used a home-made confocal system with a 80X microscope objective coupled to a 25 cm focal length spectrometer (Princeton Instruments), attached itself to a CDD camera cooled at -75°C . The CCD camera allowed us to image the surface and to measure the PL intensity spectrum of

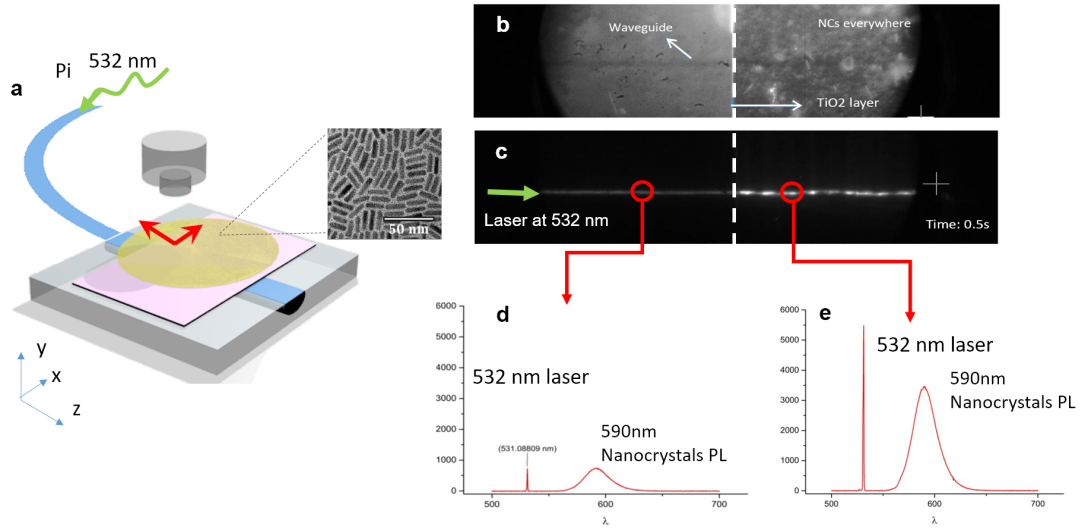


FIGURE 3.22 – a) Simplified scheme of the setup used for the photoluminescence measurements as a representation of the hybrid structure consisting of a TiO₂ layer placed on top of an IEW, and nanocrystals solution on its surface. The inset is a schematic representation of the CdSe/CdS nanocrystals. b) Image from a CCD camera of the sample after the nanocrystals deposition. c) Far-field observation of light emission from CdSe/CdS nanocrystals placed on top of the HS for TE and TM polarizations when exciting the structure from the left end of the IEW. Emission spectrum of the nanocrystals placed on the position marked by the red circles on d) the top of the IEW and e) on top of the TiO₂ layer on the IEW.

the nanocrystals from a single spot of the image. This standard microphotoluminescence system is sensitive enough to carry on time-resolved PL measurements. This experiment was performed in collaboration with the Dr. Wei Geng. More details about this technique can be found in his PhD thesis [92].

Figure 3.22c shows the PL image of the nanocrystals. Here we observe that nanocrystals on top of the IEW have a lower PL intensity than that of the nanocrystals on top of the TiO₂ layer. We also see an intensity pattern that corresponds to the beating interference pattern between the two even and odd hybrid modes. In figures 3.22d and 3.22e, we show the emission spectrum of crystals placed in the red circles of figure c. In this spectrum we observe a thin peak at 342 nm, which corresponds to the laser source (close to 700 counts was obtained). A second peak with larger width can be found close to 590 nm (about 750 counts), this is the PL spectrum emission of the nanocrystals. For the spectrum measured on top of the TiO₂ layer (figure 3.22e), we observe a PL intensity enhancement with 5500 counts for the peak corresponding to the laser source and 3600 for nanocrystals emission at 590 nm.

We define the enhancement factor of the PL of the nanocrystals (EF_{PL}) as the ratio

between the PL of the nanocrystals placed on top of the TiO_2 layer and the PL of the NCs directly placed on top of the IEW. From the results in figure 3.22d and e, we obtain a PL intensity enhancement of 5.1 for the laser source and 4.8 for the nanocrystal emission at 590 nm. It should be mentioned that these results were taken without any control of the polarization state of the incident light. In next section, we will show the relation between EF_{PL} and the EF.

3.5.1 Photoluminescence intensity measurements

After adding a polarization control at the left end of the IEW. We reproduce the measurements shown in figure 3.22 for TE and TM polarizations.

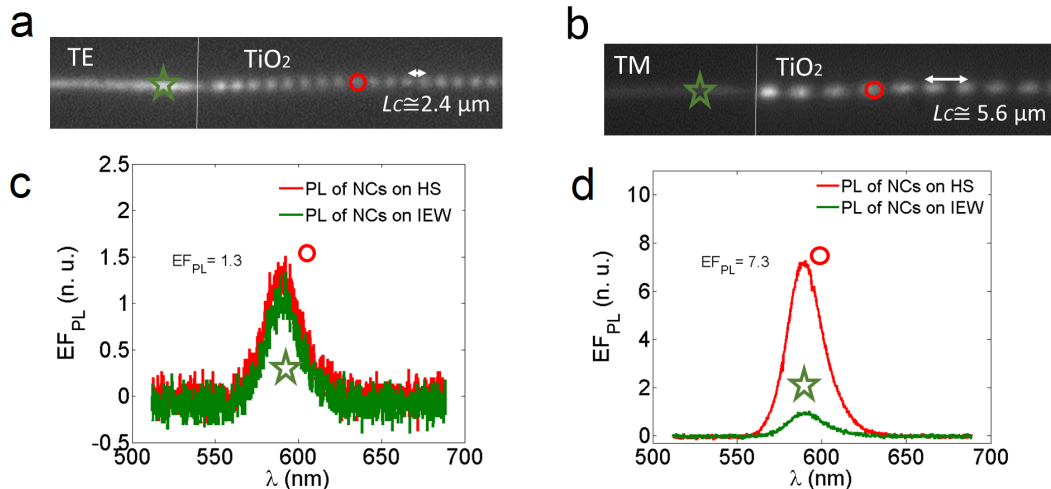


FIGURE 3.23 – Far-field observation of light emission from CdSe/CdS nanocrystals placed on top of the HS for a) TE and b) TM polarizations when exciting the structure from the inlet of the IEW. The PL spectra were extracted from the image at the surface of the IEW (star point) and at the surface of the hybrid section of the structure (circle point) for c) the TE-polarized mode and d) the TM-polarized mode. A PL enhancement factor of 1.3 times is obtained for TE polarization and 7.3 times for TM polarization at the wavelength of maximum emission of the nanocrystals (i.e. at 590 nm).

The results are presented in figure 3.23a and b, corresponding to an excitation with TE and TM modes, respectively, from the input of the IEW at a wavelength $\lambda = 532$ nm. In these images the excitation pump was spectrally filtered-out, such that the CCD images only provide information of the PL of the NCs. No blinking effects were observed due to the high concentration of the NCs. Figures b and c show the spectrum emission of nanocrystals placed on top of the IEW (green star) and for nanocrystals on top of the TiO_2

layer (red circle, HS=hybrid structure formed by the interaction with the TiO_2 layer and the IEW) for TE and TM polarization, respectively. This enhancement in the PL (EF_{PL}) is 1.3 times for the TE mode, and 7.3 times for the TM mode. Over the TiO_2 layer, we measured a coupling length of $L_c \simeq 2.4 \mu\text{m}$ for the TE mode and $L_c \simeq 5.6 \mu\text{m}$ for TM.

According to the FDTD simulations, the EF due to the propagation of TE and TM modes for a TiO_2 layer with 83 nm of thickness at wavelength of 532 nm corresponds to $\text{EF}=3.3$ for TE and $\text{EF}=10.8$ for TM with a coupling length $L_C=3.9 \mu\text{m}$ and $L_C=12.7 \mu\text{m}$, respectively (figure 3.24a and b). On the other hand, the FDTD simulations for this thickness at $\lambda=590 \text{ nm}$ (figure 3.24 c and d for TE and TM polarization, respectively) show an $\text{EF}=3.8$ and $L_C=6.4 \mu\text{m}$ for TE polarization and $\text{EF}=4.8$ with $L_C=19.5 \mu\text{m}$ for TM polarization. However, these results do not correspond to the distributions found in figure 3.23.

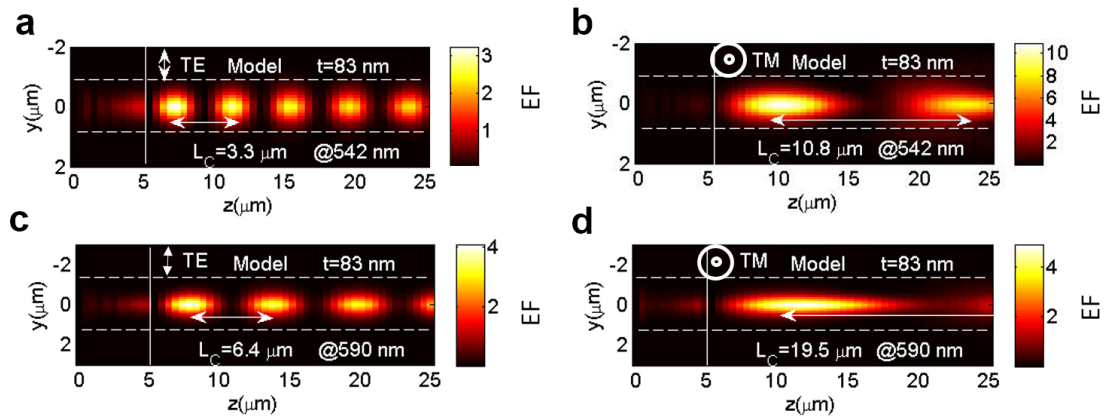


FIGURE 3.24 – Numerical FDTD simulation for the propagation of bounded modes through the hybrid structure with TiO_2 thickness of $t=83 \text{ nm}$ at 542 nm for a) TE and b) TM polarization with $L_C=3.3 \mu\text{m}$ and $L_C=10.8 \mu\text{m}$, respectively. And the propagation of bounded modes for $t=83 \text{ nm}$ at 590 nm for c) TE and d) TM polarization with $L_C=6.4 \mu\text{m}$ and $L_C=19.5 \mu\text{m}$, respectively. Here solid white lines represent the edge of the TiO_2 slab and the dashed white lines represent the edge of the IEW.

In order to understand this disagreement, we realized p-SNOM measurements in the sample 1 after the NCs deposition. Figure 3.25a is the topography image of the sample. A rough surface due to the NCs accumulations (white circles) is observed. Plotting the center profile of image 3.25a (figure 3.25b, blue line) in comparison with a profile obtained from the topography of the sample without NCs, we observe an averaged height difference of almost 40 nm. For the amplitude images of the p-SNOM, we used the same laser at $\lambda=640 \text{ nm}$ as the previous cases. This is because the photodetector is not adapted to low powers of

the green sources available in the laboratory. Figures c and d show a beating distributions that differs from the images observed in figure (3.12) for the sample without NCs. Here the EF=5.7 for the TE polarization and 9.2 for TM with $L_C=3.4\mu m$ and $L_C=11.2\mu m$, respectively.

Assuming that the solution of nanocrystals and PMMA has an average refractive index ($n_{PMMA} = 1.5$ and $n_{NC} = 2.5$) similar to the refractive index of the TiO₂ at 532 nm ($n_{TiO_2}=1.99$), we performed numerical simulations for a 120-nm-thick TiO₂ (figure 3.25 e and f). The numerical simulation has similar distribution than that of the experimental result obtained by the PL setup and the p-SNOM configuration. From the numerical simulation we obtain an EF= 5.5 for the TE polarization and 11.4 for TM with $L_C=3.4\mu m$ and $L_C=10.3\mu m$, respectively. Figures g and h show the comparison of the distribution of a central profile taken from figures c and e for TE and figures d and f for TM polarization. An agreement is obtained between the distribution patterns in term of the L_c and EF.

With this background in mind, we made the simulations for a TiO₂ layer with thickness t=120 nm for the propagation of TE and TM at $\lambda=342$ nm and $\lambda=590$ nm. The results shown in figure 3.26 a and b correspond to $\lambda=542$ nm. We measure a coupling length $L_C=2.5\mu m$ and an enhancement factor EF=3.7 for TE polarization, while for TM polarization $L_C=5.4\mu m$ and EF=8.5. From the simulations at $\lambda=590$ nm (figure 3.26 c and d), we obtain EF=1.2 with $L_C=3\mu m$ for the TE polarization and EF=4.2 with $L_C=7.3\mu m$ for TM polarization.

The beating distributions at $\lambda=542$ nm agree with those obtained in the PL measurements (figure 3.23), proving that the field distribution in figure 3.23 corresponds to the hybrid mode interference at this wavelength and not at 590 nm. However, the absolute values of the enhancement factors predicted by the simulation do not correspond to the measurements in figures 3.23 c and d. This may be because all the light emitted by the nanocrystals was not collected in the PL measurements. It is possible that some part of the emitted photons are absorbed by the sample or are emitted in other directions.

In the next experiment, the nanocrystals are excited through a microscope objective in order to observe the collection efficiency of the photo-luminescence into the waveguide.

Figure 3.27 shows the excitation positions over the surface of sample 1 (image taken from the PhD thesis of Wei Geng). We selected two excitation points over the IEW, two

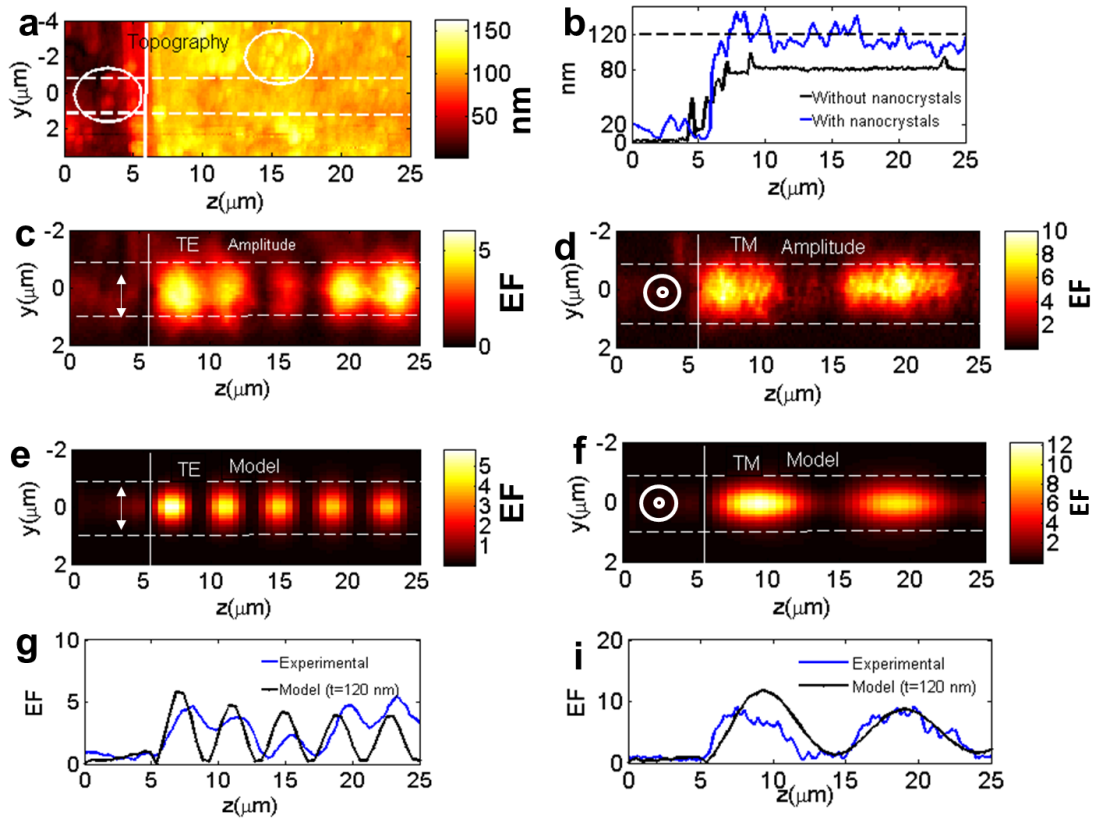


FIGURE 3.25 – a) Topography images of the sample after the nanocrystal deposition with nanocrystal accumulations are indicated by white circles. b) Center profile from figure a (blue line) in comparison with the profile of the topography images without crystals. Amplitude images for p-SNOM configuration for the propagation of light from left to right with c) TE and d) TM polarization in the region shown in figure a. Numerical simulation for a TiO_2 thickness of $t=120 \text{ nm}$. g) Plot of longitudinal profiles taken in the middle of images c) and e). i) Plot of longitudinal profiles taken in the middle of images d),f). Solid white lines represent the edge of the TiO_2 slab and the dashed white lines represent the edge of the IEW.

excitation points over the IEW with TiO_2 and one excitation point outside the IEW. The photo-luminescence is then measured at the waveguide output with an optical fiber.

The photo-luminescence spectra of the collected light for excitation positions 1 and 2 present a peak of about 170 counts (spectra 1 and 2). At excitation positions 3 and 4, we observe a collected light enhancement of 2 times in the number of counts (300 counts) in comparison with points 1 and 2. At position 5 out of the IEW, no signal can be detected into the waveguide. It is obvious since no guided modes can be excited from this location.

This enhancement of collected light $\text{EF}_c \approx 2$ can be explained according to the reciprocity theorem of electromagnetism treated in section 2.2.2. As we explained in that section, the collection efficiency depends both on the emission wavelength and on the orientation of the dipolar momentum. In the experiment done in figure 3.27 the collection efficiency is

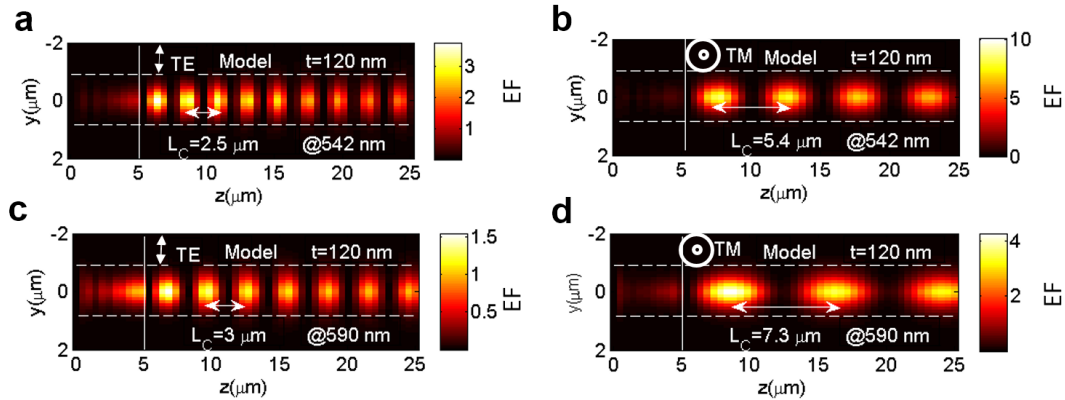


FIGURE 3.26 – a) and b) Numerical simulation of light propagation into the hybrid structure for a TiO_2 thickness of $t=120 \text{ nm}$ at wavelength 542 nm for TE and TM polarization respectively. We measure $L_C=2.5 \mu\text{m}$ and $L_C=5.4 \mu\text{m}$, respectively for TE and TM. c) and d) same as a)and b) for $t=120 \text{ nm}$ at 590 nm . We measure $L_C=3 \mu\text{m}$ and $L_C=7.3 \mu\text{m}$, respectively for TE and TM. Here solid white lines represent the edge of the TiO_2 slab and the dashed withe lines represent the edge of the IEW.

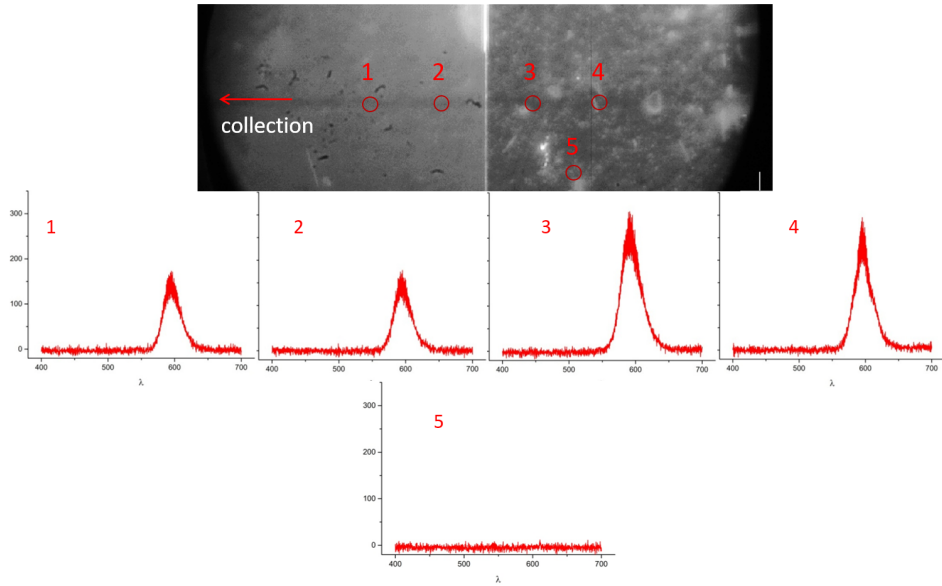


FIGURE 3.27 – Emission of nanocrystals coupled in to the hybrid system : a) Positions of the direct excitation spot on the sample. b) Photo-luminescence Spectra detected at IEW output corresponding to each position of excitation. (Image taken from [92])

thus expected to be an average between TE-mode and TM-mode excitations. From simulations 3.26 c and d we obtain a mean enhancement factor of $\langle EF \rangle = 0.5(1.2+4.2)=2.7$, between the two polarization states. Thus, by reciprocity we expect $EF_c = 2.7$ for the photo-luminescence collection efficiency into the waveguide. This value is closed to the experimental value of $EF_c \approx 2$.

3.5.2 Time-resolved photoluminescence and Purcell factor measurements

In this section we present measurements of the lifetime and the Purcell factor. This study has been done in collaboration with Dr. Nancy Rahbany and the professor Christophe Couteau. For the measurements, we used the setup shown in figure 3.28a (the complete description of the setup can be found in reference [98]). We illuminated the sample through a confocal system with 50X magnification and numerical aperture of 0.95. This excitation was done with a pulsed laser centered at $\lambda=405$ nm with a pulse width of FWHM=55 ps, a repetition rate of 8 MHz and average power of 40 μ W. The nanocrystals photo-luminescence collected by the same confocal system is sent to a spectrometer where the wavelength of 590 nm is selected (according to the spectra emission shown in figures 3.22, 3.23 and 3.27). The time decay distribution is built making use of a time-correlated single photon counting (TCSPC).

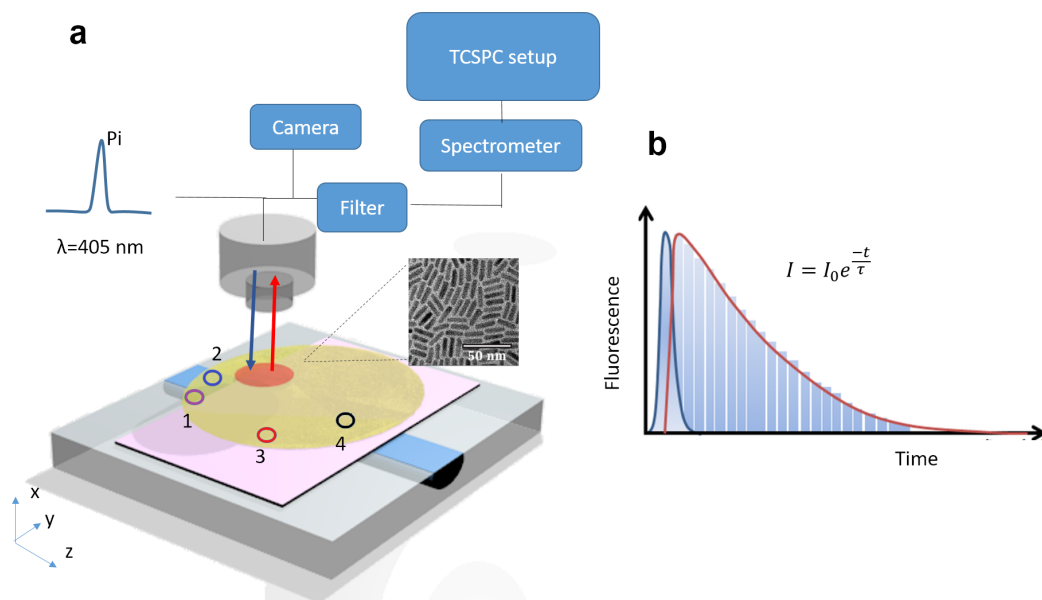


FIGURE 3.28 – a) Scheme of the setup for the lifetime measurements of NCs deposited on the hybrid photonic structure. The excitation and detection of the photo-luminescence were done with a confocal microscope. b) A schematic histogram of the lifetime measurement obtained with the TCSPC setup.

The TCSPC detection system is based on the excitation of a single photon source using a pulsed source. The system detect the arrival time of photons relative to the pulsed excitation to built a histogram of the photons collected in a time resolution of 264 ps

(figure 3.28b [99]).

The distribution of the histogram built by the TCSPC takes the form of an exponential decaying profile in the time. This distribution corresponds to the expected behavior of the fluorescence decay of photons discussed in chapter 1. This decay is described as $I = I_0 e^{(-t/\tau)}$ with I the number of measured counts, I_0 the counts at time equal zero and τ the lifetime of the nanocrystals.

We measured the fluorescence signal of the CdSe/CdSe nanocrystals placed in four specific locations over the sample (figure 3.28a) :

- Point 1 : over the glass (purple circle).
- Point 2 : over the IEW (blue circle).
- Point 3 : over the TiO_2 layer on glass (red circle).
- Point 4 : over the TiO_2 layer on the IEW (black circle).

Figure 3.29a shows the fluorescence lifetime at the emission wavelength for the four points previously defined. In the plot, the lines colour corresponds to the color of the circles in figure 3.28a.

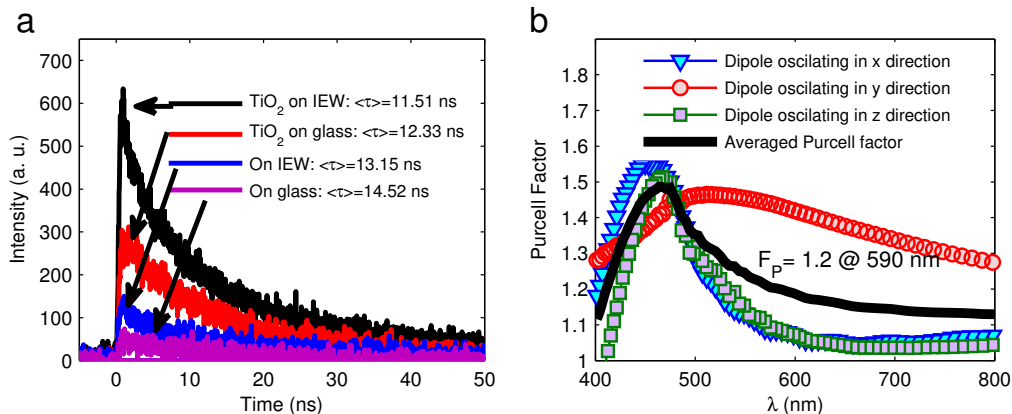


FIGURE 3.29 – Lifetime measurements at an emission wavelength $\lambda=590$ nm, of CdSe/CdS nanocrystals on glass, on WG in glass, on TiO_2 on glass and on HS. The NCs were excited at $\lambda=405$ nm. b) Purcell factor obtained with the FDTD method for dipoles oriented along the three orientations of the coordinates axes (blue, red and green) and averaged Purcell factor (black).

The line-shape of the decay time was approximated to an exponential decay function $I = I_0 e^{(-t/\tau)}$, where τ is the NCs lifetime [100, 101]. According to the analysis showed in chapter 1, the Purcell factor (F_p) is defined in terms of the lifetime and the local density of states (LDOS) seen by the nanocrystals as $F_p = \tau_0/\tau = \rho/\rho_0$ (equation 1.1.52), where

τ is the modified lifetime for the sample and τ_0 is the lifetime for the NCs on top of the glass substrate. For nanocrystals placed on top of the TiO₂ layer on the IEW, we measured a Purcell factor $F_p = 1.3$.

We performed numerical simulations of the expected Purcell factor. For that, we model a nanocrystal as a dipolar source placed at 20 nm above the surface of the structure (half of the average thickness of the nanocrystals layer). The Purcell factor was obtained by measuring the light radiated by the dipole oscillating in the three coordinates axes, to determine the LDOS.

In figure 3.29b are plotted the numerical estimations of the Purcell factor as a function of the wavelength for the 3 principal orientations of the dipole momentum. Blue triangles represent the x direction, red circles for the y direction, green squares for the z direction and black line for an average among x, y and z. Due to the random distribution of the nanocrystals, the experimental Purcell factor of $F_P = 1.3$ has to be compared with the averaged theoretical Purcell factor calculated at 590 nm, which is equal to 1.2. We conclude that numerical and experimental results agree well. However, this value might be increased by changing the orientation of the nanocrystals, a challenging situation requiring further engineering. In addition, according to the simulations, higher Purcell factors might be found using nanoemitters with an emission wavelength at 460 nm.

The results presented in this section inspired the publication of an article in Applied Optics journal [102].

3.6 Conclusion

In this chapter we presented an experimental study of the hybrid photonic structure designed previously in chapter 2. The experimental measurements have been systematically compared to theoretical simulations. The characterization technique, based on the SNOM configurations, seems to be a useful tool for the measurement of waveguides. Particularly, the i-SNOM configuration allowed us to make a study of the interaction between an idealized single nano-source and photonic waveguides. The reciprocal behavior between i-SNOM and s-SNOM configurations opens a new route for the characterization of integrated photonic circuits.

We measured the enhancement of the confined light on the surface due to the TiO₂ layer placed on top of the IEW in comparison with the confined light on top of the IEW. For modes at 640 nm, we measured EF=3.5 and 5.5 for the TE and TM polarization, respectively. They have a good agreement with the EF calculated with numerical simulations (EF=3.2 and EF=5.8).

In addition, we presented a preliminary study concerning the coupling between our waveguiding platform and real CdSe/CdS nanocrystals. We found out a collection efficiency of two times greater by using the TiO₂ layer instead of using a bare ions exchange waveguide. This enhancement should be improved up to 10 by controlling precisely the orientation of the dipolar momentum of the emitter. We also found that the fluorescence of the nanocrystals can be generated for guided modes propagating through the hybrid structure. We found a fluorescence enhancement for nanocrystals on top of the TiO₂ layer instead IEW. The enhancement are the EF=1.3 for a TE mode and 8.5 for a TM mode.

In the next chapter we will investigate the design of hybrid photonic/plasmonic component able to be integrated on top of our hybrid ions exchanged platform. This new structure will increase the overall collection efficiency of the photo-luminescence into the ions exchange waveguide.

Chapter 4

Integration of an adiabatic photonic-plasmonic mode coupler

In this chapter we present the design and the fabrication of the plasmonic component that is promised to be integrated into the hybrid ions exchange platform. The final goal is to proposed the design of the plasmonic/photonic mode coupler discussed in the last section of chapter 1. The integrated structure will consist in a field concentrator able to focus the light in an effective volume of few nm cubes and thus, efficiently excite a nanosource placed close to this point. The plasmonic mode confinement will increase both the Purcell factors and the collection efficiency compared to that obtained previously with a full dielectric hybrid waveguide.

These structures were fabricated during the last months of my thesis and therefore, the characterization process of the structure was not yet completely done.

4.1 Prismatic gold nanotaper as a enhancer of LDOS

As we mentioned in chapter 1, surface plasmon modes are strongly confined to the interface between a metal and a dielectric. For structures smaller than the wavelength of excitation, the concentration of the electromagnetic fields take place in volumes of few nanometers cubes. It easy to observe from equation 1.1.7 that the DOS of the system is linked to the volume of the interaction of the NS. Therefore the enhancement of the LDOS can be achieved with strongly confined optical modes as SPP modes. In order to observe

the enhancement of the LDOS in the case of a gold nanotaper, we simulated by FDTD its interaction with a NS. As shown in figure 4.1a , The prism has a base $B_{Taper}=300$ nm, a length of $L_{Taper}= 800$ nm, a thickness of 20 nm , and a curved apex with curvature radius of 25 nm. This nanotaper is placed on top of a glass substrate. As in the chapter 2, the NS is modeled as a electric point-like dipole.

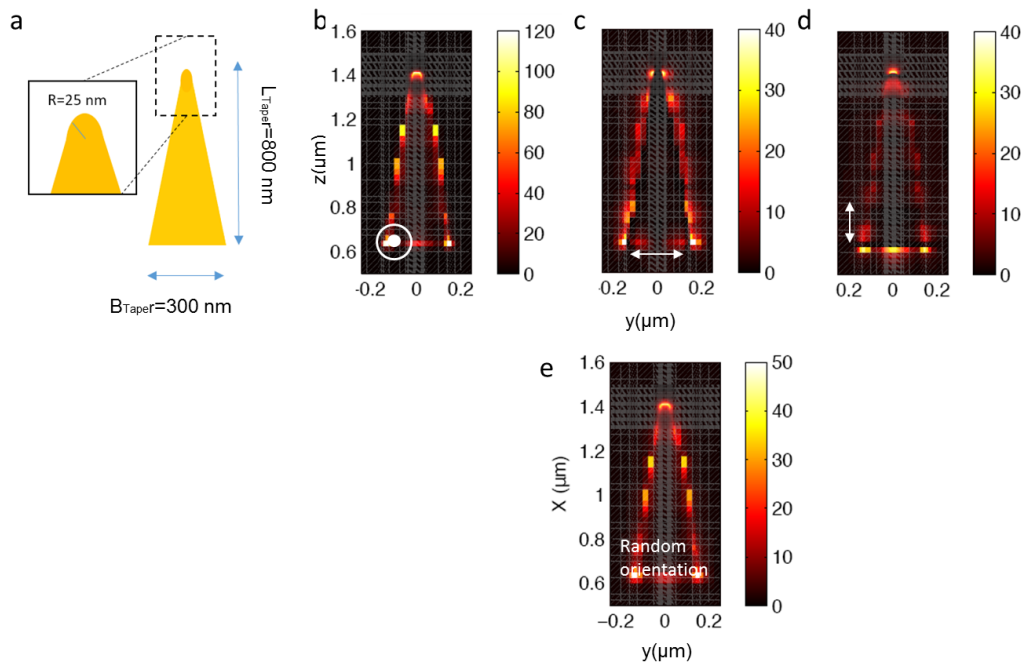


FIGURE 4.1 – Calculated partial LDOS above the plasmonic structure with a dipole source at $\lambda= 680$ nm. a) The plasmonic structure is a gold nanotaper with $L_{Taper} = 800$ nm, base of $B_{Taper}=300$ nm and curved apex with curvature radius of 25nm. LDOS map obtained by FDTD for a dipole oscillating in directions a) x , b) y , and (c) z . d) Average LDOS over the three dipole orientations (total LDOS).

The dipole is placed at 5 nm above the surface of the metallic nanotaper. We change the position of the dipole in order to scan the sample in a yz plane. We calculated the total radiated power for the dipole, and this is normalized by the total radiated power of the dipole in the vacuum. According to equation 1.1.52 this power ratio is equal to the normalized LDOS and the Purcell Factor. We modeled this interaction for the three directions of the dipole at wavelength 680 nm, in order to reproduce the experimental results, which will be presented in the next sections. The numerical results are depicted in figure 4.1b, c and d. These simulations show a enhancement of the LDOS (Purcell factor) at the edges of the nanotaper. This behavior is the consequence of the excitation surface plasmon polaritons. The highest enhancements are found at the apex of the nanotaper.

Figure 4.1e shows the average of figures 4.1d, c, and d. The maximum value of the LDOS is up to 50, which is more than 10 times than that found for the photonic mode (chapter 2 and 3).

4.1.1 Fluorescence mapping of the prismatic gold nanotaper on glass

In collaboration with the Institute Néel, we made fluorescence intensity measurements of the gold nanotaper on a glass substrate. These measurements were performed using an aperture SNOM setup (in appendix D it is possible to found some basic concept of this SNOM configuration). The SNOM probe was a functionalized optical fiber with a aperture of 200 nm at its apex. A single nanodiamond with radius R ($R = 40$ nm) and with several NV centers is attached to the apex of the SNOM tip and this tip is used as a probe to scan the sample.

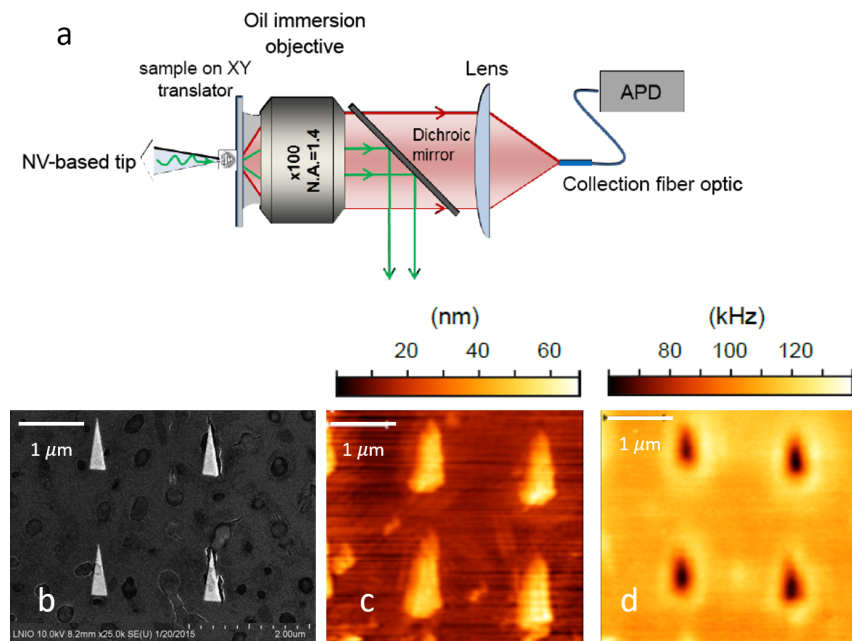


FIGURE 4.2 – Experimental near-field fluorescence intensity imaging of a plasmonic structure with a nanodiamond with NV centers. a) Scheme of the setup using to mapping the fluorescence intensity of the NV centers (in red) and separate the 532 nm excitation (in green). b) SEM image of the nanotaper on a glass substrate used in the experiments. c) Topography image of the plasmonic structure. The thickness of the gold nanostructure is 20 nm. d) Experimental optical near-field fluorescence intensity image of the plasmonic structure with a nanodiamond.

The setup used in this experiment is shown in figure 4.2a. In this setup the NV center is excited through the SNOM tip with unpolarized light at 532 nm (green path). Due to the

excitation, the nanodiamond emits light at 680 nm (red path) and it is collected by an diachronic mirror (named "lens" in the figure 4.2a) and measured by a avalanche photodiode (APD). The green light is blocked by a filter, assuring that only the fluorescence signal is taken. The probe is attached a quartz tuning-forks which vibrations allows to measure the topography of the sample. The fabricated nanotaper has the dimension of the structure presented figure 4.1. It is placed on top of a glass substrate.

Figure b shows a SEM image of the fabricated structure and figure c is topography images of the sample taken with the setup of figure a. Figure c is the fluorescence map after the scanning of the sample (these results were done by Dr. Martin Berthel, more details about this technique can be found in his PhD thesis [103]). In figure c we can observe an enhancement of the fluorescence of 1.4 for the zones close to the edges of the nanotaper. However, these results do not show any strong field enhancement effect in the apex of the nanotaper as we see in figure 4.12. The low level of fluorescence enhancement can be explained by a lack of high spatial resolution.

Indeed, according to FDTD simulations, for an ideal single electric dipole oscillating at $x_0 = 25$ nm from the surface of the nanotaper, the total LDOS distribution for this structure is plotted in figure 4.3a. We observe the highest enhancement of the fluorescence intensity (up to 8) close to the edge of the nanotaper and mainly concentrated at its apex.

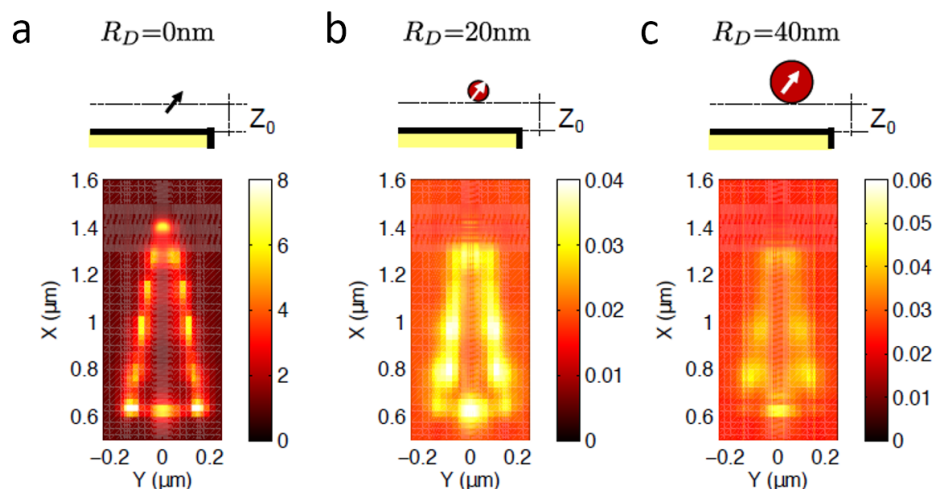


FIGURE 4.3 – Calculated total LDOS above the plasmonic structure. Total LDOS at 25nm from the nanotaper with a sphere of radius a) RD = 0 nm, b) RD = 20 nm, and c) RD = 40 nm.

In order to explained the difference between the figures 4.2d and 4.3a, we perform simulations where we consider the NV as a single electric dipole embedded into a diamond nanosphere with radius R_D and effective index of 2.4 (refractive index of the diamond [104]). Figures b and c show the results of the total LDOS for a $R_D= 20$ nm and 40 nm, respectively. Here we observe that for bigger diamonds the resolution in the mapping decreases and in consequence the total "measured" LDOS also decreases. SNOM in aperture mode promises to be a useful tool to the local excitation of NS and the characterization of the samples shown in this thesis.

In the next section, we propose to integrate this plasmonic nanotaper into our hybrid ions exchange platform.

4.2 Integration of a prismatic gold nanotaper into the hybrid IEW platform

As we presented in chapter 2, the mode coupling allows the transfer of energy between optical modes in dielectric waveguides, but this phenomenon also occurs between dielectric and metal waveguides. In figure 4.4 we show the scheme of a photonic-plasmonic waveguide formed by a dielectric waveguide and a metallic thin film. Here we observe that a photonic mode of a dielectric waveguide (figure 4.4a) and a plasmonic mode of a metallic waveguide (figure 4.4b) couple in a two-parallel waveguide (hybrid photonic-plasmonic structure).

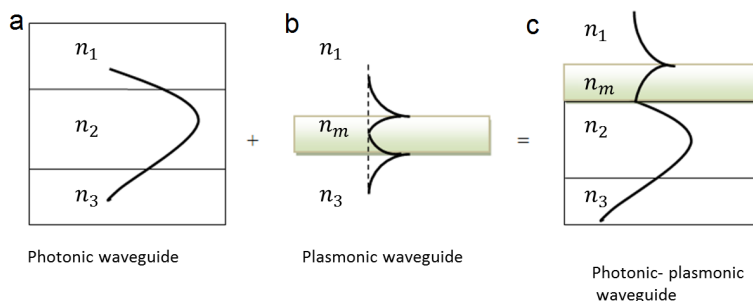


FIGURE 4.4 – Plasmonic-photonic modes coupling. a) Scheme of a guided mode in a dielectric waveguide. b) Scheme of a plasmonic mode in a metallic thin film, and c) a hybrid mode of the photonic-plasmonic structure.

The plasmonic and photonic mode coupling in hybrid waveguides has been shown in different works at the LNIO/UTT [105–107]. In these works silicon waveguides were used for their interesting electromagnetic properties at telecomm wavelengths. They allow strong confinement of the photonic modes due to their high refractive index contrast. This leads to phase matching and strong coupling efficiency with SPP modes in metallic materials. However, for nanosources with emission and excitation wavelengths in the visible spectrum it is necessary to explore other materials. For this reason, we work with suitable materials in the visible spectrum such as glass and titanium dioxide.

In our design, the gold nanotaper is integrated on top of a thin SiO_2 layer all placed on top of the surface of the TiO_2 layer (figure 4.5a). The gold nanotaper has a curved apex with a radius of curvature $R = 15 \text{ nm}$, base $B_{\text{Taper}} = 250 \text{ nm}$, length $L_{\text{Taper}} = 1 \mu\text{m}$ and thickness of 50 nm. The TiO_2 layer has a width of 500 nm and thickness of 150 nm, while the SiO_2 layer has a width of 500 nm and thickness of 30 nm (figure 4.5b). The nanotaper base is placed at $7 \mu\text{m}$ from the edge of the TiO_2 layer according with the L_c of the hybrid mode TM_0 for the structure formed by the TiO_2 layer and the IEW. The distance between the right end of the IEW and the left edge of the TiO_2 layer is $5 \mu\text{m}$.

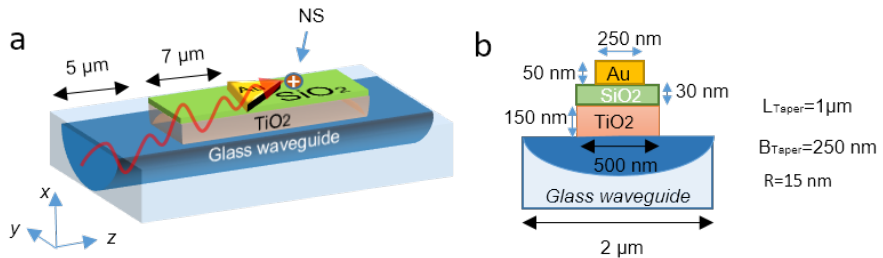


FIGURE 4.5 – Scheme of the hybrid photonic-plasmonic structure. a) An ion exchange waveguide, a TiO_2 layer, a SiO_2 layer, and a gold nanotaper. It can be seen the path of light through the hybrid structure (red line). b) Front view of the structure .

In this structure, the nanotaper has three main objectives : the slowly transformation of photonic modes into plasmonic modes, the focusing of this mode at its apex to excite the NS and reciprocally, this nanotaper works as a collector of light from the NS that transform plasmonic mode into photonic mode. The first and the second objectives will be discussed in this section, where we explain the principle of operation of this structure.

Due to the shape of the gold nanotaper, a mode propagating through the hybrid structure experiments a slowly change of its energy distribution due to a change of the effective

index. Then, the mode is slowly confined into the metallic structure and it excites the plasmonic modes of the nanotaper. Eventually, the plasmonic modes are confined in the apex of the nanotaper, generating a nanofocusing effect. This strong confined field is then used to excite a NS placed in the vicinity of the apex (figure 4.5a).

In order to model the nano focusing effect, we use the FDTD by Rsoft. The design of the structure was made taking into consideration real refractive indexes of the materials shown in figure 4.5b. Figure 4.6 shows the refractive indexes for gold and SiO_2 (the refractive index of the TiO_2 and the IEW, were given in figure 2.6). Each material was thermally evaporated on top of a silicon substrate. Its refractive index was measured by making use of the ellipsometry. Here, it must be noticed that the refractive index of gold (figure 4.6a) has a high imaginary part and a low real part, while the refractive index of SiO_2 has a low real part.

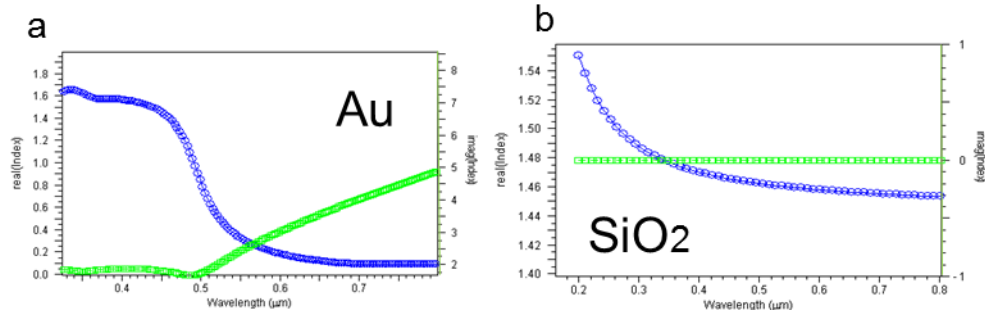


FIGURE 4.6 – Materials used in the design of the structure. Refractive index of a) gold (Au) and b) for silicon dioxide (SiO_2 obtained by ellipsometry).

The next step is to make an modal analysis of the structure, in order to improve the good matching between photonic and plasmonic modes and to reduce the propagation losses. Then, we will present a study of the enhancement factor EF of the confined field in the vicinity of the apex.

4.2.1 Plasmonic-photonic mode coupling analysis

Because our structure is formed by several layers positioned one above the other in the x direction, the effect of confined light is mainly lateral, this means the confinement of light in the upper layers is higher for the component E_x of the electric field and therefore

for the TM polarization. For this reason, in our structure we consider as a priority the propagation of the TM modes. The structure is designed for the propagation of modes with $\lambda=640$ nm, in order to improve the its performance at the emission wavelength of the NS.

Firstly, we will observe the mode of the photonic structure formed by a TiO_2 ridge and the IEW. The dispersion relation of TiO_2 layer used in the design is shown in figure 4.7a. The dimensions of the ridge (width $W=500$ nm and thickness $t=150$ nm) were selected in order to obtain the best EF, as we did in chapter 2, section 2.2.1.

The figure 4.7a shows the dispersion relation of the TM_0 mode of the photonic structure with $\lambda = 640$ nm. Herein, we observe the crossing between the IEW mode and the TiO_2 optical mode. As we discussed in the section 2.2.1., this crossing represents the maximal energy transfer,

The coupling between photonic and plasmonic modes is efficient when their effective indexes match. In figure 4.7b we observe the effective index of the fundamental TM mode (TM_0) for different thicknesses of gold (T_{Au}) and SiO_2 (T_{SiO_2}). The violet line represents the effective index of the even photonic mode (figure 4.7a). Here we can see that for $T_{SiO_2} = 0$ the effective index is far from the even mode (violet line). For higher values of T_{SiO_2} the n_{eff} decreases and approaches to the violet line. We can observe a similar behavior when T_{Au} is increasing, for T_{Au} higher than 30 nm and larger values of T_{SiO_2} the effective index is almost the effective index of the even mode. We selected a thickness of $T_{Au}=50$ nm. Figure 4.7c shows the even and odd modes of the photonic-plasmonic structure with TM polarization for different thicknesses of the SiO_2 layer. We observe that for $T_{SiO_2}=30$ nm the odd mode can be coupled to the even mode of the photonic structure. From these results we define the parameters as $T_{SiO_2}=30$ nm and $T_{Au}=50$ nm.

The figure 4.7d shows the variation of the effective index as a function of the width of the gold nanotaper (B_{Taper}). For narrow widths, when B_{Taper} decreases, the mode effective index increases also. For $B_{Taper} < 0.1\mu\text{m}$, the effective index of the TM_0 mode increases dramatically. A high refractive index is synonym of highly confined field at the apex of the nanotaper, generating higher EF and PF. In this graph we also plot the dispersion relation of the TE modes. TE mode effective index is almost constant for all values of B_{Taper} . This discards any nanofocusing effect at the apex for TE incident

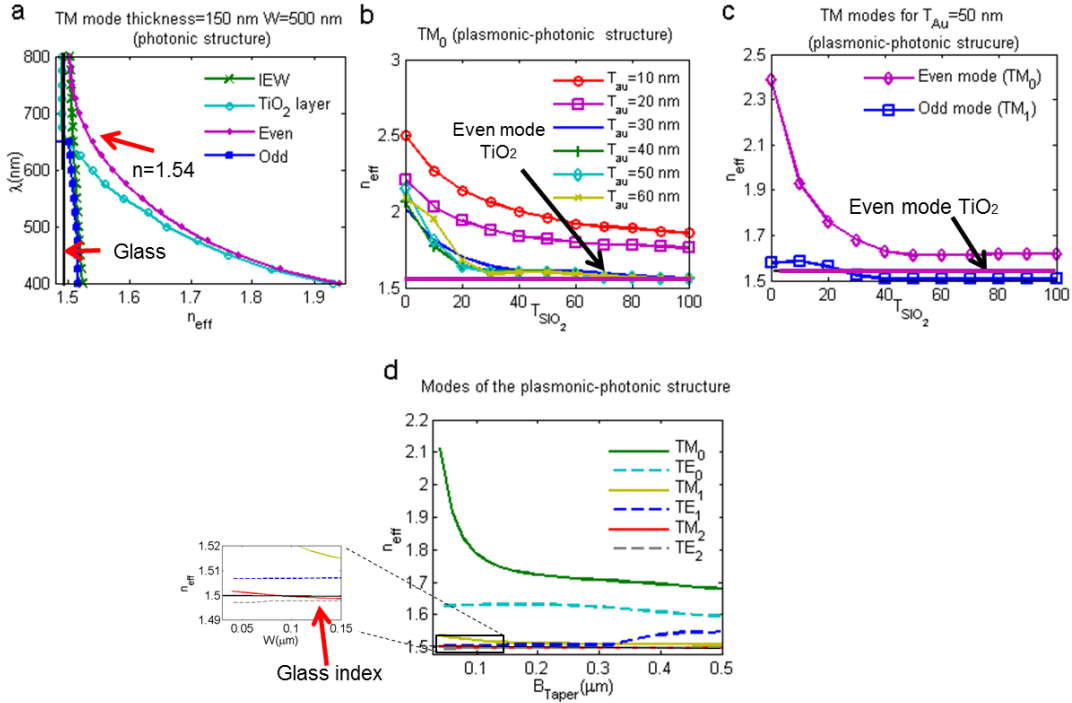


FIGURE 4.7 – Dispersion relations of the bounded modes in the hybrid photonic-plasmonic structure. a) Dispersion relation of the photonic structure formed for the TiO_2 ridge and the IEW, where green line and cyan line correspond to the isolated IEW and the isolated TiO_2 ridge, respectively. Purple and blue lines correspond to even and the odd mode of the hybrid structure. b) Effective index of the TM_0 mode in the plasmonic-photonic structure as a function of the SiO_2 layer thickness (T_{SiO_2}), for different thicknesses of gold $T_{\text{au}}=10, 20, \dots, 60$. c) Effective indexes of TM_0 and TM_1 modes (even and odd modes, respectively) in photonic-plasmonic structure as a function of T_{SiO_2} for a gold thickness $T_{\text{au}}=50\text{nm}$. d) effective indexes of the TM_0 (green solid line), TM_1 (yellow solid line), TM_2 (red solid line), TE_0 (cyan dashed line), TE_1 (blue dashed line), TE_2 (brown dashed line) modes as a function of taper's base B_{Taper} .

polarization.

4.2.2 Analysis of the field propagation along the hybrid integrated plasmonic-photonic structure

Figure 4.8a shows the evolution of a mode propagating through the structure. The cross-section maps of the electric field shows how the mode gradually confines itself to the apex of the gold nanotaper (maps from 1 to 4) .

The figure 4.8 b depicts the intensity distribution of the electric field in the metallic structure, showing a maximal concentration of the field at its apex. The figures c, d and e show the distribution of the electric field components E_x , E_y and E_z , respectively (fi-

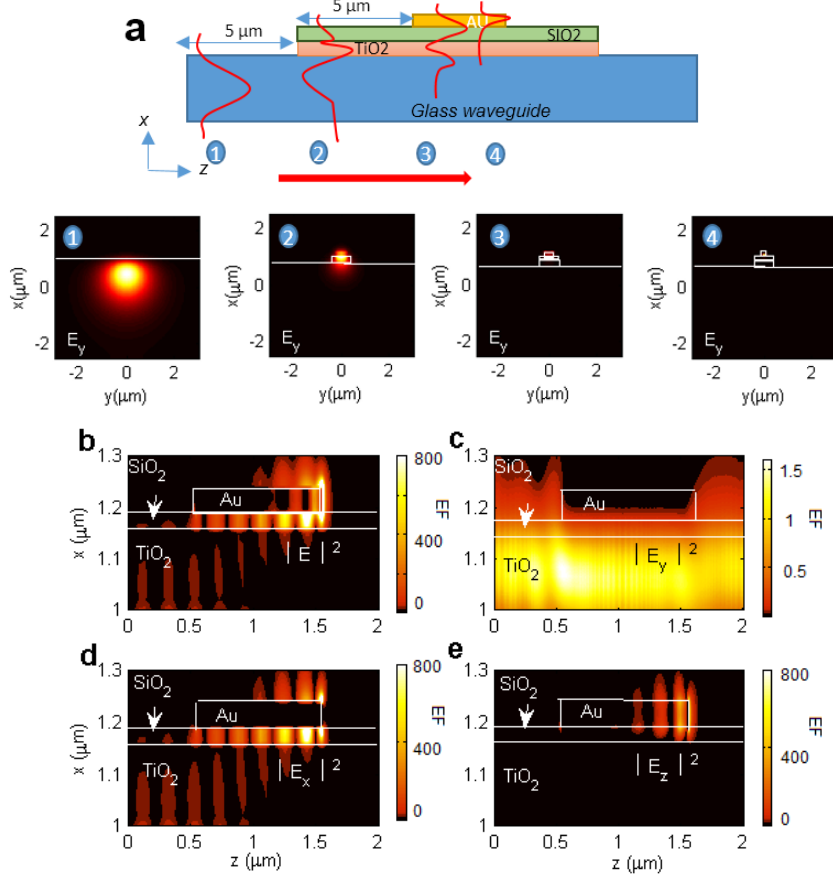


FIGURE 4.8 – Light propagation through the hybrid plasmonic-photonic structure. a) Evolution of field profiles at different cross sections indicated by locations 1, 2,3, and 4. b) Total electric field intensity, c) d) and e) intensity maps of field's components E_x , E_y and E_z respectively. The incident field is the fundamental guided mode into the IEW and is propagating from left to right (over saturated images with maximal values at 4253, 6, 3256, and 4152, respectively). The photonic mode is gradually converted into a well-confined plasmonic mode.

gures b, d and e are presented in a over-saturated scale in order to reveal the distribution all along of the structure). These maps show that the component E_z is more confined to the apex. The component E_x is mainly confined to the corners of the nanotaper and this is because the directional coupling of the structure which facilitates the propagation of TM modes (modes oscillating in the x direction). Figures 4.8b, d and e show an interference pattern that corresponds to a Fabry-Pérot cavity effect [108] produced for the gold nano-structure (longitudinal resonance). Finally component E_x seems to be badly confined in the nanotaper.

Figure 4.9 shows the enhancement factor of the total electric field ($EF_{nanotaper}$) due to the light focusing in comparison with the electric field calculated on top of the IEW

when it is excited by TM mode. These values were calculated at a point r_0 localized 25 nm from the TiO_2 layer in the x direction and 10 nm from the apex of the nanotaper in the z direction. The enhancement is normalized by the electric field over 25 nm from the bare IEW.

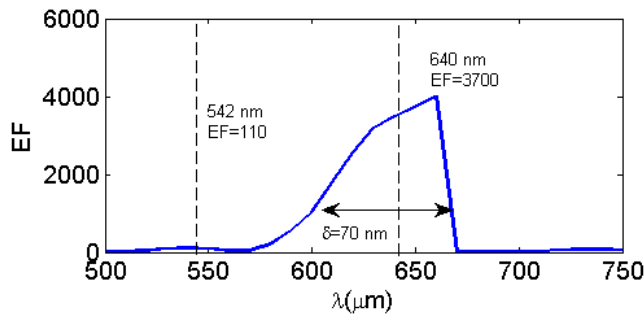


FIGURE 4.9 – Electric field enhancement factor (EF) for an electric dipole as a function of the wavelength. The dipole source is placed at 10 nm from the nanotaper apex in the z direction and at 25 nm from the TiO_2 layer and oriented along the x direction. The enhancement is normalized by the electric field at 25 nm from the surface of the IEW .

The operating range is relatively large (from 590 nm to 660 nm). For a mode at $\lambda=542$ nm we calculated an EF of 110. We observe a peak at 640 nm with an EF= 3700 due to an efficient mode matching at this wavelength.

4.2.3 Analysis of the field propagation along the hybrid integrated plasmonic-photonics structure : the reciprocal scenario

Now we present a study of the reciprocal case, i.e. the NS is integrated on top of the structure and its radiated light is collected by the IEW. We consider the wavelength $\lambda = 640$ nm. We calculate different entities : the total power dissipated by the dipole (total LDOS), the absorbed power (absorbed LDOS or ρ_{abs}), the radiated power (radiated LDOS) $\rho_{rad} = \text{total LDOS} - \text{absorbed LDOS}$, the collected power in the left end of the IEW due to the excitation of backward modes (backward LDOS or $\rho_{backward}$) and the collected power at the right end of the IEW due to the coupling to the forward modes (forward LDOS or $\rho_{forward}$). The calculation has been done for different values of L_{Taper} (from 50 nm to 1500 nm) and for 3 dipole orientations (the 3 direction of the coordinated axes, x , y , and z). The results of these calculations are shown in figure 4.10b,d and f.

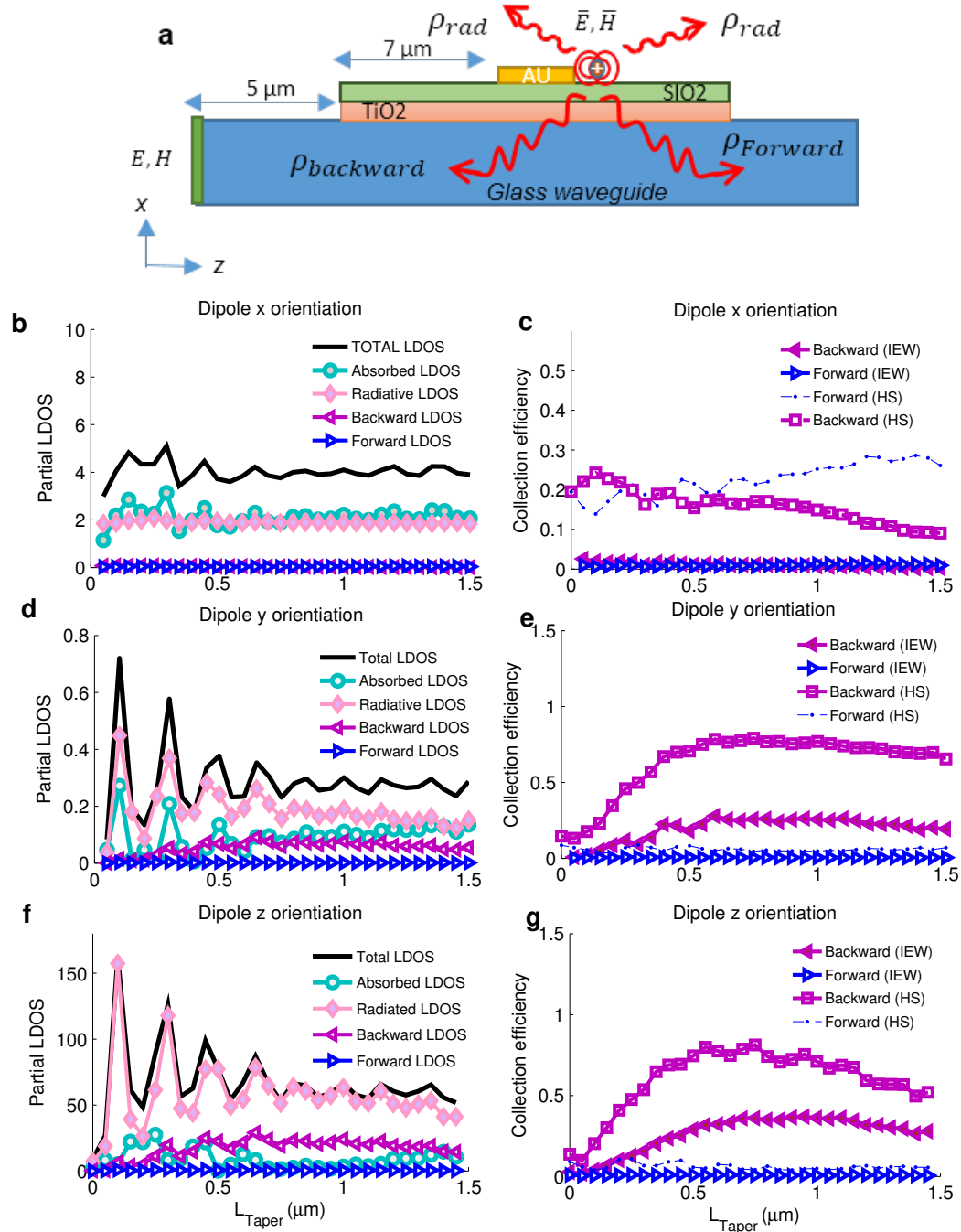


FIGURE 4.10 – Dipole radiation coupled to the guided modes of a hybrid photonic-plasmonic structure. a) Dipole position in relation to the structure. b), d), f), total, absorbed, radiative, backward and forward LDOS normalized to the LDOS in vacuum for different values of L_{Taper} . c), e), g) Collection efficiency into backward and forward modes for 3 directions of the dipole (x,y and z), for a monitor placed at the edge of TiO_2 (hybrid structure HS) and for a monitor at the end of the IEW.

In these curves, we clearly see some periodic oscillations. These oscillations are due to a longitudinal cavity effect generated by the finite size of the gold nanotaper (figure. 4.8). From the results obtained for a dipole oscillating along the z direction, we calculated a LDOS up to two orders of magnitude higher than those for the dipoles oscillating along the x and y directions. This behavior is explained for figure 4.8, where we show that the light is preferentially confined in the apex for the E_z component. Therefore using the reciprocity of the system it is expected a better coupling efficiency for a dipole oscillating in the z direction. For all three components the amplitude of the oscillations amplitude decreases as L_{Taper} increases.

In figures 4.10c, e and g, we plot the ratio of collected power (collection efficiency) into the IEW in both backward and forward directions .

We obtain that the collection efficiency increases for longer nanotapers. At the same time, the oscillation amplitude of the values in 4.10b, d and f decreases. Indeed, for shorter lengths, the nanotaper behaves likely as gold nanoparticle that mainly excites the radiative modes of the system, therefore the backward and forward modes are badly excited. When L_{Taper} is increased, the tapered shape of the nanoprism plays the role of a quasi-adiabatic mode converter (as we explained in the last section). Then the plasmonic modes excited by the NS are transformed into photonic modes and subsequently in IEW modes, increasing the collected power at the end of the IEW.

According to the equation 1.1.53, the collection efficiency is defined as $\eta_{backward} = \rho_{backward}/(\rho_{abs} + \rho_{rad})$ and $\eta_{forward} = \rho_{forward}/(\rho_{abs} + \rho_{rad})$. From these results, we observe that the collection efficiency was 3%, 28% and 38% for the backward modes and 0.01%, 5% and 6% for the forward modes with maximum normalized LDOS of 5.1, 0.7, and 158, for a dipole oscillating in x , y and z direction, respectively. From these results we can observe that the dipoles oscillating in y and z direction have a good coupling efficiency. However, it should be mentioned that a high Purcell Factor generate a high emission photon rate and in consequence more photons can be detected at the end of the IEW. For this reason, a dipole oscillating in the z direction with good efficiency in both end of the IEW, and the best Purcell Factor (normalized LDOS), can be seem as the source with best performance.

It is interesting to observe that the collection efficiency is higher in the left end of the

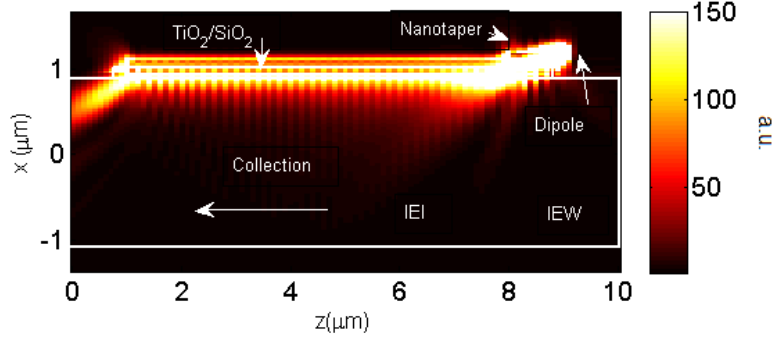


FIGURE 4.11 – Electric field distribution of the light emission from the dipole through the photonic-plasmonic hybrid structure (over saturated image whith a maximum real value is 28 000). It is evident that the even mode is mainly excited.

IEW than in the right one. It is due to the reciprocity of the system and the nanofocusing effect. We conclude that the coupling is highly unidirectional for the three oscillation directions of the dipole. However, for this system, about the 60% of the light is lost in radiated light to the free space and absorbed light.

In order to clarify the reason of these losses, we also took the information of the collected power at $1 \mu m$ before the edge of the TiO_2 . At this location, we defined the collected power as a sum of the power in the IEW and the power in the TiO_2 waveguide. The collection efficiencies for a $L_{Taper} = 1 \mu m$ are 30%, 75% and 82% for the backward modes and 3%, 8% and 8% for the forward modes using a dipole oscillating in the x , y ad z direction, respectively. This shows that the losses are mainly due to scattering at the edge of the TiO_2 ridge.

As we observed in the s-SNOM results (figure 3.17 c and g), the edge of the TiO_2 acts as a strong discontinuity for the light and this might generate scattering losses. Figure 4.11 shows the distribution of the electric field intensity propagating into the structure from the dipole source. Herein we see that the light is mainly confined in the TiO_2 ridge. This indicates that the even mode of the hybrid TiO_2 /IEW structure is mainly excited by the nanotaper. Since the odd mode is badly excited, the directional coupling between the two dielectric waveguides is not efficient. In consequence the mode is not efficiently transformed into an IEW mode and the collected scattering increases at the end of the TiO_2 ridge.

This preferential excitation looks like the results obtained in section 2.3, where we

presented the tapered TiO_2 ridges. The use of a taper at the end of the TiO_2 ridge is a good solution to efficiently transform the even mode into an IEW mode by decreasing the scattering losses. However, the taper lengths over than $50 \mu\text{m}$ make a problem in the computation time. We simulated the the case for a taper length of $50 \mu\text{m}$. We found that the efficiency increases up to 64% into the backward modes. According to the results discussed in section 2.3, higher collection efficiencies using longer tapers seems straightforward to obtain.

One important conclusion about the figure 4.11 is the excitation of the structure form a IEW and for a dipole source are not reciprocal scenarios, due to these two source are not able to excite the same guided modes.

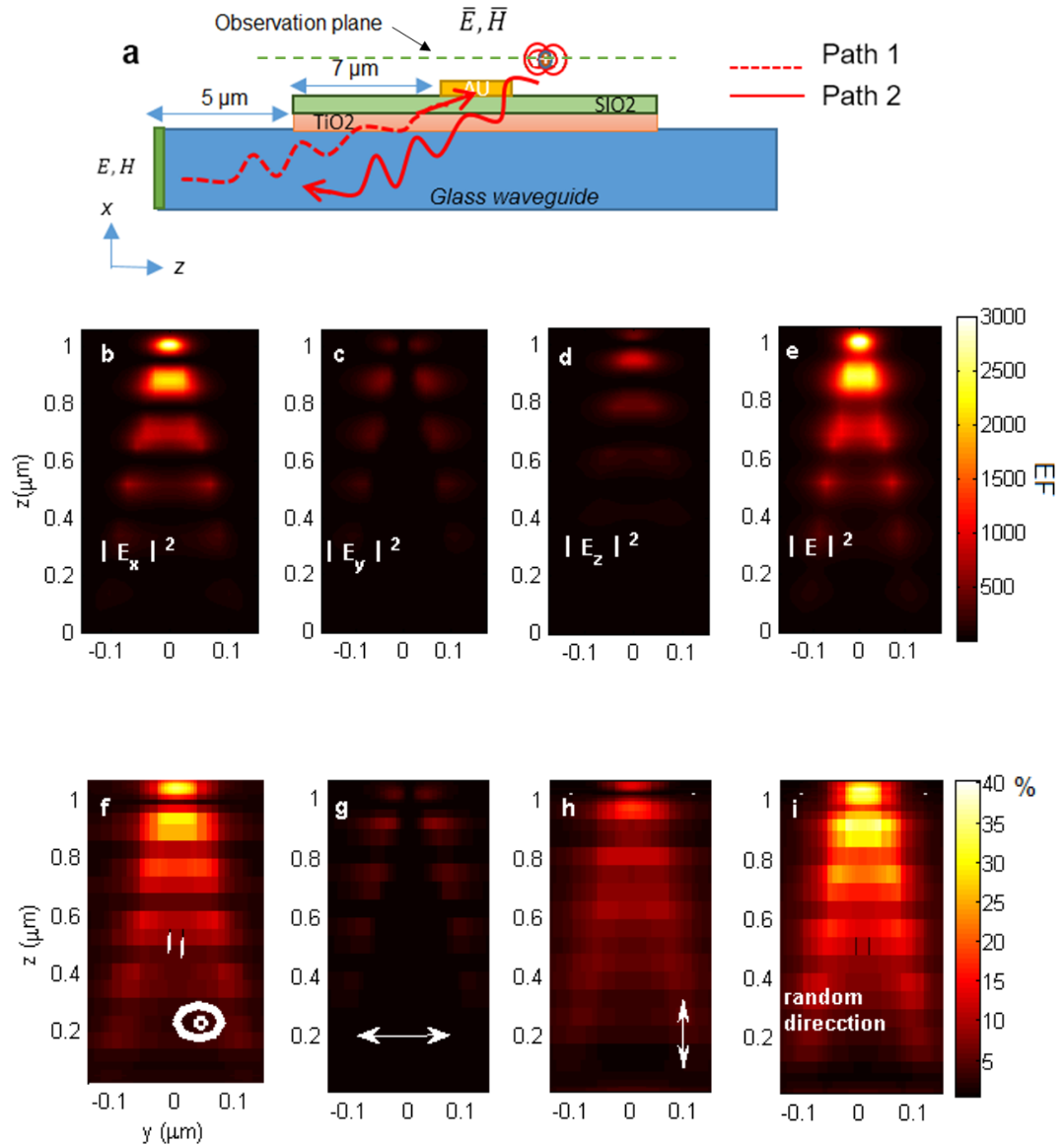


FIGURE 4.12 – Reciprocal behavior of the excitation of the nanotaper. a) Observation plane and dipole position in relation with the hybrid structure. The path 1 represents the nanotaper excitation by a forward guided mode of the IEW and the path 2 represents the coupling between the radiated light from the dipole and the backward guided modes. EF of the electric field at the observation plane at 25 nm from the nanotaper (dashed green line) in comparison with the electric field on top of the IEW at 25 nm from its surface, for the b) E_x , c) E_y , d) E_z components and e) the total electric field intensity at an observation plane placed 25nm from the gold nanostructure in the x direction. Collection efficiency into the backward guided modes when the dipole is used as a probe scanning the nanotaper across an observation plane for three oscillation directions of the dipole (f) x , (g) y and (h) z . i) Average of the figures f), g) and h).

In order to observe this behavior, we simulated these scenarios for a nanotaper with $L_{taper} = 1\mu\text{m}$ (figure 4.12). In the path 1, we simulated the excitation of the plasmonic modes by a IEW mode and we observe the distributions of the components of electric

field (figure 4.12b,c and d) and the total electric field (figure 4.12e) on a plane localized at 25 nm above the surface of the gold nanotaper. As we did in chapter 2, these components are normalized for the components of the electric field confined at 25 nm from the surface of the IEW.

For the second scenario or path 2, we scanned the observation plane using the dipole as a source for the three principal directions of oscillation (x , y and z). The collection efficiency into the backward modes of the IEW is shown in figures 4.12f, g and h.

According to these maps a dipole oscillating in the x direction has the best collection efficiency. This is because at the selected observation plane the E_x component of the electric field is stronger than the others as shown in figure 4.8. Figure j shows the average of figures e f and g in order to represent the collection efficiency of a dipole oscillating in a random direction. The results from figures 4.10 and 4.12 show that this structure is able increase the EF and collect its radiated light. It can be seen that the spatial distributions of the electric field distributions for both scenarios are reciprocal. This because the distribution of the plasmonic field is mainly due to the excitation by even mode and this is mainly excited at the position of the nanotaper for the both scenarios. However, the EF and the collection efficiency are no proportional as it was in the case of the photonic structure (figure 2.10). This behavior is a evidence of that saw in figure 4.11, where we observed the mode excitation is not the same in the two scenarios.

4.2.4 Optimal shape of the adiabatic photonic mode coupler

As we mentioned in the last section and the chapter 2, we propose to reduce the losses in the collected light for the IEW by using an adiabatic photonic mode coupler. However, to reduce the amplitude of the beating between the hybrid modes it is necessary to use a coupler with length above 100 μm . This long coupler has been fabricated but we had some problems to characterize them due to the limited scanning area of the AFM (close to 70 μm by 70 μm).

In order to improve the performance of the taper, we made a study of the effective index of the structure and its dependence with the dimensions of the taper. Here we present an example of this study, where we use a TiO_2 ridge with width of $W = 2 \mu\text{m}$ and thickness of 120 nm with a tapered shape of one of its ends.

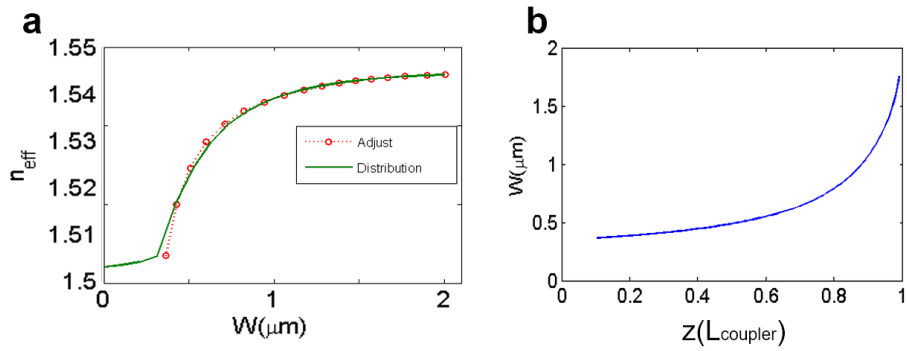


FIGURE 4.13 – a) Relation between the effective index of the even mode and W . For a TiO_2 ridge with thickness $t=120$ nm. b) Dependence of W in terms of Z in order to obtain a linear change of the effective index.

Figure 4.13 shows the relation between the effective index of even mode for this ridge as a function of W . Here we observe that for $W < 0.4\mu m$ the n_{eff} linearly changes but for $W > 0.4\mu m$ the effective index changes abruptly. In a taper as the showed in chapter 2 (a linear taper), W is linearly related with z . As consequence a mode propagating through the structure is affected for this abrupt change in the effective index. For longer tapers this change is less evident that the coupling mode is made in an adiabatic way. If we consider that n_{eff} can be written as

$$n_{eff} = f(W) \quad (4.2.1)$$

with $f(W)$ an unknown function. We can built a linear relation between the distance z and n_{eff} as

$$z = An_{eff} + B, \quad (4.2.2)$$

and therefore

$$z = Af(W) + B. \quad (4.2.3)$$

In the example shown figure 4.13a we adjust a curve to the results for $W > 0.4\mu m$, obtaining the relation of W and z as it showed in figure 4.13 b.

In figure 4.14 a we present the values of effective index for the even and the odd mode (the hybrid modes) of the structure in terms of the z direction for a linear taper (figure a) and for the optimal shape of the taper (figure b). The end of the optimal shape taper was designed as a linear taper with length equal to the 10% of the length taper (figure

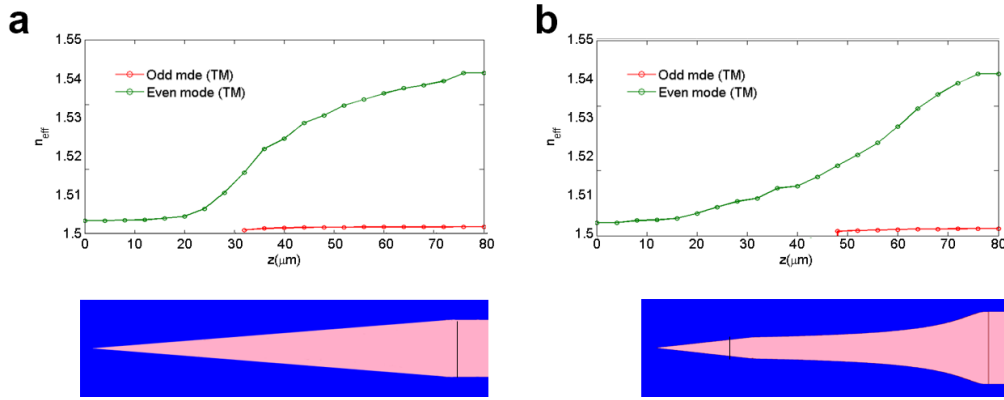


FIGURE 4.14 – Effective index of the hybrid modes of the structure with a) lineal shape and b) optimal shape.

4.13b). The image show the example for a taper with length of $60 \mu m$. From this figure, we observe that in the point of the abrupt change, the odd mode starts to leak and the effective index of the even and the odd mode are similar. For the taper with optimal shape, at the point where the odd mode appears the even mode has a higher effective index than that of the linear taper. This effect can help to mainly excite the even mode.

In order to observe the coupling efficiency of modes, we used the overlap integral that represent the energy transfer from a mode 1 to a mode 2 [88].

$$\eta = \frac{1}{P_0} \text{Re} \left(\frac{\int_A E_1 \times H_2^* \cdot \hat{z} dA \cdot \int_A E_2 \times H_1^* \cdot \hat{z} dA}{\int_A E_1 \times H_1^* \cdot \hat{z} dA} \right), \quad (4.2.4)$$

where E_1 and H_1 correspond to the electromagnetic field of the mode 1 and E_2 and H_2 for the mode 2. A is the area of the mode. Here the mode 1 is the even mode of the hybrid structure with $W = 2 \mu m$ and P_0 is the power of this mode.

Figure 4.15a shows the correlation coefficient as a function of the z for the taper with linear shape (blue line) and with optimal shape (red line) with length of the coupler of $60 \mu m$.

Here we observe that for the linear taper the overlap integral is lower than 1, that means the even mode can not be reproduced by this taper. While for the optimal shape taper it is possible to excite it. Figure 4.15b shows the change of the correlation coefficient in relation with the length of the coupler ($L_{Coupler}$) for the linear taper (blue line) and the taper with optimal shape (red line). These curves show that for a taper with lineal shape

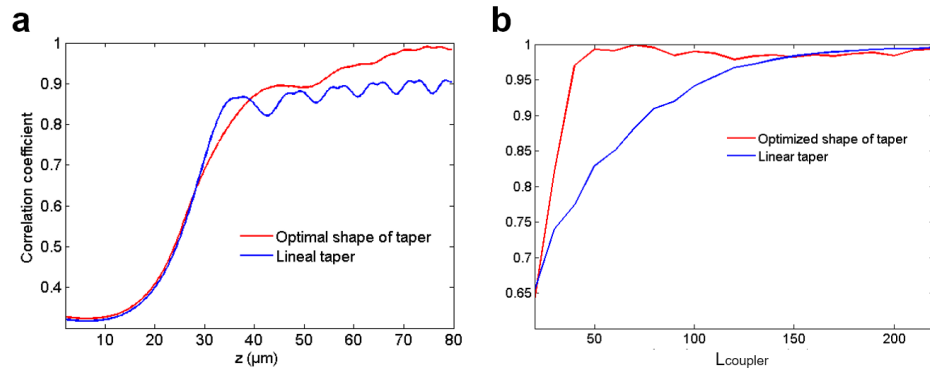


FIGURE 4.15 – Correlation coefficient for the taper with linear shape (blue line) and optimal shape (red line) in terms of a) z and b) $L_{coupler}$.

a correlation coefficient of 1 can be obtained for $L_{Coupler}$ s longer than $100 \mu\text{m}$ while than the taper with the optimal shape this coefficient is obtained for lengths longer than $60 \mu\text{m}$. This result will help us to design shorter structures that can reduce the losses of coupling light due to the adiabatic change of energy.

4.3 Fabrication of the plasmonic-photonic structure

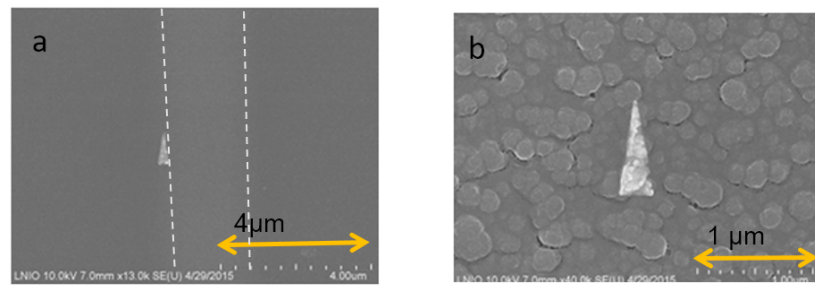
The fabrication of the gold nanotaper placed on top of the TiO_2 layer was made using the process described in section 3.2. The steps from 1 to 5 and 7 described in figure 3.4 are also used for metal deposition, where the material used in step 6 was changed for gold. The difference between the fabrication of TiO_2 layer and gold nanostructures is the selection of lithographic parameters. The electron-beam lithography and the material parameters in the electron-beam evaporator used for the fabrication of gold structures are showed in table 4.1.

Figure 4.16 are SEM images of the first efforts to fabricate the gold nanotaper. Here we observe the fabrication issue described in section 3.2.2, where a misalignment of the mask is evident (figure a). Here the gold nanostructure is placed $1 \mu\text{m}$ far away from the center of the IEW (white lines). In figure 4.16b it is observed the comparison between the size of the defects of TiO_2 deposition and the size of the nanotaper.

Indeed, we fabricated a sample where all the parameters were controlled and the problems of fabrications were minimized. This sample includes TiO_2 waveguide ridges with

TABLE 4.1 – Parameters of electron beam lithography for the fabrication of Au nanostructure.

Parameter	Value
EHT (Extra High Tension)	20kV
Working distance	5.6 mm
Aperture	10 μ m
Dose area	300 μ C/cm ²
Dose line	400 pC/cm ²
Step size (area)	0.0024 μ m
Step size (line)	0.0024 μ m
Beam current	40 pA

FIGURE 4.16 – SEM images of the fabricated nanotaper structures . a) example of misalignment between the gold nanotaper and the IEW (dashed white line) and b) zoom into a gold nanotaper fabricated on top TiO_2 layer.

width of 1.5 μ m, thickness of 100 nm with and without tapered ends with the optimal shape (figure 4.17a, b and c). Over this ridges we placed gold nanotapers with base of 200 nm, $L_{taper}=400$ nm and curvature radius of 25 nm (figure d). Below this nanotaper, we placed a SiO_2 layer with the same form of the gold nanotaper in order to reproduce the effect observed in chapter 2, section 4.2.

In figure 4.17f, g, h and i, we show the SEM images of this sample where we see the well-defined edges of the TiO_2 ridges and tapers. In figures h, it is possible to verify the alignment of the gold nanotaper in the center of the ridge and in figure i we observe the quality of the fabrication of the gold nanotaper. Some fabrication issues were fixed when we realized the electron beam lithography, the TiO_2 deposition and the lift off in the same day. This procedure reduced the exposition of the PMMA to some agents in the environment and facilitated the lift-off process.

Unfortunately, as we previously mentioned, this sample was fabricated in the last months and it was not possible to make the characterization of the sample and include

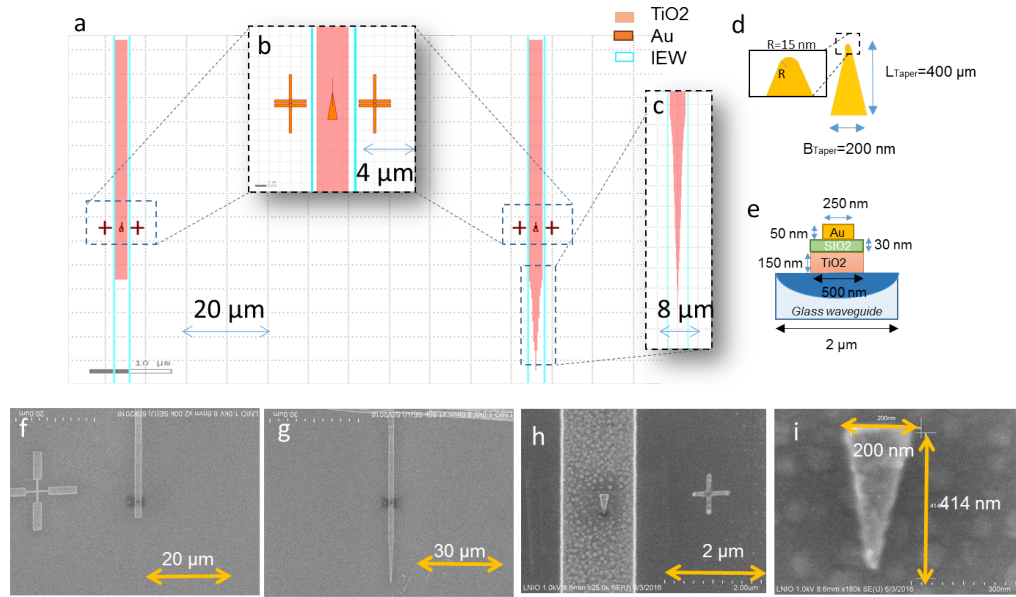


FIGURE 4.17 – a) Design of the new sample that includes b) the TiO₂ ridges with and without tapered ends on IEWs with c) optimal shape and d) gold nanotapers. e) Dimensions of the materials used in the sample. SEM images of the fabricated sample, including f) ridges, g) the tapers, h) the well-aligned nanotaper and i) zoom into the nanotaper.

this results in the thesis.

4.4 Conclusion

A parametric study of the gold nanotaper was presented. We observed that longer tapers can efficiently transform photonic to plasmonic modes. Due to the geometry of the taper we observed a field concentration effect in the vicinity of the apex, generating a strong nanofocusing effect that can be reproduced in a large range of wavelengths.

We performed a study of the coupling efficiency of a dipole radiation into the optical mode of the structure. We found an higher efficiency for a dipole oscillating in z direction when it is placed close to the nanotaper apex. We also found that the coupling is directional for any orientation of the dipole.

We presented also preliminary results about fluorescence imaging of gold nanotapers deposited on glass and we concluded that smaller fluorescent nanostructures (<20nm) are needed in order to correctly measure the field enhancement factor at the edges of this nanotaper.

Using the hybrid structure, the excitation strength could be increased by a factor 110 times higher than using a bare IEW. At the dipole nominal radiation wavelength of 640 nm, the overall collection efficiency is about 38%, and we expect an increase of this value up to 64% by considering a tapered ridge TiO₂ structure.

Chapter 5

General conclusion

The hybrid photonic-plasmonic structure proposed in this thesis promises to be an important milestone towards the integration of nanoemitters on waveguides. This structure can be easily adapted to several scientific applications. Field enhancement factors of thousands and Purcell factors of several hundreds are remarkable properties that can be used in areas such as bio sensing for instance. The efficient information transfer from a nanoemitter through either short or long distance is also demanded for quantum information applications, encryption and data processing.

Using the electrodynamics and considering the single photon source as a dipole, we were able to associate the emission characteristics of nanoemitters with its local density of states (chapter 1).

We conducted numerical simulations using the FDTD method in order to study the physics involved in the working principle of the structure. For an hybrid structure consisting of an ion exchange waveguide (IEW), a structured layer of TiO_2 and a gold nanotaper placed on top, we observed that a IEW mode with area of some square micrometers can be transformed into a plasmonic mode that is focused in an area of some square nanometers at the apex of the nanotaper (chapter 2). Close to the apex and with a working wavelength of 640 nm, a high enhancement of confined electric field was found ($\text{EF}=3700$).

Following the reciprocity theorem of electromagnetism, we studied a reciprocal case, where a dipole oscillating close to the surface of our hybrid structure. We quantified the Purcell factor (up to 150) and the collection efficiency of the radiated light from the dipole into the guided mode of the IEW. A collection efficiency up to 40% for a dipole oscillating

along the Z direction was obtained (chapter 2). These losses of 60% are mainly due to the breaking of the reciprocity of the directional coupling mechanism consecutive to the insertion of the gold nanotaper. Indeed that last selects preferentially the excitation of one of the two necessary hybrid modes involved in the directional coupling mechanism. We could observe that the reciprocity is found when the both sources are able to excite the same superposition of hybrid modes in the structure. This breaking of reciprocity can be resolved by making use of monomodal guided systems.

In our case, we proposed to filter the odd mode by using tapered structures. They work as an adiabatic mode converter between the modes of the IEW and those of the TiO_2 structure (chapter 2 and 4). We demonstrated that the linear tapered structures allow increasing the coupling efficiency from 40% to 64%. We also discussed the design of the optimal shape of the taper taking into consideration a linear change of effective index for the hybrid modes. This optimal shape can significantly improve the adiabatic mode conversion with reduced propagation lengths.

Through our experimental work, we demonstrated that perturbation and scattering SNOM configurations are useful tools for the characterization of our device.

Moreover we developed a new apertureless SNOM configuration which consists in illuminating directly the AFM tip and collecting the coupled light into the waveguide. We demonstrated that this original setup allows measuring the local density of guided modes (LDOM) transmitted through the device. Indeed, this configuration mimics the excitation of a dipole like emitter and is useful to predict the properties of a fluorescent nano source in interaction with an integrated photonic circuit. We studied experimentally the reciprocity between s-SNOM and i-SNOM in our specific experimental arrangement.

We conducted some spectroscopic measurements using CdSe/CdS nanocrystals deposited on top of our hybrid TiO_2/IEW photonic structure. We demonstrated the use of the photonic platform in the two quasi-reciprocal ways : excitation of the nanocrystals by the waveguide and external detection of the luminescence and, reciprocally, excitation by an external source and luminescence measurement through the waveguide. Lifetime measurements were obtained showing a Purcell Factor of 2.

Due to fabrication issues, only two real samples were studied in this thesis. However, the characterization showed that some imperfection in the TiO_2 deposition process can

generate strong deviations from the theoretical design. Finally by better controlling the fabrication process, we succeeded in doing the fabrication of a structure with good geometrical characteristics. The next step will consist in probing the performance of the new sample by making use of SNOM techniques in order to measure the LDOM and LDOS on the gold nanotaper.

There is still a long work to do to succeed in realizing the deterministic integration of a single photon emitter into a complex photonic waveguiding structure. Many issues especially in the fabrication process need to be explored. This actually feeds strong research activities in the laboratory at the frontier between guided optics, plasmonics, nano-spectroscopy and nano-photochemistry.

The final goal is of course the development of an efficient waveguide-coupled nano-source able to deliver single photons on demand into a photonic chip. The middle term development perspective of this project is the conception of a device prototype. Such a device would be powerful to be used in the future quantum integrated optics technology.

Chapter 6

Résumé en français

La miniaturisation des dispositifs joue un rôle important dans nos vies. Les dispositifs électroniques qui occupaient autrefois de grands volumes, s'intègrent actuellement sur puces dans des appareils tels que les ordinateurs et les téléphones portables dits "intelligents". Les technologies actuelles de la miniaturisation permettent d'envisager la fabrication de dispositifs structurés à l'échelle manométrique qui promettent des grandes avancées dans les filières de l'opto-électronique : notamment pour les télécommunications du futur, le traitement de l'information, ou encore pour l'élaboration de micro-capteurs permettant la détection de molécules individuelles.

Dans ces composants, le transport d'électrons est peu à peu remplacé par la manipulation de particules individuelles comme le photon, qui est la particule la plus couramment utilisée. En information quantique, les photons uniques qui sont vecteurs d'un quantum d'énergie peuvent produire grâce au contrôle de leur état de polarisation des *qubits* (analogue du *bit* en information classique) [1]. Chaque *qubit* peut être distingué et classé en fonction de l'information de la superposition de ses deux états propres [2, 3]. Des études montrent que l'usage de *qubits* pourrait améliorer certaines tâches comme la cryptographie [4–6], le calcul numérique et le traitement des données [7, 8]. En plus des applications dans l'information quantique, les sources de photons uniques ont été utilisées comme biomarqueurs, et nanosources localisées [17, 18], pour ne citer que deux exemples récents.

Ces nouvelles applications prometteuses ont fait de l'intégration des sources de photons uniques sur puces un sujet d'étude récurrent au cours des dernières années. La propa-

gation et la manipulation de photons uniques à travers des circuits complexes sur longues distances à faibles pertes reste un défi qui nécessite l'élaboration de dispositifs de haute qualité.

Cette thèse propose un ensemble de méthologies et d'outils permettant la concevoir, de fabriquer et de caractériser des structures hybrides photoniques-plasmoniques en vue de l'intégration d'une source de photons uniques sur une puce optique.

Nous proposons le design d'un circuit photonique intégré capable d'exciter et de collecter efficacement l'émission spontanée d'un nanoémetteur unique intégré en son sein. Pour la conception, nous recherchons l'excitation et la collection efficace de l'émission spontanée d'un nanoémetteur en interaction avec une nanotaper d'or (Au) sur une structure photonique intégrée formée par une couche haut indice de dioxyde de titane (TiO_2) placée sur un guide d'onde à échange d'ions sur verre (IEW).

Comme on le voit sur la Fig. 6.1, la structure est formée par un guide d'onde réalisé par échange d'ions (IEW) sur verre et relié à des fibres optiques commerciales, une couche TiO_2 , un nanotriangle d'or (gold nanotaper) et une source de photon unique placée à proximité du sommet du nanotriangle. Cette structure a été imaginée en utilisant la théorie des modes couplés et le théorème de réciprocité de l'électromagnétisme.

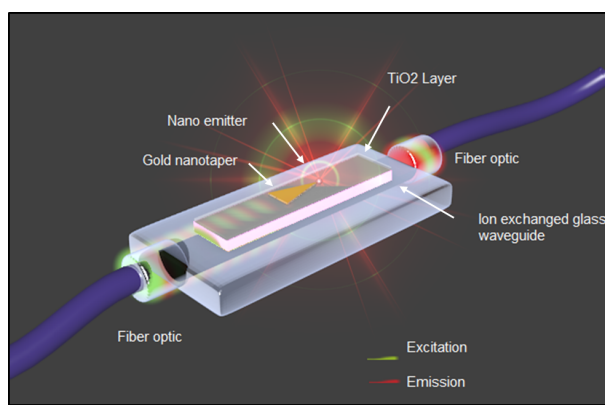


FIGURE 6.1 – Représentation schématique de la structure conue pour l'intégration des nanoémetteurs sur puce.

Le principe de fonctionnement du composant est le suivant : la lumière à la longueur d'onde d'excitation du nanoémetteur (lumière verte) est propagée à travers la fibre de gauche sur le dessin. Le mode guidé incident se couple aux modes propagatifs du guide à échange et à la couche de TiO_2 . Les modes guides se transforment progressive-

ment en modes confins plasmoniques en raison de l'interaction entre la couche TiO₂ et le nanotriangle en Au. La transformation adiabatique des modes génère un champ fortement confiné au sommet du nanotriangle qui agit comme un concentrateur de champ électromagnétique. Le champ électromagnétique ainsi confiné excite l'émission spontanée du nano émetteur placé à proximité du sommet du triangle. Les canaux de désexcitation radiative génèrent de l'émission spontanée de photons. Les photons émis (lumière rouge) sont alors guidés le long du chemin optique réciproque à l'excitation et par la suite se couple dans la fibre optique excitatrice (fibre de gauche). Si le design du système est bien réalisé, peu de lumière émise par le nanoémetteur se couple sur la fibre de droite. Cette fibre peut alors être utilisée pour monitorer la puissance du faisceau excitateur par exemple.

6.1 Concepts préliminaires

Le concept de photon a été introduit par Max Planck en 1900 afin d'expliquer le spectre de rayonnement du corps noir [19], cette particule élémentaire est un quantum d'énergie de rayonnement électromagnétique .

Afin de comprendre les concepts physiques impliqués dans la manipulation et la propagation de photons uniques, nous avons étudié l'interaction lumière-matière en utilisant la théorie de l'électromagnétisme.

6.1.1 Une source de photons uniques idéale

Une source de photons uniques idéale est caractérisée par l'émission d'un seul photon dans un intervalle de temps régulier déterminé par l'utilisateur (source déterministe) [20–22]. Dans ce type de source, la probabilité d'émission d'un seul photon est de 100% et la probabilité d'émission de photons multiples est de 0%. La Fig. 6.2 représente le principe d'émission de photons dans un système à deux niveaux d'énergie. Un photon de pompe est au préalable absorbé et l'état $|e\rangle$ est excité. Puis, après une période de temps τ , l'état se relaxe vers l'état fondamental en émettant un photon (émission spontanée). Cette période de temps (τ) est connue comme *la durée de vie* d'émission spontanée du système.

A cause de la désintégration du niveau $|e\rangle$ vers le niveau $|g\rangle$, la population N_e de

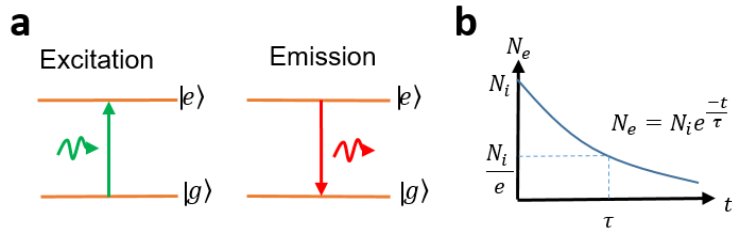


FIGURE 6.2 – Sources de photon uniques. a) Excitation et émission d'un photon dans une source de photon unique idéal. b) Taux d'extinction de la fluorescence avec N_i le nombre des atomes à $t = 0$ avec τ la durée de vie de fluorescence.

molécules excitées dans l'état $|e\rangle$ décroît exponentiellement en fonction du temps. Cette décroissance exponentielle peut être décrite comme

$$N_e(t) = N_i e^{-t/\tau}, \quad (6.1.1)$$

où N_i est la population initiale à $t = 0$. Au temps $t = \tau$, la population N_e est égale à N_i/e (la population a été réduite à 38% de la population initiale). La durée de vie est également définie en terme de taux de désintégration γ :

$$\tau = 1/\gamma. \quad (6.1.2)$$

Densité locale d'états

Dans la Fig. 6.3, nous montrons un système à deux niveaux d'énergie. Le système se trouve dans un volume V petit devant la longueur d'onde d'excitation λ (Fig. 6.3). Les états excités sont dans l'état $|e\rangle$ et ils transitent vers un état final $|g\rangle$ quand l'électron libère une énergie égale à $E = \hbar\omega_0$, où $\omega_0 = 2\pi/\lambda$.

Ce système peut être décrit par l'équation de Helmholtz [23]. La densité d'états (DOS, "Density of Optical States") montre le nombre d'états du système dans le volume V [24], et elle peut être écrite comme

$$\rho(\omega) = \frac{1}{V} \sum_n \delta(\omega - \omega_n). \quad (6.1.3)$$

La densité locale des états (LDOS, "Local Density of Optical States") $\rho_e(\mathbf{r}, \omega)$ est une sommation sur l'ensemble complet des solutions (modes électromagnétiques) de l'équation

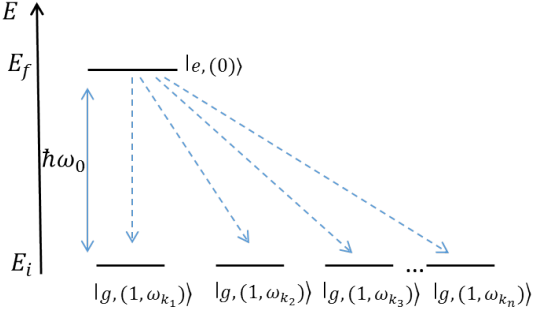


FIGURE 6.3 – Transition d'un état excité e vers un groupe d' états finaux dégénérés g avec E_i l'énergie initiale, E_f l'énergie finale et $(E_i - E_f) = \hbar\omega_0$ (Image reproduite de [23]).

de Helmholtz (e_n), chaque solution étant pondéré par son amplitude normalisée à une position spécifique \mathbf{r} dans le volume V . Pour cette raison la LDOS s'écrit comme

$$\rho_e(\mathbf{r}, \omega) = \sum_n |e_n(\mathbf{r})|^2 \delta(\omega - \omega_n). \quad (6.1.4)$$

Décroissance radiative et durée de vie

La probabilité de transition entre les états e et g est connue comme le taux de *décroissance radiative* ou encore *relaxation radiative* . Nous considérons que si le système débute dans l'état e avec un hamiltonien $\hat{\mathbf{H}}_0$. Il peut être affecté pour un hamiltonien perturbatif $\hat{\mathbf{H}}'$ et être transmis vers l'état g . Le système peut alors être décrit par un hamiltonien $\hat{\mathbf{H}} = \hat{\mathbf{H}}_0 + \hat{\mathbf{H}}'$. Cet Hamiltonien intervient dans l'équation de Schrödinger dépendante du temps :

$$i\hbar \frac{\delta |\psi(t)\rangle}{\delta t} = (\hat{\mathbf{H}}_0 + \hat{\mathbf{H}}') |\psi(t)\rangle \quad (6.1.5)$$

avec

$$|\psi(t)\rangle = \sum_e e^{-iE_e t/\hbar} a_e(t) |e\rangle \quad \text{et} \quad \hat{\mathbf{H}}_0 |e\rangle = E_e |e\rangle, \quad (6.1.6)$$

En observant l'interaction de $\hat{\mathbf{H}}'$ avec les états g et e ($\langle g | \hat{\mathbf{H}}'(t') | e \rangle$), nous obtenons le taux de relaxation spontanée :

$$\gamma = \frac{2\pi}{\hbar} |\langle g | \hat{\mathbf{H}} | e \rangle|^2 \delta(E_e - E_g). \quad (6.1.7)$$

Cette équation bien connue est appelée la règle d'or de Fermi.

Une source de photons uniques peut être modélisée par un dipôle électrique défini par un courant \mathbf{j} et un moment dipolaire \mathbf{p} . L'Hamiltonien décrivant une interaction dipolaire est $\hat{H} = -\hat{\mathbf{p}} \cdot \hat{\mathbf{E}}$ [23].

En utilisant 6.1.7 et partant de l'hypothèse que le dipôle peut exciter de solution de l'équation de Helmholtz (e_k) [23], nous pouvons réécrire l'équation 6.1.7 comme

$$\gamma = \frac{2\omega_0}{3\hbar\varepsilon_0} |\mathbf{p}|^2 \rho_p(\mathbf{r}_0, \omega_0), \quad \text{et} \quad \rho_p(\mathbf{r}_0, \omega_0) = 3 \sum_k [\mathbf{n}_p \cdot (\mathbf{e}_k \mathbf{e}_k) \cdot \mathbf{n}_p] \delta(\omega_k - \omega_0) \quad (6.1.8)$$

Avec ρ_p la densité locale d'états excités par le dipôle, n_p et p indiquent la direction du moment dipolaire.

Les équations 6.1.7 et 6.1.8 peuvent être ré-écrites en introduisant la fonction et le tenseur de Green (Appendice B), de sorte que

$$\gamma = \frac{2\omega_0}{3\hbar\varepsilon_0} |\mathbf{p}|^2 \rho_u(\mathbf{r}_0, \omega_0) \quad \text{et} \quad \rho_p(\mathbf{r}_0, \omega_0) = \frac{6\omega_0}{\pi c^2} [\mathbf{n}_p \cdot \text{Im} \{ \mathbf{G}^E(\mathbf{r}, \mathbf{r}'; \omega) \} \cdot \mathbf{n}_p] \quad (6.1.9)$$

LDOS totale et LDOS dans l'espace libre

La LDOS totale est la moyenne des LDOS partielles correspondant aux trois orientations principales du dipôle (les axes coordonnées) dans l'espace, ainsi,

$$\rho(\mathbf{r}_0, \omega_0) = \frac{2\omega_0}{\pi c^2} \text{Im} \{ \text{Tr} [\mathbf{G}^E(\mathbf{r}, \mathbf{r}'; \omega)] \} = \sum_k |e_k(\mathbf{r})|^2 \delta(\omega_k - \omega_0). \quad (6.1.10)$$

Où Tr est la trace de la fonction de Green de l'équation 6.1.9. Dans l'espace libre, la partie imaginaire de la trace est égale à $\frac{\omega_0}{6\pi c}$, en conséquence la LDOS et γ dans le vide sont donnés par :

$$\rho_0 = \frac{\omega_0^2}{3\pi^2 c^3} \quad \text{et} \quad \gamma_0 = \frac{\omega_0^3 |\mathbf{p}|^2}{3\hbar\varepsilon_0 \pi c^3}. \quad (6.1.11)$$

Facteur de Purcell et rendement quantique

En 1965 Purcell [26] a montré que le taux de relaxation radiative d'un atome varie lorsqu'il est soumis à un changement physique de son environnement proche. Une façon de mesurer ce changement est le facteur de Purcell (PF) qui est défini comme γ/γ_0 . En utilisant les équations 6.1.9 et 6.1.11, nous obtenons

$$\frac{\gamma}{\gamma_0} = \frac{\pi^3 c^3}{\omega_0^2} \rho_u(\mathbf{r}_0, \omega_0) = \frac{\rho(r, \omega_0)}{\rho_0(r, \omega_0)}. \quad (6.1.12)$$

Cette équation peut être interprétée en fonction des propriétés d'un dipôle. Le champ électrique du dipôle est $\mathbf{E}(\mathbf{r}) = \mu_0 \omega_0^2 \mathbf{G}^E(\mathbf{r}, \mathbf{r}', \omega) \mathbf{p}$, où \mathbf{p} est le moment dipolaire.

La puissance du dipôle est $P = -\frac{1}{2} \operatorname{Re} \int \mathbf{j}^*(\mathbf{r}) \cdot \mathbf{E}(\mathbf{r}) d^3(\mathbf{r})$ et son courant $\mathbf{j}(\mathbf{r}) = i\omega \mathbf{p} \delta(\mathbf{r} - \mathbf{r}_s)$, nous avons ainsi :

$$P = \frac{\mu_0 \omega_0^3}{2} |\mathbf{p}|^2 [\mathbf{n}_p \cdot \operatorname{Im} \{ \mathbf{G}^E(\mathbf{r}, \mathbf{r}'; \omega) \} \cdot \mathbf{n}_p]. \quad (6.1.13)$$

Grâce à la relation entre la fonction de Green et la LDOS, nous pouvons utiliser les équations 6.1.9 et 6.1.13 et obtenir que $\frac{P}{P_0} = \frac{\pi^3 c^3}{\omega_0^2} \rho_u(\mathbf{r}_0, \omega_0)$. En conséquence et en utilisant l'équation 6.1.9, le facteur de Purcell est donné par :

$$\frac{\gamma}{\gamma_0} = \frac{P}{P_0} = \frac{\rho(\mathbf{r}, \omega_0)}{\rho_0(\mathbf{r}, \omega_0)} = \frac{\tau_o}{\tau}. \quad (6.1.14)$$

où τ est la durée de vie.

L'équation 6.1.14 montre que le taux de relaxation radiative du système peut être amélioré en changeant les propriétés du système. Cependant, nous devons considérer que γ total prend en compte tous les canaux de désexcitation autorisés. Les canaux radiatifs représentent des photons rayonnant en champ lointain, c'est-à-dire éloignés de l'émetteur, tandis que les canaux non radiatifs correspondent au transfert d'énergie direct non radiatif entre l'émetteur et les matériaux dans son environnement. Il est important de noter que le terme d'absorption inclut ici tous les canaux de désexcitation non radiatifs et ne se limite pas aux modes électromagnétiques absorbés.

Afin de mesurer l'efficacité d'émission de photons, nous définissons le rendement

quantique comme

$$\eta = \frac{\gamma_{rad}}{\gamma_{rad} + \gamma_{abs}}. \quad (6.1.15)$$

Cette quantité prend en compte les états qui se relaxent par des processus non radiatifs (γ_{abs}) et ceux qui se relaxent par des processus radiatifs (γ_{rad}). Cette analyse peut être extrapolée au concept de LDOS comme :

$$\rho(r, \omega_0) = \rho_{abs}(\mathbf{r}, \omega_0) + \rho_{rad}(\mathbf{r}, \omega_0), \quad (6.1.16)$$

où $\rho_{rad}(\mathbf{r}, \omega_0)$ est la part de la LDOS totale qui décrit les états du rayonnement en champ lointain et $\rho_{abs}(\mathbf{r}, \omega_0)$ la part du rayonnement absorbé.

6.1.2 Nano émetteurs

Les nano émetteurs (NE) sont des matériaux nano structurés capables d'émettre des photons après une certaine excitation externe. Contrairement à une source de photon unique "idéale", un matériau fluorescent commun possèdent plusieurs états excités (Fig. 6.4).

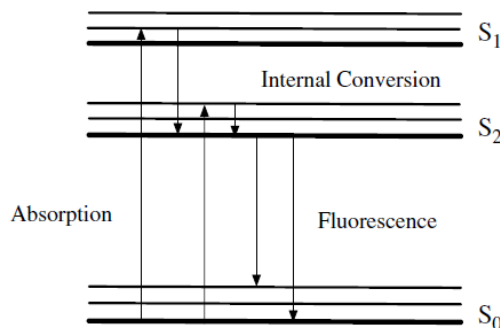


FIGURE 6.4 – Diagramme des processus de photoluminescence où nous illustrons la désintégration interne des états et le processus de fluorescence (Image prise de référence [28])

Lorsque la lumière est absorbée par le matériau, les états d'énergie les plus élevés (S_1 et S_2 dans la figure 6.4) peuvent être excités. Le processus de relaxation des états vers des états d'énergie inférieurs différents de l'état s_0 est appelé *conversion interne* et tandis que la décroissance des états excités vers l'état fondamental S_0 est définie comme *processus de fluorescence*. Le temps moyen de décroissance est τ ou durée de vie, comme nous

l'avons défini dans les sections précédentes.

De nos jours, les nano émetteurs les plus couramment utilisés sont les sources déterministes et non déterministes. La source déterministe a une forte probabilité d'émettre un seul photon pendant l'intervalle de temps τ , tandis que la source non déterministe génère des paires de photons par processus probabiliste. Quelques exemples de sources déterministes sont les boîtes quantiques [29, 30], les molécules uniques [31, 32], les atomes uniques [33, 34], les ions uniques [35, 36], et les centres colorés [37, 38]. Les sources non déterministes sont créées dans des matériaux non-linéaires comme les cristaux de KD*P (phosphate de dideutérium de potassium, KD_2PO_4), BBO (bêta bore borate, BaB_2O_4), LiNbO_3 (niobate de lithium) et LiIO_3 (iodate de lithium) [46, 48–50]. Dans cette thèse nous avons considéré des sources déterministes.

6.1.3 Exaltation de la fluorescence par des champs plasmoniques

L'exaltation de la fluorescence de surface (SEF, "surface enhanced fluorescence") est une technique basée sur la conception de surfaces micro ou nano-structurées en interaction proche avec un émetteur. [28]. Quelques exemples sont : les nanocavités [51, 52], les guides d'ondes métalliques [54–56], les cristaux photoniques [57, 58] et de sondes SNOM [59, 60]. Ces dernières années, la plasmonique est considérée comme l'un des domaines de recherche les plus prometteurs pour le SEF car elle permet un fort confinement du champ électrique aux échelles sub-longueur d'onde.

Plasmon polariton de surface

Un plasmon polariton de surface (SPP, "Surface Plasmon Polariton") est un mode d'oscillation collective des électrons libres dans un métal. Ces oscillations peuvent se propager en générant une onde surfacique à l'interface entre un métal et un milieu diélectrique. Lorsque la lumière est envoyée sur l'interface, cette oscillation de charges génère un champ électromagnétique évanescant dont l'amplitude décroît exponentiellement loin de l'interface (Fig. 6.5). La longueur de décroissance du champ dans le milieu diélectrique (δ_d) est de l'ordre de la moitié de la longueur d'onde de la lumière incidente, alors que dans le métal elle est (δ_m) est de quelques dizaines de nanomètres.

Dans la Fig. 6.6, nous montrons les résultats obtenus par Barnes et al. [63] sur le

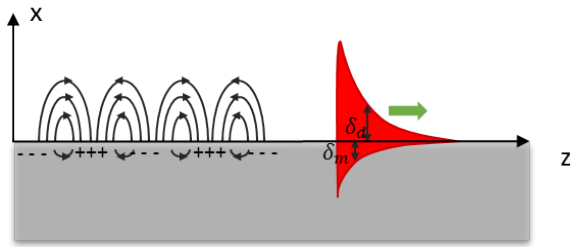


FIGURE 6.5 – Représentation schématique d'un plasmon polariton de surface avec la répartition des charges sur la surface et le profil du champ électrique en rouge.

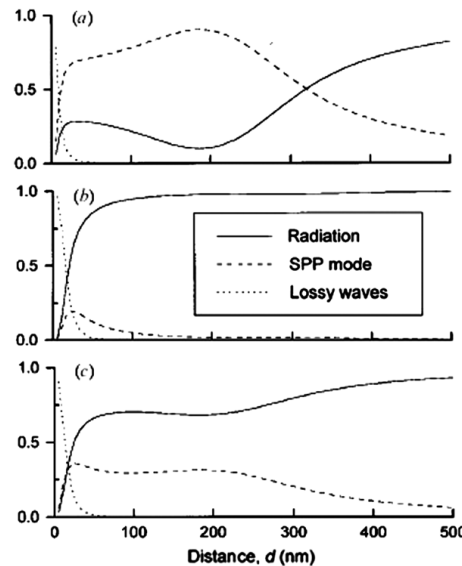


FIGURE 6.6 – Fraction normalisée de la puissance dissipée dans différents canaux de relaxation pour dipôle placé au dessus d'un miroir en argent, pour différentes distances dipôle-métal. a) dipôle orienté perpendiculairement à la surface, b) dipôle orienté parallèlement à la surface et c) pour une distribution isotrope (Figure extraite de [28]).

couplage entre un dipôle et un SPP. Les diagrammes montrent la fraction de puissance dissipée dans différents canaux de relaxation en relation avec l'orientation d'un dipôle et la distance dipôle-métal. Pour des petites distances (inférieures à 20 nm), nous observons que le dipôle est principalement couplé à des modes de surface qualifiés de modes non radiatifs (y compris le mode SPP fondamental).. En revanche, lorsque la distance augmente, l'émission radiative du dipôle se couple principalement dans des canaux radiatifs. L'énergie dissipée par le dipôle est alors perdue par rayonnement dans l'espace libre. Ces résultats montrent que jusqu'à 93% de la lumière peut être couplée au mode SPP en utilisant un dipôle qui oscille dans la direction perpendiculaire à la surface du métal. Les travaux actuels montrent de nouvelles conceptions de systèmes intégrés afin d'exciter les nano émetteurs en utilisant ces modes particuliers que sont les SPP. [65, 66], [68].

Plasmons de surface localisés

Les plasmons de surface localisés ou LSP correspondent à des oscillations collectives d'électrons de conduction qui restent confinées spatialement, par opposition avec les SPP qui se propagent le long des interfaces métalliques. On peut les observer en particulier dans les nanostructures métalliques couplées à un champ électromagnétique. Contrairement aux SPPs, le LSP peut être excité par l'illumination directe grâce au phénomène de diffraction.

Le fort confinement du champ électromagnétique généré par un mode LSP peut être exploité pour exalter de l'émission de fluorescence d'un émetteur. La Fig. 6.7 montre les résultats obtenus par Krachmalnicoff et al. sur l'exaltation de fluorescence obtenue sur des nanodisques en or. L'intensité de fluorescence et les cartographies topographiques sont mesurées avec une pointe de microscope optique de champ proche sur laquelle des Q-dots sont greffés. Les interstices générés entre les disques métalliques génèrent des champs exaltés qui augmentent très localement le taux de relaxation spontanée.

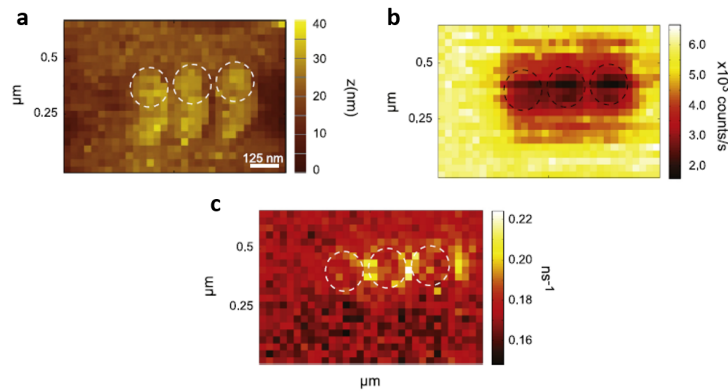


FIGURE 6.7 – Exaltation de la fluorescence et du taux de relaxation spontanée par une nanostructure métallique formée de trois nano-disques en or. a) Topographie de l'échantillon. b) Carte d'intensité de fluorescence. c) Carte des taux de relaxation. Le contour des nanodisques en or est représenté par une ligne en pointillés blancs. (Image prise de [76]).

6.1.4 Rappels d'optique guidée

Un guide d'onde peut être représenté par un système constitué de trois matériaux avec comme indice de réfraction respectifs n_1 , n_2 , et n_3 , où $n_2 > n_1, n_3$. Le matériau d'indice n_2 est le cœur du guide d'onde, tandis que les matériaux d'indices n_1 et n_3 constituent la

gaine du guide. Quand une onde plane entre dans le cur avec un angle inférieur à l'angle de réflexion totale interne, la lumière est réfléchie par le gaine et se propage le long du cur du guide.

Pour chaque réflexion, l'onde a un changement de phase de π rad. Lorsque l'onde est refléchie deux fois, le changement global de phase est égal à 2π et l'onde se reproduit identiquement à elle-même. Les champs avec ces propriétés sont appelés *modes guidés*.

Couplage entre modes

Dans un système formé par deux ou plusieurs guides d'ondes placés à proximité, il est possible d'observer un transfert d'énergie entre les guides à cause de la présence de modes hybrides. Dans l'approximation des faibles perturbations, les modes hybrides sont décrits comme une combinaison linéaire des modes des deux guides isolés.

Dans la figure 6.8 nous pouvons observer qu'un mode du guide 1 transfère son énergie vers un mode du guide 2. Lors de la propagation, les modes hybrides doivent avoir des distributions de phase de parités différentes (mode pair ou impair) pour permettre un bon transfert de l'énergie. Le transfert d'énergie se fait après une distance de propagation L_c qui est connue comme *distance de couplage*. Pour un système simple constitué de deux guides identiques et parallèles, la distance de couplage est $L_c = \frac{\pi}{\beta_e - \beta_o}$, où β_o β_e sont les constantes de propagation respectives des mode impair ("odd") et pair ("even").

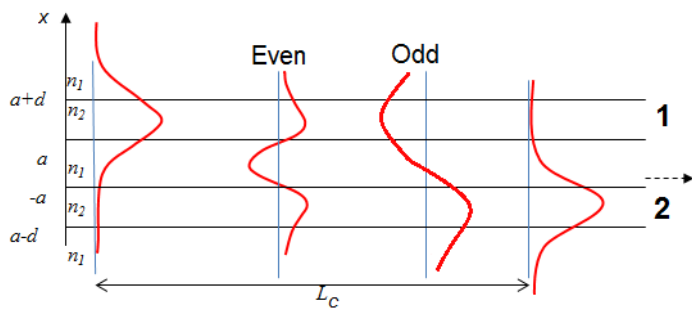


FIGURE 6.8 – Couplage et transfert d'énergie entre les modes de deux guides placés à proximité l'un de l'autre. Image reproduite à partir de la référence [85]

Le principe de couplage de modes peut être utilisé pour exciter les modes plasmoniques. Dans la figure 6.9 nous montrons le schéma d'un guide d'onde photonique-plasmonique formé par un guide d'onde diélectrique et une couche mince métallique. Ici, nous obser-

vons qu'en raison d'un couplage, il est possible d'exciter les modes plasmoniques grâce à un mode photonique.

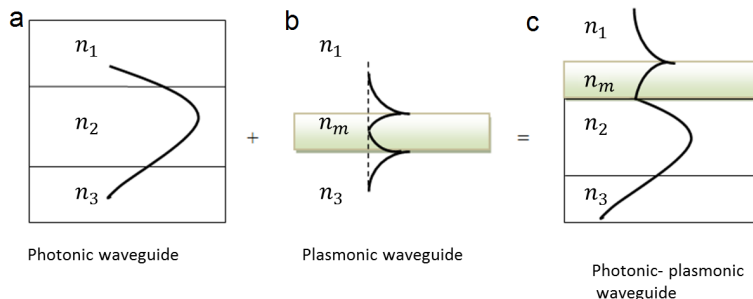


FIGURE 6.9 – a) Propagation d'un mode dans un guide d'onde diélectrique, b) mode plasmonique dans un film métallique mince, et c) mode hybride photonique-plasmonique dans un multicouches métallo-diélectrique.

6.2 Conception d'une structure hybride photonique-plasmonique vers l'intégration de sources de photons uniques sur guide d'onde

Dans cette thèse, nous avons travaillé sur le développement d'une structure hybride formée par un guide à échange d'ions (IEW, Ions Exchanged Waveguide) et une couche de TiO_2 qui présente l'intérêt d'avoir un indice de réfraction assez élevé. Le guide IEW est monomode dans un spectre de longueurs d'onde allant 400 nm à 800 nm et son cœur est caractérisé par un profil en gradient d'indice de réfraction. Ce profil s'explique par le procédé d'implantation des ions dans le cœur du guide, qui est basé sur une diffusion thermique d'ions argent. Les ions argent viennent se substituer aux ions Sodium présents dans la matrice vitreuse. L'indice de réfraction le plus élevé dans le guide IEW est de 1.57 et l'indice de réfraction du verre est considéré à un indice de réfraction proche de 1.5. La couche TiO_2 utilisée a un indice de réfraction proche de 2 pour des longueurs d'onde comprises entre 550 nm et 700 nm.

Nous sommes intéressés particulièrement sur deux longueurs d'onde : $\lambda = 542$ nm comme longueur d'onde et excitation et $\lambda = 640$ nm comme longueur d'onde d'émission d'un nanoémetteur intégré à la surface de la structure.

6.2.1 Exaltation du champ sur la surface

En raison de la proximité entre le guide IEW et la couche TiO_2 , l'onde évanescante du mode guidé est susceptible d'exciter les modes de la couche de TiO_2 qui constitue un bon guide d'onde de part son haut indice de réfraction. Cette interaction donne lieu à des modes hybrides permettant un transfert d'énergie périodique entre le guide IEW et le guide constitué par la couche de TiO_2 . Ce battement d'énergie est caractérisé par une longueur de couplage L_c [93, 94].

Nous définissons le facteur d'exaltation du champ par le rapport $EF = E_0/E$, où E_0 est le champ électromagnétique mesuré à la surface du guide IEW et E le champ électromagnétique mesuré au point d'intensité maximale sur la couche TiO_2 .

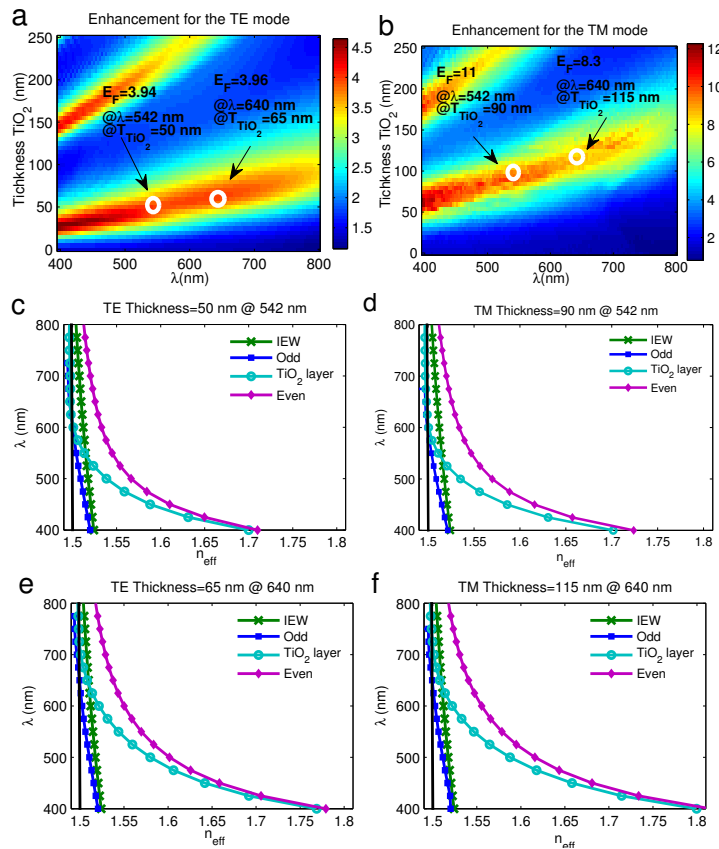


FIGURE 6.10 – Facteur d'exaltation du champ électrique et relations de dispersion des modes guidés. EF calculé en fonction de la longueur d'onde et l'épaisseur de la couche de TiO_2 pour les polarisations a) TE et b) TM. Les cercles blancs correspondants à EF maximale à $\lambda = 542 \text{ nm}$ et $\lambda = 640 \text{ nm}$.

Les figures 6.10 a et b montrent les valeurs de EF en fonction de l'épaisseur de la couche de TiO_2 et de la longueur d'onde λ pour les polarisations TE et TM. Ces résultats

ont été obtenus par la méthode des différences finies en régime temporelle (FDTD, "Finite Differences in the Time Domain"). Nous obtenons un facteur d'exaltation maximal de $EF=3.9$ pour une couche de 50 nm à 542 nm et $EF = 4$ à 640 nm pour un épaisseur de 65 nm pour le mode TE. Pour un mode TM les pics de EF sont 11 et 8.3 pour un épaisseur de 90 nm et 115 nm à 542 nm et 640 nm respectivement. Dans la gamme spectrale allant de 400 nm à 700 nm, nous observons également la propagation de modes d'ordres supérieurs pour des épaisseurs importants.

Dans les figures 6.10 c, d, e et f nous montrons les relations de dispersion $n_{eff}(\lambda)$ des différents modes guidés pour les quatre épaisseurs de TiO_2 pointées dans les figures 6.10 a et b. Ces courbes nous aident à confirmer que le facteur d'exaltation optimal est obtenu lorsque le désaccord de phase entre les modes hybrides est minimisé. C'est à dire lorsque qu'il y a un croisement entre les branches des modes du guide TiO_2 (cercles cyan) et du guide IEW(x's verts). L'hybridation des modes couplés en champ proche par la proximité des deux guides donne naissance à un anti-croisement caractéristique observable entre les courbes de dispersion des modes hybrides pair et impair.

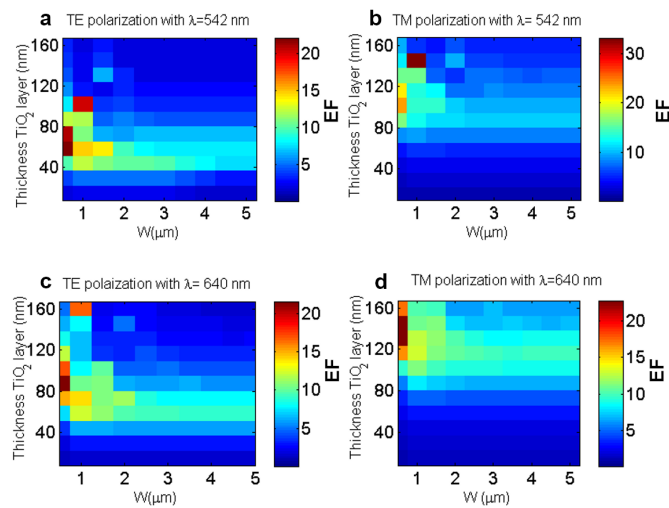


FIGURE 6.11 – Facteur d'exaltation du champ électrique. Calcul de EF en fonction de la longueur d'onde et de la largeur (W) de la couche de TiO_2 pour les modes a) TE et b) TM à $\lambda = 542$ nm et d) TE et d) TM à $\lambda = 640$ nm.

Un autre paramètre important à considérer est la largeur de la couche de TiO_2 . La Fig. 6.11 montre les valeurs de EF en fonction de l'épaisseur et de largeur (W) de la couche pour une longueur d'onde de 542 nm, en polarisation TE et TM (respectivement

figures a et b) et une longueur d'onde de 640 nm (respectivement figures c et d). Nous observons que EF augmente lorsque W décroît. Cette amélioration s'explique simplement par l'augmentation du confinement latéral du mode fondamental TE ou TM. Le champ se confine dans un volume modal plus petit, et en conséquence l'amplitude du champ augment en surface.

6.2.2 Théorème de réciprocité de l'électromagnétisme

Pour modéliser le couplage de la lumière rayonnée par un nano-émetteur (NE) dans les modes de la structure hybride, nous utilisons le théorème de réciprocité de l'électromagnétisme [88]. Le NE est modélisé comme un dipôle localisé en r_0 près de la surface de la couche de TiO₂(Fig. 2.11a).

D'après le théorème de réciprocité, deux champs électriques E et \bar{E} générés par les densités de courant J et \bar{J} , séparés par un milieu de volume V sont liés par l'équation :

$$\frac{\partial}{\partial z} \int_{A_\infty} E \times \bar{H}^* + \bar{E}^* \times H \cdot \hat{z} dA = \int_{A_\infty} \nabla \cdot [E \times \bar{H}^* + \bar{E}^* \times H] dA, \quad (6.2.17)$$

où A est une section transversale.

En utilisant cette équation pour un dipôle, nous trouvons que la puissance P_c collectée en sortie du guide IEW et la puissance P_0 du dipôle sont liés par une relation définie par [89] :

$$\frac{P_c}{P_0} = \sum_j \frac{|p \cdot E_j(r_0, \omega_0)|^2}{16P_0}, \quad (6.2.18)$$

où E_j est le champ électrique des modes de IEW.

Nous avons modelisée en FDTD l'interaction d'un dipôle placé à 25 nm de la surface de la couche de TiO₂ et la structure hybride (Fig. 6.12a). La position du dipôle est balayée dans le plan yz . Les figures 6.12b et 6.12c montrent la lumière collectée dans le guide IEW comme indiqué dans la figure 6.12a pour les directions d'oscillation du dipôle correspondant aux polarisations TE et TM.

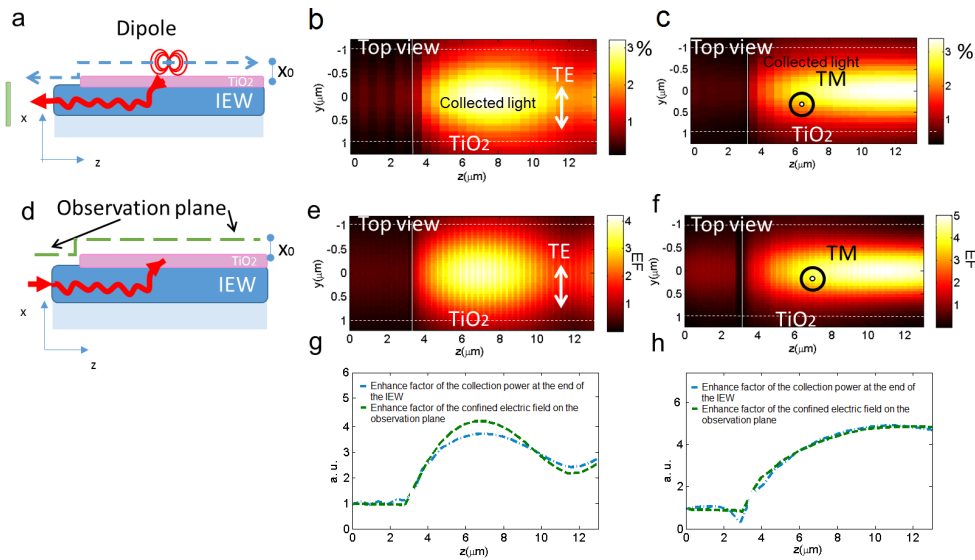


FIGURE 6.12 – Réciprocité du phénomène de couplage entre un dipôle et les modes guidés de la structure hybride. a) Position du dipôle par rapport à la structure. b), c) simulations FDTD de l'intensité du champ rayonné par le dipôle et collecté dans le guide IEW en fonction de la position du dipôle et pour une oscillation de dipôle selon x (polarisation TE) et selon y (polarisation TM), respectivement. d) propagation du mode fondamental du guide IEW et positionnement du plan d'observation. e) et f) simulations FDTD de la distribution spatiale de l'intensité du champ guidé dans le plan d'observation défini en d) lorsque la source est le mode fondamental du guide IEW, pour une polarisation TE et TM respectivement. g) et h) profils horizontaux centrés de la distribution d'intensité tracée en b, c, e et f. Les plans d'observation et plans de balayage du dipôle sont confondus

Dans un deuxième temps, nous avons simulé la propagation du mode fondamental du guide IEW à 640 nm à travers la structure hybride. Nous observons la distribution d'intensité dans un plan placé à 25 nm de la surface de la couche de TiO₂ (le même plan que celui utilisé précédemment lors du balayage du dipôle) dans les deux états de polarisation (figures 6.12e et 6.12f). Les figures g et h montrent la distribution du champ pris le long d'un profil horizontal et centré dans les graphes 6.12b et 6.12c (figure 6.12g) et dans les graphes 6.12c et 6.12f (figure 6.12h), respectivement. La similitude des résultats montre que les deux situations considérées (figure 6.12a et 6.12d) sont réciproques.

6.2.3 Coupleur adiabatique de modes plasmoniques (Nano-Taper)

Le coupleur plasmonique (ou nano-taper) est un nanoprisme isocèle en or placé sur la couche TiO₂ (Fig. 6.13a). Une couche mince intermédiaire de SiO₂ est intercalée entre ces deux objets. Les sommets du triangle en or ont un rayon de courbure $R = 25$ nm, une base $B_{Taper} = 250$ nm, une longueur $L_{Taper} = 1 \mu\text{m}$ et une épaisseur de 50 nm (Fig. 6.13

b). La couche de TiO_2 a une largeur de 500 nm et une épaisseur de 150 nm, tandis que la couche SiO_2 a une largeur de 500 nm et un épaisseur de 30 nm (Fig. 6.13c). La base du triangle est placée à 7 μm du début de la couche TiO_2 . Cette distance correspond à la longueur de couplage L_C des modes hybrides TM_0 pour la structure formée par la couche TiO_2 et le guide IEW. La distance entre l'extrémité droite du guide IEW et de la couche TiO_2 est de 5 μm .

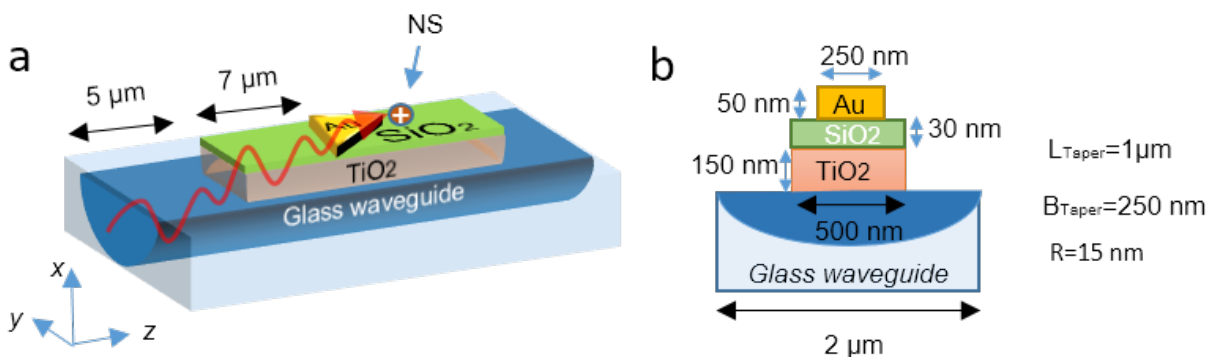


FIGURE 6.13 – Schéma du coupleur photonique-plasmonique.a) Vue en perspective. La structure est formée par un guide IEW, une couche mince de TiO_2 et un espaceur de SiO_2 , et un nano-prisme en or. On peut voir le chemin optique de la lumière à travers la structure hybride (ligne rouge). b) Vue de dessus du nano-prisme et c) vue transversale de la structure.

Le rôle joué par le nano-taper plasmonique est de coupler efficacement la lumière rayonnée par le NE dans les modes du guide IEW. Le NE est placé au point r_0 (Fig. 6.13a). Le dipôle est à 25 nm de la surface de la couche de SiO_2 (à mi-hauteur de la couche d'or) et placé à 10 nm du sommet du prisme dans la direction z .

Ces résultats montrent que les composantes du champ électrique sont fortement confinées près de l'apex du nanotaper grâce au couplage entre modes photonique et plasmonique. Nous voyons que le champ est fortement confiné dans la composante du champ E_z . L'intensité globale du champ électrique $|E|^2$ (figure a) montre que la concentration maximale du champ se trouve à proximité du sommet du prisme et au centre de la couche d'or. L'effet de nanofocalisation est utilisé dans la section suivante afin de collecter la lumière émise par un dipôle et d'exciter son émission spontanée.

Dans la figure 4.9 nous avons simulé la variation du facteur d'exaltation EF en fonction de la longueur d'onde. le facteur d'exaltation est mesuré en un point distant de 10 nm du sommet du prisme et distant de 25 nm de la couche de SiO_2 . On obtient un bon facteur

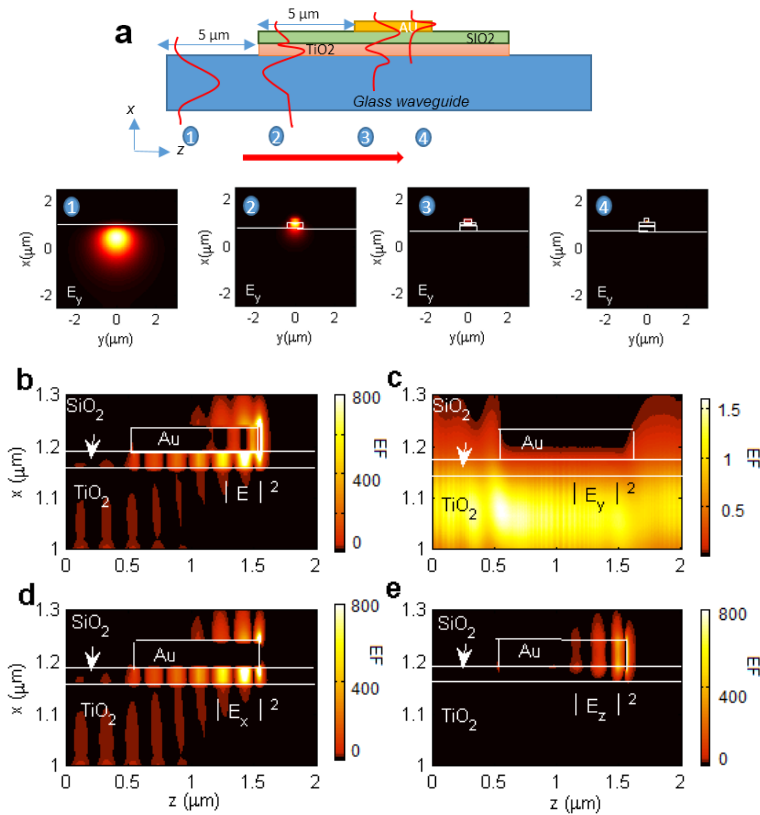


FIGURE 6.14 – Simulation FDTD de la propagation d'un mode se propageant à travers la structure hybride plasmonique-photonique depuis le guide IEW vers l'apex du nano-taper. a) cartographies transverses montrant l'évolution champ guidé b) Intensité du champ électrique. c),d),e) composantes E_x , E_y et E_z respectivement.

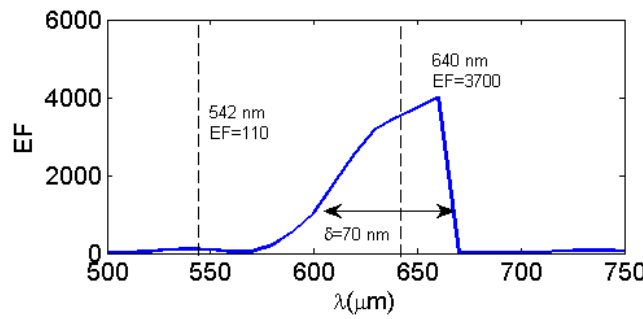


FIGURE 6.15 – Facteur d'exaltation EF du champ électrique à 10 nm à du sommet de nanotaper dans la direction z et à 25 nm de la couche TiO_2 dans la direction x . L'exaltation est normalisée par le champ électrique à 25 nm de la surface du IEW.

d'exaltation sur un intervalle de longueurs d'onde $\delta = 70$ nm assez important (de 590 nm à 660 nm). Pour $\lambda = 542$ nm le facteur d'exaltation est de 110. Tandis pour $\lambda=640$

nm nous obtenons $EF = 3700$.

6.2.4 Nano émetteur intégré sur une structure hybride plasmonique-photonique

Toujours en utilisant la méthode FDTD, nous avons simulé le couplage entre la lumière émise par un dipôle à 640 nm et les modes du guide IEW. Nous avons calculé la puissance totale dissipée par le dipôle (LDOS TOTAL), la puissance absorbée par la structure (LDOS abs ou ρ_{abs}), la puissance rayonnée (LDOS rayonnée ou $\rho_{rad} = \text{LDOS total} - \text{LDOS abs}$). Nous avons également calculé la puissance collectée dans le guide IEW qui se divise en deux parties : une partie couplée vers l'arrière, c'est à dire vers la base du prisme (LDOS backward ou $\rho_{backward}$) et une partie collectée vers l'avant du guide IEW, c'est à dire vers le sommet du prisme (LDOS forward ou $\rho_{forward}$). Le calcul a été fait pour différentes longueurs du prisme L_{Taper} (de 50 nm à 1500 nm) et pour les 3 orientations principales du dipôle (x , y et z). Les résultats de la simulation sont présentés dans la Fig. 6.16 b, d et f.

Dans la Fig. 6.16 nous observons que les grandeurs oscillent en fonction de la longueur L_{Taper} . Ces oscillations sont liées au transfert d'énergie entre les modes hybrides qui sont assujettis au phénomène de dispersion chromatique. De plus, la structure fonctionne comme un cavité résonante longitudinale. Pour une oscillation de dipôle dans la direction z nous avons obtenu une LDOS de deux ordres de grandeur plus élevée que pour les dipôles oscillants dans les directions x et y . Ce comportement peut être expliqué en observant la figure 6.14, où nous avons montré que la lumière est confinée dans l'apex de préférence pour le composante E_z . En conséquence, en utilisant la réciprocité du système, on attend un meilleur couplage pour une oscillation de dipôle dans la direction z .

Les figures 6.16c, e et g indiquent le pourcentage de puissance collectée dans le guide (efficacité de collection). Cette efficacité a été définie en utilisant $\eta_{backward} = \rho_{backward}/(\rho_{abs} + \rho_{rad})$ et $\eta_{forward} = \rho_{forward}/(\rho_{abs} + \rho_{rad})$. Nous observons que l'efficacité de collection maximale est de 28%, 38% et 3% pour les modes collectés vers l'arrière et 0.01 %, 5 % et 6 % pour les modes collectés vers l'avant, respectivement dans les directions x , y et z . La LDOS totale quant à elle atteint les valeurs de 5.1, 0.7 et 158,

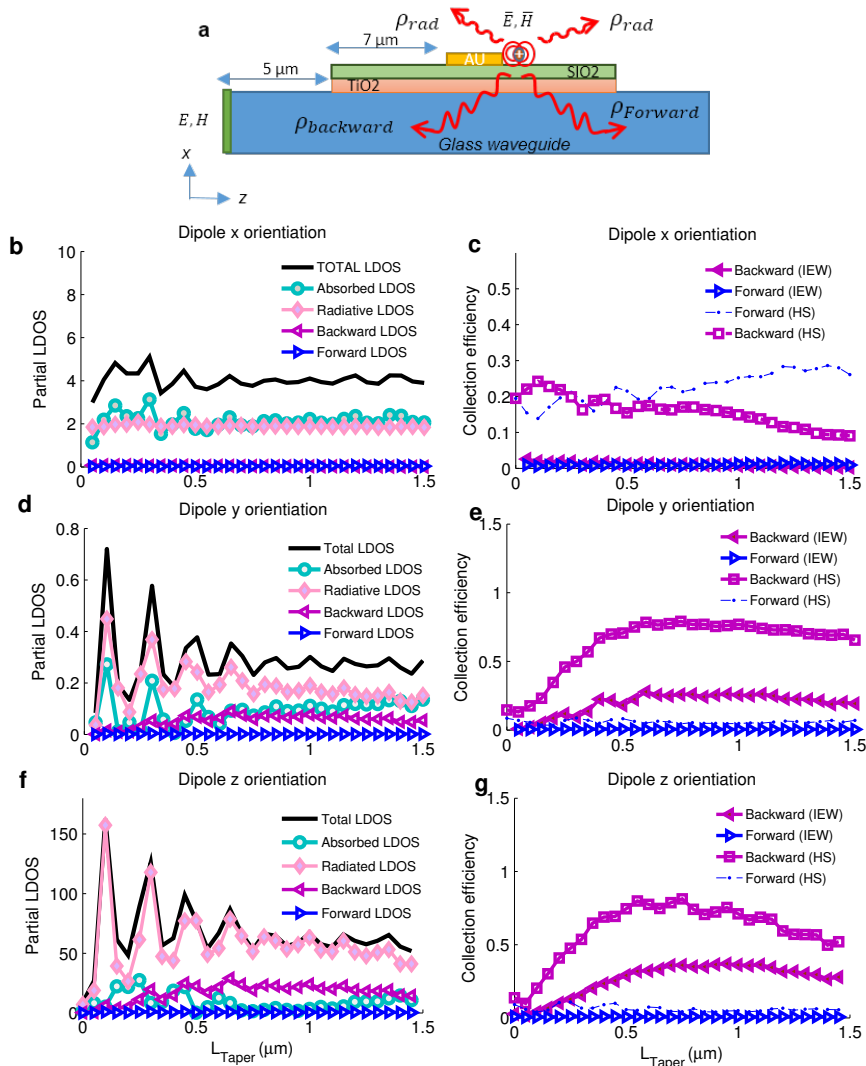


FIGURE 6.16 – LDOS et efficacité de collection pour un dipôle en interaction avec les modes guidés d'une structure hybride photonique-plasmonique . a) Position du dipôle par rapport à la structure. b), d), f), LDOS totale, LDOS absorbée , LDOS radiative, et LDOS collecté vers l'arrière (LDOS backward) et vers l'avant (LDOS forward) en fonction de la longueur du taper plasmonique (L_{Taper}). c), e), f) Efficacités de collection pour le trois directions principales d'oscillation du dipôle (x, y et z).

pour un dipôle qui oscille respectivement dans les directions x, y et z .

La puissance collectée dans la couche la couche de TiO_2 juste avant le couplage dans le guide IEW a été également calculée.

On obtient alors une efficacité maximale de collections de 30 %, 75 % et 82 % vers l'arrière et 3 %, 8 % et 8 % vers l'avant pour un dipôle oscillant dans la direction x, y ad z .

Ceci montre que des pertes apparaissent principalement au niveau de la transition

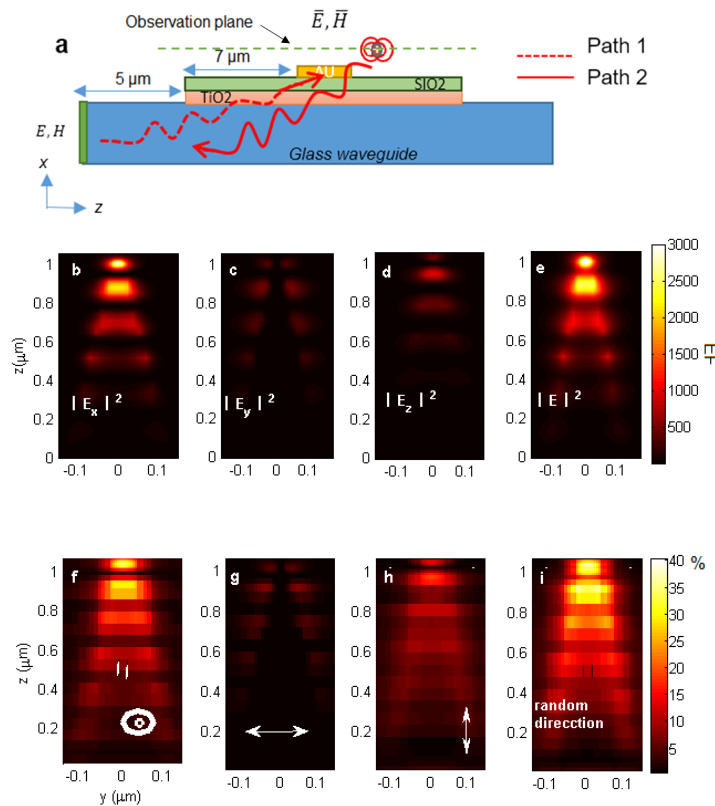


FIGURE 6.17 – Interaction réciproque entre les modes guidés et un dipôle intégré dans la structure hybride photonique/plasmonique. a) Plan d'observation et position du dipôle en interaction avec la structure hybride. Le trajet 1 (path 1) représente l'excitation du nano-taper par le mode fondamental du guide IEW. Le trajet 2 (path 2) représente le couplage entre la radiation émise par le dipôle et les modes de propagation du IEW. b) c) d) et e) Simulations FDTD de l'intensité du champ électrique obtenue selon le trajet 1 dans plan d'observation placé 25nm de la nanostructure d'or dans la direction x(a). f), g), h), i) Intensité collectée dans le guide vers l'arrière selon le trajet 1, pour différentes directions d'oscillation du dipôle. Ces cartographies représentent une LDOS partielle (LDOS backward) couplée dans le guide IEW.

abrupte entre la couche de TiO₂ et le guide IEW.

En effet une analyse plus fine de la puissance rétrocoupée sur les modes hybrides de la structure TiO₂/IEW montre que c'est le mode pair qui est principalement excité, le mode impair étant faiblement excité. Ceci montre que l'insertion du taper métallique dans la structure hybride modifie ainsi le bon fonctionnement du coupleur directionnel (figure 6.12) et augmente ainsi les pertes de couplage au niveau de la transition guide IEW et structure hybride TiO₂/IEW.

Les résultats montrés dans la figure 6.16 montrent que l'efficacité de collection augmente et que les oscillations dans la LDOS totale diminuent lorsque L_{Taper} augmente.

Pour des longueurs plus courtes, le nano-taper se comporte comme une nano-antenne

qui excite principalement les modes radiatifs du système (les pertes par rayonnement sont alors plus élevées). Lorsque la longueur augmente, le nano-taper guide mieux la lumière et devient un coupleur de mode efficace, la lumière rayonnée par le dipôle est alors principalement couplée vers les modes du guide IEW.

La figure 6.17 montre les résultats de coulage pour deux scénarios réciproques. Dans le premier scénario ou trajet 1 (path 1), un mode fondamental du guide IEW est injecté. On simule alors par FDTD les distributions d'intensité du champ électrique (figures b, c, d, e) dans un plan d'observation situé à 25 nm au-dessus de la surface du prisme métallique. Pour le second scénario ou trajet 2 (path 2), nous avons balayé la position du dipôle sur le même plan d'observation et nous mesurons la puissance collectée vers l'arrière dans le guide IEW. Le calcul est répété pour les directions principales d'oscillation du dipôle, selon x , y et z (figures f, g, et h, respectivement). Nous voyons que les distributions d'intensité pour les deux scénarios sont proportionnelles ce qui indique une bonne réciprocité du système.

D'après ces résultats, un dipôle oscillant dans la direction x a le meilleur couplage. En effet, au niveau du plan d'observation choisi, la composante E_x du champ électrique est plus forte que les autres comme le montre la figure 6.14. La figure j représente la moyenne des figures e) f) et g) pour représenter la lumière couplée d'un dipôle oscillant dans une direction aléatoire.

6.3 Mesure de la LDOM

Nous présentons une nouvelle configuration de SNOM qui permet d'obtenir des images de la lumière collectée à partir du IEW lorsque la structure est excitée par une source ponctuelle placée à proximité de la surface de l'échantillon. Lorsque la lumière rayonnée par la source ponctuelle est couplée dans les modes du IEW, ils peuvent être détectées à la fin d'une fibre optique collectée en sortie du IEW.

Afin d'imiter une source ponctuelle, nous utilisons une configuration de SNOM que nous appelons mode d'illumination ou *i-SNOM*. La Fig. 6.18 montre le schéma de cette configuration (chemin vert), où nous envoyons la lumière d'une fibre optique PM connectée au système optique. Puis une partie de la lumière arrive à la caméra et l'autre éclairent

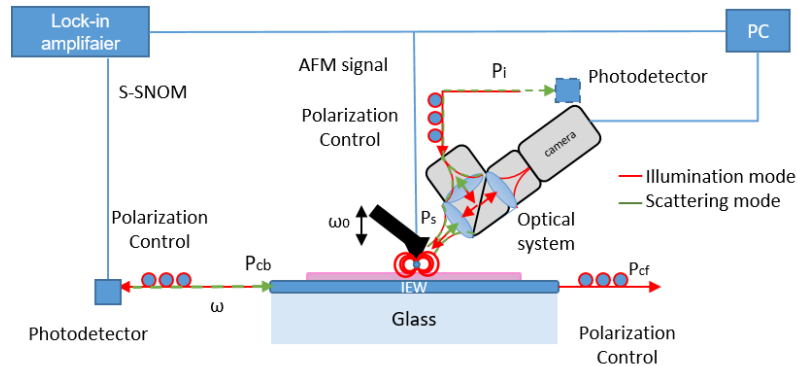


FIGURE 6.18 – Schéma du SNOM en configuration illumination (chemin rouge) et en mode diffusion(chemin vert).

l’apex de la pointe AFM, générant un point diffusant sub-longueur d’onde dont le champ électrique oscille dans la même direction que la polarisation de la lumière incidente. Lorsque la pointe approche la surface, la lumière rayonnée de la pointe se couple aux modes du guide IEW. La puissance est collectée par une fibre optique connectée au guide IEW. Finalement, la puissance couplée est mesurée par un photodétecteur. Le point intéressant de cette technique est que cette excitation est le cas réciproque du s-SNOM comme nous pouvons observer dans la figure 6.18 (le chemin rouge). Le chemin vert représente la configuration de diffusion ou scattering (s-SNOM), où la pointe du AFM perturbe le champ confiné sur la surface de l’échantillon lorsqu’elle est excitée via le guide IEW. Dans cette configuration la lumière est collectés par un microscope optique confocal relié à une fibre optique.

Dans cette configuration le signal détecté par le photodétecteur a une figure d’interférence caractérisée par un déphasage :

$$\Delta\phi = k_0(n_{eff} - \cos\alpha)z, \quad (6.3.19)$$

où α est l’angle d’inclinaison du détecteur lequel nous avons considéré petit (proche à zéro degrés). Donc le déphasage mesuré dans la figure d’interférence est $k_0(n_{eff} - 1)z$ (Fig. 6.19c). Nous avons reproduit la polarisation TE avec une lumière incidente sur un angle $\Omega=90^\circ$ et TM à $\Omega=0^\circ$ (figure 6.19d)

La Fig. 6.20 montre les images obtenues en configuration s-SNOM dans la zone de l’échantillon (figure a) en comparaison avec les images obtenues en configuration i-

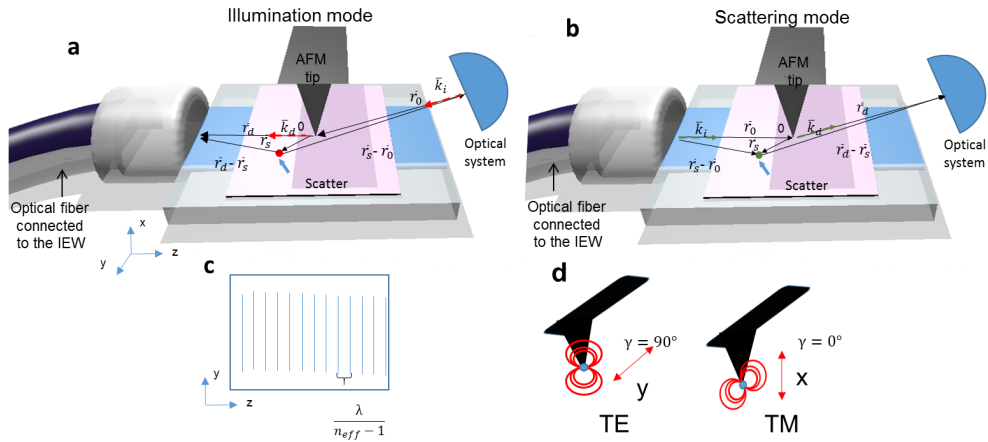


FIGURE 6.19 – Schéma de la détection pour a) la configuration i-SNOM et b) la configuration s-SNOM. Lorsqu'une fibre optique est collée à l'extrême gauche du guide IEW. c) motif d'interférence dans le signal détecté par le photodétecteur. b) Les dipôles TE et TM induits par la l'excitation lumineuse incidente avec une polarisation linéaire d'angle $\Omega = 90^\circ$ et $\Omega = 0^\circ$, respectivement.

SNOM. Les lignes blanches représentent l'interface entre la couche de TiO_2 et l'IEW sans TiO_2 alors que les lignes pointillées montrent les bords de l'IEW. Les figures 6.20 b et c sont les images s-SNOM pour la propagation des modes TE et TM de gauche à droite. Ici nous observons des lignes verticales générées par l'interférence entre la lumière diffusée à partir des dispersions et des modes du guide IEW. Dans ces images, nous observons également la période de battement caractéristique correspondant aux modes hybrides TE et TM. Les figures 6.20 d et e sont les cartographies de la transformée de Fourier des images b et c. Nous observons que la période principale se trouve dans les axes horizontaux en raison de la configuration utilisée pour cette expérience. Nous obtenons des indices effectifs de $n_{eff1} = 1.48$ et $n_{eff2} = 1.56$ correspondant respectivement au mode hybride impair et pair. Alors que pour la polarisation TM, ces indices sont $n_{eff1} = 1.48$ et $n_{eff2} = 1.53$. Les figures 6.20 f et g montrent les résultats de la lumière collectée par la fibre optique à l'extrême gauche de l'IEW obtenus avec la configuration i-SNOM. Comme cela a été mentionné, cette lumière collectée est due à la densité locale des modes (LDOM) excités par une source locale. De cette façon, les cartographies représentées sur la Fig. 6.20 f et g représentent la mesure de LDOM sortie par la pointe AFM pour chaque position de pointe sur l'échantillon. A partir des transformées de Fourier des images f et g (figure 6.20 h et i, respectivement), nous obtenons que pour la polarisation TE $n_{eff1} = 1.46$ et $n_{eff2} = 1.56$ et pour la polarisation TM $n_{eff1} = 1.47$ et $n_{eff2} = 1.54$.

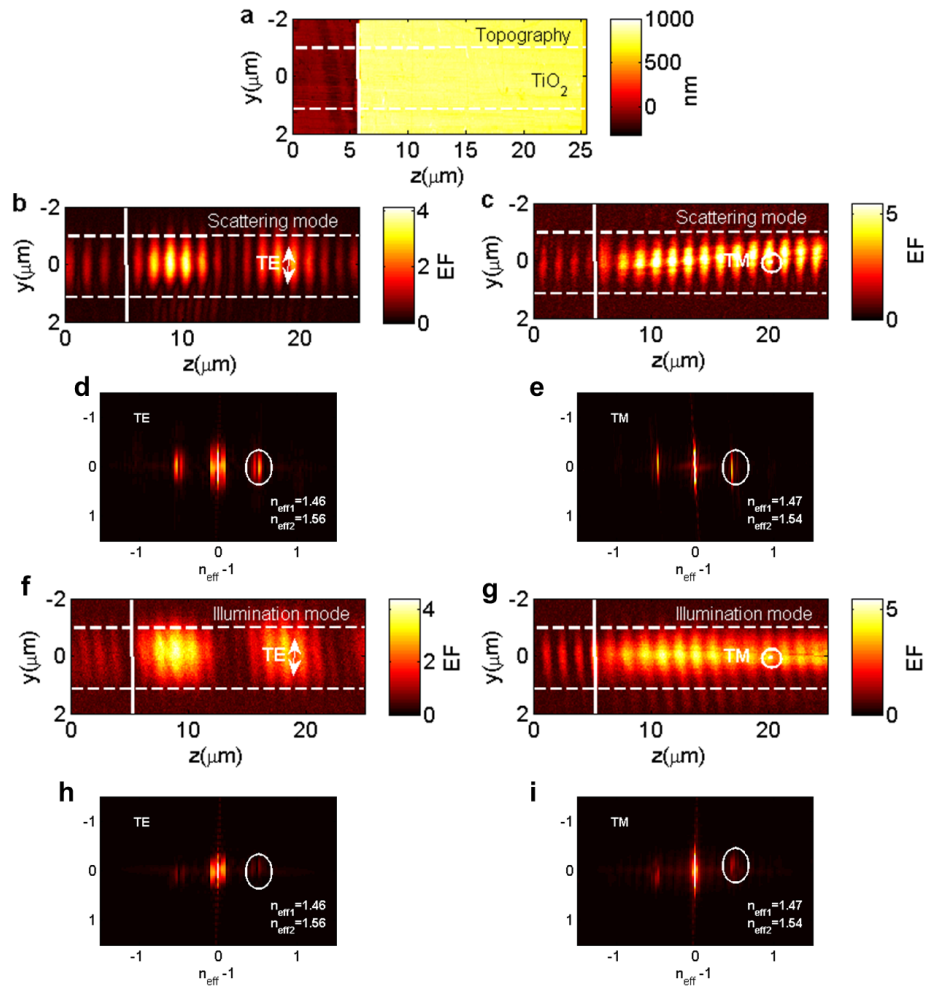


FIGURE 6.20 – a) Image de topographie. Images d'amplitude pour la configuration s-SNOM pour la propagation de l'émission lumineuse de gauche à droite en polarisation b) TE et c) TM pour la région représentée en a). d) Transformée de Fourier de la figure b) et e) pour la figure c). Images d'amplitude en configuration i-SNOM lorsque la lumière est collectée à l'extrémité gauche de l'IEW pour les polarisations f) TE et g) TM pour la région représentée en a). h) Transformée de Fourier de la figure f) et i) pour la figure g). La ligne blanche représente les bords de la couche de TiO_2 et la ligne pointillée représente le bord du IEW. Le cercles blancs correspondent à l'indice effectif des modes hybrides.

Grâce à un filtre du motif d'interférence des images montrés dans la Fig. 6.20 a, b, e et f, nous obtenons les figures 6.21 a, b, c et d, respectivement. L'un des résultats les plus intéressants de la comparaison entre les distributions d'énergie obtenus depuis les configuration s-SNOM et i-SNOM (figure a et c, et b et d). Ces résultats montrent un comportement réciproque lequel est la confirmation expérimentale du théorème de réciprocité de l'électromagnétisme.

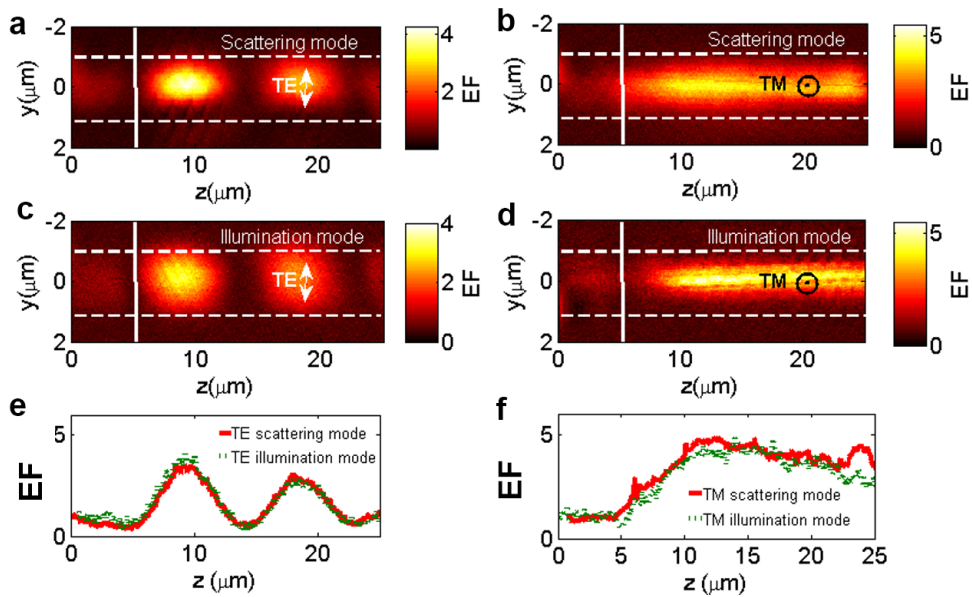


FIGURE 6.21 – I-SNOM après de filtre le motif d’interférence représenté sur la figure 6.20 pour les images s-SNOM pour polarisation a) TE et b) pour polarisation TM. I-SNOM images pour c) TE et d) TM polarisation. E) comparaison des profils centraux des images a et c, et f) comparaison des profils centraux des images d et d.

6.4 Guides hybrides en verre pour l'amélioration de la photoluminescence de nano-émetteurs dans du spectre visible

Nous avons placé sur la surface de l'échantillon une solution de nanocristaux (NC) de cadmium séléniate/sulfure de cadmium (CdSe / CdS) et nous avons mesuré leur photoluminescence (PL) et leur durée de vie. La concentration de nanocristaux est de 10^{-6} mol/L et elle a été mélangée dans une solution de Poly (méthacrylate de méthyle) (PMMA) et répartie aléatoirement sur la surface de la structure (Fig. 6.22). Dans la Fig. 6.22b, nous observons les images de ces cristaux sur la surface de l'échantillon à partir d'une vue de dessus prise avec une caméra CCD.

La PL des NC a été excitée avec un laser de 532 nm à l'entrée du IEW. Nous avons utilisé un système confocal fabriqué réalisé au laboratoire avec un objectif de microscope de 80X couplé à un spectromètre (Princeton Instruments), attaché à une caméra CDD refroidie à -75 °C. La caméra CCD nous a permis d'imager la surface et de mesurer le spectre des NC à partir d'un seul point de l'image. Ce système de PL est suffisamment

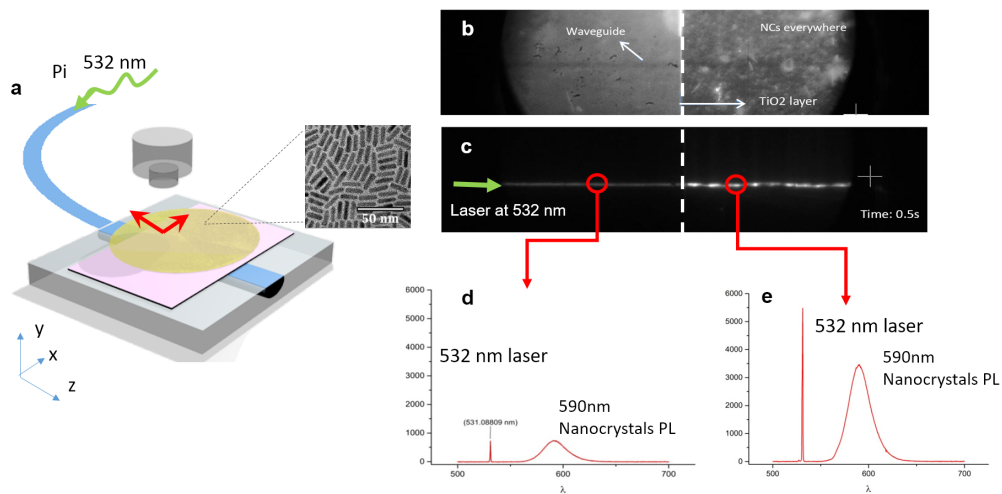


FIGURE 6.22 – a) Schéma simplifié de l'installation utilisée pour les mesures de PL pour une structure hybride constituée d'une couche TiO₂ placée au-dessus d'un IEW et d'une solution de NC sur sa surface. L'encart est une représentation schématique des NC CdSe / CdS. b) Image d'une caméra CCD de l'échantillon après le dépôt de NC. c) Observation en champ lointain de l'émission lumineuse des NC placés au-dessus de la structure pour a) TE et b) TM polarisations lors de l'excitation de la structure de l'extrême gauche de l'IEW à 542 nm. Le spectre d'émission des NC placé sur la position marquée par les cercles rouges sur d) le haut de l'IEW et e) sur le dessus de la couche TiO₂ sur l'IEW.

sensible pour effectuer des mesures de la durée de temps de vie. Cette expérience a été réalisée en collaboration avec le Dr. Wei Geng et les détails de cette technique peuvent être trouvés dans sa thèse de doctorat [92].

La figure 6.22c montre l'image de PL des NC. Nous observons que la PL de NC sur le dessus de l'IEW ont une plus faible intensité de PL NC que celle mesurée sur la couche de TiO₂. Dans ces images, nous voyons également un motif d'intensité qui correspond au battement des modes hybrides. Dans les figures d et e, on observe l'émission spectrale de cristaux placés dans les cercles rouges de la figure c. Dans ce spectre, on observe un pic à 342 nm qui correspond à la source laser. Un second pic plus large peut être trouvé près de 590 nm, il s'agit de l'émission spectrale de PL des NC. Pour le spectre mesuré sur la couche TiO₂, la Fig. 6.22e montre l'amélioration de la PL. Le facteur d'exaltation de la PL des NC (EF_{PL}) par rapport à la PL des NC placés sur la couche TiO₂ et par rapport à la PL des NCs placés directement au-dessus du IEW est également montré. On obtient une amélioration de 5,1 pour la source laser et de 4,8 pour l'émission NC à 590 nm. Il convient mentionner que ces résultats ont été obtenus sans contrôle de la polarisation.

6.4.1 Mesure de photoluminescence

Les figures 6.23a et b, correspondent à une excitation par les modes TE et TM, respectivement, à partir du IEW à une longueur d'onde de $\lambda = 532$ nm. Dans ces images, la pompe d'excitation a été filtrée spectralement. Aucun effet de clignotement a été observé en raison de la forte concentration des NCs. Les figures b et c montrent l'émission spectrale de NC placés au-dessus de l'IEW (étoile verte) et des NCs sur la couche TiO₂ (cercle rouge, HS = structure hybride formée par l'interaction avec la couche TiO₂ et l'IEW) pour la polarisation TE et TM, respectivement. Cette amélioration de la PL (EF_{PL}) est de 1.3 ± 0.2 fois pour le mode TE et de 7.3 ± 0.1 fois pour le mode TM. Sur la couche TiO₂, nous avons mesuré une longueur de couplage de $L_c \simeq 2.4 \mu\text{m}$ pour le mode TE et $L_c \simeq 5.6 \mu\text{m}$ pour le mode TM.

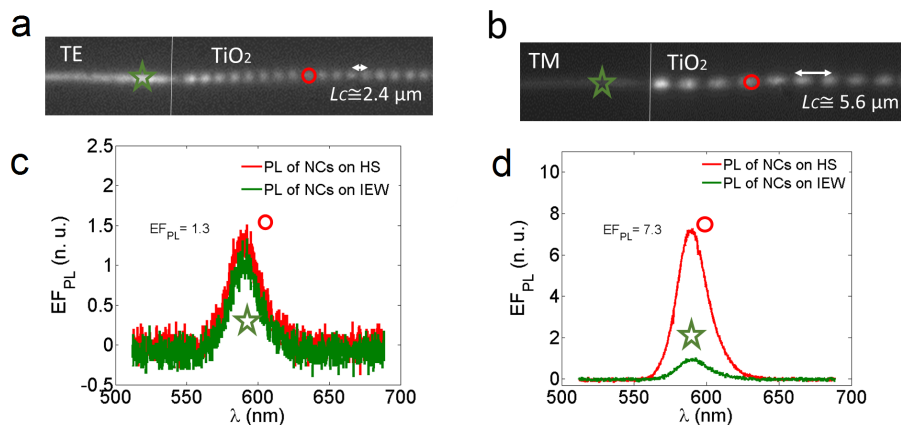


FIGURE 6.23 – Observation en champ lointain de l'émission de lumière des NC CdSe / CdS placés au-dessus du HS (structure hybride) pour a) TE et b) polarisations TM lors de l'excitation de la structure à partir de l'entrée du guide IEW. Les spectres de PL ont été extraits de l'image à la surface de l'IEW (point d'étoile) et à la surface de la HS (point de cercle) pour c) le TE polarisation et d) la polarisation TM mode. Un $EF_{PL} = 1.3$ fois pour la polarisation TE et $EF_{PL} = 7.3$ fois pour la polarisation TM à la longueur d'onde d'émission maximale des NC (à 590 nm).

Ces résultats ne correspondent pas à ceux prévus dans les simulations FDTD pour un couche de 83 nm d'épaisseur et à une longueur d'onde de λ de 542 nm (pour polarisation TE $EF=3.3$ et $L_C=3.9 \mu\text{m}$, tandis pour une polarisation TM $EF=10.8$ et $L_C = 12.7 \mu\text{m}$). Après une mesure de l'épaisseur de la couche de TiO₂ avec les NCs, nous avons observé que la présence les indices effectifs des modes guidés. En effet, l'épaisseur total NC-couche de TiO₂ est de 40 nm. Dans ce contexte, nous avons effectué des simulations

pour une couche TiO_2 avec une épaisseur de $t = 120 \text{ nm}$ pour la propagation des modes TE et TM à $\lambda = 342 \text{ nm}$ à $\lambda = 590 \text{ nm}$. Les résultats montrent que pour $\lambda = 542 \text{ nm}$, nous obtenons une période de battement de $L_C = 2.5 \mu\text{m}$ et EF = 3,7 pour la polarisation TE et pour la polarisation TM $L_C = 5.4 \mu\text{m}$ et EF = 8,5. Les distributions de battement à $\lambda = 542 \text{ nm}$ ont un bon accord avec celles obtenues dans les mesures de photoluminescence présentées dans la Gig. 6.23, ce qui prouve que la distribution de battement dans la figure 6.23 correspond au battement des modes hybrides à 542 nm.

Nous avons excité aussi les NC à travers l'objectif de microscope afin d'observer la collection de l'émission sur le guide IEW. Nous avons sélectionné deux points d'excitation sur le guide IEW et sur le guide IEW avec une couche de TiO_2 . Nous observons le spectre de la lumière collectée en bout de fibre optique collé au guide IEW. Dans cette expérience, nous avons obtenu un $\text{EF} \approx 2$ sans contrôle de la polarisation. L'EF attendu théoriquement à $\lambda=590 \text{ nm}$ est de 1,2 pour le mode TE et de 4,2 pour le mode TM. En moyen nous avons une exaltation de 2,7 en accord avec nos mesures.

6.4.2 Mesure de la durée de vie et du facteur de Purcell

Les mesures de la durée de vie et du facteur de Purcell des NC ont été réalisées en collaboration avec la Dr Nancy Rahbany. Nous avons illuminé l'échantillon par un système confocal avec amplification 50X et ouverture numérique de 0,95. Cette excitation a été faite avec un laser pulsé centré à $\lambda = 405 \text{ nm}$, une largeur d'impulsion à mi hauteur de 55 ps, un taux de répétition de 8 MHz et une puissance moyenne autour de $40 \mu\text{W}$ ([98]). La lumière émise par les NC est collectée par le même système confocal et envoyée à un spectromètre où nous avons choisi de mesurer le signal à 590 nm (selon l'émission spectrale montrée dans les figures 6.22 et 6.23).

La Fig. 6.24 montre la durée de vie de la PL à la longueur d'onde d'émission pour les NC sur verre, sur l'IEW, sur TiO_2 et sur la HS. La forme de la ligne de l'intensité de décroissance a été approchée d'une exponentielle du type $I = I_0 e^{(-t/\tau)}$ avec τ la durée de vie des NCs [100, 101]. Le facteur de Purcell (F_p) est défini en termes de durée de vie et de la densité locale des états (LDOS) des nanocristaux comme $F_p = \tau_0/\tau = \rho/\rho_0$ (équation 6.1.14), où τ est la durée de vie modifiée pour l'échantillon et τ_0 est la durée de

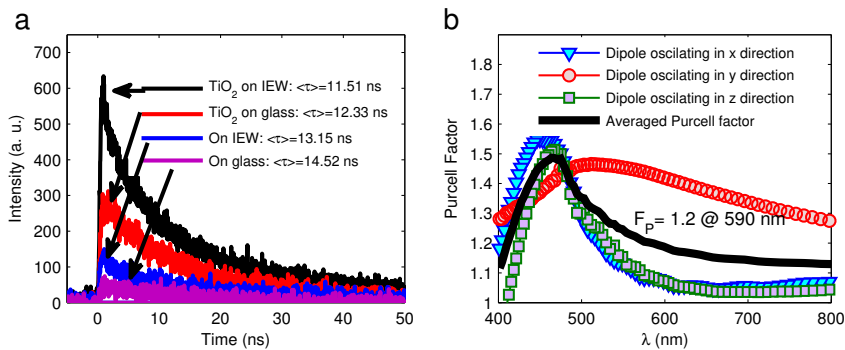


FIGURE 6.24 – a) Mesures de durée de vie à $\lambda = 590 \text{ nm}$, de Nc de CdSe/CdS sur verre, sur WG en verre, sur TiO_2 sur verre et sur HS. Les NC ont été excités à $\lambda = 405 \text{ nm}$. b) Facteur de Purcell obtenu avec la méthode FDTD pour un dipôle orienté le long des axes : bleu x , rouge y et vert le z direction et la moyenne du facteur Purcell (noir).

vie des NCs sur le substrat de verre. Pour les NC placés sur la couche TiO_2 sur l'IEW (la HS), nous avons mesuré un facteur Purcell $F_p = 1,3$.

Nous avons effectué des simulations du facteur de Purcell avec la méthode FDTD. Nous simulons les NC comme une source dipolaire placée à 20 nm de la surface de l'échantillon (la moitié de l'épaisseur moyenne de la couche de NC mesurée par l'AFM). Le facteur de Purcell a été obtenu en mesurant la lumière rayonnée par le dipôle oscillant dans les trois axes de coordonnées, afin de déterminer la densité locale des états excités LDOS.

Dans la Fig. 6.24b, nous présentons les résultats numériques pour un dipôle orienté le long de la direction x (triangles verts), y (cercles rouges), z (carrés verts) et moyenne pour ces trois contributions (ligne noire). En raison de la distribution aléatoire des nanocristaux, le facteur $F_p = 1,3$ doit être comparé avec le facteur de Purcell moyen à 590 nm qui est égal à 1,2 avec un bon accord avec les résultats numériques. Cependant, cette valeur pourrait être augmentée en changeant l'orientation des nanocristaux, une situation difficile, exigeant une ingénierie supplémentaire. En revanche, selon la simulation un facteur de Purcell plus élevé pourrait être trouvé nanoemmiters utilisés avec la longueur d'onde d'émission à 460 nm.

Les résultats présentés dans ces sections ont inspiré la publication d'un manuscrit dans la revue Applied Optics.

6.5 Conclusion générale

La structure photonique-plasmonique intégrée proposée dans cette thèse est une étape importante vers l'intégration des sources à photon unique intégrées. Ces structures peuvent être adaptées pour plusieurs applications en nanophotonique. Des facteurs d'amélioration du champ électrique de 5000 et des facteurs de Purcell de 150 peuvent être appliquée dans des domaines tels que la détection de substance chimique ou biologiques à l'échelle nanométrique ou pour les technologies quantiques de l'information et de la communication avec une efficacité de collection de 40%.

En utilisant la théorie de l'optique électromagnétique et en considérant la source de photon unique comme une source ponctuelle dipolaire, nous avons associé les caractéristiques d'émission à la densité locale d'états.

Nous avons réalisé des simulations numériques par la méthode FDTD afin d'étudier les processus physiques impliqués dans le principe de fonctionnement de la structure. Pour une structure hybride formée par un guide à échange d'ions sur verre (IEW), une couche structurée de TiO₂ et un nanotaper plasmonique en or, nous avons observé qu'un mode photonique du guide IEW faiblement confiné (surface effective modale de quelques longueur d'ondes) peut être transformé en un mode plasmonique fortement confiné dans un volume effectif de quelques nanomètres cubes. Grâce au fort confinement du champ électrique, celui-ci est exalté de plus de 3 ordres de magnitude (EF = 5000) à une longueur d'onde 640 nm.

En utilisant le théorème de réciprocité de l'électromagnétisme, nous avons étudié le cas réciproque où un dipôle oscillant près de la surface de notre structure hybride excite les modes propres de la structure hybride. Nous avons calculé une efficacité de collection de 40% pour un dipôle orienté parallèlement à la surface de la structure. Les pertes de 60% sont dues principalement aux pertes par absorption et par couplage aux modes radiatifs de la structure hybride (diffusion aux bords de la couche de TiO₂).

Afin de réduire les pertes par diffusion, nous avons proposé l'utilisation de transition adiabatiques de la couche de TiO₂. Cela permet en effet un transition adiabatique entre les modes du guide à échange d'ion et la couche TiO₂.

La configuration SNOM en mode diffusion et en mode illumination comme un outil de caractérisation des modes, de la cartographie de champ électrique confiné et de la mesure d'indice effectif des modes.

Dans la configuration en mode illumination, nous avons observé que :

- Lorsque le détecteur est placé latéralement dans la direction de propagation, le motif d'interférence observé pour le photodétecteur contient des informations sur les modes radiatifs au bord de la couche de TiO_2 et sur certains modes rayonnés générés par la sonde AFM. Dans cette configuration, il est possible d'éclairer la sonde AFM afin d'imiter l'interaction entre les modes de la structure hybride et un dipôle ponctuel proche de sa surface. Cette configuration permet d'imiter le cas où le dipôle oscille dans la direction de la polarisation TM, mais en raison de la position du système optique, il n'est pas possible l'imitation de dipôle avec polarisation TE.
- Lorsque le détecteur est placé parallèlement à z . Le motif d'interférence a des périodes plus longues que le dernier cas. Cela génère des informations dans l'espace de Fourier ont des fréquences plus définies. Cependant, cette configuration ne fournit pas d'informations sur les modes de rayonnement. Le mode d'illumination dans cette configuration permet d'imiter la TE et la polarisation TM. Cela nous a permis de cartographier le LDOM excit par le dipole et recueilli la fin de l'IEW.

Pour les expériences où nous avons déposé de NC CdSe / CdS sur une structure hybride formée par une couche de TiO_2 placée sur un guide IEW. Nous avons observé que les nanocristaux peuvent être excités par les modes photoniques du guide à échange d'ions sur verre. Nous avons observé un facteur d'exaltation de 8 pour les NC placés sur la couche TiO_2 . Nous observons que l'émission des NC ont une distribution périodique qui correspond au battement des modes hybride en considérant un païsageur additionnel de 40 nm cause des NC. Additionnellement, nous avons montré qu'il est possible d'exciter les NC par une excitation externe et de collecter la lumière en sortie du guide à échange d'ions avec une amélioration de la collection de 2 pour les NC au dessus de la couche de TiO_2 . Des mesures de durée de vie ont été obtenues et un facteur de Purcell de 2 a été mesuré.

En perspectives à ce travail de thèse, il y a la caractérisation de nouveaux échantillons par microscopie en champ proche SNOM, afin de mesurer la LDOM et la LDOS sur le nanotriangle d'or.

Il reste encore à investiguer des étapes de réalisations technologiques à avec notamment l'intégration contrôlée d'une boîte quantique unique dans la structure proposée. Une hypothèse de travail serait d'utiliser des procédés physico-chimiques comme les techniques de réhologie ou encore en utilisant un procédé de photopolymérisation locale qui exploite le principe de réciprocité optique évoqué dans cette thèse.

Appendix A

Green's functions formalism : spontaneous decay in a two-levels atom

In order to obtain the Green's function of the system of equation 1.1.5, we define

$$\mathbf{G}^E(\mathbf{r}, \mathbf{r}'; \omega) = \sum_k \mathbf{A}_k(\mathbf{r}', \omega) e_k(\mathbf{r}, \omega_k), \quad (\text{A.0.1})$$

where \mathbf{A}_k is a vectorial expansion of coefficients to determine.

Using A.0.1 and 1.1.5 in 1.1.36, we obtain

$$\sum_k \mathbf{A}_{k'}(\mathbf{r}', \omega) \left(\frac{\omega_k^2 - \omega^2}{c^2} \right) = \mathbf{I} \delta(\mathbf{r} - \mathbf{r}'). \quad (\text{A.0.2})$$

Making use of the orthogonality properties of the eigenmodes (equation 1.1.9), we multiple on both sides with $e_k'^*$, then we can write \mathbf{A}'_k as

$$\mathbf{A}_{k'}(\mathbf{r}', \omega) = e_k'^* \left(\frac{c^2}{\omega_k^2 - \omega^2} \right), \quad (\text{A.0.3})$$

Therefore, using A.0.3 in A.0.1, we obtain

$$\mathbf{G}^E(\mathbf{r}, \mathbf{r}'; \omega) = \sum_k \left(\frac{c^2 e_k'^*(\mathbf{r}', \omega) e_k(\mathbf{r}, \omega_k)}{\omega_k^2 - \omega^2} \right). \quad (\text{A.0.4})$$

Here we use a mathematical identity used by Novotny [23] in order to describe the Green's function as a delta. Where

$$Im \left\{ \lim_{\eta \rightarrow 0} \sum_k \left(\frac{c^2 e'_k(\mathbf{r}', \omega) e_k(\mathbf{r}, \omega_k)}{\omega_k^2 - \omega^2} \right) \right\} = \frac{\pi}{2} \sum_k \frac{1}{\omega_k} e'_k(\mathbf{r}', \omega) e_k(\mathbf{r}, \omega_k) \delta(\omega - \omega_k). \quad (\text{A.0.5})$$

From this equation it is easy to show that

$$Im \{ \mathbf{G}^E(\mathbf{r}, \mathbf{r}'; \omega) \} = \frac{\pi}{2} \sum_k \frac{1}{\omega_k} e'_k(\mathbf{r}', \omega) e_k(\mathbf{r}, \omega_k) \delta(\omega - \omega_k) \quad (\text{A.0.6})$$

Finally, we can rewrite the equation 1.1.35 in term of equation A.0.6 as

$$\gamma = \frac{2\omega_0}{3\hbar\epsilon_0} |\mathbf{p}|^2 \rho_u(\mathbf{r}_0, \omega_0) \quad (\text{A.0.7})$$

and

$$\rho_p(\mathbf{r}_0, \omega_0) = \frac{6\omega_0}{\pi c^2} [n_\mu \cdot Im \{ \mathbf{G}^E(\mathbf{r}, \mathbf{r}'; \omega) \} \cdot n_\mu] \quad (\text{A.0.8})$$

Appendix B

K-vector for a surface plasmon polariton

B.1 Surface polariton plasmon

The interaction between an metal-dielectric interface is describe by the Maxwell's equations :

$$\nabla \cdot \mathbf{E} = 0, \quad (\text{B.1.1a})$$

$$\nabla \cdot \mathbf{H} = 0, \quad (\text{B.1.1b})$$

$$\nabla \times \mathbf{E} = -\mu_0 \frac{\partial \mathbf{H}}{\partial t} \quad (\text{B.1.1c})$$

$$\nabla \times \mathbf{H} = \epsilon_0 n^2 \frac{\partial \mathbf{E}}{\partial t}. \quad (\text{B.1.1d})$$

with $n = \sqrt{\epsilon}$ the refractive index of the medium. using the algebraic property of $\nabla \times (\nabla \times \mathbf{A}) = \nabla(\nabla \cdot \mathbf{A}) - \nabla^2 \mathbf{A}$ and the set of equations B.1.1, we can obtain

$$\nabla^2 \mathbf{E} - \epsilon_0 \mu_0 n^2 \frac{\partial^2 \mathbf{E}}{\partial t^2} = 0, \quad (\text{B.1.2})$$

If we consider s a wave with $\mathbf{E} = \mathbf{E}(\mathbf{r})e^{i\omega t}$ and $\mathbf{H} = \mathbf{H}(\mathbf{r})e^{i\omega t}$ we can rewrite equation B.1.2 as

$$\nabla^2 \mathbf{E} + \epsilon \mathbf{k}_0^2 \mathbf{E} = 0. \quad (\text{B.1.3})$$

where $k_0 = \omega/c$ and $c = \frac{1}{\sqrt{\epsilon_0 \mu_0}}$. This is the variation of the Helmholtz equation described by equation 1.1.5

For the interface shown in figure 1.6, we take an wave traveling only in the zy plane. For this reason we consider $\mathbf{E} = \mathbf{E}(x)e^{\beta z}$ and the equation B.1.4 is modified as follows

$$\nabla^2 \mathbf{E} + (\mathbf{k}_0^2 \epsilon - \beta^2) \mathbf{E} = \mathbf{0}. \quad (\text{B.1.4})$$

For propagation along the y -direction $\frac{\delta}{\delta_x} \Rightarrow \beta$ and homogeneity in the x direction $\frac{\delta}{\delta_y} \Rightarrow 0$, the set of equations B.1.1 system of equation simplifies to

$$i\beta E_y = -i\omega\mu_0 H_x, \quad (\text{B.1.5a})$$

$$\frac{\partial E_y}{\partial x} = -i\omega\mu_0 H_z, \quad (\text{B.1.5b})$$

$$\frac{\partial H_z}{\partial x} - i\beta H_x = -i\omega\epsilon_0 n^2 E_y, \quad (\text{B.1.5c})$$

for the TE polarization and

$$\frac{\partial E_z}{\partial x} - i\beta E_x = i\omega\mu_0 H_y, \quad (\text{B.1.6a})$$

$$i\beta H_y = -i\omega\epsilon_0 n^2 E_x, \quad (\text{B.1.6b})$$

$$\frac{\partial H_y}{\partial x} = i\omega\epsilon_0 n^2 E_z. \quad (\text{B.1.6c})$$

for TM polarization.

The solution of this system can we expressed as [73]

$$H_y = A e^{i\beta z} e^{-k_m x}, \quad (\text{B.1.7a})$$

$$E_z = iA \frac{1}{\omega\epsilon_d\epsilon_m} k_m e^{i\beta z} e^{-k_m x}, \quad (\text{B.1.7b})$$

$$E_x = A \frac{\beta}{\omega\epsilon_d\epsilon_m} e^{i\beta z} e^{-k_m x}, \quad (\text{B.1.7c})$$

and for $y < 0$

$$H_y = B e^{i\beta z} e^{k_d x}, \quad (\text{B.1.8a})$$

$$E_z = -iB \frac{1}{\omega \varepsilon_d \varepsilon_m} k_d e^{i\beta z} e^{k_d x}, \quad (\text{B.1.8b})$$

$$E_x = -B \frac{\beta}{\omega \varepsilon_d \varepsilon_m} e^{i\beta z} e^{k_d x}. \quad (\text{B.1.8c})$$

where m represent the metal material and d the dielectric material Using the boundary condition in $y = 0$

$$\frac{k_m}{k_d} = \frac{-\varepsilon_m}{\varepsilon_d}, \quad (\text{B.1.9})$$

with

$$k_d^2 = \beta^2 - k_0^2 \varepsilon_d, \quad (\text{B.1.10a})$$

$$k_m^2 = \beta^2 - k_0^2 \varepsilon_m. \quad (\text{B.1.10b})$$

With k_d and k_m the k vector of dielectric and the metal materials, respectively .In this equation β can be describe the k vector of the SPP as

$$k_{SPP} = k_0 \sqrt{\frac{\varepsilon_d(\omega) \varepsilon_m}{\varepsilon_d(\omega) + \varepsilon_m}}. \quad (\text{B.1.11})$$

Appendix C

Orthogonality property of modes

This process can be found in [88]. We start taking the Maxwell equations

$$\nabla \times \bar{E} = -i \left(\frac{\mu_0}{\epsilon_0} \right)^{1/2} k \bar{H}, \quad \text{and} \quad \nabla \times \bar{H} = \bar{J} + i \left(\frac{\mu_0}{\epsilon_0} \right)^{1/2} \bar{n}^2 k \bar{E}, \quad (\text{C.0.1})$$

in equation 2.1.13 with $\nabla \cdot (A \times B) = B \cdot \nabla \times A - A \cdot \nabla \times B$ to obtain

$$\frac{\partial}{\partial z} \int_{A_\infty} \nabla \cdot [E \times \bar{H}^* + \bar{E}^* \times H] \cdot \hat{z} dA = \int_{A_\infty} -i \left(\frac{\mu_0}{\epsilon_0} \right)^{1/2} (k \bar{n}^{*2} - n^2) E \cdot \bar{E} - (\bar{E}^* \cdot J + E \cdot \bar{J}^*) dA. \quad (\text{C.0.2})$$

For two guided modes with

$$\bar{E} = e_l e^{i\beta_l z}, \quad \bar{H} = h_l e^{i\beta_l z} \quad \text{and} \quad E = e_k e^{i\beta_k z}, \quad H = h_k e^{i\beta_k z}. \quad (\text{C.0.3})$$

with $J = \bar{J} = 0$ and $\bar{n}^* = n$.

We deduce from equations 2.1.13 and C.0.2 that

$$(\beta_l - \beta_k) \int_{A_\infty} [e_l \times h_k^* + e_k \times h_l^*] = 0 \quad (\text{C.0.4})$$

then $[e_k \times h_l^* + e_l \times h_k^*] = 0$ and therefore, we can define the orthogonality property of modes as

$$\frac{1}{2} \int_{A_\infty} [e_k \times h_l^*] \cdot \hat{z} dA = \begin{cases} 0 & k \neq l \\ N_k & k = l \end{cases}, \quad (\text{C.0.5})$$

Using equation B.2.16 and the definition of \bar{E} and E from section 2.3 and equation C.0.3 in equation 2.1.13 is easy to obtain the equation 2.1.15

Appendix D

Scanning near-field optical microscopy concepts

Scanning nearfield optical microscopy is an imaging technique that breaks the classical diffraction limit. This is possible by detecting a large spectrum of evanescent waves that do not usually propagate to the far field. The principle of detection is based on the use of a probe whose size is much smaller than the excitation wavelength. There are two main configurations of SNOM, the aperture and the apertureless one ([109]).

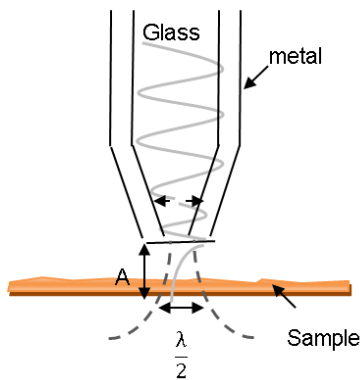


FIGURE D.1 – Principle of a SNOM tip with aperture, where A is the near-field region, λ is the illumination wavelength and the gray line represents the evanescence wave propagating through the SNOM tip.

In the aperture mode, the near-field is probed by a tapered optical fiber covered by a metal layer with a small aperture at its apex (figure D.1). When the fiber is placed in the near-field (in zone A), the evanescent waves surrounding the sample scattered and

propagated inside the optical fiber. The metal coating limits physically the detection area and thus govern directly the spatial resolution of the system. Light is detected by external photodetectors connected at the output of the optical fiber. The aperture SNOM can be used in several configurations as it show in figure D.2. Figure D.2 a, b and c show some configurations where the fiber tip is used as a source and the detection is made by external detectors, in figure d and e the excitation is made by external illumination and the detection is realized through the fiber.

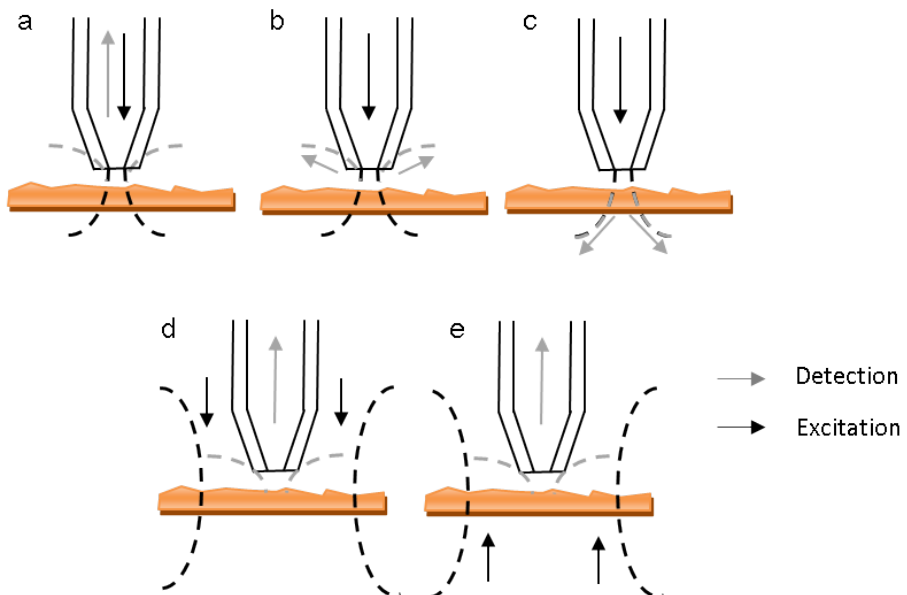


FIGURE D.2 – Operation modes for the aperture SNOM, where the gray line represent the collected light and the black line is the excitation light : a) Excitation and collection by the tip, b) the tip as a source and the detection is made by a external system over the sample, c) the tip as a source and the detection is made by a external system below the sample, d) and e) external excitation from and detection by the tip.

In this thesis we used the apertureless configuration of SNOM. It consists in a solid AFM tip (usually a Si tip) placed in the near-field (figure D.3). This tip is able to perturb evanescent waves and generate scattering of light towards an external detector located in the far field. Different configurations apertureless SNOM are shown in Fig. D.3.

In this thesis we used a home-made apertureless SNOM developed from a commercial atomic force microscope (AFM). The AFM is useful to control the position of the SNOM tip in interaction with the sample's nearfield with nanometric spatial resolution. It gives directly the topography of the structure's surface (figure D.4 a depicts two kind of AFM

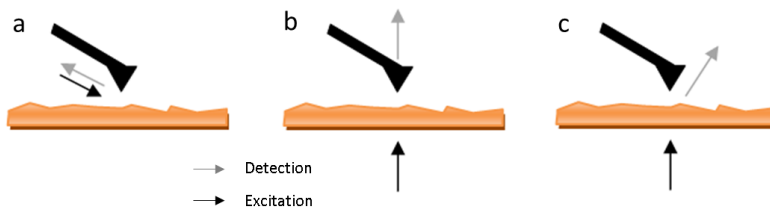


FIGURE D.3 – Apertureless modes of operation : a) back scattering mode, b) photon tunneling (PSTM) mode base on sharp transparent tip, c) transmission mode.

tips that we used in this thesis : a) a conical shape tip and b) a pyramidal shape tip). The probe itself is held by a flexible thin plate known as a cantilever, which is held by two piezoelectric crystals allowing its oscillation. The AFM commercial tips and the cantilevers are usually made of silicon or tungsten material. The AFM tip has an apex size of few tens nanometers making it a powerful scattering optical probe for SNOM measurements.

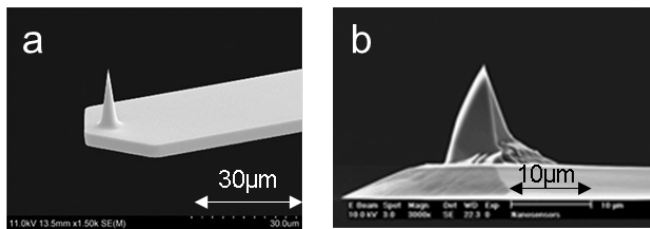


FIGURE D.4 – AFM tips shape. a) Conical tip and b) pyramidal tip

The AFM consists of a mechanical system that allows moving the tip in an xy plane in order to scan the surface of the sample. The tip has three operation modes (shown in figure D.5 a, b, and c) : the *tapping mode*, where the tip has intermittent contact with the sample while oscillating at a constant frequency ω_0 , the *contact mode*, where the tip touches the sample during the scanning and the *constant height mode*, where the tip-to-sample spacing remains equidistant.

The topography of the sample is reconstructed by the measures of variations in distances between the sample surface and the tip. This distance is referenced to an initial height $h_0 = 0$ which is measured according to the optical alignment system shown in figure D.5d. The system is properly aligned when the laser beam reflected in the cantilever is reflected in a movable mirror and it arrives at the center of the photodiodes A and B. When there are variations of height on the sample the cantilever is flexed causing the light

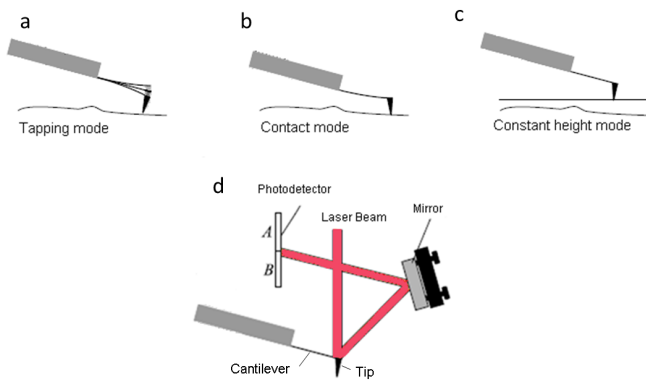


FIGURE D.5 – Operating mode of the AFM. a) Tapping mode, b) contact mode and c) constant height mode. d) Alignment system of the AFM. (Image reproduced from [110])

beam to leave its initial position at the photodiodes, this change is related to voltage V_A and V_B measured by the photodiodes and this voltages are finally related with a height value measured from h_0 .

Bibliography

- [1] M. A. Nielsen and I. L. Chuang, *Quantum Computation and Quantum Information*. Cambridge university press, 2000.
- [2] K. W. Murch, S. J. Weber, C. Macklin, and I. Siddiqi, “Observing single quantum trajectories of a superconducting quantum bit,” *Nature*, vol. 502, pp. 211–214, 2013.
- [3] G. Kirchmair, B. Vlastakis, Z. Leghtas, S. E. Nigg, H. Paik, E. Ginossar, M. Mirrahimi, L. Frunzio, S. M. Girvin, and R. J. Schoelkopf, “Observation of quantum state collapse and revival due to the single-photon kerr effect,” *Nature*, vol. 495, pp. 205–209, 2013.
- [4] S.-H. Gong, J.-H. Kim, Y.-H. Ko, C. Rodriguez, J. Shin, and Y.-H. Lee
- [5] M. Trupke, W. J. Munro, K. Nemoto, and J. Schmiedmayer, “Enhancing photon collection from quantum emitters in diamond,” *Quantum information technology*, vol. 8, pp. 33–37, 2011.
- [6] C. H. Bennett and G. Brassard, “Quantum cryptography : Public key distribution and coin tossing,” *IEEE Int. Conf. Computers, Systems and Signal Processing*, vol. 2, pp. 175–179, 1984.
- [7] L.-Y. Cheng, Q. Guo, H.-F. Wang, and S. Zhang, “Quantum state manipulation of dipole emitters with a plasmonic double-bar resonator,” *Quantum Information Processing*, vol. 13, pp. 2513–2523, 2014.
- [8] H. J. Krenner, S. Stufler, M. Sabathila, E. C. Clarka, P. Ester, M. Bichler, G. Absstreiter, J. J. Finley, and A. Zrenner, “Recent advances in exciton-based quantum information processing in quantum dot nanostructures,” *New Journal of Physics*, vol. 7, no. 5, p. 184, 2005.

- [9] P. Alivisatos, "The use of nanocrystals in biological detection," *Nature Biotechnology*, vol. 22, pp. 47–52, 2004.
- [10] B. Somogyi and A. Gali1, "Computational design of in vivo biomarkers," *Journal of Physics : Condensed Matter*, vol. 26, no. 14, p. 143202, 2014.
- [11] H. Deschout, F. C. Zanacchi, M. Mlodzianoski, A. Diaspro, J. Bewersdorf, S. T. Hess, and K. Braeckmans, "Precisely and accurately localizing single emitters in fluorescence microscopy," *Nature Methods*, vol. 11, p. 253266, 2014.
- [12] P. Winckler, L. Lartigue, G. Giannone, F. D. Giorgi, F. Ichas, J.-B. Sibarita, B. Lounis, and L. Cognet, "Identification and super-resolution imaging of ligand-activated receptor dimers in live cells," *Scientific Reports*, vol. 3, p. 2387, 2013.
- [13] R. B. Raffa and K. F. Raffa, "Potential insight for drug discovery from high fidelity receptor- mediated transduction mechanisms in insects," *Expert Opin Drug Discov.*, vol. 6, no. 10, p. 10911101, 2011.
- [14] C. M. Galloway, M. P. Kreuzer, S. S. Aimovi, G. Volpe, M. Correia, S. B. Petersen, M. T. Neves-Petersen, , and R. Quidant, "Plasmon-assisted delivery of single nano-objects in an optical hot spot," *Nano Lett*, vol. 13, no. 9, p. 42994304, 2013.
- [15] R. K. Kramer, N. Pholchai, V. J. Sorger, T. ROulton, and X. Zhang, "Positioning of quantum dots on metallic nanostructures," *Nanotechnology*, vol. 21, p. 14530, 2010.
- [16] I. Rech, A. Restelli, S. Cova, M. Ghiona, M. Chiari, and M. Cretich, "Microelectronic photosensors for genetic diagnostic microsystems," *Sens. Actuators B*, vol. 100, p. 154, 2004.
- [17] T. Isoshima, Y. Isojima, K. Hakomori, K. Kikuchi, K. Nagai, and H. Nakagawa, "Ultrahigh sensitivity singlephoton detector using a Si avalanche photodiode for the measurement of ultraweak biochemiluminescence," *Rev. Sci. Instrum*, vol. 66, p. 2922, 1995.
- [18] E. P. Etryayeva and I. L. E. W. Russ Algar, "Quantum dots in bioanalysis : A review of applications across various platforms for fluorescence spectroscopy and imaging," *Applied Spectrosc*, vol. 67, p. 215, 2013.

- [19] T. S. Kuhn, *Black-body theory and the quantum discontinuity 1894-1912*. The university of Chicago press, 1978.
- [20] S. Buckley, K. Rivoire, and J. Vucković, “Engineered quantum dot single-photon sources,” *Reports on Progress in Physics*, vol. 75, no. 12, p. 126503, 2012.
- [21] B. Lounis and M. Orrit, “Single-photon sources,” *Reports on Progress in Physics*, vol. 68, no. 5, p. 1129, 2005.
- [22] A. M. M. D. Eisaman, J. Fan1 and S. V. Polyakov, “Invited review article : Single-photon sources and detectors,” *Rev. Sci. Instrum.*, vol. 82, p. 071101, 2011.
- [23] L. Novotny and B. Hecht, *Principles of Nano-optics*. Cambridge University press, 2006.
- [24] R. Carminati, A. Cazé, D. Cao, F. Peragua, V. Krachmalnicoff, R. Pierrat, and Y. D. Wild, “Electromagnetic density of states in complex plasmonic systems,” *Surface Science Reports*, vol. 70, pp. 1–41, 2015.
- [25] L. J. Brillson, *Surfaces and Interfaces of Electronic Materials*. Wiley, 2010.
- [26] E. Purcell, “Spontaneous emission probabilities at radio frequencies,” *Phys. Rev.*, vol. 69, 1946.
- [27] D. J. Griffiths, *Introduction to Electrodynamics*. Prentice Hall, 1999.
- [28] E. Fort and S. Grésillon, “Surface enhanced fluorescence,” *Applied Physics*, vol. 41, pp. 013001–31, 2008.
- [29] A. J. Shields, “Semiconductor quantum light sources,” *Nat Photon*, vol. 1, pp. 215–233, 2007.
- [30] T. Frecker, D. Bailey, X. Arzeta-Ferrer, J. McBride, , and S. J. Rosenthal, “Review-quantum dots and their application in lighting, displays, and biology,” *ECS J. Solid State Sci. Technol.*, vol. 5, pp. R3019–R3031, 2016.
- [31] B. Lounis and W. E. Moerner, “Single photons on demand from a single molecule at room temperature,” *Nature*, vol. 407, pp. 491–493, 2000.
- [32] W. E. Moerner, “Single-photon sources based on single molecules in solids,” *New Journal of Physics*, vol. 6, p. 1367, 2004.

- [33] M. Hijlkema, B. Weber, H. P. Specht, S. C. Webster, A. Kuhn, and G. Rempe, “A single-photon server with just one atom,” *Nature Physics*, vol. 3, pp. 253–255, 2007.
- [34] M. Saffman and T. G. Walker, “Creating single-atom and single-photon sources from entangled atomic ensembles,” *Physical review A*, vol. 66, p. 065403, 2002.
- [35] H. G. Barros, A. Stute, T. E. Northup, C. Russo, P. O. Schmidt1, and R. Blatt, “Deterministic single-photon source from a single ion,” *New Journal of Physics*, vol. 11, p. 103004, 2009.
- [36] C. Maurer, C. Becher, C. Russo, J. Eschner, and R. Blatt, “A single-photon source based on a single ca⁺ ion,” *New Journal of Physics*, vol. 6, p. 94, 2004.
- [37] E. Wu, J. R. Rabeau, G. Roger, F. Treussart, H. Zeng, P. Grangier, S. Prawer, and J.-F. Roch, “Room temperature triggered single-photon source in the near infrared,” *New Journal of Physics*, vol. 9, no. 12, p. 434, 2007.
- [38] F. Jelezko and J. Wrachtrup, “Single defect centres in diamond : A review,” *phys. stat. sol.*, vol. 203, no. 13, p. 32073225, 2006.
- [39] M. F. Frasco and N. Chaniotakis, “Semiconductor quantum dots in chemical sensors and biosensors,” *Sensor*, vol. 9, pp. 7266–7286, 2009.
- [40] S. J. Charles, J. E. Butler, B. N. Feygelson, M. Newton, D. L. Carroll, J. Steeds, H. Darwish, C.-S. Yan, H.K.Mao, and R. J. Hemley, “Characterization of nitrogen doped chemical vapor deposited single crystal diamond before and after high pressure, high temperature annealing,” *physica status solidi*, vol. 201, pp. 2473–2485, 2004.
- [41] M. Leifgen, T. Schrder, F. Gdeke, R. Riemann, V. Mtillon, E. Neu, C. Hepp, C. Arend, C. Becher, K. Lauritsen, and O. Benson, “Evaluation of nitrogen- and silicon-vacancy defect centres as single photon sources in quantum key distribution,” *Quantum Physics*, vol. 201, p. 023021, 2014.
- [42] J. R. Rabeau, Y. L. Chin, S. Prawer, F. Jelezko, T. Gaebel, and J. Wrachtrup, “Fabrication of single nickel-nitrogen defects in diamond by chemical vapor deposition,” *Applied Physics Letter*, vol. 86, p. 131926, 2005.

- [43] Y. Sonnefraud, A. Cuche, O. Faklaris, J.-P. Boudou, T. Sauvage, J.-F. Roch, F. Treussart, and S. Huant, “Diamond nanocrystals hosting single nitrogen-vacancy color centers sorted by photon-correlation near-field microscopy,” *Optics Letters*, vol. 33, p. 611613, 2008.
- [44] Y.-R. Chang, H.-Y. Lee, K. Chen, C.-C. Chang, D.-S. Tsai, C.-C. Fu, T.-S. Lim, Y.-K. Tzeng, C.-Y. Fang, C.-C. Han, H.-C. Chang, and W. Fann, “Mass production and dynamic imaging of fluorescent nanodiamonds,” *Nat Nano*, vol. 3, p. 284288, 2008.
- [45] J.-P. Boudou, P. A. Curmi, F. Jelezko, J. Wrachtrup, P. Aubert, M. Sennour, G. Balasubramanian, R. Reuter, A. Thorel, and E. Gaffet, “High yield fabrication of fluorescent nanodiamonds,” *Nanotechnology*, vol. 20, p. 235602, 2009.
- [46] K. J. Resch, J. S. Lundeen, and A. M. Steinberg, “Nonlinear optics with less than one photon,” *Physical Review Letters*, vol. 87, p. 123603, 2000.
- [47] F. Laudenbach, H. Hübel, M. Hentschel, P. Walther, and A. Poppe, “Modelling parametric down-conversion yielding spectrally pure photon pairs,” *Opt. Express*, vol. 24, pp. 2712–2727, Feb 2016.
- [48] S. Lefrancois, D. Fu, G. R. Holtom, L. Kong, W. J. Wadsworth, P. Schneider, R. Herda, A. Zach, X. S. Xie, and F. W. Wise, “Fiber four-wave mixing source for coherent anti-stokes raman scattering microscopy,” *Opt. Lett.*, vol. 37, pp. 1652–1654, 2012.
- [49] C. J. McKinstrie, H. Kogelnik, R. M. Jopson, S. Radic, , and A. V. Kanaev, “Four-wave mixing in fibers with random birefringence,” *Opt. Express.*, vol. 12, pp. 2033–2055, 2004.
- [50] H. Fukuda, K. Yamada, T. Shoji, M. Takahashi, T. Tsuchizawa, T. Watanabe, J. ichi Takahashi, and S. ichi Itabashi, “Four-wave mixing in silicon wire waveguides,” *Opt. Express.*, vol. 13, p. 4629, 2005.
- [51] M. F. Susumu Noda and T. Asano, “Spontaneous-emission control by photonic crystals and nanocavities,” *Nature Photonics*, vol. 1, pp. 449–458.

- [52] M. Hiscock, C. Su, B. C. Gibson, A. Greentree, L. Hollenberg, and F. Ladouceur, “Slot-waveguide cavities for optical quantum information applications,” *Optics Express*, vol. 17, no. 9, pp. 7295–7303, 2009.
- [53] D. Bouchet, M. Mivelle, J. Proust, B. Gallas, I. Ozerov, M. F. Garcia-Parajo, A. Gulinati, I. Rech, Y. D. Wilde, N. Bonod, V. Krachmalnicoff, and S. Bidault, “Enhancement and inhibition of spontaneous photon emission by resonant silicon nanoantennas,” *Phys. Rev. applied*, vol. 6, p. 064016, Nov 2016.
- [54] E. Bermudez-Ureña, C. Gonzalez-Ballester, M. Geiselmann, R. Marty, I. P. Radko, T. Holmgard, Y. Alaverdyan, E. Moreno, F. J. García-Vidal, S. I. Bozhevolnyi, and R. Quidant, “Coupling of individual quantum emitters to channel plasmons,” *Nat Commun*, vol. 6, p. 7883, 2015.
- [55] Z. Fang, S. Huang, F. Lin, and X. Zhu, “Color-tuning and switching optical transport through CdS hybrid plasmonic waveguide,” *Optics Express*, vol. 17, no. 22, pp. 20327–20332, 2009.
- [56] S. J. P. Kress, F. V. Antolinez, P. Richner, S. V. Jayanti, D. K. Kim, F. Prins, A. Riedinger, M. P. C. Fischer, S. Meyer, K. M. McPeak, D. Poulikakos, and D. J. Norris, “Wedge waveguides and resonators for quantum plasmonics,” *Nano Lett.*, vol. 15, no. 9, pp. 6267–6275, 2015.
- [57] P. E. Barclay, K.-M. Fu, C. Santori, and R. G. Beausoleil, “Hybrid photonic crystal cavity and waveguide for coupling to diamond nv-centers,” *Opt. Express*, vol. 17, no. 12, pp. 9588–9601, 2009.
- [58] K. Hennessy, A. Badolato, M. Winger, D. Gerace, M. Atatüre, S. Gulde, S. Fält, E. L. Hu, and A. Imamoglu, “Quantum nature of a strongly coupled single quantum dotcavity system,” *Nature*, vol. 445, pp. 896–899, 2007.
- [59] G. H, G.-P. M. F, V. J. A. Novotny L, K. L, and V. Hulst, “Influencing the angular emission of a single molecule,” *Phys. Rev. Lett.*, vol. 85, pp. 5312–5337, 2000.
- [60] N. Caselli, F. L. China, W. Bao, F. Riboli, A. Gerardino, L. Li, E. H. Linfield, F. Pagliano, A. Fiore, P. J. Schuck, S. Cabrini, A. Weber-Bargioni, M. Gurioli, and F. Intonti, “Deep-subwavelength imaging of both electric and magnetic locali-

- zed optical fields by plasmonic campanile nanoantenna,” *Scientific Reports*, vol. 5, p. 9606, 2015.
- [61] A. A. M. Anatoly V. Zayats, Igor I. Smolyaninov, “Nano-optics of surface plasmon polaritons,” *Opt. Lett.*, vol. 408, no. 4082011, pp. 131–314, 2005.
- [62] N. M. Israelsen, S. Kumar, M. Taweq, J. S. Neergaard-Nielsen, A. Huck, and U. L. Andersen, “Increasing the photon collection rate from a single nv center with a silver mirror,” *Journal of optics*, vol. 11, no. 16, pp. 8867–8878, 2010.
- [63] W. L. Barnes, “Fluorescence near interfaces : the role of photonic mode density,” *J. Mod.*, vol. 45, pp. 661–99, 1998.
- [64] H. Ditlbacher, J. R. Krenn, N. Felidjl, B. Lamprecht, G. Schider, M. Salerno, A. Leitner, and F. R. Aussenegg, “Fluorescence imaging of surface plasmon fields,” *Appl. Phys. Lett.*, vol. 80, no. 404, pp. 8867–8878, 2002.
- [65] E. J. R., Vesseur, F. J. G. de Abajo, and A. Polman, “Broadband purcell enhancement in plasmonic ring cavities,” *J. Opt. Soc. Am.*, vol. 82, p. 165419, 2010.
- [66] I. Gryczynski, J. Malicka, W. Jiang, H. Fischer, W. C. W. Chan, Z. Gryczynski, W. Grudzinski, and J. R. Lakowicz, “Surface-plasmon-coupled emission of quantum dots,” *J. Phys. Chem. B*, vol. 3, pp. 1088–1093, 2005.
- [67] A. Rakovich, P. Albella, and S. A. Maier, “Plasmonic control of radiative properties of semiconductor quantum dots coupled to plasmonic ring cavities,” *Acs nano*, vol. 102, pp. 2648–2658, 2015.
- [68] K. Okamoto, S. Vyawahare, and A. Scherer, “Surface-plasmon enhanced bright emission from cdse quantum-dot nanocrystals,” *J. Opt. Soc. Am.*, vol. 23, no. 8, pp. 8867–8878, 2006.
- [69] C. Garcia-Ortiz, S. Kumar, and S. I. B. Ozhevolsky, “Local excitation of surface plasmon polaritons using nitrogen-vacancy centers,” *Optics Letters*, vol. 16, pp. 3830–3833, 2015.
- [70] S. Kumar, A. Huck, and U. L. Andersen, “Efficient coupling of a single diamond color center to propagating plasmonic gap modes,” *Nano Lett.*, vol. 13, p. 12211225, 2013.

- [71] S. Kumar, A. Huck, Y. Chen, and U. L. Andersen, “Coupling of a single quantum emitter to end-to-end aligned silver nanowires,” *Appl. Phys. Lett.*, vol. 9, p. 103106, 2013.
- [72] A. Pham, M. Berthel, Q. Jiang, J. Bellessa, S. Huant, C. Genet, and A. Drezet, “Chiral optical local density of states in a spiral plasmonic cavity,” *Physical review A*, vol. 94, p. 053850, 2016.
- [73] S. A. Maier, *Plasmonics : fundamentals and applications*. London : Springer, 2007.
- [74] J. Hammond, N. Bhalla, S. Rafiee, and P. Estrela, “Localized surface plasmon resonance as a biosensing platform for developing countries,” *Biosensors*, vol. 2, no. 4, pp. 11536–11545, 2015.
- [75] C. Y-S, F. W, K. S, and et al, “Enhanced thermal stability of silica-coated gold nanorods for photoacoustic imaging and image-guided therapy,” *Optics Express*, vol. 9, no. 8, pp. 8867–8878, 2010.
- [76] V.Krachmalnicoff, D.Cao, A.Cazé, E.Castanié, R.Pierrat, N.Bardou, S. Collin, R.Carminati, and Y.DeWilde, “Towards a full characterization of a plasmonic nanostructure with a fluorescent near-field probe,” *Opt. Express*, vol. 9, no. 21, pp. 11536–11545, 2013.
- [77] M. Aramesh, J. Cervenka, A. Roberts, A. Djalalian-Assl, R. Rajasekharan, J. Fang, K. Ostrikov, and S. Prawer, “Coupling of a single-photon emitter in nanodiamond to surface plasmons of a nanochannel-enclosed silver nanowire,” *Opt. Express*, vol. 22, no. 13, pp. 15530–15541, 2014.
- [78] A. W. Schell, G. Kewes, T. Hanke, A. Leitenstorfer, R. Bratschitsch, O. Benson, and T. Aichele, “Single defect centers in diamond nanocrystals as quantum probes for plasmonic nanostructures,” *Optic express*, vol. 19, pp. 7414–7420, 2011.
- [79] J. Choy, B. Hausmann, T. Babinec, I. Bulu, and M. L. car, “Enhanced single photon emission by diamond-plasmon nanostructures,” in *CLEO : 2011 - Laser Science to Photonic Applications*, pp. 1–2, 2011.
- [80] M. Pelton, “Modified spontaneous emission in nanophotonic structures,” *Nature Photonics*, vol. 9, p. 427435, 2015.

- [81] L. Peter, M. Sahand, and S. Stobbe, “Interfacing single photons and single quantum dots with photonic nanostructures,” *Rev. Mod. Phys.*, vol. 87, pp. 347–400, 2015.
- [82] A. SR, C. HR, P. JY, P. EY, L. D, and L. J., “Photoluminescence enhancement of quantum dots on ag nanoneedles,” *Nanoscale Research Letters*, vol. 7, no. 36, p. 438, 2012.
- [83] S. Dey and J. Zhao, “Plasmonic effect on exciton and multiexciton emission of single quantum dots,” *Phys. Chem. Lett.*, vol. 7, pp. 2921–2929, 2016.
- [84] H. Naiki, A. Masuhara, S. Masuo, T. Onodera, H. Kasai, and H. Oikawa, “Highly controlled plasmonic emission enhancement from metal-semiconductor quantum dot complex nanostructures,” *Phys. Chem. Lett.*, vol. 117, pp. 2455–2459, 2013.
- [85] B. E. A. Saleh and M. C. Teich, *Fundamentals of photonics*. Wiley, 1991.
- [86] K. Okamoto, *fundamentals of Optical Waveguides*. Eksevier, 2006.
- [87] Rsoft, “Femsim tool and finite element method.” <https://optics.synopsys.com/rsoft/rsoft-passive-device-femsim.html>, January 2017.
- [88] A. Snyder and J. Love, *Optical Waveguide Theory*. Springer US.
- [89] P. Then, G. Razinskas, T. Feichtner, P. Haas, A. Wild, N. Bellini, R. Osellame, G. Cerullo, and B. Hecht, “Remote detection of single emitters via optical waveguides,” *Phys. Rev. A*, vol. 89, p. 053801, May 2014.
- [90] J. B. Theeten and D. E. Aspnes, “Ellipsometry in thin film analysis,” *Annual Review of Materials Science*, vol. 11, no. 1, pp. 97–122, 1981.
- [91] G. L., W. J.R., V. J.B., J. A., D. Awschalom, and V. de Walle, “Hybrid integrated optical waveguides in glass for enhanced visible photoluminescence of nanoemitters,” *Quantum computing with defects*, vol. 38, no. 36, p. 802807, 2013.
- [92] W. Geng, *Coupling Nanostructures Towards Integrated Nanophotonics Devices*. PhD thesis, L’Universite de technologie de Troyes.
- [93] M. Z. Alam, J. Meier, J. S. Aitchison, and M. Mojahedi, “Propagation characteristics of hybrid modes supported by metal-low-high index waveguides and bends,” *Optics Express*, vol. 12, no. 12, pp. 12971–12979, 2010.

- [94] Halir, Robert, Bock, P. J., Cheben, Pavel, O.-M. nux, Alejandro, Alonso-Ramos, C. Schmid, J. H., L. Jean, X. Dan-Xia, J. G. Wangüemert-Pérez, I. n. Molina-Fernández, and S. Janz, “Waveguide sub-wavelength structures : a review of principles and applications,” *Laser & Photonics Reviews*, vol. 9, no. 1, pp. 25–49, 2015.
- [95] U. S. INAN and R. A. MARSHALL, *Numerical Electromagnetics : The FDTD method*. Cambridge university press, 2011.
- [96] Rsoft, “Fullwave and finite difference time domain method.” <https://optics.synopsys.com/rsoft/rsoft-passive-device-fullwave.html>, January 2017.
- [97] T. Photonics, “Ion-exchanged technology.” <https://teemphotonics.com/ioc/offer-and-products/ionex-technology.html>, November 2016.
- [98] N. Rahbany, *Towards Integrated Optics at the Nanoscale : Plasmon-emitter Coupling using Plasmonic Structures*. PhD thesis, L’Universite de technologie de Troyes.
- [99] Y. S.-C. Allison, Patterson, M. S., J. E. Hayward, and F. Qiyin, “Time-resolved fluorescence in photodynamic therapy,” *Photonics*, vol. 1, no. 4, p. 530, 2014.
- [100] A. A. Salman, A. Tortschanoff, G. van der Zwan, F. van Mourik, and M. Chergui, “A model for the multi-exponential excited-state decay of cdse nanocrystals,” *Chemical Physics*, vol. 357, no. 13, pp. 96 – 101, 2009.
- [101] S. Gabriel, I. Kohki, M. Saruyama, S. Masanori, T. Toshiharu, M. Sadahiro, and T. Naoto, “Ultrafast dynamics and single particle spectroscopy of auctdse nano-rods,” *Phys. Chem. Chem. Phys.*, vol. 15, no. 6, pp. 2141–2152, 2013.
- [102] J. B. Madrigal, R. Tellez-Limon, F. Gardillou, D. Barbier, W. Geng, C. Couteau, R. Salas-Montiel, and S. Blaize, “Hybrid integrated optical waveguides in glass for enhanced visible photoluminescence of nanoemitters,” *Appl. Opt.*, vol. 55, pp. 10263–10268, Dec 2016.
- [103] M. Berthel, *Plasmonique classique et quantique sous pointe optique par microscopie en champ proche*. PhD thesis, Universite Grenoble Alpes.

- [104] H. R. Phillip and E. A. Taft, “Kramers-kronig analysis of reflectance data for diamond,” *Phys. Rev.*, vol. 136, pp. A1445–A1448, Nov 1964.
- [105] R. Salas-Montiel, A. Apuzzo, C. Delacour, Z. Sedaghat, and A. Bruyant, “Quantitative analysis and near-field observation of strong coupling between plasmonic nanogap and silicon waveguides,” *Appl. Phys. Lett.*, vol. 100, pp. 231109–231113, 2012.
- [106] M. Fevrier, P. Gogol, A. Aassime, R. Mégy, A. Delacour, C Chelnokov, A. Apuzzo, S. Blaize, J. M. Lourtioz, and B. Dagens, “Giant coupling effect between metal nanoparticle chain and optical waveguide,” *Nano letters*, vol. 12, pp. 1032–1037, 2012.
- [107] C. Delacour, S. Blaize, P. Grosse, J. M. Fedeli, A. Bruyant, R. Salas-Montiel, G. Lerondel, and C. Alexei, “Efficient directional coupling between silicon and copper plasmonic nanoslot waveguides : toward metal-oxide-silicon nanophotonics,” *Nano Letters*, vol. 8, pp. 2922–2926, 2010.
- [108] H. G., “Fabryperot interferometers,” *Laser and Particle Beams*, vol. 4, pp. 319–320, 005 1986.
- [109] W. Pohl, W. Denk, and M. Lanz, “Optical stethoscopy : image recording with resolution wavelenght/20,” *Appl. Phys. Lett.*, vol. 44, pp. 651–653, 1984.
- [110] A. Bruyant, *Études de structures photoniques en champ proche par microscopie optique à sonde diffusante*. PhD thesis, L’Universite de Technologie de Troyes, 2004.

Josslyn BELTRAN MADRIGAL

Doctorat : Matériaux, Mécanique, Optique et Nanotechnologie

Année 2017

Intégration d'une source à photon unique dans un guide plan diélectrique

Le développement de dispositifs optiques intégrés dans des domaines tels que l'information quantique et la détection de molécules est actuellement dirigé vers l'intégration de nanosources (NS) sur des systèmes sur puce avec faible pertes de propagation.

Cette thèse montre une contribution à la conception, à la fabrication et à la caractérisation de structures photonique-plasmoniques en vue de l'intégration d'une seule NS sur des puces optiques à travers le spectre visible.

Nous recherchons à optimiser l'efficacité d'excitation et de collection de l'émission de la fluorescence d'une NS en combinant un nano-prisme en or et une structure formée par une couche de dioxyde de titane (TiO₂) et un guide d'ondes à échange d'ions (IEW) sur verre. Le couplage entre les modes permet un transfert efficace de l'énergie entre un mode faiblement confiné dans l'IEW vers un mode plasmonique confiné dans un volume effectif de quelques nanomètres cubes. Ce mode confiné interagit avec une NS en améliorant son émission de fluorescence par l'effet de facteur Purcell. En utilisant le théorème de réciprocité de l'électromagnétisme, nous avons étudié le cas réciproque où la lumière émise par la NS peut être collectée dans les modes photoniques du IEW.

La caractérisation a été réalisée en champ lointain et en champ proche avec en particulier l'utilisation d'un microscope optique de champ proche à sonde diffusante (SNOM). Nous avons proposé une configuration SNOM qui permet d'imiter l'interaction d'une NS et des systèmes guidés, cartographiant la densité locale des modes guidés (LDOM).

Mots clés : optique intégrée - plasmons - photoluminescence - nanoparticules - microscopie en champ proche - nanophotonique.

Integration of a Single Photon Source on a Planar Dielectric Waveguide

The development of integrated optical devices in areas such as quantum information and molecular sensing is currently directed towards the integration of nanosources (NS) into systems on a chip with low propagation losses.

This thesis shows a contribution on the design, fabrication, and characterization of photonic-plasmonic structures towards the integration of a NS on optical chips across the visible spectrum.

We pursue the efficient excitation and collection of the fluorescence emission of a NS by making use of the interaction between an electromagnetic field concentrator (gold nanoprism) and an integrated optics structure formed by a high-index layer of titanium dioxide (TiO₂) and a low-contrast index ion exchanged waveguide on glass (IEW). The coupling mode allows an efficient transfer of the energy between a weakly confined mode in the IEW and a plasmonic mode confined in an effective volume of few cubic nanometers. This confined mode interacts with a NS enhancing its fluorescence emission through Purcell factor effect. Using the reciprocity theorem of electromagnetism, we studied the reciprocal case where the light emitted by the NS can be collected into the photonic modes of the IEW.

The characterization was performed in the far and in the near field with the use of a scanning near-field optical microscopy (SNOM). We proposed a SNOM configuration that allows us to imitate the interaction of a NS and guided systems, mapping the local density of guided modes (LDOM).

Keywords: integrated optics - plasmons (physics) - photoluminescence - nanoparticles - near-field microscopy - nanophotonics.

Thèse réalisée en partenariat entre :



Ecole Doctorale "Sciences et Technologies"